University of Birmingham

The Development of Multimodal Nanoprobes for Cell Tracking in the Treatment of Autoimmune Hepatitis

By
Tasha Chauhan

Supervised by
Professor Michael Hannon, Professor Zoe Pikramenou,
Professor Ye Oo and Professor Hamid Dehghani

A thesis submitted to the University of Birmingham for the degree of
DOCTOR OF PHILOSOPHY

Abstract

The ability to track cells both in model systems and in the body is needed to enable scientists to better develop and understand new cell therapies and construct a wider understanding of the roles of different cell engagements. To explore this, in this thesis, cells are labelled with multimodal nanoprobes and a range of imaging modalities used for tracking and detection. Gold nanoparticles successfully performed as detectable scaffolds, holding both the coating and the luminescent compound, IrS1 (Iridium(III) bis(phenylquinoline-C2,N') 5,5'-bis(mercaptomethyl)-2,2'-bipyridine), and were able to enter human lymphocytes to allow detection utilising their optical and luminescent properties. Gold nanoparticles ranging in sizes of 13, 25, 50 and 100nm with different stabilising agents were compared for their loading abilities and biocompatibility. It was found the smaller particles with smaller-chain stabilising agents had minimal impact on the phenotypical and functional behaviour of the immune cells and were more readily taken up by the cells. Regulatory T cells dosed with nanoprobes with a gold core of 25nm coated with Zonyl and IrS1 were administered to human liver sections which were then imaged using Micro-CT and Multiphoton microscopy to observe the localisation of the transplanted cells.

Acknowledgments

Thank you for taking the time to read my thesis.

Firstly, I would like to thank my supervisors Professor Michael Hannon, Professor Zoe Pikramenou, Professor Ye Oo and Professor Hamid Dehghani for their continued guidance and support which has been greatly appreciated.

A special thank you to Mike for providing not only academic support but for also being an understanding mentor and advisor throughout this process.

I would like to thank the Hannon, Pikramenou and Oo groups and the Sci-Phy CDT cohort for support through both the laughs and tears. A special thanks to Siobhan King and Callum Campbell for training in chemical synthesis and Hannah Jeffery for training in immune cell preparations.

I wish to acknowledge the Physical Sciences for Health CDT, the EPSRC and the University of Birmingham School of Chemistry for financial support.

I would like to thank Paul Stanley from Metallurgy and Materials for help with TEM and Alessandro Di Maio from Biosciences for help and training on the Confocal Microscope. From the School of Dentistry, I would like to thank Jonathan James and Robert Harper for help with the Micro-CT instrument and from the Imaging Suite, Dean Kavanagh for training and support on the Multiphoton Microscope. I also extend thanks to Dr Song from the University of Warwick for help with ICP-MS.

Finally, I would like to thank my family: My grandparents, Tony, Sunita, Arjun and Eesha Chauhan for always pushing me to achieve the best I can and for believing in me. I hope I can make you all proud.

Table of Contents

1 Introduction

This thesis considers the design of new nanoparticle labels to track therapeutic cells. This chapter will reflect on the literature that forms the background to this study and will describe first the foundation for cell therapy and then the techniques that have been used previously for this and other applications.

1.1 Rationale for Regulatory T-Cell Therapy

Cell based therapies, despite being in their infancy, are progressively revolutionising modern medicine. Immunomodulatory therapy is the treatment of a disease which acts by stimulating or supressing the immune system[1]. There are some immunotherapies designed to reduce immune system activity and as such these are classified as suppression immunotherapies[2]. Autoimmune diseases arise from the loss of tolerance towards a patients' peripheral self-immune system. The increasing demand for liver transplantation matched with a reduction in the number of donors, has exacerbated the need for alternative therapies to prevent chronic active hepatitis, which can eventually lead to liver cirrhosis and liver cancer[2]. Developments in the field of cell isolation have led to the reliable isolation of haematological cell populations based on their cell-surface proteins, paving the way for new adoptive cell-based therapies. Currently the gold standard for Autoimmune Hepatitis (AIH) treatment involves a two-phased approach which first consists of moving a patient into a point of immunehomeostasis and then secondly to keep them at remission[3].

AIH is estimated to affect between 10 to 17 people per 100,000 in Europe and more commonly affects women over the age of 45. Although the main cause of the disease is the body's immune system attacking its own liver cells, it is thought that environmental factors and genetic predispositions can influence an individual's chances of having AIH. Symptoms of the disease vary depending on the degree of

liver damage but can lead to particularly serious conditions including hepatic encephalopathy (loss of brain function), ascites (fluid in the abdomen) and edema (swelling of the legs). The development of novel cell therapies is hoped to replace the need for prolonged global immunosuppression, which is well known to result in serious negative effects for patients. A recent systemic review looking at 319,000 people from 15 countries with a range of autoimmune diseases, including AIH, found that COVID-19 was twice as common in people with autoimmune diseases compared with the general population, largely attributed to the steroid based treatments they receive opening them up to an increased risk of getting infected[4]. The human liver contains different subsets of effector lymphocytes that are organised by a T-cell population known as regulatory T-cells. Failure of resident regulatory T-cells (Tregs) to supress effector cells is typical for autoimmunity leading to studies exploring the use of either polyclonal or antigen specific Tregs as cellular therapies[1].

The balance of effector and regulatory cells can be used to predict the outcome of hepatic inflammation. Regulatory T-cells are a sub population of CD4 T cells, characterised by the high expression of CD25 receptors and low expression of CD127 receptors. Clinicians who use Tregs for cell therapy often use a combined approach to isolate these cells either by magnetic isolation or by cell sorting. Tregs are currently considered the body's main source of tolerance regulation in the peripheral immune system. They function and communicate via cell-contact and soluble factor mediated mechanisms to supress the destructive pro-inflammatory and cytolytic activities of immune effector cells[5, 6]. One of the first clinical trials of Treg therapy reported was to investigate treatments for acute and chronic Graft vs Host Disease (GvHD) after allogenic stem cell transplantation[5]. Following this study, further trials into the use of Tregs for GvHD and type 1 diabetes mellitus have supported the feasibility of Treg

therapy in humans. Clinical trials for Treg therapy in AIH patients specifically are yet to be tested. Based on observations of proof-of-concept experiments in the maintenance of expression of the liver tissue homing chemokine CXCR3 in patients with AIH, the expectation is that infused Tregs will recruit to the inflamed autoimmune liver tissue (Figure 1)[1].

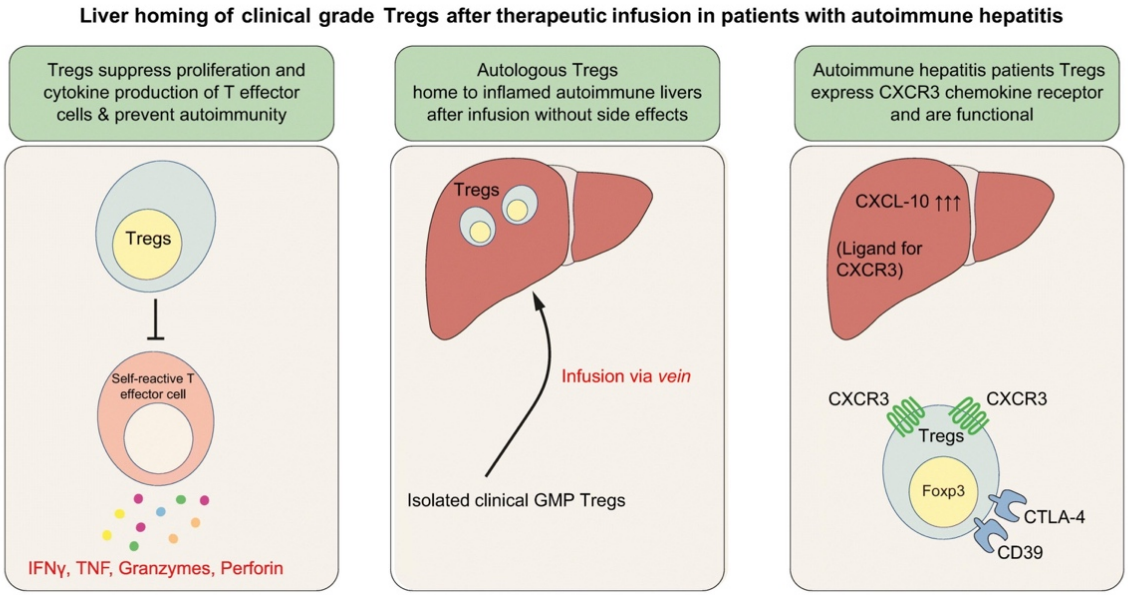

Fig. 1. Liver homing of clinical grade Tregs after therapeutic infusion in patients with AIH[1]
(Figure take from reference 1)

The liver has been widely recognised as an immunoregulatory organ, consisting of parenchymal and innate immune cells including hepatocytes and cholangiocytes, liver sinusoidal endothelial cells, hepatic stellate cells, Kupffer cells and many more[7, 8]. The intimate interactions amongst these cells and other immune cells collectively contribute to the overall immune tolerance in the liver[9]. The liver accepts blood from both the portal vein and hepatic artery and because antigens from digested food pass from the gut via the portal vein the immune feedback must be tightly regulated to provide liver protection. Significant advances in recent years have been made towards therapy for immune tolerance induction and in studying the

associated mechanisms involved in animal models, however, the translation of these assays into the clinic have presented greater challenges[9].

Autoimmune hepatitis, primary biliary cirrhosis (PBC) and primary sclerosing cholangitis (PSC) form the three main categories of chronic autoimmune liver diseases[10, 11]. PBC develops by the progressive destruction of intrahepatic bile ducts by nonsuppurative inflammatory processes. PBC prevalence varies with geographical location, with northern Europe being considered a disease hotspot[12]. Similar to AIH, PBC is more commonly found in female patients over the age of 50 years. The majority of PBC patients are asymptomatic at diagnosis and are only identified after screening tests show elevation of serum alkaline phosphatase levels. A more specific feature of PBC is the presence of antimitochondrial antibodies (AMA) in the serum of around 90% of patients affected. These antibodies are directed to the PDC-E2 antigen, a component of the pyruvate dehydrogenase enzyme complex present on the inner mitochondrial membrane, which are highly specific for PBC[13]. The presence of AMA indicates a specific B-cell response to the mitochondrial antigen, with specific T-cell responses directed against PDC-E2 observed simultaneously[14]. In patients with PBC, although the exact aetiology has not been established, it is thought that the mechanisms involved in the molecular interactions with PDC-E2 eventually lead to the breakdown of immune tolerance[13]. The only accepted therapy for PBC is ursodeoxycholic acid (UDCA), which has proved to extend transplant-free survival when started early in the disease course[15]. However, this course of treatment does not provide a disease cure, with around 40% of patients having no real biochemical response to UDCA. PSC is defined as a chronic disorder characterized by fibrosis and inflammation of the extra- and intra- hepatic biliary tree[10]. Unlike AIH and PBC, PSC is twice as likely to affect men compared to women and can manifest at a younger age

of around 30 years. The disease is often found in patients who also suffer from inflammatory bowel disease (IBD), ulcerative colitis[16, 17]. Patients with PSC are at a significantly increased risk of developing hepatobiliary cancer and colorectal cancer, particularly those in the 70% of patients who also have IBD[18]. A British study reported an incidence rate of 0.68 per 100,000 patients per year[19]. At present, there are no approved pharmacotherapies for PSC and so UDCA is still the most extensively investigated agent for treatment of the disease, however two of the larger clinical trials for UDCA in PSC were inconclusive, exposing high rates of adverse events[20, 21]. Understanding the pathways involved in the disease development have paved the way for more targeted agents to be investigated in ongoing clinical trials, such as CCR2 inhibitors and vascular adhesion protein-1 inhibitors, however liver transplantation still remains the most commonly used and potentially curative management treatment for PSC[22].

In liver transplantation, the application of hematopoietic chimerism stem cells to achieve graft tolerance has been largely studied, where chimerism may be defined as tissues from two different genetically distinct organisms that are able to coexist in one organism[23]. Application of this type of therapy helps to achieve donor-specific transplantation tolerance and allows immunocompetence for primary immune responses[24]. However, studies indicate that further modifications to this type of cell therapy are required as, despite the reports of less frequent GvHD, the risk had still not been completely mitigated[25-27].

Regulatory dendritic cells (DCs) were also recognised over 40 years ago for their potential to be potent antigen presenters due to their ability to link innate and adaptive immune responses for tolerance induction therapies[28, 29]. The absence of DCs may result in spontaneous and potentially fatal autoimmunity in the event of a

breach of self-tolerance in CD4 T-cells, largely attributed to their vital production of regulation cytokines within the tumour necrosis factor family. Preclinical studies of DCs in non-human primate renal transplant models suggested that a pre-transplant infusion of DCs increased the chances of allograft survival and various clinical studies, in autoimmune disorders, type 1 diabetes and Crohn's disease, have implied the safety and tolerability of the therapy[30-34]. As such, phase I and II clinical trials of liver transplant tolerance induction by regulatory DCs that are currently ongoing hold much promise and their results are hoped to be encouraging.

Macrophages are immune cells of hematopoietic origin and are vital in providing innate immune defence with tissue specific functionality directed towards regulation and maintaining organ homeostasis[35]. Human regulatory macrophages have distinctive attributes of macrophage differentiation, most appealing of which is their suppressive function[36]. Pilot studies of this type of cell therapy have implied that donor derived regulatory macrophages remained viable for more than 30 days post administration and tracking showed they accumulated in the liver, spleen and bone marrow[37]. The effect of regulatory macrophage therapy for liver transplantation is yet to be investigated.

Mesenchymal stromal cells (MSC) are non-hematopoietic multipotent cells that have the ability to differentiate into different cells types including osteoblasts, adipocytes and chondroblasts under specific directional conditions[38]. Bone marrow is traditionally the source of these cells, however more recent research has led to the proposal of other sources which may be more favourable when considering clinical applications. MSC induced immunosuppression for dual targeting of both the innate and adaptive immune systems have allowed for various studies, both *in vivo* and *in vitro*, to evaluate the immunoregulatory effect of MSC therapy[39-41]. As it stands, recent

studies have shown that MSCs are ineffective in providing sufficient immunoregulation, however research continues as more variables are yet to be investigated[42, 43].

Another branch of immunosuppressive cells to be investigated are regulatory B-cells which are able to suppress the differentiation of various pro-inflammatory lymphocytes[44, 45]. However, mechanisms of regulatory B-cells are still unclear and so research is still limited to pre-clinical investigations only.

Treg induced immune regulation is amongst the best studied and builds the core of tolerance mechanisms. There are many preliminary and clinical studies which have demonstrated the safety and efficacy of Treg therapy, despite the absence of a defined and optimised administration protocol in place. A clinical trial at phase I conducted by Kings College London presented results which complimented previous beliefs in showing Treg therapy exerts a donor-specific immunosuppressive effect[46].

1.2 Unknowns in Treg Therapy

The conditions which afford the greatest potential benefit of Treg cell therapy still need to be defined[47]. This includes optimal Treg dosing, the timing of the doses and whether other drugs will be administered with the Tregs. Furthermore, the relative effect of Tregs on the microenvironment *in vivo* needs further investigation. Tregs exert a dominant tolerance via an array of mechanisms including their high affinity IL-2 receptors which control effector cell expansion, stimulating the degradation of tryptophan to kynurenines which, in turn, inhibits T effector cells and directly effects antigen presentation on dendritic cells by reducing co-stimulatory molecules. These Treg functions can be enhanced by exposure to inflammation. Another area of interest that needs to be addressed is the *in vivo* stability of Tregs' phenotype post

transplantation into patients. T-cell receptor signalling enhances Treg T-cell interactions with other cell types such as DC's and interferon regulatory factor 4 expression, which contributes to a T-cells' suppressive function. The versatility of Tregs' suppressive roles makes them effective protectors of immune homeostasis and as such their phenotypic behaviour must be retained. Moreover, Treg localisation is critical for the cell therapy to function correctly. Tregs suppress locally through direct contact and paracrine actions (the signalling of one cell to induce a change in another cell) in the tissue in which they reside, thus their ability to traffic to and accumulate in specific tissue is vital to their function. Tregs can implement different combinations of suppressive activities in response to specific tissue microenvironments. Currently over 50 clinical trials of adoptive regulatory T-cell therapy have been completed or are ongoing (as listed at clinicaltrials.gov Accessed: August 2022). This work has been accomplished largely with *ex vivo* expanded Tregs which have been isolated based on the surface markers they present. Chimeric antigen receptor T-Cell (CAR-T) immunotherapies have opened a window into the development of specialised gene therapies[48]. However, CAR-T cell therapies are associated with challenges such as manufacturing difficulties, T-cell defects and treatment associated toxicities. CRISPR gene editing tools have demonstrated the ability to overcome these limitations in recent studies. CRISPR technology, based on RNA-DNA recognition, has proven to be a new platform to help improve the efficacy of CAR-T cells[49]. This can be achieved, for example, by depletion of inhibitory signalling molecules such as programmed cell death and cytotoxic T-lymphocyte antigen 4 to prevent T-cell exhaustion. However, CRISPR does not come without its own limitations, including off-target effects and difficulty in controlling delivery of the CRISPR therapy itself[50]. Innovations in the design of newer generations of CRISPR have enabled a secondary modification of CAR-T

cells to generate more efficient, inhibition-resistant products, but has not seen translation to the clinic yet due to the need to further monitor the genomic editing side effects which can be achieved with whole exome sequencing, whole genome sequencing or conventional cytogenetics[49, 50].

1.3 Safety of Commercially Available T-Cell Therapies

In clinic, CAR-T cells are manufactured via leukapheresis of peripheral blood to obtain blood mononuclear cells (PBMCs) enriched for membrane receptors CD4, CD8 and CD25. T-cells are then activated, *ex vivo*, after 3 to 21 days using antibody co-stimulatory agents[51, 52]. Commonly, the production of CAR-T cells involves the enrichment and growth of T lymphocytes that are genetically engineered under GMP conditions. At present the CAR-T cell therapies in the UK that are available include tisagenlecleucel and axicabtagene ciloleucel and brexucabtagene. These are approved for adult patients with relapsed or refractory large B-cell lymphoma (including diffuse large B-Cell lymphoma (DLBCL), high grade B-Cell lymphoma and transformed DLBCL arising from follicular lymphoma) only after 2 or more lines of systemic therapy failed to work. These products have demonstrated remarkable efficacy in these populations considering that the historic prognosis of patients after failing 2 preceding lines of therapies was poor. While acknowledging that CAR-T cells have revolutionised the treatment and prognosis of such diseases, these therapies result in unique arrays of toxicities, including cytokine release syndrome (CRS) and neurotoxicity (NT) also known as CAR-T-related encephalopathy syndrome (CRES) or immune related effector cell-associated neurotoxicity syndrome (ICANS). For monitoring purposes, various grading models are used in clinical trials to assess the usability of CAR-T cells by the severity of CRS and NT adverse events. CRS is caused by the release of cytokines during *in vivo* CAR-T cell expansion. The toxicity arises

from the systemic effect of these cytokines on multiple organ systems in the patient. Grading models assess the organ systems typically affected by CRS, but a fever is a key indicator that CRS has occurred[53]. To escalate matters, resident immune cells may augment the CRS process despite it being originated by the CAR-T cells. In worse cases, symptoms of CRS can result in hypotension responsive to fluids and hypoxia due to low-level oxygen support. There are many biological and molecular variables which have been studied as potential factors associated with NT. Endothelial activation of the CNS vasculature has been suggested, which showed that hypoalbuminemia, weight gain, disseminated intravascular dissemination signs and elevated cerebrospinal fluid protein (particularly albumin) and increased concentrations and ratio of angiopoietin 2 correlated with higher grades for NT severity, reflecting disruption of the blood brain barrier[54]. This study cross referenced the increased NT with increased serum levels of T-cell produced and stimulating cytokines such as IL-6, IL-10, IFNγ and IL-2. Animal models have helped improve understanding of the pathophysiology and potential therapeutic interventions. To work effectively, adoptively transferred Tregs must home to and mediate suppression at the target tissue selectively. Chemokines direct the trafficking and positioning of leukocytes within tissues and a deficiency in CXCR3, which drives their recruitment across hepatic sinusoids, has been associated with the exacerbation of liver disease and withdrawal of tolerance in mouse models of immune-mediated hepatitis. Research in these models highlights the importance of retaining the phenotype of CAR-T cells as well as being able to selectively track their localisation to ensure efficacy of the therapy. The precise role of CAR-T cells in the development of ICANS is still uncertain, however patients experiencing ICANS have showed signs of significantly elevated levels of cytokines in their cerebrospinal fluid post analysis. This observation suggests

a role played by stimulation of leukocytes and a subsequential increase in permeability across the blood brain barrier[55].

In recent years there has been significant improvements in managing the toxicities associated with CAR-T cell therapy. The most common strategies are more supportive in the use of tocilizumab (an immunosuppressive drug) and steroids. It is also vital to treat the symptoms of hypotension and hypoxia with IV fluids and positive oxygen pressure. However, neither of these actions directly addresses the root cause of the issue. Pre-clinical trials have sought the use of Defibrotide (a mixture of single-stranded oligonucleotides used to treat veno-occulsive disease of the liver) to prevent CAR-T cell induced ICANS by protecting endothelial cells from injury within the CNS[56].

1.4 Cell Tracking: Current Approaches

Being able to track immune cells *in vivo* is of great importance in revealing the biology of the microenvironments of target tissues and ultimately assessing the worth of cell therapies. This is of particular importance in patients who find themselves eligible for immunotherapies but where established imaging modalities such as PET and CT are not able to tell apart the true progression of the therapeutic cells from the pseudo-progression. Being able to make this distinction is vital when establishing a cell therapy's effectiveness, and usually this is assessed via the indirect measurements of either biomarkers or immunohistochemistry of tissue biopsies which are both subject to the type of clinical application and are not always the best option for the patient.

In order to determine the exact localisation of the injected Tregs, a non-invasive tracking technique needs to be implemented so immediate interreference can be administered where necessary to minimise any unwanted side effects[57]. Direct labelling consists of labelling the cells *ex vivo* with an agent that remains isolated in the cytoplasm of the cells for long enough to be injected into the tissue and be tracked to the target site. In pre-clinical trials currently, the most commonly used tracking agents are ^{111}Indium containing compounds with conjugates such as tropolonate or oxine[58] (Figure 2).

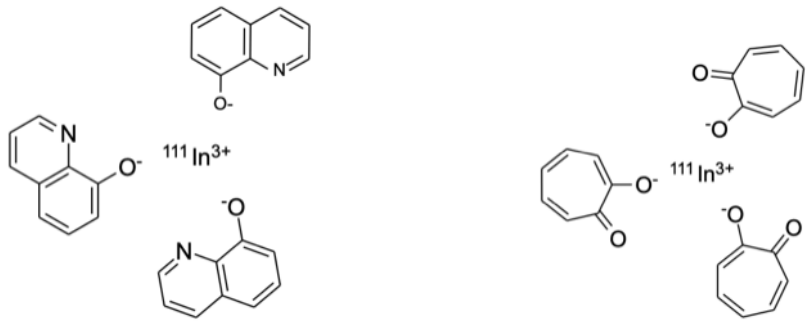

Fig 2. Left: Structure of Indium-111- Oxine, Right: Structure of Indium-111 Tropolonate.

Indium-111 is a radioactive isotope of Indium with a half-life of 2.8 days. This chemical agent is commonly used in nuclear medicine diagnostic imaging due to its radioactive decay which emits low energy gamma photons that can be imaged using planar or single photon emission computed tomography (SPECT) gamma cameras [58-60].

In cells, Indium-111 complexes dissociate, leaving Indium-111 bound intracellularly to cytosolic proteins, remaining stable, *in vivo*, over at least 24 hours [61]. Although most studies using ^{111}Indium tropolonate suggest there is little damage inflicted on the cells structurally and functionally, intra-organ localisation is a limitation

with this imaging technique. As seen in Figure 3, the indium conjugates give clear visualisation of which organs the labelled cells accumulate in.

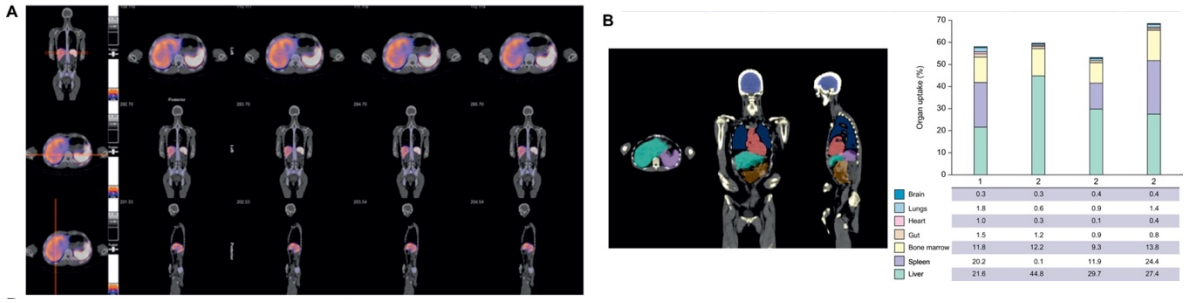

Fig. 3. SPECT-CT axial, coronal and sagittal imaging of GMP-Tregs at 24hrs after infusion and cell distribution[1]
(Figure take from reference 1)

It should also be noted that cells may die as a result of radiolysis or the agent can leak, increasing the signal from circulation and decreasing the target-to-background ratio. These issues make it difficult to image for long periods of time as well as prohibiting any evaluation of cell proliferation or function. For leukocytes, the labelling efficiency of radionucleotides is good, but a significant efflux rate has been reported, meaning image quality is considered suboptimal despite the use of a high energy single photon emitter for a contrast agent [62]. Recent advances have suggested the use of positron emitters could offer better resolution images as it would employ the use of PET imaging over SPECT, overcoming the long scan times and low-resolution images prone to artefacts and attenuation limitations associated with SPECT imaging. SPECT also cannot provide a quantifiable estimate of blood flow, which is attractive for tracking CAR-T cells. Copper-64 is a possible alternative, with a relatively long half-life of 12.7hrs[63]. Adonai *et al* used a ^{64}Cu derivative compound (^{64}Cu-pyruvaldehydebis(N4-methylthiosemicarbazone) to label C6 glioma cells, taking advantage of the compound's lipophilicity that resulted in a strong uptake (Figure 4). Despite the welcomed increase in uptake, they observed a relatively high efflux rate

and as such the compound presented the need for improvement. Another radionucleotide that has been explored by Charoenphun *et al* was ^{89}Zirconium-oxinate. Zirconium-89 has a half-life of 78.4hours, allowing for tracking of cells over a longer period of time (Figure 4). Myeloma cells were labelled effectively but they did suffer some conflicting results in terms of cell viability[64]. In 2018, Weist *et al* used PET to image adoptively transferred CAR-T cells that had been labelled with ^{89}Zr-oxinate[65] (Figure 4). Promisingly the CAR-T cells retained their *in vitro* cytokine production, migration and tumour cytotoxicity in addition to retaining up to 60% of the radionucleotide compound over a 6-day time frame.

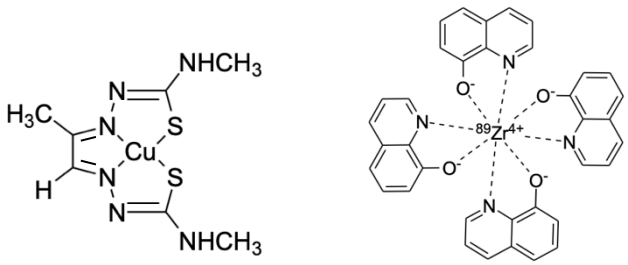

Fig. 4. Left: Structure of ^{64}Cu-pyruvaldehydebis(N4-methylthiosemicarbazone). Right: Structure of ^{89}Zirconium-oxinate.

Magnetic resonance imaging (MRI) is favourable for cell tracking owing to its known ability for greater depth penetration through tissue. MRI works using hydrogen atomic nuclei, particularly in water and fat, which are able to absorb radio frequency (RF) energy when placed under an external magnetic field. The resulting evolving spin polarisation of the nuclei can induce a RF signal in a radio frequency coil and thereby be detected. By varying the pulses of radio waves that excite the nuclear spin energy transitions, different contrasts may be generated between tissues based on the relaxation properties of the hydrogen atoms, proportional to the tissue density and water content. For more specific imaging, contrast agents may be used. Gadolinium

(III) chelates are effective contrast agents owing to their seven unpaired electrons which produce a magnetic moment that increases the relaxivity of water protons, shortens the longitudinal relaxation rate T1 and therefore increases the signal by creating a positive contrast in T1-weighted MRI images[66]. Sensitivity is limited to the amount of gadolinium that may be loaded into the cells[62]. Geng *et al* labelled rat mesenchymal stem cells with Gd-DTPA effectively enough to produce T1-weighted MRI images post injection in rat brains (Figure 5). The Gd-DTPA was shown to have minimal effect on cell viability and proliferation[67].

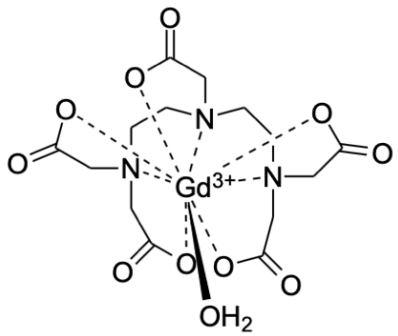

Fig. 5. Structure of Gd-DTPA.

Fluorine-19 based MRI has progressively become more attractive to image cells *in vivo* due to its specificity, quantification ability and the chemical inertness of the agents administered. Bouchlaka *et al* have shown high sensitivity detection of non-radioactive fluorine (^{19}F) using magnetic resonance[68]. Here the group labelled Human NK cells with emulsified perfluorocarbon which were detected, not only at the site of injection, but the group also followed their migration. Makela *et al* developed methods for ^{19}F MRI tracking of cells in mice on a 3 Tesla clinical scanner[69]. ^{19}F MRI has lower sensitivity compared to other tracking techniques and so ^{19}F MRI has only been performed at relatively high magnetic field strengths. The group focused on detecting macrophages in tumours as macrophage density is an indication of tumour

aggressiveness and concluded ^{19}F MRI could be used; at 3 Tesla, as few as 25,000 cells could be detected as cell pellets using perfluorocarbon labelling. ^{19}F signal was observed in the liver, spleen and tumour of mice at both 9.4 and 3 Tesla. As cells do not remain in pellet form when dosed to the subject, these observations were particularly significant.

Optical bioluminescence imaging makes use of cells which express the luciferase enzyme, which reacts with its substrate, luciferin, and emits light between 480 and 600nm depending on the type of enzyme (firefly, Renilla or bacterial) and substrate generated by the conversion of chemical energy into visible light[70]. Cells can only be monitored for up to a week post adoptive transfer, which can allow the monitoring of adverse effects on long term cell viability[71]. However, this technique is not fully reliable as it has been reported that even when cells are present, the bioluminescence signal may be lost due to metabolic changes as luciferase is reliant on energy and cofactors. As such, it is common practice to use bioluminescence in conjunction with another reporter gene such as Green Fluorescent Protein (GFP), which would allow for the detection of cells by flow cytometry or immunostaining of organs[72]. The main issue here is that this is invasive and not applicable for clinical patients. More recently, research into the improvement of bioluminescence imaging has been moving towards adopting the bioluminescence resonance energy transfer (BRET) principle to improve cell tracking by this technique. BRET is the energy transfer between a luminescence donor, typically a luciferase, and a fluorescence acceptor, namely a fluorescent protein, in specific conditions.

Wang *et al* labelled rat mesenchymal stem cells with their unique GpNLuc reporter and evaluated its cell tracking efficacy *in vitro* and *in vivo* and saw their system produced more robust bioluminescence signals with minimal background noise that

allowed for better correlation to cell numbers compared to a fluorescence-based approach[73]. The group recognised that, non-linear attenuation of photons produced as a result from deeper penetration depths in tissues, coupled with tissue optical heterogeneity, significantly diminishes the ability to quantify the signal in larger samples and that metabolic changes can also influence the consistency of bioluminescence signals even with the adapted approach.

However, the GpNLuc reporter showed a 10-fold increase in total light output compared to the use of NanoLuc moieties independently, reduction in acquisition times and demonstrated sensitive monitoring of tumorigenesis at deep tissue levels, suggesting the GpNLuc reporter could be better engineered for subcutaneous applications. Adaption of the reporter further by using LSSmOrange (OgNLuc) generates a weaker light due to a lower BRET efficiency but emits at a longer wavelength which could prove beneficial for deeper tissue penetration. More encouraging was the reporter independency of ATP seen when using GpNLuc for bone tissue engineering specifically as inorganic phosphate homeostasis is crucial for hydroxyapatite formation.

As personalised medicine and CRISPR-editing develop there is greater need to improve the efficacy and safety of targeted cell therapies. Kelly *et al* developed a non-viral vector-based system for large DNA multimodal reporter genes to be integrated into the safe harbour genomic locus AAVS1[74]. The group engineered a reporter gene probe constructed of a clinically used MRI reporter, Oatp1a1, with a fluorescent and bioluminescent gene to enable cell sorting and non-invasive BLI/MRI of engineered cells to test in a pre-clinical cancer model.

Although this work shows promise for safer nonviral genome editing for cell tracking, the effects on cell function cannot be ignored. The study showed a slower

growth rate for some cell types with the inserted reporter genes and although this was attributed to the heterogeneity in clonal populations, observations such as these could allude to underlying phenotypical changes that were not tested for in this particular series of checks. BLI also suffers poor translatability with respect to the ethical considerations surrounding genetic modifications and as such, limits the uptake of this therapy into clinics.

Kang *et al* utilised the principals of bio-orthogonal chemistry and coupled the fluorochrome dibenzyl cyclooctane to Cy5 for near infrared (NIR) fluorescence imaging by intravenous injection into mice[75]. The group intended to chemically bind the fluorochrome to the azide groups on the surface of the target cells by glycoengineering, a technique for manipulating cellular metabolism to modulate glycosylation with the hope to install non-natural substances into glycoconjugates[75]. This method of fluorescence imaging was promising but also has the disadvantage that NIR is limited with low sensitivity as a result of low absorption coefficients meaning the detection limit must be greater.

Another favourable method of tracking adoptively transferred cells is by tracking adoptive cell therapy (ACT) products using T-cell receptor (TCR) deep sequencing using pre and post-infusion samples from patients with, for example, melanoma, breast cancers and Merkell cell carcinoma[76]. ACT products here refers to the T-cells transplanted. This study tracked clonotypes in the days to months post infusion and compared clonotype parameters with clinical parameters. This strategy facilitated tracking by quantitative polymerase chain reaction (PCR) – based approaches[77]. TCR deep sequencing allows for thousands to millions of clonotypes to be determined per run, with platforms based on T-cell receptor beta variable primer specific multiples PCR or DNA using illumine sequencing.

An additional technique even allows for *de novo* determination of clonotypes using total RNA-Seq data permitting TCR mining across the many publicly available RNA-Seq databases[78]. Using TCR deep sequencing, studies have shown the clonotype diversity and clonal hierarchy of the ACT products pre-infusion were heterogenous and could not predict a clinical outcome. For some patients the clonal hierarchies in the ACT products did not correlate with the peak clonotype hierarchy post infusion. Results such as these indicate considerable restructuring of the T-cell repertoire once the product went *in vivo.*

Although TCR could provide predictive information on ACT product quality and patient outcome in the future, the discrepancies within clonal frequencies means this technique is still in early development for this application. Other studies have described this technique as limited also, since such monoclonal T-cell products exhibited only a short survival *in vivo* (<14 days) in most patients, likely reflecting the extensive expansion required to attain therapeutic cell doses and the associated terminal differentiation.

At research level, various cell labelling methods have been developed for bioluminescence imaging, fluorescence imaging, MRI and PET scans (Figure 6)[79, 80].

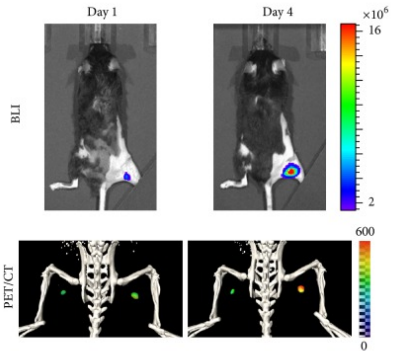

Fig. 6. Visualization of DC migration into the lymph node in vivo using multimodal imaging. Cells were injected in the left or right mouse footpad, respectively. Signals were observed in the lymph node[79]
(Figure taken from reference 79)

Direct labelling may present itself as the simplest approach as all that is required are labelled monoclonal antibodies or peptides that are able to bind to target cells *in vivo* without the need for *ex vivo* genetic manipulation. Nonetheless, a limitation of direct labelling via antigen binding arises when expression of the target antigen occurs on other subpopulations or even physiological uptake of the label by surrounding cells. These concerns can be overcome using reporter genes. Bioluminescence requires cells to be transfected with a reported gene which provides its own challenges due to low transfection efficiency and the weak signal at the single cell-level. Fluorescence dyes do not allow for quantitative biodistribution information to be obtained due to the restriction in penetration depth[81]. MRI can perform 3D tracking, but the results are not quantitative and PET scans do not provide information on a single cell level[82, 83]. Therefore, an approach is needed that combines the advantages of each of the techniques.

1.5 Cell Tracking: Nanoparticles

Nanoparticle-based imaging is rapidly growing in the field of molecular imaging[84]. Two main objectives drive this research; one being the *in vitro* internalisation of the nanoparticles into the therapeutic cells and the other being the non-invasive imaging of the cells post *in vivo* injection of the cells[85]. Biocompatible nanoparticles (NP) have the potential to be broadly used in the clinic to enable longer time periods of tracking with simultaneous imaging. NP loading into cells is vital to investigate as higher concentrations of NPs will directly increase the contrast in images produced, however it is important to retain a cell's viability and functionality, especially in ACT where the T-cells in question are expected to perform immunosuppressive behaviour when they have reached their target sites. A reliable and clinically applicable imaging modality needs to be implemented so that small clusters of cells are identifiable against the surrounding soft tissue. The ability to quantify the number of cells detected is another requirement that could be greatly of interest. The introduction of gold nanoparticles (AuNPs) as contrast agents has expanded the use of CT to that of molecular and functional imaging[86, 87].

Gold nanoparticles have been extensively studied and are well known for their biosafety and *in vivo* chemical stability, biodistribution and pharmacokinetics[88-94]. Other favourable features of AuNPs include their high density and high degree of flexibility in terms of particle size, shape and their ability to conjugate a range of functional groups, allowing them to become the scaffold for multimodal imaging probes.

Direct visualisation of AuNPs in biological systems can be obtained using a variety of techniques, including Darkfield (DF) Microscopy, brightfield microscopy and transmission electron microscopy. In the nm scale these techniques allow for

visualising of single AuNPs interacting with the biological environment. DF microscopy is a scattering based technique which produces a bright image of the specimen on a dark background. The strong scattering signal of AuNPs is attributed to their high scattering coefficients which are approximately 5 orders of magnitude higher than most conventional fluorescent dyes[95]. For many imaging methods that are based on the AuNPs Rayleigh scattering, their signal needs to be differentiated from the background meaning that the minimum size these particles need to be is around 40nm. Photothermal imaging makes use of the fact that for smaller AuNPs, their strong absorbance of light could be converted to heat that warms up the environment surrounding the AuNPs. The temperature change of the medium results in a reflection index change that shifts the phase of the transmitted light beam[96]. AuNPs have been shown to greatly increase the excitation of fluorescent probes where the overlap between the surface plasmon resonance (SPR) of the AuNPs and the absorption and emission spectra of the fluorophore occurs giving the opportunity for plasmon enhanced spectroscopy [97]. However, for most optical imaging techniques, the imaging depth is limited to several hundred μm. This is due to the strong scattering that greatly decreases the depth a photon can travel within tissues. Recent advances have enabled deep tissue imaging such as multiphoton microscopy and photoacoustic imaging. The SPR of the AuNPs enables the enhancement of multiphoton absorption and can act as a contrast agent with addition of functional groups[98].

Gold Nanoparticles are also undergoing development for multimodal imaging, with and without radiotracers [99, 100]. Using a CD19 CAR-T cell model system, cells were loaded with ^{64}Cu-labelled gold nanoparticles by electroporation (Figure 7).

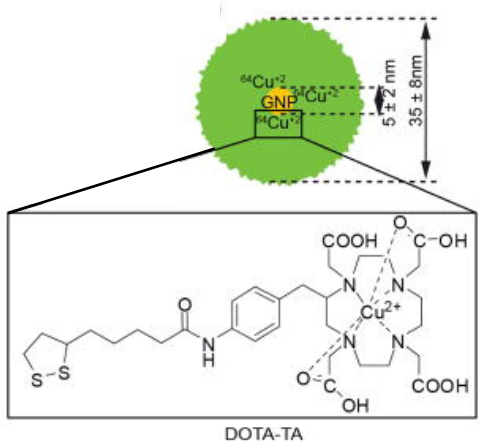

Fig. 7. Schematic of 64Cu-labelled AuNP[100]
(Figure taken from reference 100)

After an intravenous delivery, PET signal was recorded in the lungs after 14 hours, whereas cell-free administered NPs accumulated 25-fold and 17.5-fold more in the spleen and liver, respectively. However, the electrotransfer caused a 50% death in cells after 12 hours. The same research group then went on to develop a PET/MRI contrast agent using superparamagnetic iron oxide nanoparticles (SPIONS) and demonstrated internalisation of the positively charged NPs which bettered the cell viability to 80% (Figure 8)[80].

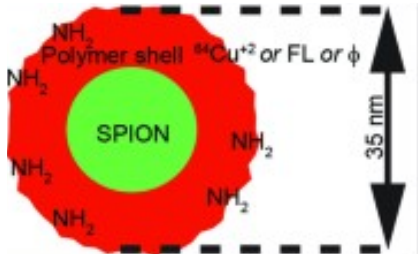

Fig. 8. Positively charged SPION with polymer shell and either FL or ^{64}Cu coating[80]
(Figure taken from reference 80)

Fairclough *et al* looked at adding radionucleotides to chitosan nanoparticles to reduce efflux rates of tracking devices out of the cell, using mixed lymphocyte cell populations, whilst also improving cell viability and function; which are significantly impaired when dosing the radionucleotides independently (Figure 9)[101, 102].

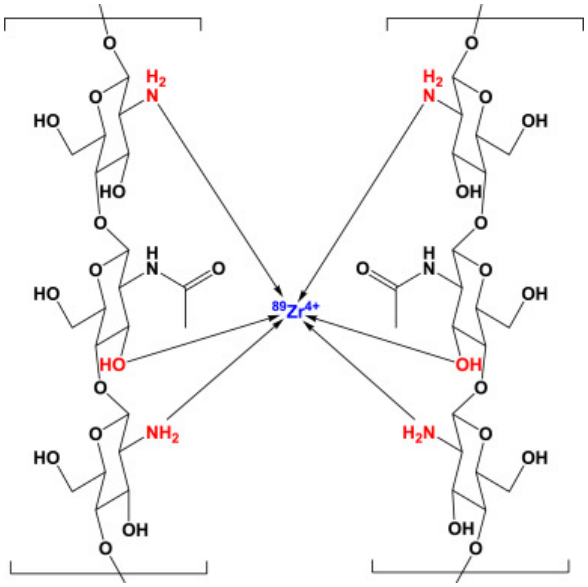

Fig. 9. Proposed representation of the binding of zirconium-89 to chitosan NPs [102]
(Figure taken from reference 102)

SPIONS have an inherently larger effect on MRI relaxivity than soluble paramagnetic agents, such as gadolinium chelates. Their core can contain up to serval thousand Fe atoms, thus increasing the local Fe concentration and sensitivity. To eliminate the notorious toxicity of Fe in the body, commonly, SPIONS are coated with more biocompatible compounds such as dextran, silica, citrate, polymers and even gold nanoparticles. The superparamagnetic agents result in negative contrast in T2-weighted images by causing inhomogeneities in the local magnetic field and spin-spin dephasing, which shortens transverse relaxation times[103]. A review by Kircher *et al* exhibited that SPIONS of varying sizes have been explored, ranging from ultra-small superparamagnetic iron oxide (USPIOs) of 10-50nm into micrometre-sized iron oxide (MPIOs) at >1μm[104]. As with all nanoparticles for *in vitro* labelling of cells, size influences cellular uptake, retention, biocompatibility, efflux, image contrast intensity and cell functionality. The larger the NP, the less a cell can hold before viability is significantly impaired, limiting intracellular concentrations and thus the sensitivity of cell detection. Foley *et al* showed that macrophages, which inherently like to take in

extracellular material, were easily labelled with micro-meter sized iron oxide particles and were able to be analysed via *ex vivo* MRI as well as being monitored post injection via MRI[105]. *Smirnov et al* alluded to another advantage of using MRI as a tracking tool in that it affords the ability to detect a smaller number of cells that may be difficult to label compared with using other imaging modalities[106]. More recently, Dallet *et al* investigated the use of two micrometric commercial iron oxide particles and analysed their endocytic pathways into glioma cells[107]. They saw that although the particles were good T2 and T2* contrast agents, they had potential to be used as T1 contrast agents which would be more advantageous as it would clarify their interpretation, eliminating any doubt related to other T2* generating species such as air. It is well established that particle uptake into cells is largely size dependant. The group suggest that the smaller diameter particles (~50nm) are internalised by caveolae-dependant pathways, whereas the larger MPIO particles (~1μm) are internalised by macropinocytosis (the ingestion by cells of extracellular liquids and dissolved molecules). However, some larger MPIOs could also be taken into cells via clathrin-dependant endocytic pathways, though this process is highly dependent on cell type[108]. Although the group showed the particles to be effective for MRI cell tracking as the larger sizes enable more effective use of the applied external magnetic field, cells suffered degrees of cytotoxicity which cannot be ignored. Functionalisation or shell-coating could avoid these issues, albeit they do not disrupt the T1 weighted signal.

Liu *et al* have looked at incubating immune cells with gold nano-stars for tracking in mice models[109]. The group used two-photon photoluminescence (TPL) for high resolution sensitive optical imaging to locate their macrophage cells labelled with the PEGylated nano-stars. TPL imaging confirmed that the liver, spleen and lung had

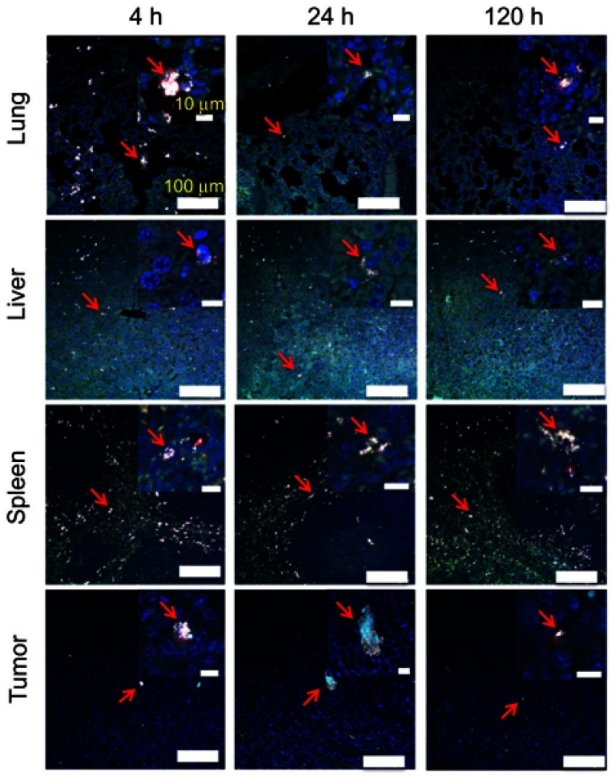

Fig. 10. Macrophage cell tracking with GNS. TPL imaging of DAPI stained tissue section 4 h, 24 h or 120 h after the systematic administration of GNS-loaded macrophage cells into mice with E.G7 tumour. The red arrow shows GNS-loaded macrophage cells. GNS nanoparticles are shown as white spots under TPL. Scale bar is 100um and 10um (zoom in)[109]
(Figure taken from reference 109)

high macrophage cell accumulation which correlated positively with their results obtained by inductively coupled plasma mass spectrometry (ICP-MS) which showed 46.5% ID/g Liver uptake, 151.2% ID/g spleen uptake and 111.5% ID/g lung uptake (Figure 10). Chhour *et al* used X-ray CT to image coronary arteries non-invasively post injection of AuNP labelled monocytes in apolipoprotein E deficient mice (Figure 11)[110].

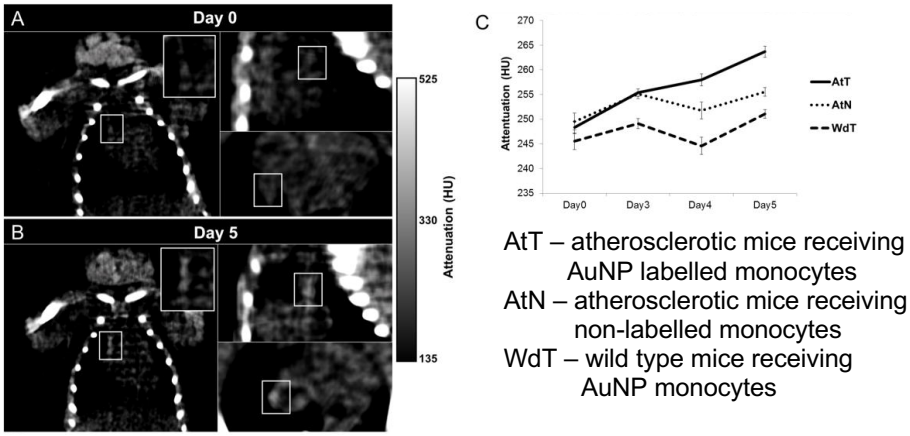

Fig. 11. CT scans of AtT for (A) day 0 and (B) day 5. Boxes indicate aortic region. Attenuation increases in the aorta over 5 days. (C) Graph plotting average intensities on the aorta of the mice in CT scans over time[110]
(Figure taken from reference 110)

The AuNPs used were synthesised as citrate AuNPs which underwent ligand exchange with 11-mercaptoundecanoic acid to give monodispersed spheres of 14.6±1.5nm, by TEM. With consideration for the attenuation values obtained each day and random effects, the group found a statistically significant increase in attenuation for the AuNP incubated cells model compared to their control group of blank cells. This increase in attenuation suggested that the recruitment of AuNP labelled monocytes can be detected by CT imaging[110, 111]. Ning *et al* developed novel AuNPs synthesised

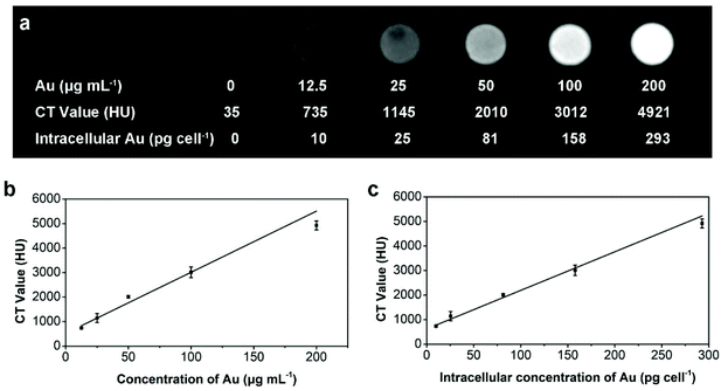

Fig. 12. a) In vitro micro-CT imaging of the hMSCs (1 × 106 cells) labelled with Au@BSA@PLL at different Au concentrations. (b) Calculated HU values as a function of the concentration of Au@BSA@PLL added for cell labelling. (c) Calculated HU values as a function of the intracellular Au Concentrations[112]
(Figure taken from reference 112)

with bovine serum albumin via an *in situ* growth method and modified them with a poly-L-lysine layer yielding Au@BSA@PLL nanotracers which showed enhanced biocompatibility and intracellular uptake with a hydrodynamic size of 21.28nm[112]. These nanotracers were investigated *in vitro* and *in vivo* for tracking human mesenchymal stem cells (hMSCs) with CT (Figure 12 and 13).

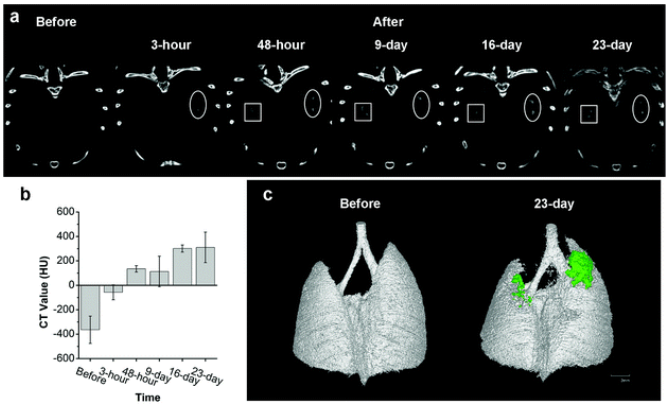

Fig. 13. a) In vivo micro-CT images of the Au@BSA@PLL labelled hMSCs at 3 h, 48 h, 9 d, 16 d and 23 d, respectively, after transplantation into the lung of a PFI mouse. The micro-CT image of the lung before transplantation acted as a control. (b) The CT values of the labelled hMSCs before and after transplantation into the lung at 3, 48hr, 9 d, 16d, and 23d respectively. C) 3D CT images of the labelled hMSCs at 23days post transplation[112]
(Figure taken from reference 112)

The group observed high loading of the nano-tracers at 293pg per cell had negligible influence on the viability, proliferation and osteogenic and adipogenic differentiation of the labelled hMSCs. Using pulmonary fibrosis injury mouse models, they were able to track the cells up to 23 days post transplantation *in vivo*. Although this group showed that the nano-tracer worked effectively as a CT contrast agent, this technique could not provide information on the viability of the cells post injection. Simultaneous use of reporter genes for labelling the hMSCs would be a way of overcoming this issue.

Fluorescent NPs have unique advantages of higher brightness, tuneable fluorescence and better photobleaching resistance[113]. Quantum dots are a class of inorganic semiconductor nanocrystals with unique photophysical properties, including

long fluorescence lifetimes, high fluorescence quantum yields and excellent photostability[114, 115]. Traditionally, QDs have shown limitations such as high toxicity and short circulation times and, when encapsulated with polymer materials, have induced undesired immune responses[116]. In overcoming these limitations, silver sulphide (Ag_2S) QDs have been most successful for cell tracking due to their superior photostability and high quantum yields in the second near-infrared (NIR-II) window[114]. Li *et al* encapsulated an Ag_2S QD with fluorescence in the NIR-II window (1000-1700nm) with protein nanocages using simian virus 40 as a model [117]. The dynamic *in vivo* distribution of the nanocages in living mice was tracked in a real time manner due to the high spatiotemporal resolution and deep tissue penetration of NIR-II fluorescence imaging[118].

Silica dye-doped fluorescent NPs are a type of fluorescent probe that have been applied to stem cell labelling and tracking[119]. The encapsulation of a dye within

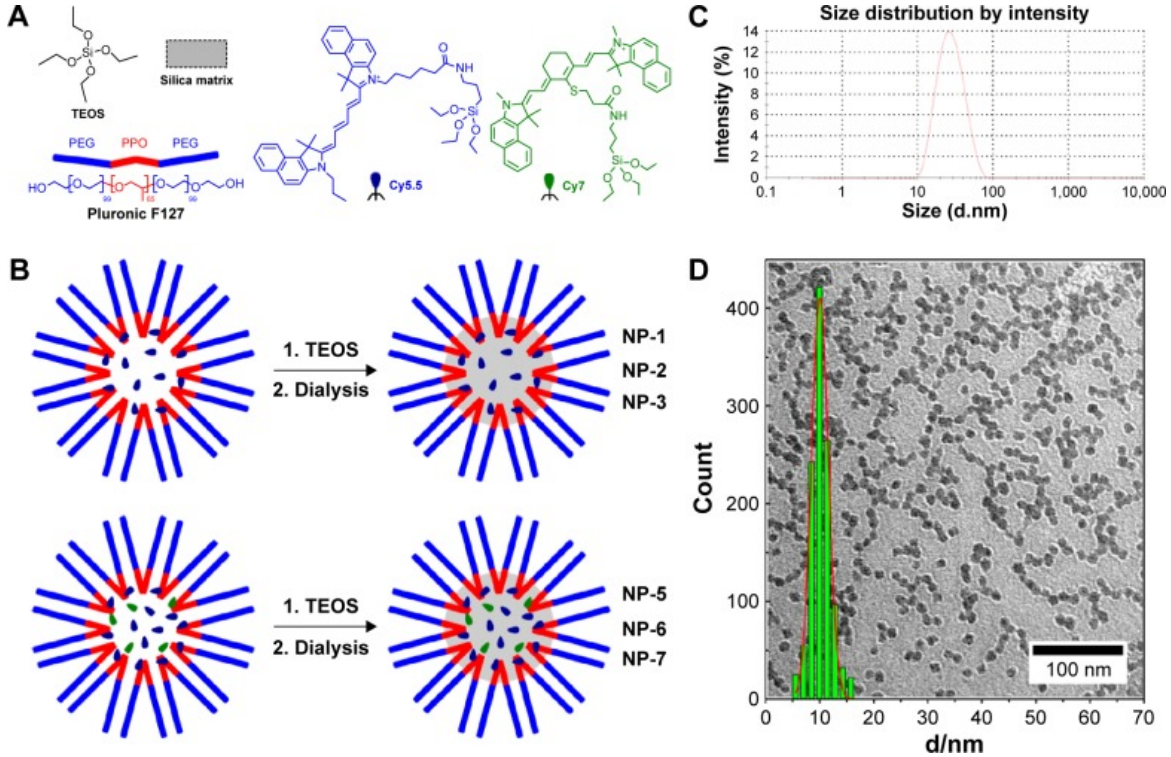

Fig. 14. a) Silica dye-doped fluorescent NPs chemical structures. b) schematic representation of NIR-Plus NPs synthesis. C) representative DLS hydrodynamic diameter distribution in water. D) representative TEM image with core diameter distribution[119]
(Taken from reference 119)

the silica affords better photostability, high biocompatibility and surface functionalities. Biffi *et al* developed core-shell silica-PEG NPs with strong NIR emission which showed promise for cell tracking abilities (Figure 14). By doping with cyanine 5.5 and cyanine 7 dyes into the silica NPs, fluorescence can be detected at 720 and 860nm respectively.

AuNPs on their own can be used for ultrasound and photoacoustic imaging of transplanted cells[120]. These AuNPs can be functionalised to form multimodal fluorescent probes. *Lee et al* synthesised multi-layered nanoprobes by combining poly – L – lysine (PLL) with cy5.5 and poly-D-lysine (PDL) with FITC dye onto an AuNP core[121]. The fluorescence of cy5.5 and FITC can be quenched by the AuNP in the intact multi-layered nanoprobe. In living cells, PLL in the multi-layered nanoprobe can be degraded by intracellular proteases and the red fluorescence of cy5.5 is produced. In apoptotic and necrotic cells, the protease resistant PDL can be degraded by the produced reactive oxygen species and the green fluorescence of FITC is produced. By this way the fate of the cells can be tracked both *in vitro* and *in vivo*. This is a promising strategy for tracking the viability of transplanted cells and has potential to evaluate the efficacy of treatment[114].

AuNPs are typically obtained by reduction of a gold salt and coated in an organic or inorganic layer to provide colloidal stability[122, 123]. The localised surface plasmon resonance (SPR) due to the oscillation of free electrons at the surface of the AuNP allows for very specific characterisation of the NPs formed and allows for a discriminative method for the fine tuning of desired optical properties via different sizes and shapes of the AuNPs (Figure 15)[124, 125].

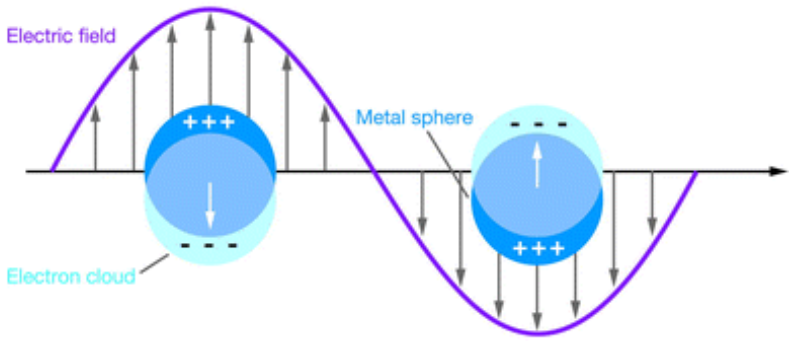

Fig. 15. Schematic illustrating a localised surface plasmon resonance[125]
(Taken from reference 125)

Adjusting the synthesis of spherical NPs gives the potential for modifying the size of the NPs formed which is of great interest in terms of molecular imaging [126, 127]. Varying the size of the AuNPs has surface to volume ratio benefits when considering the addition of surface functionalising moieties for purposes such as protein targeting or bioimaging. Increasing the size of the NPs red-shifts the SPR which in itself can be beneficial given that many optical biomedical imaging techniques take advantage of the near-infrared region (NIR) as it is well known that tissue absorption at this end of the spectrum is low[128]. However, it should also be noted that larger NPs are less easily taken up by cells and may induce toxicities that were not so prominent with the smaller NPs. The increased volume of exogenous material in a cell can cause phenotypical and pharmacokinetic issues.

Another way of adjusting the SPR to fit into the NIR region would be to adjust the shape of the NP[129]. Spherical NPs are advantageous in terms of uniformity and cellular uptake, however, gold nanorods (AuNR) have significant advantages in that they possess both transvers and longitudinal SPRs which can be manipulated by adjusting the length to width ratio and interestingly even very small AuNRs have landed within the NIR region as a result[130]. Core-shell nanorods have also been developed that are effective agents for multiple imaging modalities[131]. Pohling *et al*

show that their spindle shaped iron oxide core NRs coated with gold offer T2 contrast using MRI and also were multimodal, giving imaging opportunities with photoacoustic imaging and SERS[132]. Other shapes have also been investigated, mainly with the desire to optimise the surface to volume ratio of NPs to obtain maximum loading potentials of functional groups. Nanostars, for example, provide a very high surface to volume ratio and prism shape NPs have even been shown to have greater uptake in some cell linages[133].

Darrigues *et al* used multimodal Au-nanorods to track their interaction with pancreatic-stromal tumour spheroids by multimodal imaging[134]. The group were able to use fluorescence live imaging, photothermal and photoacoustic analysis to examine the nanoparticle behaviour in the spheroids. Interestingly, the study showed that the dye and NR signal did not always overlap, suggesting the need for further development into the binding of functional groups, however the research did demonstrate the potential for creating multi-source tracking.

The fine tuning of the physiochemical properties of AuNPs is greatly exploited in the field of cell tracking to evaluate the efficiency of cell-based therapies. The significance of the physiochemical parameters of AuNPs for cellular uptake has been investigated in the literature with the clear goal to maximise cellular uptake while

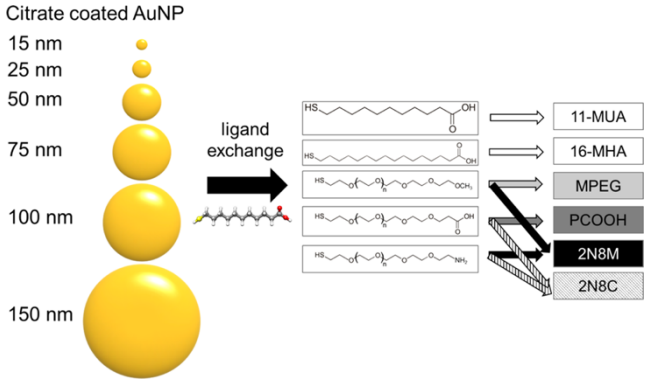

Fig. 16. Schematic depiction of the range of AuNPs used in the study. PEG-amine coatings were mixed in 1:4 ratios with MPEG and PCOOH to provide stability. The ligands examined represent different functionalities and charges[135]
(Taken from reference 135)

having as little as possible effect on cell function. A study by Chhour *et al* looked at the effect of size and surface chemistry of AuNPs in monocytes (Figure 16)[135]. The effect of both the coating and size of the AuNPs on their cellular uptake was investigated using AuNPs with a core diameter ranging from 15 to 150nm and functionalised with a variety of different organic coatings. AuNPs with a terminal carboxylic group were taken up less than those coated with methoxy-PEG despite the increase in size. The terminal carboxylic group coated NPs were found to have an optimum size uptake at 50-75nm, rather than being at the smaller or larger end of the spectrum.

The group also highlighted the need to optimise the time for incubation and the dose concentration of the AuNPs. Recent studies have also emphasised the importance of considering the effect of the serum protein corona on NP interactions with cells and ultimately their internalisation[136-138]. The size and the functionalisation of the AuNP heavily influence the formation of the protein corona and thus their cellular uptake[139-141]. A conclusion that all these studies agree on is that when labelling cells for cell tracking, the formulation of the AuNP must be optimised for that specific cell type and this includes the size and surface chemistry of the AuNP[142].

These requirements for a tracking probe make AuNPs very attractive given the ease for manipulation of the morphology and functionalisation. Meir *et al* used a glucose coating to enhance the labelling of primary T-cells which were genetically engineered to act against melanoma specific T-cell receptors. After a 1 hour incubation of the 20nm coated NPs, CT attenuation was observed at the tumour site after just 24 hours post intravenous injection[87].

This follows on to another very important factor when designing nanoprobes for cell tracking; the longitudinal visualisation of cell migration to provide data on the long-

term fate of therapeutic cells. Betzer *et al* showed, using CT, cells in the body can be tracked for a period up to 1 month post injection, here using the example of mesenchymal stem cells administered via the intracerebroventricular in rats, validated by immunohistochemistry[143].

Mier *et al* also showed that mesenchymal stem cells administered intramuscularly in mice with muscular dystrophy that were incubated with NPs were detected up to 4 weeks post injection (Figure 17)[144].

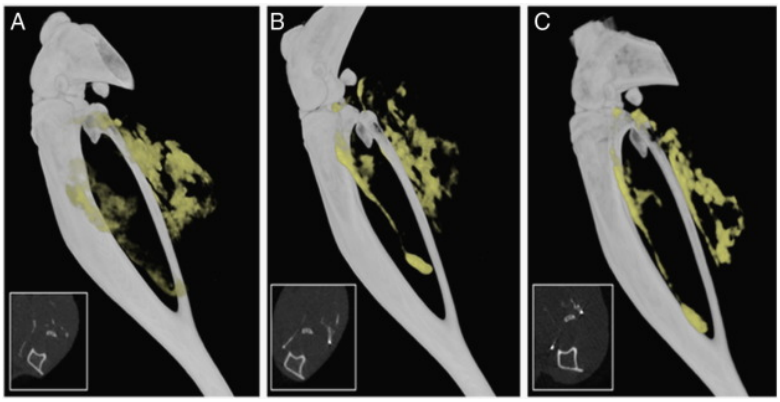

Fig. 17. Longitudinal cell tracking with CT. 3D volume rendering of CT scans after transplantation of $2x10^6$ mesenchymal stem cells in the muscle of the mouse limb. A) 24 hours, b) 2 weeks, c) 4 weeks post injection[144]
(Taken from reference 144)

Here the use of AuNPs displays yet another advantage for cell tracking over those techniques currently being used in clinics in that tracking with CT over long periods of time negates the use of radiolabelling which can only be used for shorter periods of time due to the radioisotope decay. The aspect to consider here, however, is the differentiation of cells and the fact that AuNPs will be distributed amongst the daughter cells. The implications of this are that despite the amount of gold in the body remaining unchanged, the amount of gold per cell will decrease and as such this leads to a less accurate quantification of cell numbers and even depletion of signal as the intensity may decrease. For techniques such as CT this effect may be observed less depending on the core size of the AuNP being used. Here leads to another

consideration that requires attention; whether the AuNPs remain in the cell for the entirety of the tracking process or whether they come out, meaning cells are no longer being tracked, but rather the AuNPs.

This is a consideration for all cell tracking probes and not just gold nanoparticles. It can be assumed that imaging immediately post injection will show the incubated cells, this issue progressively becomes of greater concern the longer the imaging time frame. One method of achieving data on this area and design would be to use reporter genes that would provide information of the health of the incubated cell, that is if the researcher can overcome the limitations of stable transfections and concerns of immunogenicity that come with using reporter genes[85].

Harmonic nanoparticles have recently offered strong platforms for multimodal imaging. Vuilleumier *et al* have developed non centrosymmetric crystal structure based harmonic nanoparticles to image and track cells using multiphoton microscopy[145, 146]. The nanomaterials $BiFeO_3$ and $LiNbO_3$ were heavily characterised using their second harmonic scattering properties. When two photons are combined, by the system, in time and space, while their frequencies do not add up to an existing transition of the material there is a possibility to generate an emitting photon at exactly twice the frequency and half the wavelength.

This differs from upconverting nanoparticles where they absorb two photons and add their frequencies to match the difference between two molecular levels. In the harmonic generation process, there is no energy that is deposited onto the sample as you only reach a virtual level. Advantages of implementing harmonic nanoparticles are greatly attributed to their excitation wavelength tunability, meaning it is possible to select an excitation wavelength away from any absorption on your sample tissue. Additionally, the harmonic nanoparticles also have narrow emission bands, which are

favourable when imaging biological tissues. Cell culture studies showed that the harmonic nanoparticles displayed better photostability up to a period of 5 hours of excitation compared to that of selected organic fluorescent dyes.

The group also investigated the third harmonic scattering process of the nanomaterials, where three photons are combined, producing one emitting photon at a third of the wavelength and three times the frequency, by adjusting the imaging set up. This can be especially advantageous when imaging more complex environments. The multimodal functionality can be added to the harmonic nanoparticles by the addition of Gd^{3+} chelates to the surface to the nanoparticle in order to facilitate magnetic resonance imaging. Upon functionalisation with Gd^{3+} chelates, the group were able to see an increase in the relaxation rates of water protons in both longitudinal and transverse measurements.

Quantitative and qualitive T1 mapping showed a strong enhancement of contrast in the agarose phantom used to test the MRI capabilities of the harmonic nanoparticles. The nanoparticles presented great potential to move forward the field of multimodal imaging, however, this field lacks the necessary biological assessments required for clinical application of cell tracking. Kilin *et al* successfully showed the use of harmonic nanoparticles for photo-induced cell damage before investigating the nanoparticles for use in cell tracking [146, 147].

To allow more sensitive imaging in a clinical setting, Harmsen *et al* designed a non-genomic labelling strategy which constituted of a PET/NIRF-active nanotag to afford whole-body imaging alongside wide-field imaging and high resolution microscopic NIRF imaging (Figure 18)[148].

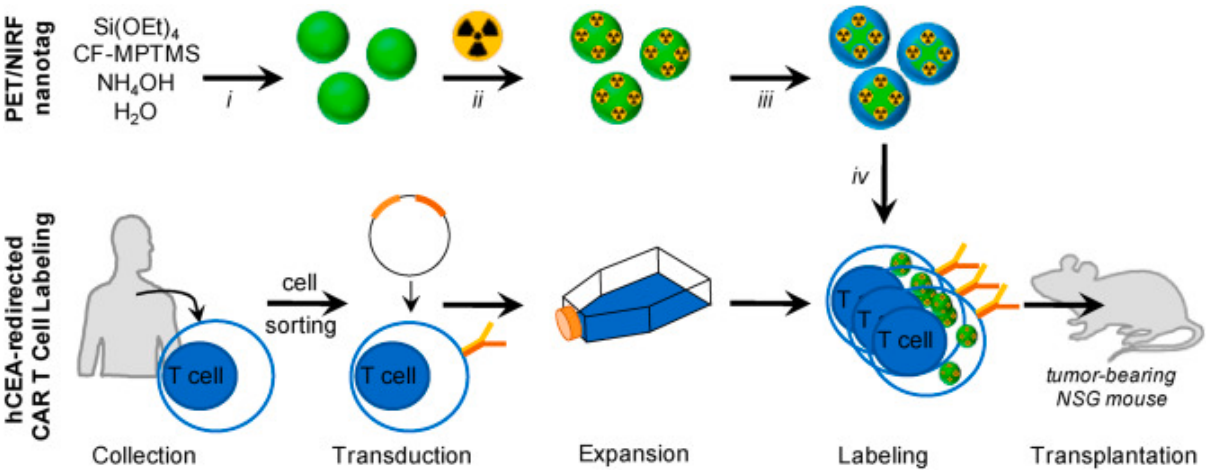

Fig. 18. Schematic showing the near infrared fluorescent silica nanoparticles with silane-appended near-infrared fluorophore CF-MPTMS and radiolabel ^{89}Zr yielding dual-modal PET/NIRF nanotags[148]
(Taken from references 148)

Biocompatible silica nanoparticles ($\lambda_{ex/em}$: 680/700nm) were radiolabelled with ^{89}Zr- clinically approved positron emitters[149]. With a half-life of 78.4 hours, the ^{89}Zr-positron emitter allowed for long term PET cell tracking. Cells were incubated with the nanotags *ex vivo* prior to transplantation.

For the application of intracellular radiolabelling, Griessinger *et al* demonstrated internalisation of radiotracer labelled antibodies upon binding to antigens on cell surfaces[150]. However, this approach limited the cells applicable to labelling and limited the quantity of radioisotopes per cell to the loading capability of the antibody.

To overcome these limitations, Harmsen *et al* adapted the approach by creating nanotags that would not rely on the expression of specific target proteins[135]. The nanotags were complexed with protamine and heparin in the presence of CAR-T cells to allow direct and efficient labelling of the cells which ultimately afforded whole-body cell tracking using PET for up to one week following the cell transfer (Figure 18).

The advantage the group utilised was the commercial availability of protamine, heparin and ^{89}Zr, meaning the fluorescent silica nanoparticles was the single

component having only recently been translated to the clinic. With the radioactive dose sufficiently below the accepted level of cell safety in terms of viability and functionality, the group saw dynamic monitoring of immune cells in the critical window post translation. Post-mortem analysis showed that past 1 week, the nanotags were no longer associated with the immune cells. Although this is a drawback to nanoparticle labelling for regulatory immunotherapies, further investigation showed that the tags were ultimately taken up by the tumour cells, which here presents a potential for selective drug delivery to tumour sites.

1.6 Effects of Cell Tracking on Phenotypical Behaviour of Tregs

As mentioned, phenotypical behaviour of Tregs is vital for efficacy as an adoptive cell therapy. Chemokines are a family of chemoattractant cytokines which play a vital role in cell migration with their ability to induce directed chemotaxis in nearby responsive cells. CXCR3 is highly expressed in T-cells and plays an important role in T-cell trafficking and function. Tregs that express CXCR3 acquire trafficking properties to allow them to localise and control excessive T helper cell responses at sites of inflammation[151, 152]. Chemokine CCR6 only binds to chemokine receptor CCLR20 (macrophage inflammatory protein). Pro inflammatory cells migrate via the chemokine gradient of CCLR20 to inflammatory sites and themselves can express more CCLR20 to bring in more Tregs. This can lead to chronic inflammation. In some models, the lack of CCR6 leads to less severe autoimmune inflammation of the brain and spinal cord (encephalomyelitis). Upregulation has been associated with the functional development and metastatic spread of some malignancies[153].

Cytokines are small secreted proteins released by cells to have a specific effect on the interactions and communications between cells[154]. IL-17 (interleukin-17) is a pro inflammatory cytokine. After binding to its receptor, it activates several signalling cascades that turn into the induction of chemokines and several immune regulatory functions. IL-17 induces pro inflammatory responses and is involved in the pathogenesis of various diseases whilst playing critical roles in antimicrobial defence and controlling autoimmunity and inflammation[155]. TNFα (tumour necrosis factor alpha) is a cell signalling protein involved in systemic inflammation and is produced by activated macrophages and CD4+ lymphocytes. Its primary role is in immune cell regulation, promoting the inflammatory response. TNFα also has immunosuppressive facets, with a positive effect on Tregs[154]. IFNγ is an immune interferon which inhibits

T helper 2 cells immune response and a further induction of T helper 1 cells immune response[156]. IFNγ is an antiviral agent that modulates functions of the immune system, including upregulation of major histocompatibility complex molecules and increasing immunoproteasome activity. Higher MHC II expression increases the presentation of peptides to helper T cells; these cells release cytokines that signal to and co-ordinate the activity of other immune cells.

Much research in the last 5 years claim PEG-coated nanoparticles have great biocompatibility and uptake into a variety of cells, including cancer, immune and healthy cell lines[157]. Most studies base these conclusions on the fact that the cells remain viable for basic cell functions such as proliferation and growth. This is mainly assessed by looking at MTT assays, a colorimetric assay for assessing NADH-dependant cellular metabolic activity. A lot of these studies also consider the pharmacokinetic effects of incubating cells and tissues with PEG coated gold nanoparticles[158, 159]. These assays measure parameters such as plasma distribution, clearance, biliary excretion rate, residence time and blood concentration. The main conclusion that most, if not all, these studies come to is that the presence of PEG coated NPs is biocompatible, especially compared to uncoated NPs (which could be due to the less negative zeta potential of the NPs post coating with PEG)[160]. An important and significant finding from these studies is that the NPs are apparently not metabolised despite accumulating in the liver and spleen (mostly). A lot of groups also study the effect of surface chemistry and size on the biodistribution and pharmacokinetics of the NPs[161]. NPs with PEG coatings have longer blood half-lives. In terms of cancer research, a lot the PEG coated NPs have good accumulation in tumours, a result of the lengthened blood half-life. Some studies also show increased levels of reactive oxygen species generation at tumour sites.

Interestingly there is significantly less research in looking at the phenotypical effects of coated NPs. In the studies that do, the presence of the NPs in cells caused either upregulation or downregulation of cytokine/chemokine production in cells; dependant on concentration and size of the NPs[110, 162-164]. They also observe an increase in inflammation markers as a result of incubation with the PEG coated NPs. These studies looked at the phenotypical effects of injecting the PEG NPs into the blood and then assessed their accumulation in each organ and checked the cytokine/chemokine production of the tissue. Studies rarely look at this effect on a single cell level. Additionally, it is worth noting, some groups have compared coatings and found their PEG coated NPs significantly reduced cell viability, so they did not continue with those.

To consider NPs in T-cells only, with a mixture of coatings, studies have shown slightly upregulated levels of growth factors and downregulation of cytokines[165, 166]. Another review study compares coated NPs and it is apparent some coatings have real impacts on immune response and cytokine production[167]. Studies have attributed this response to the NPs inducing an inflammatory response in the cells[168]. Additionally, it is important to consider the protein corona that forms around the NPs, as this will further impact the immune response, but studies are unclear how this happens.

Incubation of any exogenous probe with immune cells will cause a change of some kind in the environment of the cell, but that does not mean the cell is no longer viable. In fact, a downregulation in cytokine production could be an advantage in that one of the major side effects of cell therapy is the cytokine storm which infiltrates non-target organs. This could be advantageous as long as the cell can still carry out its immunosuppressive behaviour at the desired target site. PEG coated NPs are termed

biocompatible in the literature with non-immune cells because the retention of phenotypic function may not be the greatest concern. This is a more immune cell specific consideration.

Cytokine and chemokine molecules can also be used to monitor the activation and expansion of the immune system to monitor the safety and adverse effects of the cell therapy. *Gibson et al* used IFNγ PET imaging as a predictive tool for monitoring response to tumour immunotherapy[169]. In mice, an antibody against the cytokine IFNγ, which becomes sequestered at the surface of tumour cells after its production by T lymphocytes, was shown to reflect the activation status of cytotoxic T-cells. Activation of the immune system also results in vascular endothelial growth factor (VEGF) release and subsequently in significant lymph node volume increase. This can be measured using various techniques such as MRI, CT and Ultrasound[170].

1.7 Data Analysis

As new tracking techniques are developed, concurrently new advances in image interpretation must also progress. Recently, micro-laser particles (LPs) have emerged for use in single cell labelling with unique attributes to replace optical probes[171]. LPs have very narrow spectral bandwidths of less than 0.3nm, this feature alone make them attractive candidates for cell labelling[172]. Tang *et al* were able to demonstrate how traces of omnidirectional LPs based on their output spectra in live cells showed a high signal to noise ratio in a two-hour period and preluded to future applications including deep tissue imaging, where the intrinsic tissue scattering will not override the low signal collection. The high brightness of the emission produced by these omnidirectional LPs resulted in reliable spectral identification and spatial tracking without the need for prolonged exposure times. Interestingly, this work could

help facilitate single cell analysis in microfluidic models, which in turn could aid in evaluating immunotherapies.

Chen *et al* proposed cell segmentation and tracking frameworks that are able to perform both events simultaneously within a unified neural network, reducing the need for post-processing[173]. The group developed a method by which spatial information represented as relative position encodings of cell instances is incorporated in the network and greatly enhances the tracking process in real time and could be translated for clinical applications with further modifications.

Leslie *et al* showed the potential to reveal multidimension cellular interactions through use of an *in vivo* spectral un-mixing tool for monitoring multiple biological processes in real time[174]. Optical imaging works via the detection of photons emitted from fluorophores that, ideally, have specific spectral signatures. Consequently, these imaging modalities could facilitate complex imaging of various probes with different spectral properties, but this is limited due to tissue depth and scattering of light. The development of spectral un-mixing algorithms have provided a rare opportunity to enhance the contrast and sensitivity of these images by separating pure signal from autofluorescence[175]. Herein lies the opportunity to image larger tissue samples, making optical imaging more ideal for longitudinal cell tracking applications. The group aimed to develop a novel *in vivo* imaging methodology capable of identifying the spectral signatures of two different NIR dyes in a deep-seated organ, in mice which have known defects in immune cell recruitment to the liver following injury. Using this model, they were able to optimise a dual fluorescence imaging technique.

Oh *et al* investigated the use of ultra-sensitive accelerator mass spectrometry (AMS) to follow the distribution and localisation of transplanted mesenchymal stem cells post IV injection into mice[176]. Prior to injection, the cells were loaded with

radioactive ^{14}C-thymidine labels, which was detectable in the lung, spleen, liver, heart, kidney and brain, for up to 7 days, by both liquid scintillator counter (LSC) and AMS. Quantitative analysis of cell concentrations was conducted, showing that AMS, being a highly sensitive technique, was able to quantify one cell per mg in various tissues, where LSC failed to do so.

Development of a fully automated cell tracking pipeline has allowed Xu *et al* to use convolutional neural networks (Oligo-track) to deliver speedy volumetric segmentation and tracking of large volumes of cells over lengthy periods of time *in vivo*[177]. The group demonstrated a useful application of deep learning to resolve multi-dimensional tracking but also allows for future predictions to be made on cell behaviours. Using a copper chelating agent, Cuprizone, mouse cortex images were taken, *in vivo*, using two-photon microscopy for up to 12 weeks.

1.8 Conclusion

New immune and cell-based therapies are paving the way towards setting new standards for diagnostic accuracy and the accompanying cell tracking technologies are allowing for these therapies to be evaluated in terms of efficacy and safety[178]. The greatest challenges the field of CAR-T cell tracking faces is to be able to distinguish between true and pseudo progression, overcoming penetration depth limitations of imaging modalities and the retention of phenotypic behaviour of the cells. Imaging the biodistribution of the CAR-T cells will be of great importance, especially when assessing the efficacy of the therapy and will translate directly in increasing the success rate of future immunotherapies. Cell tracking imaging is shifting more heavily towards MRI and optical modalities, however both techniques still encompass varying degrees of suitability. MRI is more appropriate for in-human studies, whereas optical imaging offers greater potential in a pre-clinical setting. Despite the high spatial

resolution obtained with MRI there are many concerns regarding sensitivity and specificity, which have on occasion been found to be lower than that achieved by nuclear radiolabelling techniques. It is also worth noting the influence native iron concentrations, in both healthy and pathologic tissues, have on MRI interpretations. Combining MRI with PET scanning could help overcome the limitations observed in either technique, producing an outcome that could include increased spatial resolution and diagnostic accuracy[179, 180]. Direct labelling, itself, is a fairly straight forward practice, however, being able to limit the rate of efflux of the labelling probe from the cells is vital. To successfully develop the probe, the design of the label must consider the uptake pathway into the cell and consequently allow for a degree of control in predicting the efflux pathway. Furthermore, it is crucial to ensure structural and functional viability of the transplanted cells in order for the therapy to be effective, as such genetic manipulation becomes the least desirable technique for tracking.

Although there a plethora of both direct and indirect labelling techniques available, there have been relatively few that achieve recognition in a clinical setting and as such, clinicians are still using radiolabelling techniques, established years ago.

Indium-111 oxine compounds remain amongst the only FDA-approved cell tracking agents for nuclear imaging techniques for *in vivo* cell tracking[181]. Groups such as Castaneda *et al* have improvised with existing FDA-approved drugs such as Ferumoxytol, indicated as an iron supplement for the treatment of anaemia, and investigated its “off-label” use as a tracking agent using MRI[182] . Other ferumoxides and ferucarbotrans, which are FDA-approved as liver contrast agents have also been investigated as commercially available SPIONs but suffered from a lack of signal specificity and persistence of extracellular interactions which ultimately interfered with signal detection[183, 184]. Currently no nanoparticle-based cell labelling tracking agents

are available for clinical use. Gold nanoparticles indicated as drug delivery, therapeutic and radiosensitizing agents have been FDA approved, however they have not yet been cleared for cell tracking purposes[185]. At current, there is only one actively recruiting clinical trial, a randomised double-blind study evaluating the safety and immunogenicity of a T-cell priming peptide vaccine against COVID-19, using a gold nanoparticle scaffold for peptide delivery (as listed at clinicaltrials.gov Accessed: Aug 2022). The study utilities the gold nanoparticles for physical functionality but does not make use of its imaging properties but rather measures success based on PCR products.

The greatest challenges with cell tracking agents and those still under investigation, both nanoparticle and non-nanoparticle, is the efficient corporation of the label into the cell, such that the label may be imaged at high sensitivity for prolonged periods of time, without the probe affecting any functionality within the cell. An educated assumption would recognise the reason why so many potential probes do not make it to clinic is due to the lack of studies into assessing the phenotypical behaviour of cells post incubation or labelling and more importantly the absence of this consideration when designing the probe. It appears there is more interest in the detectability of a labelling probe, however, without the appropriate biocompatibility, some may argue detectability becomes inconsequential if the label is not translatable in clinic.

1.9 Thesis Outline

A pivotal challenge for this research is to design a probe which affords the ability to track cells both in model systems and in the body to develop a better understanding of new cell therapies with minimal impact on normal cell behaviours. This thesis aims to explore this with the use of labelled cells with multimodal nanoprobes and the application of a range of imaging modalities for tracking and detection. The objective of this thesis is to design a nanoprobe which combines gold nanoparticles with an iridium luminescent probe to allow for enhanced intrinsic optical and photophysical properties to be exploited to tackle the current challenges faced by existing cell tracking systems, encompassing properties such as high loading, long term retention and minimal bio-interreference. This inorganic scaffold affords a cell tracking potential at different scales using different imaging modalities whilst remaining biocompatible, a feature which other nanoparticle systems have failed to achieve due to off target toxicities causing adverse events.

Chapter one will address the design of gold nanoparticles ranging in sizes of 13, 25, 50 and 100nm with different stabilising agents and compare their photophysical properties.

Chapter two explores the impact of the nanoprobes on the phenotypical and functional behaviour of incubated immune cells and shows smaller AuNPs were more readily taken up by the cells as well as presenting as the most biocompatible.

Chapter three showcases regulatory T-cells dosed with nanoprobes with a gold core of 25nm coated with Zonyl and IrS1 administered to human liver sections which were then imaged using Micro-CT and Multiphoton microscopy to decipher the localisation of the transplanted cells.

1.10 References

1. Oo, Y. H.; Ackrill, S.; Cole, R.; Jenkins, L.; Anderson, P.; Jeffery, H. C.; Jones, N.; Jeffery, L. E.; Lutz, P.; Wawman, R. E.; Athwal, A. K.; Thompson, J.; Gray, J.; Guo, K.; Barton, D.; Hirschfield, G. M.; Wong, T.; Guest, P.; Adams, D. H., Liver homing of clinical grade Tregs after therapeutic infusion in patients with autoimmune hepatitis. *JHEP Reports* **2019,** *1* (4), 286-296.
2. Jeffery, H. C.; Braitch, M. K.; Brown, S.; Oo, Y. H., Clinical potential of regulatory T cell therapy in liver diseases: an overview and current perspectives. *Frontiers in immunology* **2016,** *7*, 334.
3. Than, N. N.; Jeffery, H. C.; Oo, Y. H., Autoimmune Hepatitis: Progress from Global Immunosuppression to Personalised Regulatory T Cell Therapy. *Can J Gastroenterol Hepatol* **2016,** *2016*, 7181685-7181685.
4. Akiyama, S.; Hamdeh, S.; Micic, D.; Sakuraba, A., Prevalence and clinical outcomes of COVID-19 in patients with autoimmune diseases: a systematic review and meta-analysis. *Annals of the Rheumatic Diseases* **2021,** *80* (3), 384.
5. Hoffmann, P.; Ermann, J.; Edinger, M.; Fathman, C. G.; Strober, S., Donor-type CD4(+)CD25(+) regulatory T cells suppress lethal acute graft-versus-host disease after allogeneic bone marrow transplantation. *J Exp Med* **2002,** *196* (3), 389-399.
6. Romano, M.; Fanelli, G.; Albany, C. J.; Giganti, G.; Lombardi, G., Past, Present, and Future of Regulatory T Cell Therapy in Transplantation and Autoimmunity. *Frontiers in Immunology* **2019,** *10* (43).
7. Wang, P.; Jiang, Z.; Wang, C.; Liu, X.; Li, H.; Xu, D.; Zhong, L., Immune tolerance induction using cell-based strategies in liver transplantation: clinical perspectives. *Frontiers in Immunology* **2020,** *11*.
8. Huang, H.; Lu, Y.; Zhou, T.; Gu, G.; Xia, Q., Innate immune cells in immune tolerance after liver transplantation. *Frontiers in immunology* **2018,** *9*, 2401.
9. Zheng, M.; Tian, Z., Liver-mediated adaptive immune tolerance. *Frontiers in immunology* **2019,** *10*, 2525.
10. Washington, M. K., Autoimmune liver disease: overlap and outliers. *Modern Pathology* **2007,** *20* (1), S15-S30.
11. FELD, J.; HEATHCOTE, E., Epidemiology of autoimmune liver disease. *Journal of Gastroenterology and Hepatology* **2003,** *18* (10), 1118-1128.
12. Selmi, C.; Invernizzi, P.; Keefe, E. B.; Coppel, R. L.; Podda, M.; Rossaro, L.; Ansari, A. A.; Gershwin, M. E., Epidemiology and pathogenesis of primary biliary cirrhosis. *Journal of clinical gastroenterology* **2004,** *38* (3), 264-271.
13. Kaplan, M. M., Primary biliary cirrhosis. *New England Journal of Medicine* **1996,** *335* (21), 1570-1580.
14. Kita, H.; Naidenko, O. V.; Kronenberg, M.; Ansari, A. A.; Rogers, P.; He, X. S.; Koning, F.; Mikayama, T.; Van de Water, J.; Coppel, R. L., Quantitation and phenotypic analysis of natural killer T cells in primary biliary cirrhosis using a human CD1d tetramer. *Gastroenterology* **2002,** *123* (4), 1031-1043.
15. Carey, E. J.; Ali, A. H.; Lindor, K. D., Primary biliary cirrhosis. *The Lancet* **2015,** *386* (10003), 1565-1575.
16. Lindberg, B. U.; Broomé, U.; Persson, B., Proximal colorectal dysplasia or cancer in ulcerative colitis. The impact of primary sclerosing cholangitis and sulfasalazine. *Diseases of the colon & rectum* **2001,** *44* (1), 77-83.

17. Bergquist, A.; Ekbom, A.; Olsson, R.; Kornfeldt, D.; Lööf, L.; Danielsson, Å.; Hultcrantz, R.; Lindgren, S.; Prytz, H.; Sandberg-Gertzén, H., Hepatic and extrahepatic malignancies in primary sclerosing cholangitis. *Journal of hepatology* **2002,** *36* (3), 321-327.
18. Tabibian, J. H.; Ali, A. H.; Lindor, K. D., Primary sclerosing cholangitis, part 1: epidemiology, etiopathogenesis, clinical features, and treatment. *Gastroenterology & hepatology* **2018,** *14* (5), 293.
19. Liang, H.; Manne, S.; Shick, J.; Lissoos, T.; Dolin, P., Incidence, prevalence, and natural history of primary sclerosing cholangitis in the United Kingdom. *Medicine* **2017,** *96* (24).
20. Lindor, K. D.; Kowdley, K. V.; Luketic, V. A.; Harrison, M. E.; McCashland, T.; Befeler, A. S.; Harnois, D.; Jorgensen, R.; Petz, J.; Keach, J., High-dose ursodeoxycholic acid for the treatment of primary sclerosing cholangitis. *Hepatology* **2009,** *50* (3), 808-814.
21. Olsson, R.; Boberg, K. M.; de Muckadell, O. S.; Lindgren, S.; Hultcrantz, R.; Folvik, G.; Bell, H.; Gangsøy–Kristiansen, M.; Matre, J.; Rydning, A., High-dose ursodeoxycholic acid in primary sclerosing cholangitis: a 5-year multicenter, randomized, controlled study. *Gastroenterology* **2005,** *129* (5), 1464-1472.
22. Martin, P.; DiMartini, A.; Feng, S.; Brown Jr, R.; Fallon, M., Evaluation for liver transplantation in adults: 2013 practice guideline by the American Association for the Study of Liver Diseases and the American Society of Transplantation. *Hepatology* **2014,** *59* (3), 1144-1165.
23. Wu, S.; Xu, H.; Ravindra, K.; Ildstad, S. In *Composite tissue allotransplantation: past, present and future—the history and expanding applications of CTA as a new frontier in transplantation*, Transplantation proceedings, Elsevier: 2009; pp 463-465.
24. Trivedi, H.; Vanikar, A.; Modi, P.; Shah, V.; Vakil, J.; Trivedi, V.; Khemchandani, S. In *Allogeneic hematopoietic stem-cell transplantation, mixed chimerism, and tolerance in living related donor renal allograft recipients*, Transplantation proceedings, Elsevier: 2005; pp 737-742.
25. Tryphonopoulos, P.; Tzakis, A. G.; Weppler, D.; Garcia-Morales, R.; Kato, T.; Madariaga, J. R.; Levi, D. M.; Nishida, S.; Moon, J.; Selvaggi, G., The role of donor bone marrow infusions in withdrawal of immunosuppression in adult liver allotransplantation. *American journal of transplantation* **2005,** *5* (3), 608-613.
26. Sasaki, H.; Oura, T.; Spitzer, T. R.; Chen, Y.-B.; Madsen, J. C.; Allan, J.; Sachs, D. H.; Cosimi, A.; Kawai, T., Preclinical and clinical studies for transplant tolerance via the mixed chimerism approach. *Human immunology* **2018,** *79* (5), 258-265.
27. Perruche, S.; Marandin, A.; Kleinclauss, F. M.; Angonin, R.; Fresnay, S.; Baron, M. H.; Tiberghien, P.; Saas, P., Association of mixed hematopoietic chimerism with elevated circulating autoantibodies and chronic graft-versus-host disease occurrence. *Transplantation* **2006,** *81* (4), 573.
28. Steinman, R. M.; Cohn, Z. A., Identification of a novel cell type in peripheral lymphoid organs of mice II. Functional properties in vitro. *Journal of Experimental Medicine* **1974,** *139* (2), 380-397.
29. Steinman, R. M.; Cohn, Z. A., Identification of a novel cell type in peripheral lymphoid organs of mice: I. Morphology, quantitation, tissue distribution. *J Exp Med* **1973,** *137* (5), 1142-1162.
30. Benham, H.; Nel, H. J.; Law, S. C.; Mehdi, A. M.; Street, S.; Ramnoruth, N.; Pahau, H.; Lee, B. T.; Ng, J.; Brunck, M. E., Citrullinated peptide dendritic cell immunotherapy in

HLA risk genotype–positive rheumatoid arthritis patients. *Science translational medicine* **2015,** *7* (290), 290ra87-290ra87.
31. Bell, G.; Anderson, A.; Diboll, J.; Reece, R.; Eltherington, O.; Harry, R.; Fouweather, T.; MacDonald, C.; Chadwick, T.; McColl, E., Autologous tolerogenic dendritic cells for rheumatoid and inflammatory arthritis. *Annals of the rheumatic diseases* **2017,** *76* (1), 227-234.
32. Giannoukakis, N.; Phillips, B.; Finegold, D.; Harnaha, J.; Trucco, M., Phase I (safety) study of autologous tolerogenic dendritic cells in type 1 diabetic patients. *Diabetes care* **2011,** *34* (9), 2026-2032.
33. Jauregui-Amezaga, A.; Cabezón, R.; Ramírez-Morros, A.; España, C.; Rimola, J.; Bru, C.; Pinó-Donnay, S.; Gallego, M.; Masamunt, M. C.; Ordás, I., Intraperitoneal administration of autologous tolerogenic dendritic cells for refractory Crohn's disease: a phase I study. *Journal of Crohn's and Colitis* **2015,** *9* (12), 1071-1078.
34. Ezzelarab, M.; Raich-Regue, D.; Lu, L.; Zahorchak, A.; Perez-Gutierrez, A.; Humar, A.; Wijkstrom, M.; Minervini, M.; Wiseman, R.; Cooper, D., Renal allograft survival in nonhuman primates infused with donor antigen-pulsed autologous regulatory dendritic cells. *American Journal of Transplantation* **2017,** *17* (6), 1476-1489.
35. Lavin, Y.; Mortha, A.; Rahman, A.; Merad, M., Regulation of macrophage development and function in peripheral tissues. *Nature Reviews Immunology* **2015,** *15* (12), 731-744.
36. Hutchinson, J. A.; Riquelme, P.; Geissler, E. K.; Fändrich, F., Human regulatory macrophages. In *Suppression and Regulation of Immune Responses*, Springer: 2010; pp 181-192.
37. Hutchinson, J. A.; Riquelme, P.; Sawitzki, B.; Tomiuk, S.; Miqueu, P.; Zuhayra, M.; Oberg, H. H.; Pascher, A.; Lützen, U.; Janßen, U., Cutting edge: immunological consequences and trafficking of human regulatory macrophages administered to renal transplant recipients. *The Journal of Immunology* **2011,** *187* (5), 2072-2078.
38. Dominici, M.; Le Blanc, K.; Mueller, I.; Slaper-Cortenbach, I.; Marini, F.; Krause, D.; Deans, R.; Keating, A.; Prockop, D.; Horwitz, E., Minimal criteria for defining multipotent mesenchymal stromal cells. The International Society for Cellular Therapy position statement. *Cytotherapy* **2006,** *8* (4), 315-317.
39. Le Blanc, K.; Mougiakakos, D., Multipotent mesenchymal stromal cells and the innate immune system. *Nature Reviews Immunology* **2012,** *12* (5), 383-396.
40. Beyth, S.; Borovsky, Z.; Mevorach, D.; Liebergall, M.; Gazit, Z.; Aslan, H.; Galun, E.; Rachmilewitz, J., Human mesenchymal stem cells alter antigen-presenting cell maturation and induce T-cell unresponsiveness. *Blood* **2005,** *105* (5), 2214-2219.
41. Di Nicola, M.; Carlo-Stella, C.; Magni, M.; Milanesi, M.; Longoni, P. D.; Matteucci, P.; Grisanti, S.; Gianni, A. M., Human bone marrow stromal cells suppress T-lymphocyte proliferation induced by cellular or nonspecific mitogenic stimuli. *Blood* **2002,** *99* (10), 3838-3843.
42. Casiraghi, F.; Perico, N.; Remuzzi, G., Mesenchymal stromal cells for tolerance induction in organ transplantation. *Human immunology* **2018,** *79* (5), 304-313.
43. Detry, O.; Vandermeulen, M.; Delbouille, M.-H.; Somja, J.; Bletard, N.; Briquet, A.; Lechanteur, C.; Giet, O.; Baudoux, E.; Hannon, M., Infusion of mesenchymal stromal cells after deceased liver transplantation: a phase I–II, open-label, clinical study. *Journal of hepatology* **2017,** *67* (1), 47-55.

44. Mauri, C.; Bosma, A., Immune regulatory function of B cells. *Annual review of immunology* **2012,** *30*, 221-241.
45. Rosser, E. C.; Mauri, C., Regulatory B cells: origin, phenotype, and function. *Immunity* **2015,** *42* (4), 607-612.
46. Sánchez-Fueyo, A.; Whitehouse, G.; Grageda, N.; Cramp, M. E.; Lim, T. Y.; Romano, M.; Thirkell, S.; Lowe, K.; Fry, L.; Heward, J., Applicability, safety, and biological activity of regulatory T cell therapy in liver transplantation. *American Journal of Transplantation* **2020,** *20* (4), 1125-1136.
47. Esensten, J. H.; Muller, Y. D.; Bluestone, J. A.; Tang, Q., Regulatory T-cell therapy for autoimmune and autoinflammatory diseases: The next frontier. *Journal of Allergy and Clinical Immunology* **2018,** *142* (6), 1710-1718.
48. Manriquez-Roman, C.; Siegler, E. L.; Kenderian, S. S., CRISPR Takes the Front Seat in CART-Cell Development. *BioDrugs* **2021**, 1-12.
49. Cong, L.; Ran, F. A.; Cox, D.; Lin, S.; Barretto, R.; Habib, N.; Hsu, P. D.; Wu, X.; Jiang, W.; Marraffini, L. A., Multiplex genome engineering using CRISPR/Cas systems. *Science* **2013,** *339* (6121), 819-823.
50. Peng, R.; Lin, G.; Li, J., Potential pitfalls of CRISPR/Cas9-mediated genome editing. *The FEBS journal* **2016,** *283* (7), 1218-1231.
51. Maher, J.; Brentjens, R. J.; Gunset, G.; Rivière, I.; Sadelain, M., Human T-lymphocyte cytotoxicity and proliferation directed by a single chimeric TCRζ/CD28 receptor. *Nature biotechnology* **2002,** *20* (1), 70-75.
52. Carpenito, C.; Milone, M. C.; Hassan, R.; Simonet, J. C.; Lakhal, M.; Suhoski, M. M.; Varela-Rohena, A.; Haines, K. M.; Heitjan, D. F.; Albelda, S. M., Control of large, established tumor xenografts with genetically retargeted human T cells containing CD28 and CD137 domains. *Proceedings of the National Academy of Sciences* **2009,** *106* (9), 3360-3365.
53. Chavez, J. C.; Jain, M. D.; Kharfan-Dabaja, M. A., Cytokine release syndrome and neurologic toxicities associated with chimeric antigen receptor T-cell therapy: A comprehensive review of emerging grading models. *Hematology/Oncology and Stem Cell Therapy* **2020,** *13* (1), 1-6.
54. Gust, J.; Hay, K. A.; Hanafi, L.-A.; Li, D.; Myerson, D.; Gonzalez-Cuyar, L. F.; Yeung, C.; Liles, W. C.; Wurfel, M.; Lopez, J. A.; Chen, J.; Chung, D.; Harju-Baker, S.; Özpolat, T.; Fink, K. R.; Riddell, S. R.; Maloney, D. G.; Turtle, C. J., Endothelial Activation and Blood–Brain Barrier Disruption in Neurotoxicity after Adoptive Immunotherapy with CD19 CAR-T Cells. *Cancer Discovery* **2017,** *7* (12), 1404.
55. Santomasso, B.; Bachier, C.; Westin, J.; Rezvani, K.; Shpall, E. J., The other side of CAR T-cell therapy: cytokine release syndrome, neurologic toxicity, and financial burden. *American Society of Clinical Oncology Educational Book* **2019,** *39*, 433-444.
56. Zahid, A.; Siegler, E. L.; Kenderian, S. S., CART Cell Toxicities: New Insight into Mechanisms and Management. *Clinical hematology international* **2020,** *2* (4), 149.
57. Kircher, M. F.; Gambhir, S. S.; Grimm, J., Noninvasive cell-tracking methods. *Nature Reviews Clinical Oncology* **2011,** *8* (11), 677-688.
58. Salmanoglu, E.; Kim, S.; Thakur, M. L., Currently Available Radiopharmaceuticals for Imaging Infection and the Holy Grail. *Semin Nucl Med* **2018,** *48* (2), 86-99.
59. Peters, A. M.; Roddie, M. E.; Danpure, H. J.; Osman, S.; Zacharopoulos, G. P.; George, P.; Stuttle, A. W.; Lavender, J. P., 99Tcm-HMPAO labelled leucocytes: comparison with 111In-tropolonate labelled granulocytes. *Nucl Med Commun* **1988,** *9* (6), 449-463.

60. Potts, Jonathan R.; Farahi, N.; Howard, Mark R.; Taylor, Mark R.; Heard, S.; Shankar, Arun N.; Alexander, Graeme J.; Chilvers, Edwin R.; Verma, S.; Peters, A. M., In vivo imaging of hepatic neutrophil migration in severe alcoholic hepatitis with 111In-radiolabelled leucocytes. *Bioscience Reports* **2018,** *38* (4).
61. Gupta, S.; Lee, C. D.; Vemuru, R. P.; Bhargava, K. K., 111Indium labeling of hepatocytes for analysis of short-term biodistribution of transplanted cells. *Hepatology* **1994,** *19* (3), 750-757.
62. Perrin, J.; Capitao, M.; Mougin-Degraef, M.; Guérard, F.; Faivre-Chauvet, A.; Rbah-Vidal, L.; Gaschet, J.; Guilloux, Y.; Kraeber-Bodéré, F.; Chérel, M.; Barbet, J., Cell Tracking in Cancer Immunotherapy. *Frontiers in Medicine* **2020,** *7* (34).
63. Adonai, N.; Nguyen, K. N.; Walsh, J.; Iyer, M.; Toyokuni, T.; Phelps, M. E.; McCarthy, T.; McCarthy, D. W.; Gambhir, S. S., Ex vivo cell labeling with 64Cu–pyruvaldehyde-bis (N4-methylthiosemicarbazone) for imaging cell trafficking in mice with positron-emission tomography. *Proceedings of the National Academy of Sciences* **2002,** *99* (5), 3030-3035.
64. Charoenphun, P.; Meszaros, L. K.; Chuamsaamarkkee, K.; Sharif-Paghaleh, E.; Ballinger, J. R.; Ferris, T. J.; Went, M. J.; Mullen, G. E.; Blower, P. J., [89 Zr] Oxinate 4 for long-term in vivo cell tracking by positron emission tomography. *European journal of nuclear medicine and molecular imaging* **2015,** *42* (2), 278-287.
65. Weist, M. R.; Starr, R.; Aguilar, B.; Chea, J.; Miles, J. K.; Poku, E.; Gerdts, E.; Yang, X.; Priceman, S. J.; Forman, S. J., PET of adoptively transferred chimeric antigen receptor T cells with 89Zr-oxine. *Journal of Nuclear Medicine* **2018,** *59* (10), 1531-1537.
66. Caravan, P.; Ellison, J. J.; McMurry, T. J.; Lauffer, R. B., Gadolinium (III) chelates as MRI contrast agents: structure, dynamics, and applications. *Chemical reviews* **1999,** *99* (9), 2293-2352.
67. Geng, K.; Yang, Z. X.; Huang, D.; Yi, M.; Jia, Y.; Yan, G.; Cheng, X.; Wu, R., Tracking of mesenchymal stem cells labeled with gadolinium diethylenetriamine pentaacetic acid by 7T magnetic resonance imaging in a model of cerebral ischemia. *Molecular medicine reports* **2015,** *11* (2), 954-960.
68. Bouchlaka, M. N.; Ludwig, K. D.; Gordon, J. W.; Kutz, M. P.; Bednarz, B. P.; Fain, S. B.; Capitini, C. M., 19F-MRI for monitoring human NK cells in vivo. *Oncoimmunology* **2016,** *5* (5), e1143996.
69. Makela, A. V.; Foster, P. J., Preclinical 19F MRI cell tracking at 3 Tesla. *Magnetic Resonance Materials in Physics, Biology and Medicine* **2019,** *32* (1), 123-132.
70. Kim, J. E.; Kalimuthu, S.; Ahn, B.-C., In vivo cell tracking with bioluminescence imaging. *Nuclear medicine and molecular imaging* **2015,** *49* (1), 3-10.
71. Xie, P.; Hu, X.; Li, D.; Xie, S.; Zhou, Z.; Meng, X.; Shan, H., Bioluminescence Imaging of Transplanted Mesenchymal Stem Cells by Overexpression of Hepatocyte Nuclear Factor4α: Tracking Biodistribution and Survival. *Molecular Imaging and Biology* **2019,** *21* (1), 44-53.
72. Muñoz, M. F.; Argüelles, S.; Guzman-Chozas, M.; Guillén-Sanz, R.; Franco, J. M.; Pintor-Toro, J. A.; Cano, M.; Ayala, A., Cell tracking, survival, and differentiation capacity of adipose-derived stem cells after engraftment in rat tissue. *Journal of cellular physiology* **2018,** *233* (10), 6317-6328.
73. Wang, L.; Lee, D. J.; Han, H.; Zhao, L.; Tsukamoto, H.; Kim, Y.-I.; Musicant, A. M.; Parag-Sharma, K.; Hu, X.; Tseng, H. C., Application of bioluminescence resonance energy

transfer-based cell tracking approach in bone tissue engineering. *Journal of Tissue Engineering* **2021,** *12*, 2041731421995465.
74. Kelly, J. J.; Saee-Marand, M.; Nyström, N. N.; Evans, M. M.; Chen, Y.; Martinez, F. M.; Hamilton, A. M.; Ronald, J. A., Safe harbor-targeted CRISPR-Cas9 homology-independent targeted integration for multimodality reporter gene-based cell tracking. *Science advances* **2021,** *7* (4), eabc3791.
75. Kang, S.-W.; Lee, S.; Na, J. H.; Yoon, H. I.; Lee, D.-E.; Koo, H.; Cho, Y. W.; Kim, S. H.; Jeong, S. Y.; Kwon, I. C., Cell labeling and tracking method without distorted signals by phagocytosis of macrophages. *Theranostics* **2014,** *4* (4), 420.
76. Watkins, T. S.; Miles, J. J., Tracking the T-cell repertoire after adoptive therapy. *Clinical & Translational Immunology* **2017,** *6* (5), e140.
77. Chapuis, A. G.; Desmarais, C.; Emerson, R.; Schmitt, T. M.; Shibuya, K.; Lai, I.; Wagener, F.; Chou, J.; Roberts, I. M.; Coffey, D. G.; Warren, E.; Robbins, H.; Greenberg, P. D.; Yee, C., Tracking the Fate and Origin of Clinically Relevant Adoptively Transferred CD8(+) T Cells In Vivo. *Sci Immunol* **2017,** *2* (8), eaal2568.
78. Li, B.; Li, T.; Pignon, J.-C.; Wang, B.; Wang, J.; Shukla, S. A.; Dou, R.; Chen, Q.; Hodi, F. S.; Choueiri, T. K., Landscape of tumor-infiltrating T cell repertoire of human cancers. *Nature genetics* **2016,** *48* (7), 725.
79. Lee, H. W.; Gangadaran, P.; Kalimuthu, S.; Ahn, B.-C., Advances in Molecular Imaging Strategies for In Vivo Tracking of Immune Cells. *Biomed Res Int* **2016,** *2016*, 1946585-1946585.
80. Bhatnagar, P.; Alauddin, M.; Bankson, J. A.; Kirui, D.; Seifi, P.; Huls, H.; Lee, D. A.; Babakhani, A.; Ferrari, M.; Li, K. C.; Cooper, L. J. N., Tumor lysing genetically engineered T cells loaded with multi-modal imaging agents. *Sci Rep* **2014,** *4*, 4502-4502.
81. Tavri, S.; Jha, P.; Meier, R.; Henning, T. D.; Müller, T.; Hostetter, D.; Knopp, C.; Johansson, M.; Reinhart, V.; Boddington, S., Optical imaging of cellular immunotherapy against prostate cancer. *Molecular imaging* **2009,** *8* (1), 7290.2009. 00002.
82. Kang, S.; Lee, H. W.; Jeon, Y. H.; Singh, T. D.; Choi, Y. J.; Park, J. Y.; Kim, J. S.; Lee, H.; Hong, K. S.; Lee, I.; Jeong, S. Y.; Lee, S.-W.; Ha, J.-H.; Ahn, B.-C.; Lee, J., Combined Fluorescence and Magnetic Resonance Imaging of Primary Macrophage Migration to Sites of Acute Inflammation Using Near-Infrared Fluorescent Magnetic Nanoparticles. *Molecular Imaging and Biology* **2015,** *17* (5), 643-651.
83. Griessinger, C.; Kehlbach, R.; Bukala, D.; Wiehr, S.; Bantleon, R.; Cay, F.; Schmid, A.; Braumüller, H.; Fehrenbacher, B.; Schaller, M.; Eichner, M.; Sutcliffe, J.; Ehrlichmann, W.; Eibl, O.; Reischl, G.; Cherry, S.; Röcken, M.; Pichler, B.; Kneilling, M., In Vivo Tracking of Th1 Cells by PET Reveals Quantitative and Temporal Distribution and Specific Homing in Lymphatic Tissue. *Journal of nuclear medicine : official publication, Society of Nuclear Medicine* **2014,** *55*.
84. Fixler, D.; Nayhoz, T.; Ray, K., Diffusion Reflection and Fluorescence Lifetime Imaging Microscopy Study of Fluorophore-Conjugated Gold Nanoparticles or Nanorods in Solid Phantoms. *ACS Photonics* **2014,** *1* (9), 900-905.
85. Meir, R.; Popovtzer, R., Cell tracking using gold nanoparticles and computed tomography imaging. *Wiley Interdisciplinary Reviews: Nanomedicine and Nanobiotechnology* **2018,** *10* (2), e1480.
86. Shilo, M.; Reuveni, T.; Motiei, M.; Popovtzer, R., Nanoparticles as computed tomography contrast agents: current status and future perspectives. *Nanomedicine* **2012,** *7* (2), 257-269.

87. Meir, R.; Shamalov, K.; Betzer, O.; Motiei, M.; Horovitz-Fried, M.; Yehuda, R.; Popovtzer, A.; Popovtzer, R.; Cohen, C. J., Nanomedicine for Cancer Immunotherapy: Tracking Cancer-Specific T-Cells in Vivo with Gold Nanoparticles and CT Imaging. *ACS Nano* **2015,** *9* (6), 6363-6372.
88. Sherman, A. I.; Ter-Pogossian, M., Lymph-node concentration of radioactive colloidal gold following interstitial injection. *Cancer* **1953,** *6* (6), 1238-1240.
89. Connor, E. E.; Mwamuka, J.; Gole, A.; Murphy, C. J.; Wyatt, M. D., Gold nanoparticles are taken up by human cells but do not cause acute cytotoxicity. *Small* **2005,** *1* (3), 325-327.
90. Johnston, H. J.; Hutchison, G.; Christensen, F. M.; Peters, S.; Hankin, S.; Stone, V., A review of the in vivo and in vitro toxicity of silver and gold particulates: particle attributes and biological mechanisms responsible for the observed toxicity. *Critical reviews in toxicology* **2010,** *40* (4), 328-346.
91. Lasagna-Reeves, C.; Gonzalez-Romero, D.; Barria, M.; Olmedo, I.; Clos, A.; Ramanujam, V. S.; Urayama, A.; Vergara, L.; Kogan, M. J.; Soto, C., Bioaccumulation and toxicity of gold nanoparticles after repeated administration in mice. *Biochemical and biophysical research communications* **2010,** *393* (4), 649-655.
92. Zhang, G.; Yang, Z.; Lu, W.; Zhang, R.; Huang, Q.; Tian, M.; Li, L.; Liang, D.; Li, C., Influence of anchoring ligands and particle size on the colloidal stability and in vivo biodistribution of polyethylene glycol-coated gold nanoparticles in tumor-xenografted mice. *Biomaterials* **2009,** *30* (10), 1928-1936.
93. Arvizo, R.; Bhattacharya, R.; Mukherjee, P., Gold nanoparticles: opportunities and challenges in nanomedicine. *Expert opinion on drug delivery* **2010,** *7* (6), 753-763.
94. Ghosh, P.; Han, G.; De, M.; Kim, C. K.; Rotello, V. M., Gold nanoparticles in delivery applications. *Advanced drug delivery reviews* **2008,** *60* (11), 1307-1315.
95. Jain, P. K.; Huang, X.; El-Sayed, I. H.; El-Sayed, M. A., Noble metals on the nanoscale: optical and photothermal properties and some applications in imaging, sensing, biology, and medicine. *Accounts of chemical research* **2008,** *41* (12), 1578-1586.
96. Nedosekin, D. A.; Galanzha, E. I.; Dervishi, E.; Biris, A. S.; Zharov, V. P., Super-resolution nonlinear photothermal microscopy. *Small* **2014,** *10* (1), 135-142.
97. Li, J.-F.; Li, C.-Y.; Aroca, R. F., Plasmon-enhanced fluorescence spectroscopy. *Chemical Society Reviews* **2017,** *46* (13), 3962-3979.
98. Wu, Y.; Ali, M. R.; Chen, K.; Fang, N.; El-Sayed, M. A., Gold nanoparticles in biological optical imaging. *Nano Today* **2019,** *24*, 120-140.
99. Martinez, O.; Sosabowski, J.; Maher, J.; Papa, S., New Developments in Imaging Cell-based Therapy. *Journal of Nuclear Medicine* **2019,** *60* (6), 730-735.
100. Bhatnagar, P.; Li, Z.; Choi, Y.; Guo, J.; Li, F.; Lee, D. Y.; Figliola, M.; Huls, H.; Lee, D. A.; Zal, T.; Li, K. C.; Cooper, L. J. N., Imaging of genetically engineered T cells by PET using gold nanoparticles complexed to Copper-64. *Integr Biol (Camb)* **2013,** *5* (1), 231-238.
101. Fairclough, M.; Prenant, C.; Ellis, B.; Boutin, H.; McMahon, A.; Brown, G.; Locatelli, P.; Jones, A., A new technique for the radiolabelling of mixed leukocytes with zirconium-89 for inflammation imaging with positron emission tomography. *Journal of Labelled Compounds and Radiopharmaceuticals* **2016,** *59* (7), 270-276.
102. Fairclough, M.; Ellis, B.; Boutin, H.; Jones, A.; McMahon, A.; Alzabin, S.; Gennari, A.; Prenant, C., Development of a method for the preparation of zirconium-89 radiolabelled chitosan nanoparticles as an application for leukocyte trafficking with positron emission tomography. *Applied Radiation and Isotopes* **2017,** *130*, 7-12.

103. Weissleder, R.; Cheng, H. C.; Bogdanova, A.; Bogdanov Jr, A., Magnetically labeled cells can be detected by MR imaging. *Journal of Magnetic Resonance Imaging* **1997,** *7* (1), 258-263.
104. Kircher, M. F.; Gambhir, S. S.; Grimm, J., Noninvasive cell-tracking methods. *Nature reviews Clinical oncology* **2011,** *8* (11), 677.
105. Foley, L. M.; Hitchens, T. K.; Ho, C.; Janesko-Feldman, K. L.; Melick, J. A.; Bayır, H.; Kochanek, P. M., Magnetic resonance imaging assessment of macrophage accumulation in mouse brain after experimental traumatic brain injury. *Journal of neurotrauma* **2009,** *26* (9), 1509-1519.
106. Smirnov, P., Cellular magnetic resonance imaging using superparamagnetic anionic iron oxide nanoparticles: applications to in vivo trafficking of lymphocytes and cell-based anticancer therapy. In *Inflammation and Cancer*, Springer: 2009; pp 333-353.
107. Dallet, L.; Stanicki, D.; Voisin, P.; Miraux, S.; Ribot, E. J., Micron-sized iron oxide particles for both MRI cell tracking and magnetic fluid hyperthermia treatment. *Sci Rep* **2021,** *11* (1), 1-13.
108. Zauner, W.; Farrow, N.; Haines, A., In Vitro Uptake of Polystyrene Microspheres: Effect of Particle Size, Cell Line and Cell Density. *Journal of controlled release: official journal of the Controlled Release Society* **2001,** *71* (1), 39-51.
109. Liu, Y.; Huang, W.; Xiong, C.; Huang, Y.; Chen, B. J.; Racioppi, L.; Chao, N.; Vo-Dinh, T., Biodistribution and sensitive tracking of immune cells with plasmonic gold nanostars. *Int J Nanomedicine* **2019,** *14*, 3403-3411.
110. Chhour, P.; Naha, P. C.; O'Neill, S. M.; Litt, H. I.; Reilly, M. P.; Ferrari, V. A.; Cormode, D. P., Labeling monocytes with gold nanoparticles to track their recruitment in atherosclerosis with computed tomography. *Biomaterials* **2016,** *87*, 93-103.
111. Aminabad, N. S.; Farshbaf, M.; Akbarzadeh, A., Recent Advances of Gold Nanoparticles in Biomedical Applications: State of the Art. *Cell Biochemistry and Biophysics* **2019,** *77* (2), 123-137.
112. Ning, X.; Bao, H.; Liu, X.; Fu, H.; Wang, W.; Huang, J.; Zhang, Z., Long-term in vivo CT tracking of mesenchymal stem cells labeled with Au@ BSA@ PLL nanotracers. *Nanoscale* **2019,** *11* (43), 20932-20941.
113. Ni, X.; Jia, S.; Duan, X.; Ding, D.; Li, K., Fluorescent nanoparticles for noninvasive stem cell tracking in regenerative medicine. *Journal of biomedical nanotechnology* **2018,** *14* (2), 240-256.
114. Chen, G.; Zhang, Y.; Li, C.; Huang, D.; Wang, Q.; Wang, Q., Recent Advances in Tracking the Transplanted Stem Cells Using Near-Infrared Fluorescent Nanoprobes: Turning from the First to the Second Near-Infrared Window. *Advanced healthcare materials* **2018,** *7* (20), 1800497.
115. Resch-Genger, U.; Grabolle, M.; Cavaliere-Jaricot, S.; Nitschke, R.; Nann, T., Quantum dots versus organic dyes as fluorescent labels. *Nature methods* **2008,** *5* (9), 763.
116. Shvedova, A. A.; Kagan, V. E.; Fadeel, B., Close encounters of the small kind: adverse effects of man-made materials interfacing with the nano-cosmos of biological systems. *Annual review of pharmacology and toxicology* **2010,** *50*, 63-88.
117. Li, C.; Li, F.; Zhang, Y.; Zhang, W.; Zhang, X.-E.; Wang, Q., Real-time monitoring surface chemistry-dependent in vivo behaviors of protein nanocages via encapsulating an NIR-II Ag2S quantum dot. *Acs Nano* **2015,** *9* (12), 12255-12263.
118. Ni, J.-S.; Li, Y.; Yue, W.; Liu, B.; Li, K., Nanoparticle-based cell trackers for biomedical applications. *Theranostics* **2020,** *10* (4), 1923.

119. Biffi, S.; Petrizza, L.; Garrovo, C.; Rampazzo, E.; Andolfi, L.; Giustetto, P.; Nikolov, I.; Kurdi, G.; Danailov, M. B.; Zauli, G., Multimodal near-infrared-emitting PluS Silica nanoparticles with fluorescent, photoacoustic, and photothermal capabilities. *Int J Nanomedicine* **2016,** *11*, 4865.
120. Jokerst, J. V.; Thangaraj, M.; Kempen, P. J.; Sinclair, R.; Gambhir, S. S., Photoacoustic imaging of mesenchymal stem cells in living mice via silica-coated gold nanorods. *ACS nano* **2012,** *6* (7), 5920-5930.
121. Lee, S. K.; Mortensen, L. J.; Lin, C. P.; Tung, C.-H., An authentic imaging probe to track cell fate from beginning to end. *Nature communications* **2014,** *5* (1), 1-8.
122. Sun, L.; Joh, D. Y.; Al-Zaki, A.; Stangl, M.; Murty, S.; Davis, J. J.; Baumann, B. C.; Alonso-Basanta, M.; Kao, G. D.; Tsourkas, A., Theranostic application of mixed gold and superparamagnetic iron oxide nanoparticle micelles in glioblastoma multiforme. *Journal of biomedical nanotechnology* **2016,** *12* (2), 347-356.
123. Moreira, A. F.; Rodrigues, C. F.; Reis, C. A.; Costa, E. C.; Correia, I. J., Gold-core silica shell nanoparticles application in imaging and therapy: A review. *Microporous and Mesoporous Materials* **2018,** *270*, 168-179.
124. Amendola, V.; Pilot, R.; Frasconi, M.; Maragò, O. M.; Iatì, M. A., Surface plasmon resonance in gold nanoparticles: a review. *Journal of Physics: Condensed Matter* **2017,** *29* (20), 203002.
125. Willets, K. A.; Van Duyne, R. P., Localized surface plasmon resonance spectroscopy and sensing. *Annu. Rev. Phys. Chem.* **2007,** *58*, 267-297.
126. Grzelczak, M.; Pérez-Juste, J.; Mulvaney, P.; Liz-Marzán, L. M., Shape control in gold nanoparticle synthesis. *Chemical Society Reviews* **2008,** *37* (9), 1783-1791.
127. Wall, M. A.; Harmsen, S.; Pal, S.; Zhang, L.; Arianna, G.; Lombardi, J. R.; Drain, C. M.; Kircher, M. F., Surfactant-Free Shape Control of Gold Nanoparticles Enabled by Unified Theoretical Framework of Nanocrystal Synthesis. *Advanced Materials* **2017,** *29* (21), 1605622.
128. Maturi, M.; Locatelli, E.; Monaco, I.; Franchini, M. C., Current concepts in nanostructured contrast media development for in vivo photoacoustic imaging. *Biomaterials science* **2019,** *7* (5), 1746-1775.
129. Knights, O. B.; Ye, S.; Ingram, N.; Freear, S.; McLaughlan, J. R., Optimising gold nanorods for photoacoustic imaging in vitro. *Nanoscale Advances* **2019,** *1* (4), 1472-1481.
130. Chen, Y.-S.; Zhao, Y.; Yoon, S. J.; Gambhir, S. S.; Emelianov, S., Miniature gold nanorods for photoacoustic molecular imaging in the second near-infrared optical window. *Nature nanotechnology* **2019,** *14* (5), 465-472.
131. Li, J.; Hu, Y.; Yang, J.; Wei, P.; Sun, W.; Shen, M.; Zhang, G.; Shi, X., Hyaluronic acid-modified Fe3O4@ Au core/shell nanostars for multimodal imaging and photothermal therapy of tumors. *Biomaterials* **2015,** *38*, 10-21.
132. Pohling, C.; Campbell, J. L.; Larson, T. A.; Van de Sompel, D.; Levi, J.; Bachmann, M. H.; Bohndiek, S. E.; Jokerst, J. V.; Gambhir, S. S., Smart-Dust-Nanorice for Enhancement of Endogenous Raman Signal, Contrast in Photoacoustic Imaging, and T2-Shortening in Magnetic Resonance Imaging. *Small* **2018,** *14* (19), 1703683.
133. Xie, X.; Liao, J.; Shao, X.; Li, Q.; Lin, Y., The effect of shape on cellular uptake of gold nanoparticles in the forms of stars, rods, and triangles. *Sci Rep* **2017,** *7* (1), 1-9.
134. Darrigues, E.; Nima, Z. A.; Nedosekin, D. A.; Watanabe, F.; Alghazali, K. M.; Zharov, V. P.; Biris, A. S., Tracking Gold Nanorods' Interaction with Large 3D Pancreatic-Stromal

Tumor Spheroids by Multimodal Imaging: Fluorescence, Photoacoustic, and Photothermal Microscopies. *Sci Rep* **2020,** *10* (1), 3362.
135. Chhour, P.; Kim, J.; Benardo, B.; Tovar, A.; Mian, S.; Litt, H. I.; Ferrari, V. A.; Cormode, D. P., Effect of gold nanoparticle size and coating on labeling monocytes for CT tracking. *Bioconjugate chemistry* **2017,** *28* (1), 260-269.
136. Chinen, A. B.; Guan, C. M.; Ko, C. H.; Mirkin, C. A., The impact of protein corona formation on the macrophage cellular uptake and biodistribution of spherical nucleic acids. *Small* **2017,** *13* (16), 1603847.
137. Melby, E. S.; Lohse, S. E.; Park, J. E.; Vartanian, A. M.; Putans, R. A.; Abbott, H. B.; Hamers, R. J.; Murphy, C. J.; Pedersen, J. A., Cascading effects of nanoparticle coatings: Surface functionalization dictates the assemblage of complexed proteins and subsequent interaction with model cell membranes. *ACS nano* **2017,** *11* (6), 5489-5499.
138. Mirshafiee, V.; Kim, R.; Park, S.; Mahmoudi, M.; Kraft, M. L., Impact of protein pre-coating on the protein corona composition and nanoparticle cellular uptake. *Biomaterials* **2016,** *75*, 295-304.
139. Obst, K.; Yealland, G.; Balzus, B.; Miceli, E.; Dimde, M.; Weise, C.; Eravci, M.; Bodmeier, R.; Haag, R.; Calderón, M., Protein corona formation on colloidal polymeric nanoparticles and polymeric nanogels: impact on cellular uptake, toxicity, immunogenicity, and drug release properties. *Biomacromolecules* **2017,** *18* (6), 1762-1771.
140. Piella, J.; Bastús, N. G.; Puntes, V., Size-dependent protein–nanoparticle interactions in citrate-stabilized gold nanoparticles: the emergence of the protein corona. *Bioconjugate chemistry* **2017,** *28* (1), 88-97.
141. Saha, K.; Rahimi, M.; Yazdani, M.; Kim, S. T.; Moyano, D. F.; Hou, S.; Das, R.; Mout, R.; Rezaee, F.; Mahmoudi, M., Regulation of macrophage recognition through the interplay of nanoparticle surface functionality and protein corona. *ACS nano* **2016,** *10* (4), 4421-4430.
142. Bouché, M.; Hsu, J. C.; Dong, Y. C.; Kim, J.; Taing, K.; Cormode, D. P., Recent Advances in Molecular Imaging with Gold Nanoparticles. *Bioconjugate Chemistry* **2020,** *31* (2), 303-314.
143. Betzer, O.; Shwartz, A.; Motiei, M.; Kazimirsky, G.; Gispan, I.; Damti, E.; Brodie, C.; Yadid, G.; Popovtzer, R., Nanoparticle-based CT imaging technique for longitudinal and quantitative stem cell tracking within the brain: application in neuropsychiatric disorders. *ACS nano* **2014,** *8* (9), 9274-9285.
144. Meir, R.; Betzer, O.; Motiei, M.; Kronfeld, N.; Brodie, C.; Popovtzer, R., Design principles for noninvasive, longitudinal and quantitative cell tracking with nanoparticle-based CT imaging. *Nanomedicine: Nanotechnology, Biology and Medicine* **2017,** *13* (2), 421-429.
145. Vuilleumier, J.; De Matos, R.; Staedler, D.; Bonacina, L.; Gerber, S., Functionalized Harmonic Nanoparticles for Bioimaging, Cell Tracking and Controlled Drug Delivery.
146. Dubreil, L.; Leroux, I.; Ledevin, M.; Schleder, C.; Lagalice, L.; Lovo, C.; Fleurisson, R.; Passemard, S.; Kilin, V.; Gerber-Lemaire, S., Multi-harmonic imaging in the second near-infrared window of nanoparticle-labeled stem cells as a monitoring tool in tissue depth. *ACS nano* **2017,** *11* (7), 6672-6681.
147. Kilin, V.; Campargue, G.; Fureraj, I.; Sakong, S.; Sabri, T.; Riporto, F.; Vieren, A.; Mugnier, Y.; Mas, C.; Staedler, D., Wavelength-Selective Nonlinear Imaging and Photo-Induced Cell Damage by Dielectric Harmonic Nanoparticles. *ACS nano* **2020,** *14* (4), 4087-4095.

148. Harmsen, S.; Medine, E. I.; Moroz, M.; Nurili, F.; Lobo, J.; Dong, Y.; Turkekul, M.; Pillarsetty, N. V. K.; Ting, R.; Ponomarev, V., A dual-modal PET/near infrared fluorescent nanotag for long-term immune cell tracking. *Biomaterials* **2021,** *269*, 120630.
149. Shaffer, T. M.; Wall, M. A.; Harmsen, S.; Longo, V. A.; Drain, C. M.; Kircher, M. F.; Grimm, J., Silica nanoparticles as substrates for chelator-free labeling of oxophilic radioisotopes. *Nano letters* **2015,** *15* (2), 864-868.
150. Griessinger, C. M.; Maurer, A.; Kesenheimer, C.; Kehlbach, R.; Reischl, G.; Ehrlichmann, W.; Bukala, D.; Harant, M.; Cay, F.; Brück, J., 64Cu antibody-targeting of the T-cell receptor and subsequent internalization enables in vivo tracking of lymphocytes by PET. *Proceedings of the National Academy of Sciences* **2015,** *112* (4), 1161-1166.
151. Tan, T. G.; Mathis, D.; Benoist, C., Singular role for T-BET+CXCR3+ regulatory T cells in protection from autoimmune diabetes. *Proc Natl Acad Sci U S A* **2016,** *113* (49), 14103-14108.
152. Paust, H.-J.; Riedel, J.-H.; Krebs, C. F.; Turner, J.-E.; Brix, S. R.; Krohn, S.; Velden, J.; Wiech, T.; Kaffke, A.; Peters, A.; Bennstein, S. B.; Kapffer, S.; Meyer-Schwesinger, C.; Wegscheid, C.; Tiegs, G.; Thaiss, F.; Mittrücker, H.-W.; Steinmetz, O. M.; Stahl, R. A. K.; Panzer, U., CXCR3⁺ Regulatory T Cells Control T_H1 Responses in Crescentic GN. *Journal of the American Society of Nephrology* **2016,** *27* (7), 1933.
153. Littringer, K.; Moresi, C.; Rakebrandt, N.; Zhou, X.; Schorer, M.; Dolowschiak, T.; Kirchner, F.; Rost, F.; Keller, C. W.; McHugh, D., Common features of regulatory T cell specialization during Th1 responses. *Frontiers in immunology* **2018,** *9*, 1344.
154. Zhang, J.-M.; An, J., Cytokines, inflammation, and pain. *Int Anesthesiol Clin* **2007,** *45* (2), 27-37.
155. Jäger, A.; Kuchroo, V. K., Effector and regulatory T-cell subsets in autoimmunity and tissue inflammation. *Scand J Immunol* **2010,** *72* (3), 173-184.
156. Voo, K. S.; Wang, Y.-H.; Santori, F. R.; Boggiano, C.; Wang, Y.-H.; Arima, K.; Bover, L.; Hanabuchi, S.; Khalili, J.; Marinova, E.; Zheng, B.; Littman, D. R.; Liu, Y.-J., Identification of IL-17-producing FOXP3⁺ regulatory T cells in humans. *Proceedings of the National Academy of Sciences* **2009,** *106* (12), 4793.
157. Betzer, O.; Meir, R.; Dreifuss, T.; Shamalov, K.; Motiei, M.; Shwartz, A.; Baranes, K.; Cohen, C. J.; Shraga-Heled, N.; Ofir, R.; Yadid, G.; Popovtzer, R., In-vitro Optimization of Nanoparticle-Cell Labeling Protocols for In-vivo Cell Tracking Applications. *Sci Rep* **2015,** *5*, 15400-15400.
158. Al-Harbi, N. S.; Alrashood, S. T.; Siddiqi, N. J.; Arafah, M. M.; Ekhzaimy, A.; Khan, H. A., Effect of naked and PEG-coated gold nanoparticles on histopathology and cytokines expression in rat liver and kidneys. *Nanomedicine* **2020,** *15* (3), 289-302.
159. You, J.; Zhou, J.; Zhou, M.; Liu, Y.; Robertson, J. D.; Liang, D.; Van Pelt, C.; Li, C., Pharmacokinetics, clearance, and biosafety of polyethylene glycol-coated hollow gold nanospheres. *Particle and Fibre Toxicology* **2014,** *11* (1), 26.
160. Lin, Z.; Monteiro-Riviere, N. A.; Riviere, J. E., A physiologically based pharmacokinetic model for polyethylene glycol-coated gold nanoparticles of different sizes in adult mice. *Nanotoxicology* **2016,** *10* (2), 162-172.
161. Wang, J.; Bai, R.; Yang, R.; Liu, J.; Tang, J.; Liu, Y.; Li, J.; Chai, Z.; Chen, C., Size-and surface chemistry-dependent pharmacokinetics and tumor accumulation of engineered gold nanoparticles after intravenous administration. *Metallomics* **2015,** *7* (3), 516-524.

162. Bailly, A.-L.; Correard, F.; Popov, A.; Tselikov, G.; Chaspoul, F.; Appay, R.; Al-Kattan, A.; Kabashin, A. V.; Braguer, D.; Esteve, M.-A., In vivo evaluation of safety, biodistribution and pharmacokinetics of laser-synthesized gold nanoparticles. *Sci Rep* **2019,** *9* (1), 12890.
163. Patlolla, A. K.; Kumari, S. A.; Tchounwou, P. B., A comparison of poly-ethylene-glycol-coated and uncoated gold nanoparticle-mediated hepatotoxicity and oxidative stress in Sprague Dawley rats. *Int J Nanomedicine* **2019,** *14*, 639-647.
164. del Pino, P.; Yang, F.; Pelaz, B.; Zhang, Q.; Kantner, K.; Hartmann, R.; Martinez de Baroja, N.; Gallego, M.; Möller, M.; Manshian, B. B., Basic physicochemical properties of polyethylene glycol coated gold nanoparticles that determine their interaction with cells. *Angewandte Chemie International Edition* **2016,** *55* (18), 5483-5487.
165. Yang, Y.-S. S.; Moynihan, K. D.; Bekdemir, A.; Dichwalkar, T. M.; Noh, M. M.; Watson, N.; Melo, M.; Ingram, J.; Suh, H.; Ploegh, H., Targeting small molecule drugs to T cells with antibody-directed cell-penetrating gold nanoparticles. *Biomaterials science* **2019,** *7* (1), 113-124.
166. Dykman, L. A.; Khlebtsov, N. G., Immunological properties of gold nanoparticles. *Chemical science* **2017,** *8* (3), 1719-1735.
167. Ahmad, S.; Zamry, A. A.; Tan, H.-T. T.; Wong, K. K.; Lim, J.; Mohamud, R., Targeting dendritic cells through gold nanoparticles: A review on the cellular uptake and subsequent immunological properties. *Molecular immunology* **2017,** *91*, 123-133.
168. Fernández, T. D.; Pearson, J. R.; Leal, M. P.; Torres, M. J.; Blanca, M.; Mayorga, C.; Le Guével, X., Intracellular accumulation and immunological properties of fluorescent gold nanoclusters in human dendritic cells. *Biomaterials* **2015,** *43*, 1-12.
169. Gibson, H. M.; McKnight, B. N.; Malysa, A.; Dyson, G.; Wiesend, W. N.; McCarthy, C. E.; Reyes, J.; Wei, W.-Z.; Viola-Villegas, N. T., IFNγ PET imaging as a predictive tool for monitoring response to tumor immunotherapy. *Cancer research* **2018,** *78* (19), 5706-5717.
170. Streeter, J. E.; Gessner, R. C.; Tsuruta, J.; Feingold, S.; Dayton, P. A., Assessment of molecular imaging of angiogenesis with three-dimensional ultrasonography. *Molecular imaging* **2011,** *10* (6), 7290.2011. 00015.
171. Tang, S.-J.; Dannenberg, P. H.; Liapis, A. C.; Martino, N.; Zhuo, Y.; Xiao, Y.-F.; Yun, S.-H., Laser particles with omnidirectional emission for cell tracking. *Light: Science & Applications* **2021,** *10* (1), 1-11.
172. Martino, N.; Kwok, S. J.; Liapis, A. C.; Forward, S.; Jang, H.; Kim, H.-M.; Wu, S. J.; Wu, J.; Dannenberg, P. H.; Jang, S.-J., Wavelength-encoded laser particles for massively multiplexed cell tagging. *Nature photonics* **2019,** *13* (10), 720-727.
173. Chen, Y.; Song, Y.; Zhang, C.; Zhang, F.; O'Donnell, L.; Chrzanowski, W.; Cai, W., CellTrack R-CNN: A Novel End-To-End Deep Neural Network for Cell Segmentation and Tracking in Microscopy Images. *arXiv preprint arXiv:2102.10377* **2021**.
174. Leslie, J.; Robinson, S. M.; Oakley, F.; Luli, S., Non-invasive synchronous monitoring of neutrophil migration using whole body near-infrared fluorescence-based imaging. *Sci Rep* **2021,** *11* (1), 1-11.
175. Xu, H.; Rice, B. W., In-vivo fluorescence imaging with a multivariate curve resolution spectral unmixing technique. *Journal of biomedical optics* **2009,** *14* (6), 064011.
176. Oh, M.-S.; Lee, S.-G.; Lee, G.-H.; Kim, C.-Y.; Kim, E.-Y.; Song, J. H.; Yu, B.-Y.; Chung, H. M., In vivo tracking of 14 C thymidine labeled mesenchymal stem cells using ultra-sensitive accelerator mass spectrometry. *Sci Rep* **2021,** *11* (1), 1-10.

177. Xu, Y. K. T.; Call, C. L.; Sulam, J.; Bergles, D. E., Automated in vivo tracking of cortical oligodendrocytes. *bioRxiv* **2021**.
178. Galli, F.; Varani, M.; Lauri, C.; Silveri, G. G.; Onofrio, L.; Signore, A., Immune cell labelling and tracking: implications for adoptive cell transfer therapies. *EJNMMI Radiopharmacy and Chemistry* **2021,** *6* (1), 1-19.
179. Signore, A.; Glaudemans, A. W.; Gheysens, O.; Lauri, C.; Catalano, O. A. In *Nuclear medicine imaging in pediatric infection or chronic inflammatory diseases*, Semin Nucl Med, Elsevier: 2017; pp 286-303.
180. Glaudemans, A. W.; Quintero, A. M.; Signore, A., PET/MRI in infectious and inflammatory diseases: will it be a useful improvement? Springer: 2012.
181. Bernsen, M. R.; Guenoun, J.; van Tiel, S. T.; Krestin, G. P., Nanoparticles and clinically applicable cell tracking. *Br J Radiol* **2015,** *88* (1054), 20150375.
182. Castaneda, R. T.; Khurana, A.; Khan, R.; Daldrup-Link, H. E., Labeling stem cells with ferumoxytol, an FDA-approved iron oxide nanoparticle. *J Vis Exp* **2011,** (57), e3482.
183. Daldrup-Link, H. E.; Meier, R.; Rudelius, M.; Piontek, G.; Piert, M.; Metz, S.; Settles, M.; Uherek, C.; Wels, W.; Schlegel, J., In vivo tracking of genetically engineered, anti-HER2/neu directed natural killer cells to HER2/neu positive mammary tumors with magnetic resonance imaging. *European radiology* **2005,** *15* (1), 4-13.
184. Frank, J. A.; Zywicke, H.; Jordan, E.; Mitchell, J.; Lewis, B. K.; Miller, B.; Bryant, L. H.; Bulte, J. W., Magnetic intracellular labeling of mammalian cells by combining (FDA-approved) superparamagnetic iron oxide MR contrast agents and commonly used transfection agents. *Academic radiology* **2002,** *9* (2), S484-S487.
185. Sibuyi, N. R. S.; Moabelo, K. L.; Fadaka, A. O.; Meyer, S.; Onani, M. O.; Madiehe, A. M.; Meyer, M., Multifunctional Gold Nanoparticles for Improved Diagnostic and Therapeutic Applications: A Review. *Nanoscale Research Letters* **2021,** *16* (1), 174.

Chapter 2

Luminescent Iridium coated Gold nanoparticles: Synthesis and Characterisation

2.1 Chapter Summary

This Chapter describes the processes involved in the synthesis and design of the iridium (III) complex (IrS1) used and its attachment onto gold nanoparticles to form the first batch of nanoprobes to take forward onto biological assays. To optimise the nanoprobes for tracking and detectability, the size and coating on the AuNPs were varied and tested to adjust for the highest loading of IrS1 onto the AuNP vs the best detectability of the probe vs the most biocompatible formulation. The photophysical impacts of attaching luminescent probes onto AuNPs are widely studied and any differences exhibited by the AuNPs were investigated to eliminate any limitations that may arise when detecting the nanoprobes in biological samples. This included comparing the UV-VIS absorption, excitation, emission and lifetimes of the nanoprobe composites with IrS1 independently.

2.1.1 Introduction

The use of molecular probes for fluorescence microscopy allows for highly sensitive imaging techniques to be utilized in *in vitro* and *in vivo* studies for detecting and visualizing morphological details in cells that cannot be seen by other imaging techniques. Metal-based, emissive dyes display many desired physicochemical properties for bioimaging, with favourable characteristics including a long luminescence lifetime (100ns to ms), a large Stokes shift and enhanced photostability allowing for lower photobleaching[1]. Iridium(III) complexes have surfaced as prospective phosphorescent probes for bioimaging, biolabeling, *in vivo* tumour imaging and staining of the nucleus, in the cytoplasm and the mitochondria[2]. The iridium centre itself is considered relatively inactive, however many efficient synthetic methods have been developed to facilitate the coordination of organic ligands[3].

Iridium(III) complexes coordinate with octahedral geometry. Upon coordinating with either strong or weak field ligands, the d^6 iridium(III) with cyclo-metalated ligands forms a low spin complex with a large splitting energy. The luminescence signal emitted by the iridium(III) cyclo-metalated complexes can be tuned by modifying the ligands that are attached within the complex framework[1,3]. Choice of ligand can also influence biological applications and can help predict intracellular interactions and localisation.

Two principles are observed in the excited state of iridium(III) polypyridyl complexes, firstly the metal to ligand charge transfer (MLCT) in which an electron is promoted from a metal d orbital to a vacant π^* orbital on one of the ligands and the

second being a ligand centred (LC) transition in which an electron is promoted from a π orbital to a π^* orbital of the ligand[4]. MLCT occurs between the HOMO of the metal and the LUMO of the ligand.

Strong spin-orbit coupling from the iridium(III) centre facilitates intersystem crossing to energetically similar triplet states and enables the formation of an emissive, mixed triplet excited state[5]. Understanding the processes involved during the interaction of iridium(III) complexes with biomolecules has been of great interest over recent years. Successful iridium(III) probes for the tracking of mitochondrial morphology in a study conducted by Chen *et al* explored the photostability, cytotoxicity and targeted mitochondrial specificity of potential probes[1]. Each iridium complex was found to possess a different emission colour, low cell cytotoxicity and good photostability allowing for observation of mitochondrial morphology. Additional investigations explored the probes' cellular uptake and bio-distribution using inductively coupled plasma mass spectrometry analysis[1]. Other studies have focused more acutely on biomolecular binding interactions with nucleic acids, peptides and proteins[6]. The possible coordination of a wide range of ligands enables fine tuning of the chemical and photophysical properties of the whole complex allowing for intracellular trafficking and distribution to be followed by imaging techniques such as confocal and fluorescence lifetime imaging, facilitated by the complexes' long-lived phosphorescence[2]. Cyclo-metalated iridium(III) polypyridine complexes have displayed good uptake in cell line studies, largely attributed to their increased lipophilicity[7, 8]. For cell tracking applications, uptake into biological material is critical in achieving the desired detectability required for most imaging techniques. The main difficulty with high loading of iridium(III) complexes into cells stems from their

cytotoxicity, resultant from the high levels of influx into cells by passive diffusion[9]. This problem has been circumvented by the combination of iridium(III) complexes onto more biocompatible gold nanoparticles.

The field of nanotechnology is bridging the gap between chemistry, biology and medicinal studies. Nanoparticles comprise of particles with a diameter of 100nm to 1nm and can be formed from a range of specialized materials that include metals, self-assembly lipids and semiconductors[10]. Metal nanoparticles, notably gold nanoparticles (AuNPs), present high optical activity permitting exclusive targeting of certain macromolecules within cells for cell work applications. Nanoparticles have become progressively widespread in the field of biomedical studies, allowing cell imaging with a range of modalities incorporating fluorescence and confocal microscopy[11]. On their own, AuNPs are detectable via their localised Surface Plasmon Resonance (SPR) effect exhibited by the oscillation of electrons at its surface[12]. The surface electrons oscillate in resonance with light waves and cause polarisation at the surface and are responsible for the scattering and absorption properties characteristic for AuNPs which in turn can affect luminescence of attached compounds[13, 14]. The SPR allows for the scattering and absorption of light as electrons are free to travel through the material. Smaller particles will exhibit less scattering when compared with larger particles[13].

The gold-sulphur bond is an easily formed and stable connection able to bind ligands and surfactants at the surface of an AuNP whilst remaining robust enough to stay intact in changing environments[15]. Many studies have utilised the gold-sulphur

bond to successfully functionalise AuNPs with an array of useful compounds for medical applications (Figure 2.1.1).

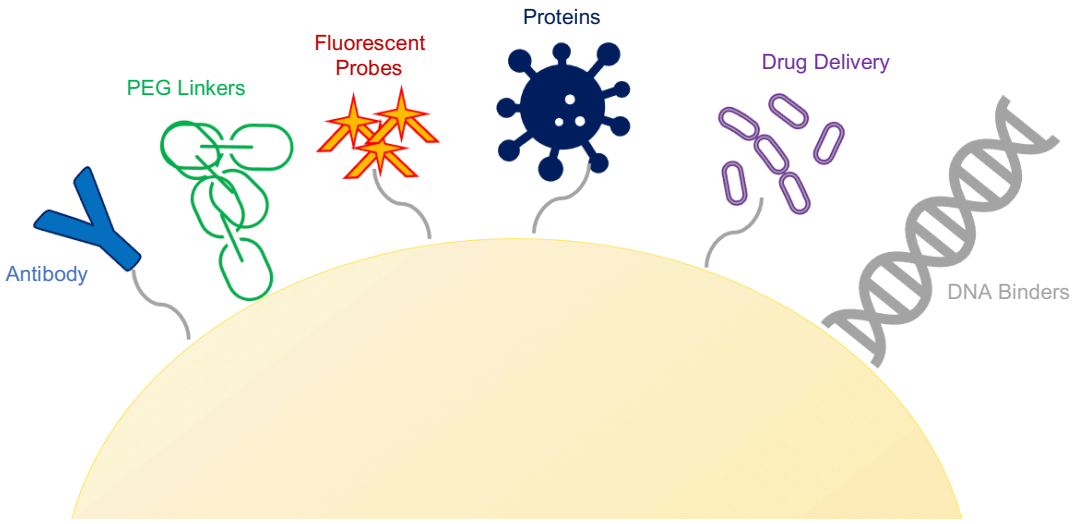

Fig.2.1.1. Diagram of AuNP functionalised with array of possible compounds.

The aforementioned iridium(III) luminescent transition metal complexes have been reported to exhibit suitable imaging properties and so possess the potential as cellular probes[16]. AuNPs are widely utilized in biomedical applications owing to their minimal cytotoxicity compared to other metal particles as a result of their scale and useful cellular interactions, size and shape dependant optical properties, high surface area to volume ratio and surfaces ready for functionalisation[17]. The exploitation of such features has permitted amalgamation of the intrinsic optical and physical characteristics of AuNPs through the addition of surface-active luminescent probes. Combining probes to nanoparticles conserves the photophysical, desired properties of the complexes whilst complementing the nanoparticle qualities. Additional coating of either stabilising or targeting agents onto the nanoparticle along with the luminescent probes presents photophysical benefits including improvement of

luminescence and increased lifetime of the probe and enhanced biological uptake[18].

Currently, transferring cell therapies to the clinic has faced many issues, the greatest of which is the inconsistency of results seen from preclinical trials and post clinical studies. Discrepancies include different patients exhibiting contradicting results where some show signs of improvement whilst others do not. Study has shown that the core reason for these opposing results is due to the lack of data on the fate of cell therapies in the body. At present, the most commonly used method of determining if the desired cells have reached their target location is by monitoring symptoms of the patients. The underlining demand herein is to find a way to follow the cells from the moment they are introduced to the time they reach their destination with real time tracking. Creating a probe that has multimodal properties means that information can be attained all the way through from sub cellular levels up to whole body parameters. Combining fluorescence, multiphoton microscopy and CT imaging encompasses an array of advantages including spatial resolution, penetration depth, reliability and providing anatomical information.

The use of biocompatible nanoparticles for cell tracking has increasingly gathered more interest, enabling tracking over long periods of times as a result of their efficient uptake. However, this does not come without its challenges. When designing nanoprobes for tracking, certain aspects need to be considered, such as, *in vitro* labelling and *in vivo* injection of the cells, along with non-invasive imaging. Here it is vital to obtain the balance between achieving the maximum loading of probes to achieve the most contrast whilst maintaining the biological functionality of the cells for the greatest therapeutic effect. Once inside the body there are further considerations

that need to be addressed. These include accurate analysis of the images with the objective to identify clusters of cells and to differentiate them from surrounding tissue, to quantify the number of cells delivered to the target site and ultimately, whether the probes remain in the cells they arrived in so longitudinal studies can be acquired over a period time. These are some of the challenges facing commercially available tracking devices that need to be overcome with a more purpose driven approach to probe design.

2.2 IrS1 Synthesis

The iridium complex, IrS1 is based on a bis(2-phenyl quinoline-C2,N') luminophore with a modified bipyridine ligand with incorporated surface binding thiols for attachment to gold nanoparticles[19]. IrS1 is formed by placing tetrakis(phenylquinoline-C2,N')(μ-dichloro)diiridium and 5,5′-bis(mercaptomethyl)-2,2′-bipyridine under reflux in ethylene glycol and precipitating the hexafluorophosphate salt (Scheme 2.1). The complex is then characterised by ^{1}H NMR and $ES^{+}MS$. Through a Dowex ion exchange, the hexafluorophosphate salt is converted to the chloride to improve the complexes' aqueous stability for further application to form nanoprobes and for greater efficiency in cellular studies[20-22].

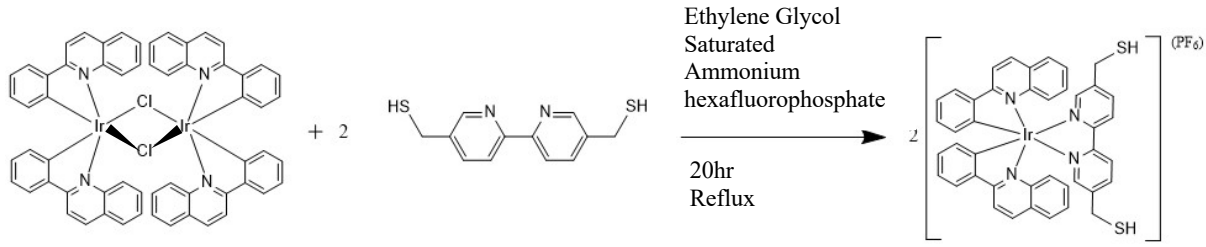

Scheme 2.1: Synthesis of IrS1.
Bonds drawn to allow for full presentation of compound and do not accurately reflect true bond angles and compound geometry

The 5,5′-bis(mercaptomethyl)-2,2′-bipyridine ligand was synthesised through radical addition of bromine to 5,5'-dimethyl-2-2'-bipyridine (Scheme 2.2) which was then followed by an exchange with the thiol group (Scheme 2.3)[23].

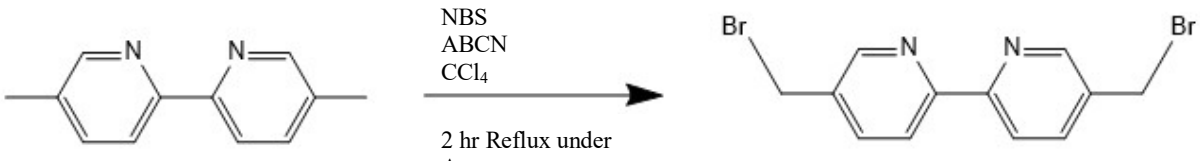

Scheme 2.2: Synthesis of 5,5'-dibromomethyl-2,2'-bipyridine.

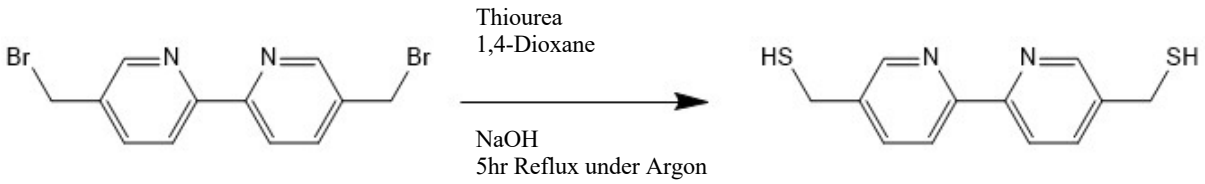

Scheme 2.3: Synthesis of 5,5′-bis(mercaptomethyl)-2,2′-bipyridine.

The cyclometalated chloro-bridged dimer was synthesised using a similar route to previously reported methods[1, 24, 25]. A mixture of 2-ethoxylethanol and water was added to a flask containing $IrCl_3 \bullet xH_2O$ and the 2-phenylquinoline and heated to reflux for 24 hours (Scheme 2.4). After cooling, the tetrakis(phenylquinoline-C2,N')(μ-dichloro)diiridium is filtered and dried.

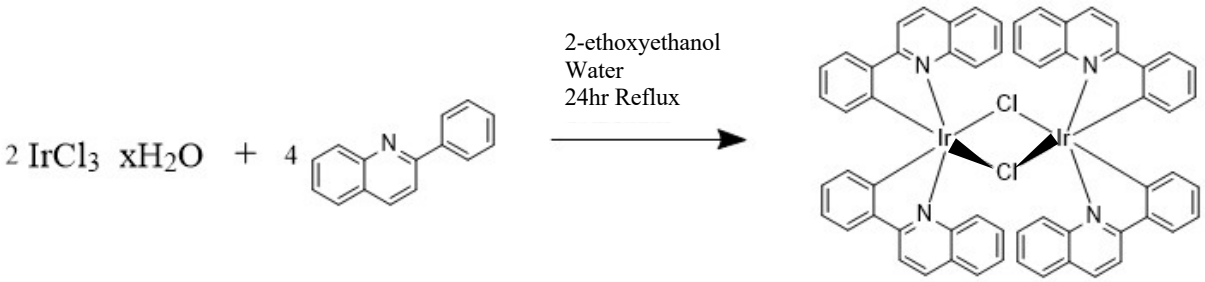

Scheme 2.4: Synthesis of tetrakis(phenylquinoline-C2,N')(μ-dichloro)diiridium.

2.3 Photophysical Characterisation of IrS1

The solution based photophysical characterisation of IrS1 was performed to record the absorption, steady state emission, excitation and lifetime of the compound in water.

The absorbance spectra suggest the presence of a singlet Metal to Ligand Charge Transfer (MLCT) (d - π^*) between 400 – 500nm with the maximum at 420nm (Figure 2.3.1)[1, 2]. The singlet MLCT molar absorptivity for IrS1 is 2,500 M^{-1} cm^{-1}. The Ligand Centred (LC) state (π - π^*) and the Metal Centred (d - d) are suggested between 200 – 350nm with absorptions at 280nm and 310nm respectively[1, 2]. The molar absorptivity for LC (280nm) is 28,000 M^{-1} cm^{-1}.

The emission for IrS1 shows the triplet MLCT broad band between 500-700nm, with a maximum at 580 nm. The excitation spectra mirror the absorption spectra, with the singlet MLCT between 400-500nm and the LC between 200-350nm (Figure 2.3.2 left). The luminescent lifetime of IrS1 was recorded in aerated water and measured at 470ns (Figure 2.3.2 right, Table 2.3.1).

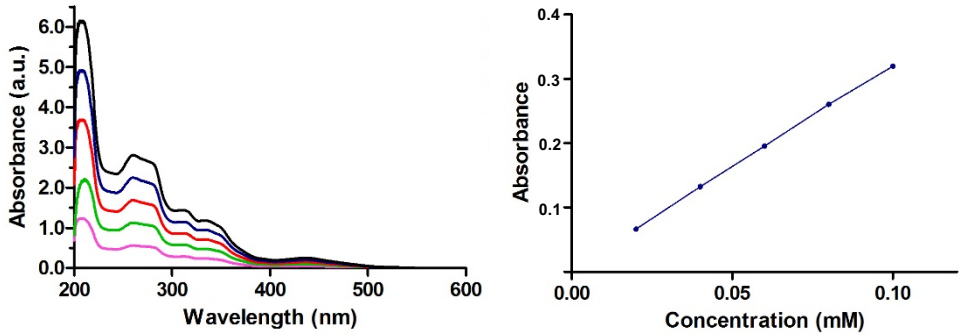

Figure 2.3.1: (left) UV-VIS Absorption IrS1 in water, (1.5% MeOH) (pink = 0.02mM, green = 0.04mM, red = 0.06mM, blue = 0.08mM, black = 0.10mM). (right) Concentration vs Absorbance of MLCT band at λ_{max} = 420nm.

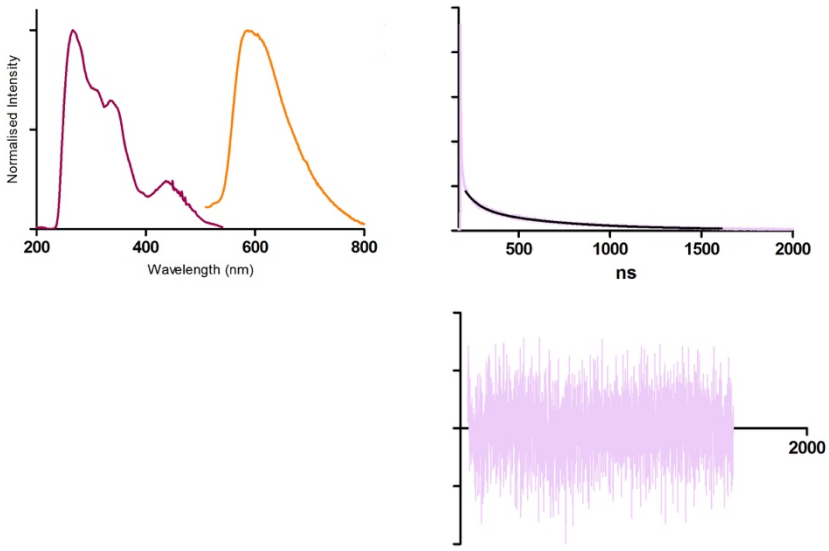

Figure 2.3.2: (left) Normalised excitation and emission spectra for 0.02mM IrS1 in aerated solvent 1.5% aqueous MeOH (purple = excitation, Em580nm, orange = emission, Ex405nm). (right) Luminescent Lifetime Decay in aerated solvent and fitting for IrS1 λ_{exc} = 375nm and λ_{det} 580nm. Global analysis, Tail fitting. Fitting range (430; 3300) channels. Global Chi square 1.039. Two component analysis.

Table 2.3.1: Luminescent Lifetime Decay, 2 component analysis for IrS1 in water

	χ^2	τ (ns)	F_i (%)
IrS1	1.060	75	10
		470	90

2.4 Synthesis of Nanoprobe Library

2.4.1 Synthesis of Gold Nanoparticles

Monodispersed 13nm Gold Nanoparticles (Au13NPs) were synthesised using a modified version of the Turkevich synthesis[26-28]. The first step of the synthesis involves forming Au13NP seeds which are stabilised by citrate anions. In 1951 Turkevich originally developed the synthesis of citrate stabilised aqueous AuNPs that fell within the size range of 5 – 150nm[29]. This method is seemingly straightforward and has notably become the foundation of most nanoparticle preparations, largely due to its reproducibility. The method was later adapted by Grabar *et al* in 1995[27]. In the synthesis, the addition of trisodium citrate reduces the Au^{3+} salt, $HAuCl_4$, in water to produce Au13NPs. However, this preparation alone has been found to give a large size distribution, giving rise to inconsistencies between repeats. The inverse Turkevich method was developed by Vossmeyer *et al* by changing the environment during synthesis to lower the size distribution of the particles formed[28]. They found that as the size is mainly determined by the ratio of Au^{3+} salt to citrate ions, increasing the rate of reaction, thus forcing a quicker nucleation meant a narrower size distribution of the particles formed[30-33]. Increasing the rate of reaction is directly proportional to the formation of the precursors in the reaction. The group investigated increasing the rate of reaction by increasing the reactivity of acetonedicarboxylate, the citrate derivative involved in the nucleation step. Reactivity can be increased by reversing the addition of reagents meaning the Au^{3+} salt mixture would be added to the citrate solution. Another known method for increasing the rate of reaction would be to influence the pH so that it is lowered to increase reactivity of the Au^{3+} precursor [34-38]. By using sodium citrate with citric acid, a buffer solution is produced and when nucleation occurs, the nanoparticles are encouraged to seed with a narrower size distribution. As such, using

the inverse method, hot Au^{3+} salt is added to a mixture of sodium citrate, citric acid and ethylenediaminetetraacetic acid (to aid with spherical shape uniformity) under reflux to afford monodisperse 13nm gold nanoparticles (2nM) with a consistent polydispersity index lower than 0.2 (Scheme 2.5).

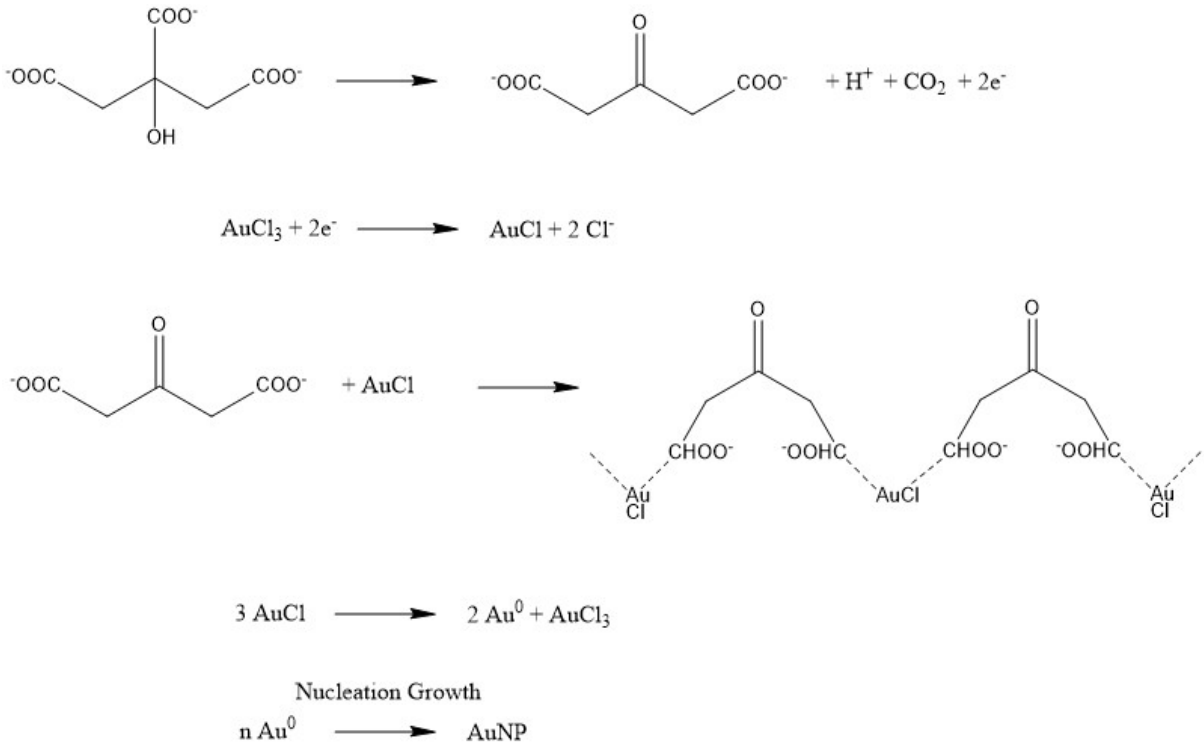

Scheme 2.5: Redox reactions occurring during AuNP synthesis. First, acetonedicarboxylate and Au(I) are produced. The precursors arrange for the disproportionation of Au(I) to Au(0) and Au(III) before nucleation growth of Au(0) to form AuNPs.

In order to seed to larger nanoparticles, more Au^{3+} salt solution is titrated into the solution to combine with the existing nanoparticles. Using this slightly modified synthesis, no new nanoparticles are formed[26]. Monodisperse 25, 50 and 100nm AuNPs were synthesised using the slightly modified synthesis[26]. 0.7nM Au25NP, 80pM Au50NP and 40pM Au100NP were seeded through serial seeding of Au^{3+} salt and sodium citrate to Au13NP seeds (Figure 2.4.1.1).

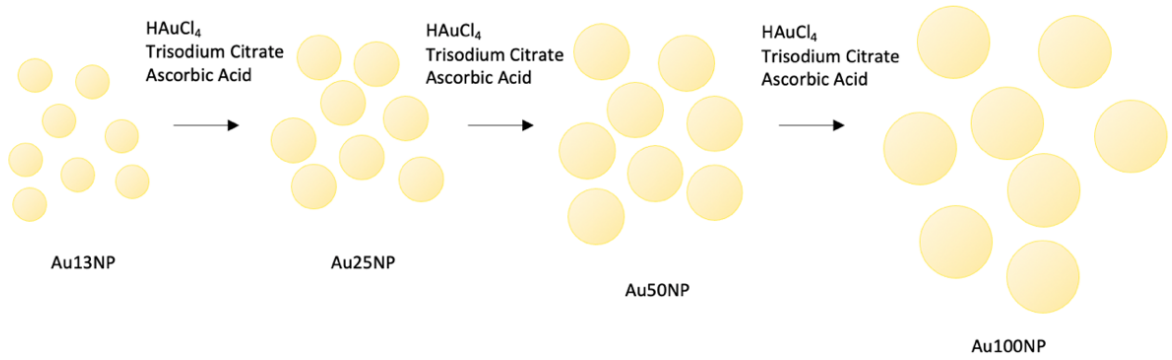

Figure 2.4.1.1: Schematic to show the increase in size when seeding Au13NP to Au100NP.

In order to calculate the concentration of AuNPs at each step in the synthesis, initially two assumptions must be made to determine the number of gold atoms in a nanoparticle (Equation 2.1, Table 2.4.1.1); firstly, that nanoparticles are comprised of perfect spheres and secondly, that the atoms are packed in a uniform face-centred cubic crystalline structure, for which the density of gold is ρ_{gold} = 19.32gcm^{-3} [39]. The diameter for each size of nanoparticle must be obtained experimentally either by DLS or TEM and so the calculated value may differ slightly for each batch synthesised.

Defining the volume, v, of a sphere as:

$$v = \frac{4}{3}\pi R^3 = \frac{1}{6}\pi D^3$$

Where R and D are the radius and diameters of the sphere respectively, it follows that the density, ρ, of a sphere of mass m is:

$$\rho = \frac{m}{v} = \frac{n \times Mr}{v}$$

Where Mr is the molecular mass (196.96657g mol^{-1}), and n is the number of moles. Rearranging for n and substituting for v gives:

$$n = \frac{\rho \times v}{Mr} = \frac{\rho \times \pi D^3}{6 \times Mr}$$

To convert the number of moles to the number of atoms N, we multiply by Avogadro's number N_A = 6.022140857x10^{-23} mol^{-1} :

$$N = \frac{\rho \times \pi D^3}{6 \times Mr} \times N_A$$

Converting ρ_{gold} = 19.32g cm^{-3} to g nm^{-3} (i.e. 19.32 x (10^{-2} x 10^{-9})$^{-3}$ = 19.32 x10^{-23} g nm^{-3} and substituting into the above equation with the other numerical constants, we can simplify to:

$$N = \frac{\rho \times \pi D^3}{6 \times Mr} \times N_A = \frac{19.32 \times 10^{-21} g\ nm^{-3} \times \pi \times D^3}{6 \times 196.96657 g\ mol^{-1}} \times 6.022140857 \times 10^{23} mol^{-1}$$

$$\therefore N = 30.89685812 \times D^3$$

Where : N is the number of atoms per nanoparticle of diameter D (nm).

Equation 2.1: Determining the number of gold atoms in a nanoparticle.

The next step would be to calculate the molar concentrations of a nanoparticle solution (Equation 2.2, Table 2.4.1.1).

To determine the molar concentration of gold nanoparticles, C, we determine the number if moles of gold nanoparticles per unit volume, V, in the gold colloid. The total number of gold nanoparticles, N_{NP}, is defined as the number of moles multiplied by Avogadro's constant:

$$C = \frac{n}{V} = \frac{N_{NP}}{V \times N_A}$$

The total number of gold nanoparticles can be determined by dividing the total number of gold atoms, N_{atoms}, in the solution by the number of gold atoms per nanoparticle, N :

$$N_{NP} = \frac{N_{atoms}}{N} \rightarrow C = \frac{N_{NP}}{V \times N_A} = \frac{N_{atoms}}{N \times V \times N_A}$$

The total number of atoms in solution can be determined by using the initial amount of gold (mass $m_{i,Au}$) introduced into the reaction and assuming 100% conversion into nanoparticles:

$$n_{i,Au} = \frac{m_{i,Au}}{Mr} \rightarrow N_{atoms} = n_{i,Au} \times N_A = \frac{m_{i,Au \times N_A}}{Mr}$$

$$C = \frac{N_{atoms}}{N \times V \times N_A} = \frac{m_{i,au} \times N_A}{N \times V \times N_A \times Mr}$$

$$\rightarrow C = \frac{m_{i,Au}}{N \times V \times Mr}$$

Equation 2.2: Determining the molar concentrations of a nanoparticle solution.

Table 2.4.1.1: Calculated number of gold atoms per nanoparticle and calculated molar concentrations of a nanoparticle solution.

	Calculated number of Gold atoms per nanoparticle	**Calculated molar concentration of a nanoparticle solution**
Au13NP	70,000	1.62 nM
Au25NP	480,000	0.689 nM
Au50NP	3,860,000	77.5 pM
Au100NP	30,900,000	38.8 pM

The AuNPs were characterised by their individual surface plasmon resonance (SPR) bands by UV-VIS, dynamic light scattering (DLS) and zeta potential measurements. Solutions of Au13NP, Au25NP, Au50NP and Au100NP displayed an absorption band with a maximum, λ_{max}, at 517, 522, 526 and 559 nm respectively, characteristic of their SPR band and in agreement with previously published data (Figure2.4.1.2)[12, 40].

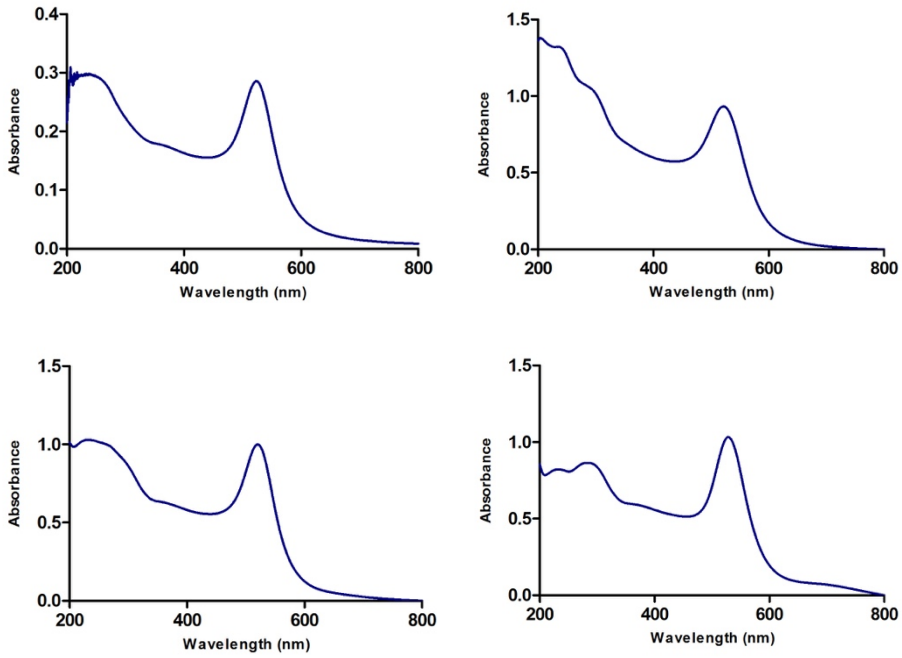

Figure 2.4.1.2: UV-VIS spectra for Au13NP (top left), Au25NP (top right), Au50NP (bottom left) and Au100NP (bottom right) each at stock concentrations; 1.62nM, 0.689nM, 77.5pM and 38.8pM respectively.

DLS was conducted to confirm the size assignments for each group of gold nanoparticles (Figure 2.4.1.3, Table 2.4.1.2). The small PDI's confirm good monodispersity amongst the solutions of nanoparticles, suggesting they are spherical and of similar size. The zeta potential measurements show that the net charge of all synthesised nanoparticles is similar. The negativity of the zeta potentials can be attributed to the citrate ions stabilising the nanoparticles.

Table 2.4.1.2: DLS size analysis by intensity and number with corresponding PDI and zeta potential for Au13NP, Au25NP, Au50NP and Au100NP at stock concentrations; 1.62nM, 0.689nM, 77.5pM and 38.8pM respectively.

	Size by Intensity/ nm	**Size by number/ nm**	**PDI**	**Zeta Potential/ mV**
Au13NP	16 ± 8	15 ± 4	0.076	-39 ± 12
Au25NP	27 ± 7	20 ± 5	0.058	-39 ± 13
Au50NP	58 ± 9	31 ± 9	0.133	-41 ± 13
Au100NP	100 ± 28	72 ± 20	0.064	-41 ± 13

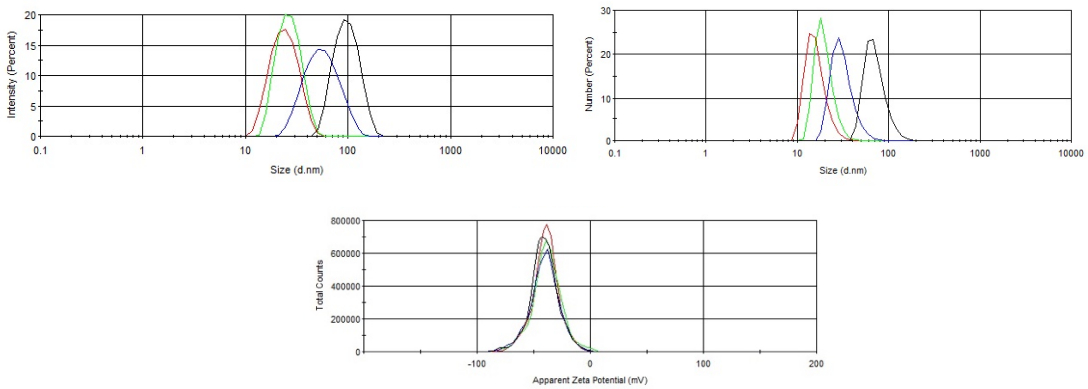

Figure 2.4.1.3: (Top) Dynamic Light Scattering data by intensity(left) and number(right) of Au13NP(red), Au25NP(green), Au50NP(blue) and Au100NP(black). (Bottom) Zeta Potential data of Au13NP(red), Au25NP(green), Au50NP(blue) and Au100NP(black) at stock concentrations; 1.62nM, 0.689nM, 77.5pM and 38.8pM respectively.

2.4.2 Coating of AuNPs with Stabilising Agents and IrS1

IrS1 attaches to the gold nanoparticles via a sulphur-gold bond formed between the thiol groups on the bipyridine ligand and the gold atoms on the AuNP[22, 41]. The AuNPs are negatively charged and IrS1 has a charge of 1+. As such, IrS1 cannot be added directly into the aqueous solution of AuNPs due to electrostatic interactions which cause the AuNPs to aggregate as a result of destabilisation[18, 42-44]. To better stabilise the AuNPs so the IrS1 can be added to the solution, lipophilic agents can be used. Zonyl FSA is a precursor fluorosurfactant comprising of a fluorinated chain which increases the stability and lipophilicity of the surfactant and provides a carboxylic acid group for attachment to the AuNP. Functionalisation of AuNPs can be monitored by following the wavelength shift of the AuNP's characteristic SPR band in the visible absorption range. As changes occur to the surface of the nanoparticle, the λ_{max} of the SPR band also changes. Upon addition of Zonyl, a shift of up to 2nm is observed (Figure 2.4.2.2). The surfactant coated particles were isolated by centrifugation and were further titrated, monitored by UVVIS, with IrS1, concurrently monitoring the SPR (Figure 2.4.2.1, 2.4.2.2, Appendix 2.1).

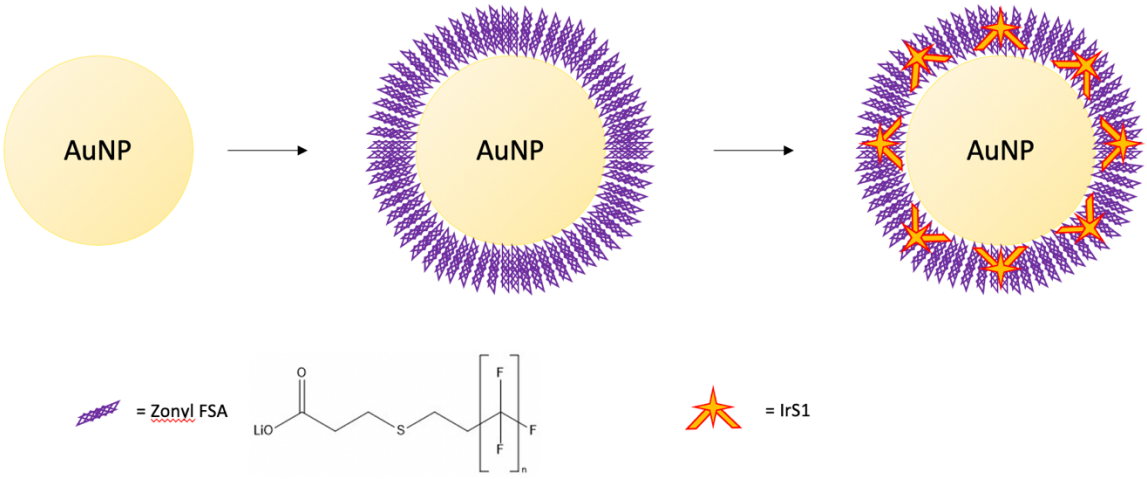

Figure 2.4.2.1: Schematic showing the attachment of Zonyl and IrS1 to AuNPs.

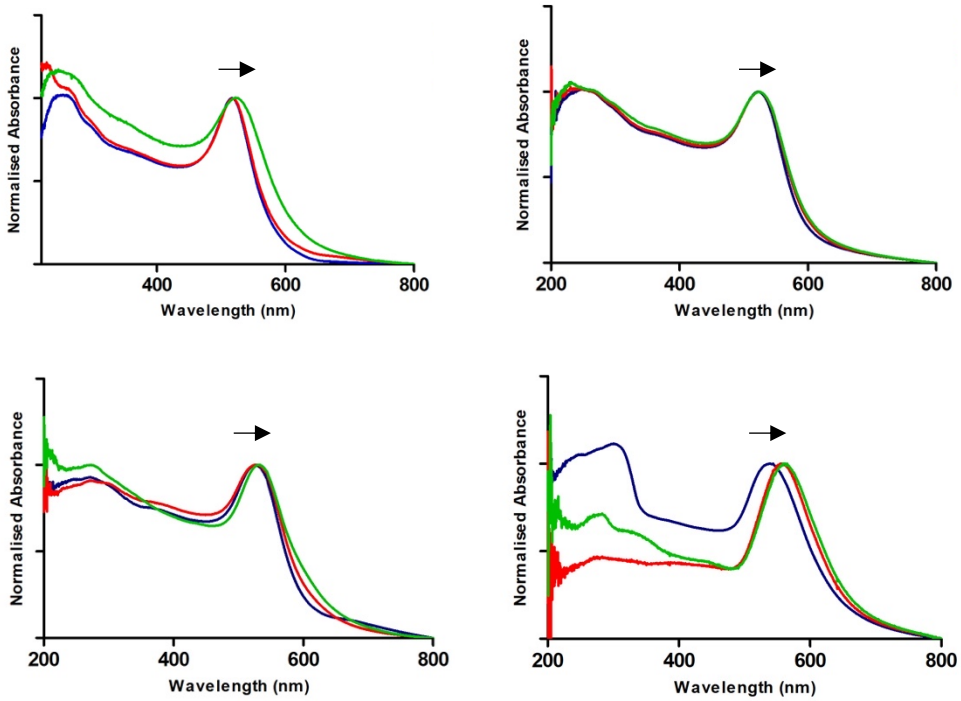

Figure 2.4.2.2: UV-VIS profile for Au13NP(top left) 1nM, Au25NP(top right) 1nM, Au50NP(bottom left) 0.5nM and Au100NP(bottom right) 0.1nM, with blank NPs(blue), coated with Zonyl(red)(w:w 10%) and coated with IrS1(green)(1μM).

Monitoring the change in the λ_{max} of the SPR band during a titration is used to determine the saturation of the AuNP surface (Table 2.4.2.1). As more probe is added, a red shift in wavelength is observed until the AuNPs lose their stability and become aggregated. Using this data, an optimum loading volume can be determined for the loading of IrS1 onto each size of AuNP. Given that the volume and concentration of both the AuNP solution and IrS1 are known, theoretical calculations can be made to determine how many IrS1 molecules are attached to each AuNP. To accurately determine the ratio of IrS1 to AuNP, ICP-MS was carried out (Table 2.4.2.4).

In the same way to Zonyl, two thio-lated PEG linker chains were investigated as potential stabilising agents for the AuNPs. PEG linkers are known, in the literature, to enhance uptake of foreign species into biological environments and can aid in the endocytic process[45]. The first PEG chain used was O-(2-carboxyethyl)-O'-(2-

mercaptoethyl)heptaethylene glycol (SPEG) with Mn 458 and the second was Poly(ethylene glycol) 2-mercaptoethyl ether acetic acid (LPEG) with Mn 2,100 (Figure 2.4.2.2). Both PEG chains were titrated onto each AuNP (Appendix 2.2 and 2.3), followed by titration with IrS1 (Table 2.4.2.2 and 2.4.2.3). As with Zonyl, a red shift in the λ_{max} of the SPR band is observed and monitored to allow for the optimum loading of IrS1 (Figure 2.4.2.3 and 2.4.2.4).

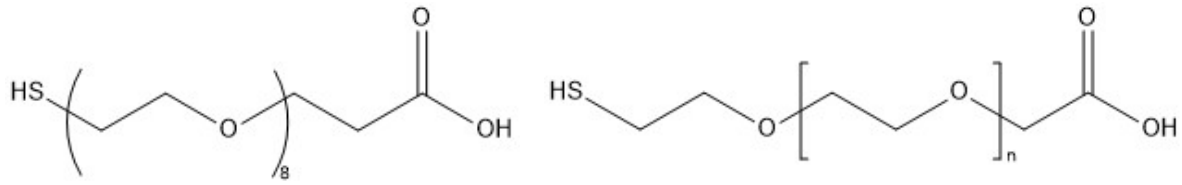

Figure 2.4.2.2: Chemical structures of SPEG(left) and LPEG(right).

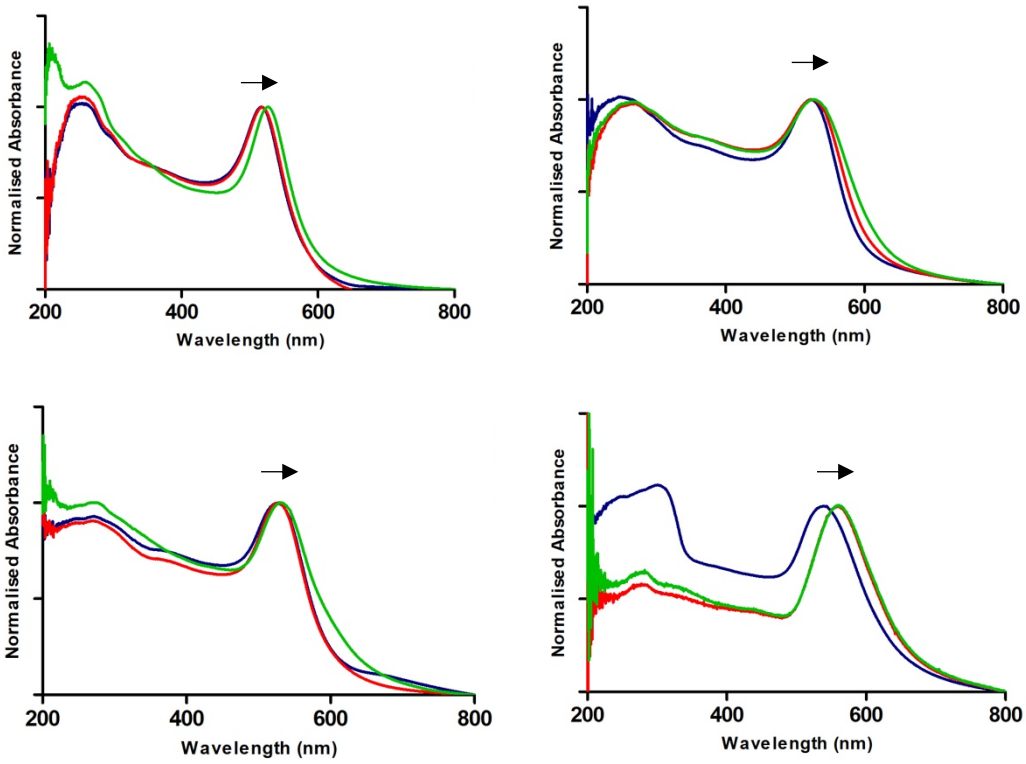

Figure 2.4.2.3: UVVIS profile for Au13NP(top left) 1nM, Au25NP(top right) 1nM, Au50NP(bottom left) 0.5nM and Au100NP(bottom right) 0.1nM, with blank NPs(blue), Coated with SPEG(red) (0.1mM) and coated with IrS1(green) (0.1μM).

A noticeable difference observed between Zonyl and the PEG chains was the amount of PEG that could be added to the AuNP solution without causing aggregation.

Although the shift in SPR reaches a plateau after reaching a maximum loading point, excess PEG in the solution appears to have no aggregation effect on the stability of the AuNPs. This observation supports the use for PEG as a stabilising agent for AuNPs. The strength of the sulphur-gold bonds is observed in the greater shifts in SPR of the PEG coated AuNPs compared to that of Zonyl coated AuNPs (Table 2.4.2.1, 2.4.2.2 and 2.4.2.3).

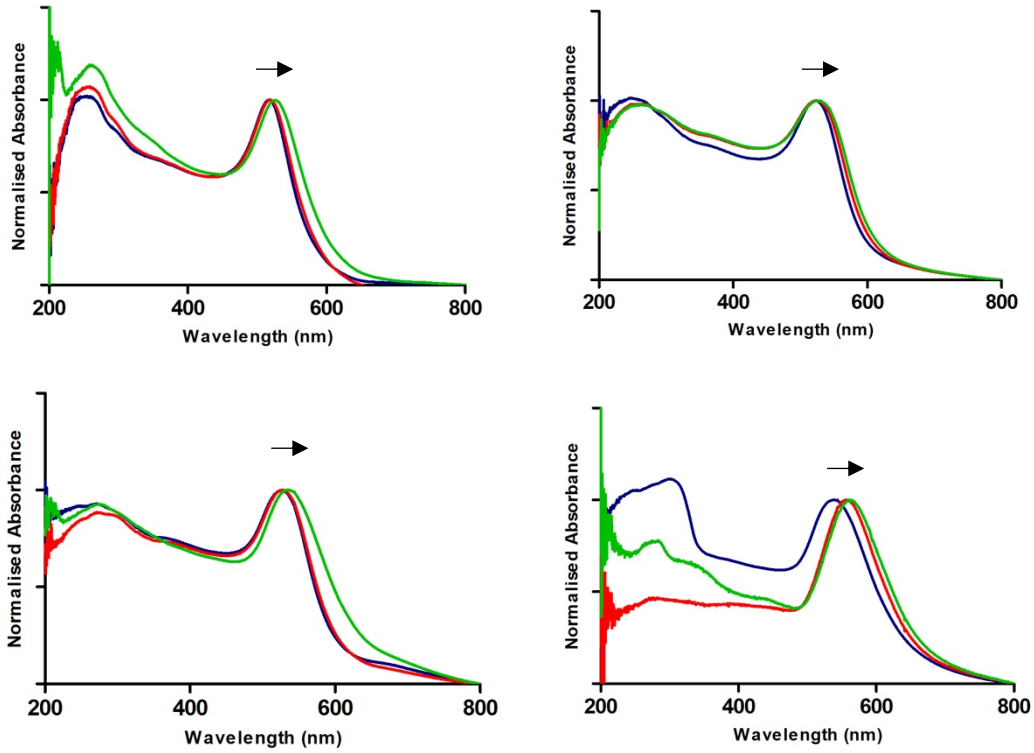

Figure 2.4.2.4: UVVIS profile for Au13NP(top left) 1nM, Au25NP(top right) 1nM, Au50NP(bottom left) 0.5nM and Au100NP(bottom right) 0.1nM, with blank NPs(blue), Coated with LPEG(red) (0.1mM) and coated with IrS1(green) (0.1μM).

Table 2.4.2.1: Summary of AuNP SPR shifts for Zonyl coated Au13NP (1nM), Au25NP (1nM), Au50NP (0.5nM) and Au100NP (0.1nM) with IrS1 (1μM).

	λ_{max} /nm	Shift / nm		λ_{max} /nm	Shift / nm		λ_{max} /nm	Shift / nm
Au13NP	517	-	Au13NP.Zonyl	518	1	Au13NP.Zonyl.IrS1	520	3
Au25NP	522	-	Au25NP.Zonyl	523	1	Au25NP.Zonyl.IrS1	525	3
Au50NP	526	-	Au50NP.Zonyl	528	2	Au50NP.Zonyl.IrS1	532	6
Au100NP	559	-	Au100NP.Zonyl	559	1	Au100NP.Zonyl.IrS1	562	3

Table 2.4.2.2: Summary of AuNP SPR shifts for SPEG coated Au13NP (1nM), Au25NP (1nM), Au50NP (0.5nM) and Au100NP (0.1nM) with IrS1 (0.1μM).

	λ_{max} /nm	Shift / nm		λ_{max} /nm	Shift / nm		λ_{max} /nm	Shift / nm
Au13NP	517	-	Au13NP.SPEG	518	1	Au13NP.SPEG.IrS1	527	10
Au25NP	522	-	Au25NP.SPEG	525	3	Au25NP.SPEG.IrS1	528	6
Au50NP	526	-	Au50NP.SPEG	527	1	Au50NP.SPEG.IrS1	531	5
Au100NP	559	-	Au100NP.SPEG	561	2	Au100NP.SPEG.IrS1	564	5

Table 2.4.2.3: Summary of AuNP SPR shifts for LPEG coated Au13NP (1nM), Au25NP (1nM), Au50NP (0.5nM) and Au100NP (0.1nM) with IrS1 (0.1μM).

	λ_{max} /nm	Shift / nm		λ_{max} /nm	Shift / nm		λ_{max} /nm	Shift / nm
Au13NP	517	-	Au13NP.LPEG	519	2	Au13NP.LPEG.IrS1	526	9
Au25NP	522	-	Au25NP.LPEG	526	4	Au25NP.LPEG.IrS1	528	6
Au50NP	526	-	Au50NP.LPEG	529	3	Au50NP.LPEG.IrS1	535	9
Au100NP	559	-	Au100NP.LPEG	562	3	Au100NP.LPEG.IrS1	566	7

In contrast to the Zonyl coated AuNPs, PEG coated AuNPs aggregated upon addition of IrS1 at 1μM, yet, at 0.1μM, IrS1 was comfortably added to the PEG coated AuNPs. With the lower concentration, a higher volume of IrS1 was added to the solutions and so theoretically, each 1ml of 1nM AuNPs received similar moles of IrS1. ICP-MS shows that slightly different amounts of the IrS1 were bound to the AuNPs of the same size, but with different coatings (Table 2.4.2.4, 2.4.2.5 and 2.4.2.6). This difference in loading could be attributed to the steric hinderance of the larger molecules of both SPEG and LPEG in comparison with Zonyl. Another explanation could be related to the sulphur-gold bonds that attach SPEG and LPEG to the AuNP. The carboxylic acid group on Zonyl that forms a bond with the gold is far more labile than the sulphur-gold bond between the PEG chains and the gold. As such, when IrS1

is added to the Zonyl coated particles, some Zonyl may be displaced, allowing for the IrS1 to competitively bind to the AuNP, whereas, the IrS1 molecules must sterically orientate themselves correctly to bind around the PEG coating.

Table 2.4.2.4: Calculated ratios for Zonyl coated Au13NP, Au25NP, Au50NP and Au100NP with IrS1compared to those calculated by ICP-MS.

	Ratio of Ir/Au	**ICP-MS calculated number of IrS1 per AuNP**
Au13NP.Zonyl.IrS1	$3.1x10^{-2}$	2,100
Au25NP.Zonyl.IrS1	$5.8x10^{-3}$	2,800
Au50NP.Zonyl.IrS1	$1.3x10^{-3}$	5,100
Au100NP.Zonyl.IrS1	$3.2x10^{-4}$	9,700

Table 2.4.2.5: Calculated ratios for SPEG coated Au13NP, Au25NP, Au50NP and Au100NP with IrS1compared to those calculated by ICP-MS.

	Ratio of Ir/Au	**ICP-MS calculated number of IrS1 per AuNP**
Au13NP.SPEG.IrS1	$2.1x10^{-2}$	1,400
Au25NP.SPEG.IrS1	$5.6x10^{-3}$	2,700
Au50NP.SPEG.IrS1	$1.3x10^{-3}$	5,000
Au100NP.SPEG.IrS1	$3.2x10^{-4}$	9,900

Table 2.4.2.6: Calculated ratios for LPEG coated Au13NP, Au25NP, Au50NP and Au100NP with IrS1compared to those calculated by ICP-MS.

	Ratio of Ir/Au	**ICP-MS calculated number of IrS1 per AuNP**
Au13NP.LPEG.IrS1	$2.3x10^{-2}$	1,100
Au25NP.LPEG.IrS1	$5.6x10^{-3}$	2,700
Au50NP.LPEG.IrS1	$1.1x10^{-3}$	4,300
Au100NP.LPEG.IrS1	$3.0x10^{-4}$	9,200

DLS size analysis and Zeta Potential (Table 2.4.2.7, Appendix 2.4, 2.5, 2.6) were used to determine good monodispersity of the coated particles and to check the negative potential of the probes (AuNP+coating+IrS1), as is studied in the literature, the surface charge of a probe influences its uptake into biological material[46].

Table 2.4.2.7: Summary of DLS size analysis and Zeta Potentials of full probe library.

	Size by Intensity/ nm	**Size by number/ nm**	**PDI**	**Zeta Potential/ mV**
Au13NP.Zonyl	26 ± 9	15 ± 4	0.111	-52 ± 12
Au13NP.SPEG	28 ± 9	18 ± 5	0.094	-69 ± 13
Au13NP.LPEG	35 ± 10	23 ± 6	0.170	-65 ± 15
Au13NP.Zonyl.IrS1	26 ± 9	15 ± 4	0.103	-44 ± 13
Au13NP.SPEG.IrS1	29 ± 9	18 ± 5	0.103	-36 ± 12
Au13NP.LPEG.IrS1	37 ± 14	23 ± 6	0.114	-40 ± 12
Au25NP.Zonyl	35 ± 16	26 ± 5	0.176	-56 ± 12
Au25NP.SPEG	34 ± 13	29 ± 5	0.186	-67 ± 14
Au25NP.LPEG	45 ± 16	26 ± 7	0.125	-69 ± 14
Au25NP.Zonyl.IrS1	35 ± 13	28 ± 5	0.158	-47 ± 14
Au25NP.SPEG.IrS1	35 ± 13	29 ± 5	0.148	-40 ± 12
Au25NP.LPEG.IrS1	45 ± 16	34 ± 7	0.118	-37 ± 12
Au50NP.Zonyl	64 ± 25	34 ± 10	0.149	-59 ± 7
Au50NP.SPEG	71 ± 26	41 ± 12	0.134	-65 ± 13
Au50NP.LPEG	79 ± 35	38 ± 12	0.200	-63 ± 13
Au50NP.Zonyl.IrS1	65 ± 25	34 ± 10	0.149	-46 ± 13
Au50NP.SPEG.IrS1	73 ± 25	43 ± 12	0.123	-61 ± 16
Au50NP.LPEG.IrS1	85 ± 40	38 ± 12	0.199	-62 ± 13
Au100NP.Zonyl	104 ± 30	74 ± 21	0.056	-64 ± 11
Au100NP.SPEG	107 ± 29	79 ± 22	0.049	-67 ±14
Au100NP.LPEG	107 ± 28	78 ± 22		-66 ± 14
Au100NP.Zonyl.IrS1	106 ± 32	74 ± 22	0.070	-45 ± 13
Au100NP.SPEG.IrS1	107 ± 26	79 ± 21	0.024	-63 ± 13
Au100NP.LPEG.IrS1	107 ± 23	78 ± 20	0.012	-63 ± 13

The luminescence spectra of the probe library were recorded to deduce if the size of gold and stabilizing agent had any impact on the emission of IrS1 (Figure 2.4.2.5, Table 2.4.2.8). There was no significant change in the λ_{max} for the emission data for the full probe library compared to IrS1 in solution on its own, suggesting the loading onto AuNPs had not affect the MLCT luminescence.

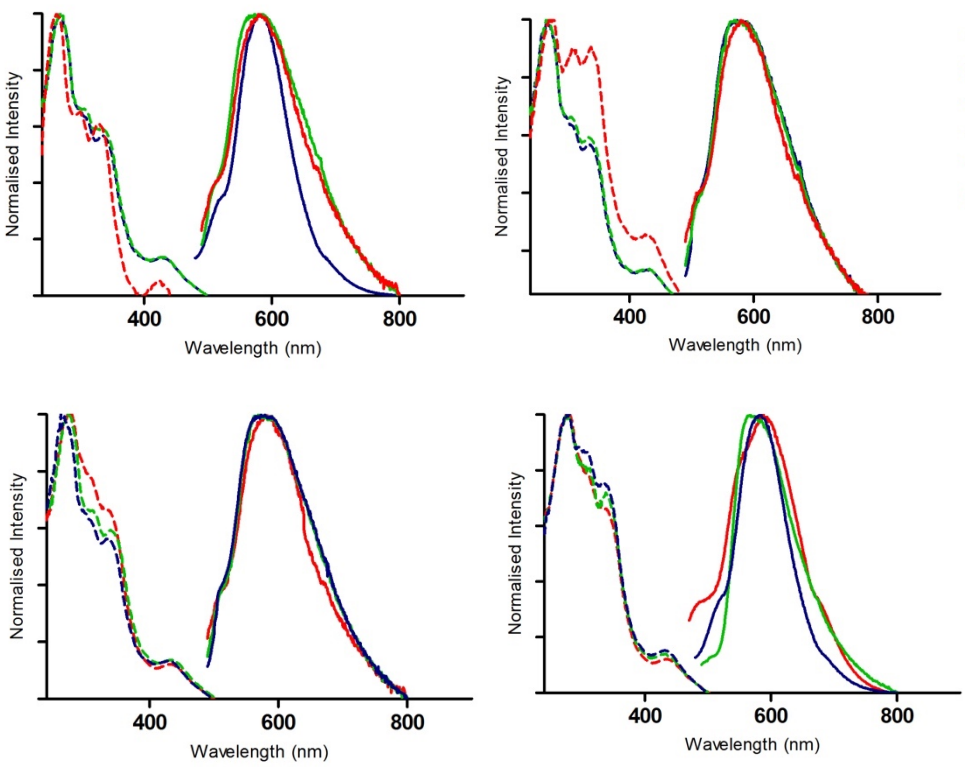

Figure 2.4.2.5: Luminescent spectra of full probe library. λ_{exc} = 405 and λ_{det}(Top Left) Au13NP, (Top Right) Au25NP, (Bottom Left) Au50NP and (Bottom Right) Au100NP. Dashed lines = Excitation spectra. Filled lines = Emission spectra. (Blue) Zonyl coating, (Green) SPEG coating and (Red) LPEG coating. All coated AuNPs are also coated with IrS1.

Table 2.4.2.8: Summary of λ_{max} of the emission spectra for full probe library.

	λ_{max} /nm		λ_{max} /nm		λ_{max} /nm
Au13NP.Zonyl.IrS1	573	Au13NP.SPEG.IrS1	573	Au13NP.LPEG.IrS1	579
Au25NP.Zonyl.IrS1	570	Au25NP.SPEG.IrS1	579	Au25NP.LPEG.IrS1	585
Au50NP.Zonyl.IrS1	580	Au50NP.SPEG.IrS1	575	Au50NP.LPEG.IrS1	580
Au100NP.Zonyl.IrS1	579	Au100NP.SPEG.IrS1	579	Au100NP.LPEG.IrS1	598

The long component lifetime for IrS1 experiences a reduction of approximately 30-60 ns (7-13%) upon loading onto AuNPs, which is in agreement with previously published data (Figure 2.4.2.6, Table 2.4.2.9, 2.4.2.10 and 2.4.2.11)[2, 21, 22].

Table 2.4.2.9: Summary of lifetime (τ/ns) for Zonyl coated AuNPs.

	χ^2	τ/ns
Au13NP.Zonyl.IrS1	0.983	420 (90%)
		70 (10%)
Au25NP.Zonyl.IrS1	1.010	410 (90%)
		70 (10%)
Au50NP.Zonyl.IrS1	1.068	410 (90%)
		70 (10%)
Au100NP.Zonyl.IrS1	1.001	440 (90%)
		90 (10%)

Table 2.4.2.10: Summary of lifetime (τ/ns) for SPEG coated AuNPs.

	χ^2	τ/ns
Au13NP.SPEG.IrS1	1.006	430 (90%)
		80 (10%)
Au25NP.SPEG.IrS1	0.995	400 (90%)
		70 (10%)
Au50NP.SPEG.IrS1	1.041	400 (90%)
		60 (10%)
Au100NP.SPEG.IrS1	1.017	430 (90%)
		90 (10%)

Table 2.4.2.11: Summary of lifetime (τ/ns) for LPEG coated AuNPs.

	χ^2	τ/ns
Au13NP.LPEG.IrS1	1.070	410 (90%)
		70 (10%)
Au25NP.LPEG.IrS1	1.064	420 (90%)
		70 (10%)
Au50NP.LPEG.IrS1	1.047	400 (90%)
		70 (10%)
Au100NP.LPEG.IrS1	0.963	440 (90%)
		90 (10%)

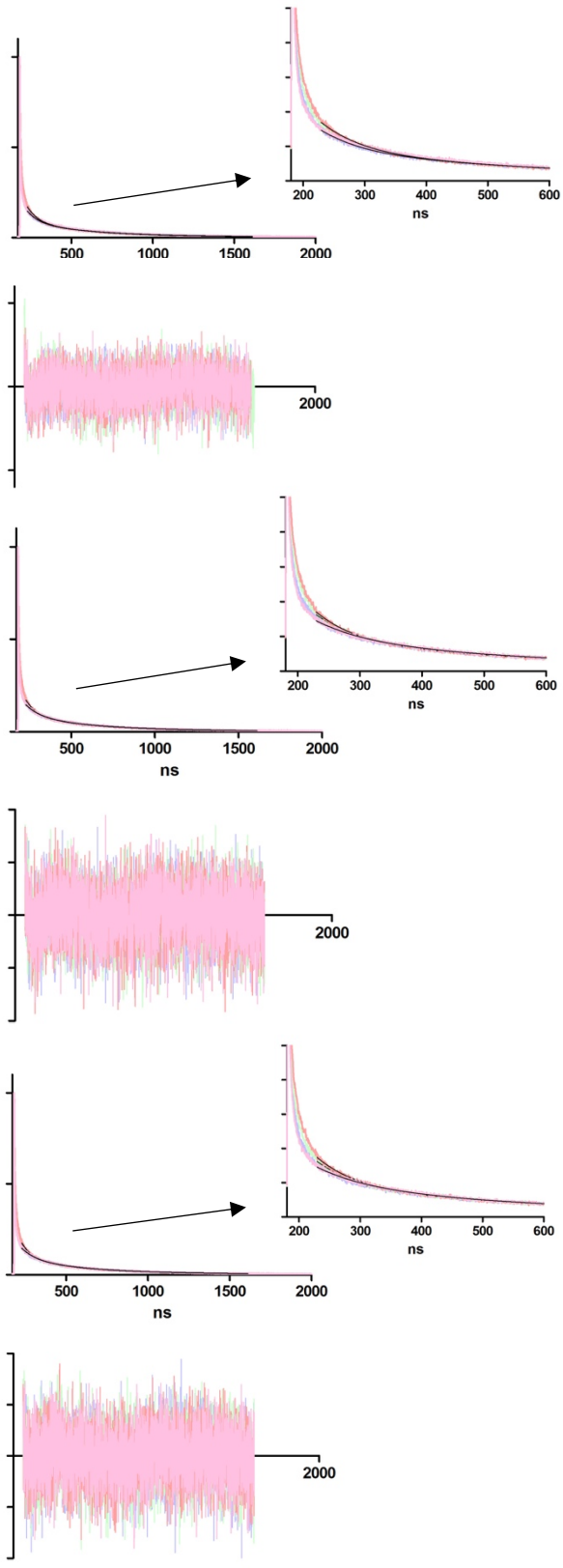

Figure 2.4.2.6: Luminescent Lifetime Decay in aerated H_2O and fitting for Au13NP (Blue), Au25NP (Green), Au50NP (Red) and Au100NP (Pink) coated with Zonyl (TOP), or SPEG (Middle), or LPEG (Bottom) and all with IrS1 (IrS1 λ_{exc} = 375nm and λ_{det} 580nm). Global analysis, Tail fitting. Fitting range (430; 3300) channels. Two component analysis.

2.5 Conclusion

Gold nanoparticles successfully operated as participating scaffolds, holding both stabilising agents and the luminescent compound, IrS1. In keeping with the aim of this project, loading IrS1 onto AuNPs is required for a dual purpose, firstly to facilitate increased uptake of IrS1 into biological material and secondly to provide a multimodal imaging platform. Thus far, it has been shown that attaching IrS1 onto an AuNP surface, of a range of sizes including 13, 25, 50 and 100nm, has maintained luminescence signal from IrS1. Logically, the larger the AuNP, the more IrS1 present on the surface, further increasing chances for detection, however, the full probe library will still be considered for further experiments. Larger particles cause more issues with regards to cytotoxicity and uptake in biological assays so may not always be the first choice. Additionally, changing the coating of the AuNP between Zonyl, SPEG and LPEG has also maintained IrS1 luminescence and so all three are promising to take forward on to perform biological assays.

2.6 Experimental

Starting materials, solvents and deuterated solvents, for NMR, were purchased from Sigma Aldrich/Merck, Fisher Scientific or Alfa Aesar.

2.6.1 Synthesis of IrS1

Synthesis of tetrakis(2-phenylquinoline-C2,N')(μ-dichloro)diiridium

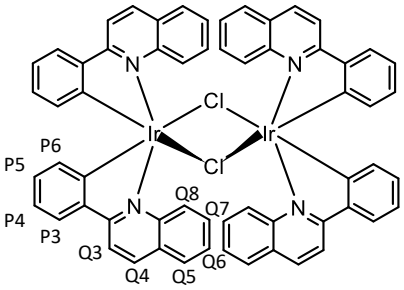

Synthesis of the iridium dimer was performed using a published protocol by Chen *et al* [1]. A solution of iridium(III) chloride hydrate (0.39 g, 1.0 mmol) and 2-phenylquinoline (0.51 g, 2.5 mmol), in 2-ethoxyethanol (30 mL) and deionised water (10 mL) was heated to reflux at 140 ˚C for 24 hr with continuous stirring. The mixture was cooled to room temperature and the yellow precipitate was collected on a glass filter frit. The precipitate was washed with methanol (60ml) and acetone (60ml) to give the final cyclometalated Ir(III)chloro-bridged dimer (397.7 mg, 47%). δ_H (300MHz, DMSO) 9.51 (d, J= 8.8Hz, 1H,Q4), 8.52 (dd, *J*= 8.8, 1.2Hz, 1H, Q3), 8.38 (d, *J*= 8.9Hz, 1H, P3), 8.06 (m, 1H, Q5), 7.92 (dd, *J*= 8.0, 1.3Hz, 1H, Q6), 7.65 (m, 2H, Q8, Q7), 6.83 (td, *J*=7.5, 1.2Hz, 1H, P4), 6.50 (t, 1H, P5), 6.15 (dd, *J*=7.8, 1.2Hz, 1H, P6). m*/z* (TOF MS ES$^+$) 1273 ([M+H]$^+$), (Appendix 2.7 and 2.8).

Synthesis of 5,5'-bis(bromomethyl)-2,2'-bipyridine

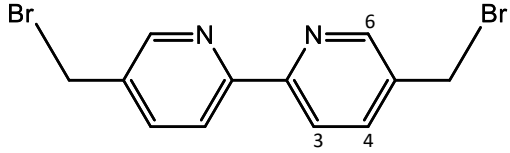

The synthesis of 5,5'-bis(bromomethyl)-2,2'-bipyridine was performed using a method published by Bertoncello *et al.* [23]. A solution of 5,5'-dimethyl-2-2'-bipyridine (0.57 g, 3.09 mmol), N-bromosuccinimide (NBS) (2.90 g,

16.3 mmol) and 1,1'-azobis(cyclohexanecarbonitrile) (ABCN) (1 pellet, ~120.0 mg, ~0.29 mmol) was heated to reflux in dry CCl_4 (40 mL) for 2 hr at 90 °C with continuous stirring. The residual precipitate was washed with 10 mL of CCl_4 and the combined phases were evaporated *in vacuo.* The remaining solid was dissolved in dichloromethane (DCM) (100 ml) and extracted with a solution of $Na_2S_2O_3$ (0.5 M, 2 x 150mL). The combined $Na_2S_2O_3$ phases were extracted with DCM (5 x 50 ml) and the combined DCM phases were dried over Na_2SO_4. DCM was removed *in vacuo.* The crude product was recrystallized from hot DCM, yielding a white solid powder of 5,5'-bromomethyl-2-2'-bipyridine, (0.11 g, 0.79 mmol, 10%). δ_H (300MHz, $CDCl_3$) 8.71 (dd, *J*=2.4, 0.7Hz, 1H, H6), 8.43 (dd, *J*= 8.1, 0.8Hz, 1H, H3), 7.88 (dd, *J*= 8.2, 2.4Hz, 1H, H4), 4.56 (s, 1H, CH_2). m/z (TOF MS ES$^+$) 342.92 ([M+H]$^+$) (Appendix 2.9 and 2.10).

Synthesis of 5,5'-bis(mercaptomethyl)-2,2'-bipyridine

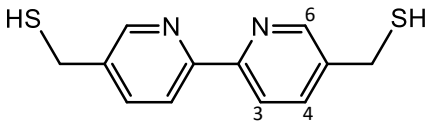

5,5′-bis(mercaptomethyl)-2,2′-bipyridine synthesized using the same protocol by Bertoncello *et al*[23]. A solution of 5,5'-bis(bromomethyl)-2,2'-bipyridine (100 mg, 0.58 mmol) and thiourea (70 mg, 1.83 mmol) in dry 1,4-dioxane (15 mL) was heated to reflux while stirring for 3 hr at 120 °C under N_2. NaOH (40 mg, 2 mmol) dissolved in degassed water (10 mL) was added and the mixture was heated at reflux for another 2 hr. The solvent was removed *in vacuo*, producing a pale yellow solid. Degassed acidified water (30 mL, pH ~4, HCl) was added and the aqueous phase extracted with DCM (6 x 40 ml). The combined DCM phases were dried *in vacuo* to yield the final yellow solid (44 mg, 0.36 mmol, 61%). δ_H (400MHz, DMSO) 8.65 (d, *J*= 2.2Hz, 1H, H6), 8.34 (dd, *J*= 8.2, 0.8Hz, 1H, H3), 7.89 (dd, *J*=8.2, 2.4Hz, 1H, H4), 3.83 (s, 1H, CH_2). m/z (TOF MS ES$^+$) 249 ([M+H]$^+$) (Appendix 2.11 and 2.12).

Synthesis of [Ir(2-PQ)$_2$BPYSH]Cl

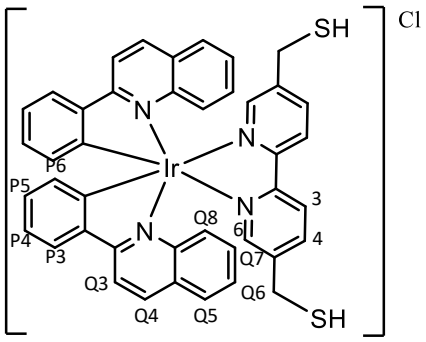

Synthesis was carried out using a modified method by Slinker *et al*[20-22]. A solution of tetrakis (2-phenylquinoline-C2,N')(μ-dichloro)diiridium (40mg, 0.06 mmol) and 5,5′-bis(mercaptomethyl)-2,2′-bipyridine (18 mg, 0.14 mmol) was suspended in ethylene glycol (3.25 mL) and heated to 150 ^{o}C for 19 hr with continuous stirring. The mixture was cooled to room temperature before deionised water (75 mL) was added. The mixture was further heated for 1 hr with continuous stirring at 70 ^{o}C. Saturated aqueous ammonium hexafluorophosphate (0.5 g in 1.25 mL deionised water) was added, forming a yellow precipitate. The solution was cooled on ice, filtered and washed with deionised water. The solid was dissolved in minimal acetone and vacuum dried to yield [Ir(2-PQ)$_2$BPYSH] PF_6. Ion exchange of [Ir(2-pq)$_2$bpySH]PF6$^+$ to [Ir(2-pq)2bpySH]Cl$^-$ was performed to prepare a stock solution of IrS1 of ~1 mM concentration in methanol. The pH of a suspension of Dowex (1x8 200-400 mesh) in deionised water (30 mL) was lowered to 1 using HCl (10%) and stirred for 1 hour. The HCl was removed and the resin washed with deionised water (30 mL). The resin was resuspended in MeOH (30 mL) and left to stir for 1 hr. A solution of [Ir(2-PQ)$_2$BPYSH]PF_6 (5 mg, in 5ml MeOH) was added and the mixture was stirred for 2 hr. The [Ir(2-PQ)$_2$BPYSH]Cl was isolated and washed with MeOH until the resin was colourless. The solution was dried under vacuum to give IrS1, (0.043 g, 62%) δ_H (400MHz, $CDCl_3$) δ 8.10 (dd, *J*=8.3 Hz, 1H, Q4), 8.01 (d, *J*=8.3 Hz, 1H, Q3), 7.93 (dd, *J*=8.2, 1.3 Hz, 1H, BPY3), 7.77 (d, *J*=2.1Hz, 1H, P3), 7.64 (dd, *J*=5.7, 3.3 Hz, 2H, BPY4, BPY6), 7.46 (dd, *J*=5.7, 3.3 Hz, 2H, Q5, Q6), 7.31 (ddd, *J*=8.0, 6.9 1.0 Hz, 1H, Q8), 7.09 (ddd, *J*=8.0, 6.9 1.0 Hz, 1H, P4), 6.93 (ddd, *J*=8.0,

6.9 1.0 Hz, 1H, Q7), 6.75 (td, *J*=7.5, 1.3 Hz, 1H, P5), 6.45 (dd, *J*=8.8,1.3 Hz, 1H, P6), 4.15 (s, 2H, CH_2), 2.14 (s, 1H, SH) m/z (TOF MS ES^+) 901 ($[M+Na+MeO]^+$) (breaking of sulphur bonds in Mass Spectrometry causes analyte to form salts with elutant) (Appendix 2.13 and 2.14).

2.6.2 Synthesis of AuNPs

Au13NP. Nanoparticles were synthesized using published protocols[28]. A solution of trisodium citrate dihydrate (0.0606 g, 0.21 mmol), citric acid (0.0133 g, 0.07 mmol) and ethylenediaminetetraacetic acid (EDTA) (0.0010 g, 0.003 mmol) in ultrapure MilliQ water (100 mL) was placed under rapid stirring and brought to reflux. The mixture was allowed to reflux for 15 min at 150^{o}C before addition of a preheated solution (80 ^{o}C) of gold(III) chloride trihydrate (0.008g, 0.020 mmol) in ultrapure MilliQ water (25 mL). The mixture was allowed to reflux for a further 15 min before being cooled to room temperature. After the mixture cooled, the solution remaining was a dark red colour containing 13nm AuNPs at a concentration of 2 nM. λ_{max} (H2O) / nm 517 (SPR).

Au25NP. The synthesis for seeding of Au13NP to larger sizes was implemented using a previously published modified method[26]. Three stock solutions were prepared using trisodium citrate dihydrate (34 mM), ascorbic acid (57 mM) and gold(III) chloride trihydrate (5mM) in ultrapure MilliQ water. Au13NPs (34 mL, 2 nM) were diluted to 40 mL with ultrapure MilliQ water (6 mL) and placed under rapid stirring. From the stock solutions, 2 further dilutions were made to gold(III) chloride trihydrate (1 mM), ascorbic acid (3 mM) and trisodium citrate dihydrate (0.75 mM). Using a peristaltic pump, the two solutions (gold(III) chloride trihydrate and ascorbic acid with trisodium citrate dihydrate) were added dropwise, simultaneously to the Au13NP solution over 25 min.

The mixture was allowed to reflux for 30 min with continuous stirring at 150°C. The solution was cooled to room temp to yield Au25NPs of 0.7 nM. λ_{max} (H2O) / nm 522 (SPR).

Au50NP. The synthesis for seeding of Au25NP to larger sizes was implemented using a previously published modified method[26]. Three stock solutions were prepared using trisodium citrate dihydrate (34 mM), ascorbic acid (57 mM) and gold(III) chloride trihydrate (5mM) in ultrapure MilliQ water. Au25NPs (9 mL, 0.7 nM) were diluted to 40 mL with ultrapure MilliQ water (31 mL) and placed under rapid stirring. From the stock solutions, 2 further dilutions were made to gold(III) chloride trihydrate (1 mM), ascorbic acid (3 mM) and trisodium citrate dihydrate (0.75 mM). Using a peristaltic pump, the two solutions (gold(III) chloride trihydrate and ascorbic acid with trisodium citrate dihydrate) were added dropwise, simultaneously to the Au25NP solution over 25 min. The mixture was allowed to reflux for 30 min with continuous stirring at 150°C. The solution was cooled to room temp to yield Au50NPs of 80 pM. λ_{max} (H2O) / nm 526 (SPR).

Au100NP. The synthesis for seeding of Au50NP to larger sizes was implemented using a previously published modified method[26]. Three stock solutions were prepared using trisodium citrate dihydrate (34 mM), ascorbic acid (57 mM) and gold(III) chloride trihydrate (5mM) in ultrapure MilliQ water. Au50NPs (40 mL, 80 pM) placed under rapid stirring. From the stock solutions, 2 further dilutions were made to gold(III) chloride trihydrate (4 mM), ascorbic acid (12 mM) and trisodium citrate dihydrate (3.4 mM). Using a peristaltic pump, the two solutions (gold(III) chloride trihydrate and ascorbic acid with trisodium citrate dihydrate) were added dropwise, simultaneously

to the Au50NP solution over 25 min. The mixture was allowed to reflux for 30 min with continuous stirring at 150^{o}C. The solution was cooled to room temp to yield Au100NPs of 40 pM. λ_{max} (H2O) / nm 559 (SPR).

2.6.3 Coating of AuNPs

The AuNPs were ajusted to different concentrations from those obtained in the synthesis. AuNP solutions were centrifuged at 13.3 RPM for 30, 25, 15 and 1.5 min for Au13NP, Au25NP, Au50NP and Au100NP respectively. The supernatant was removed allowing the lose pellet of AuNPs to be extracted and resuspended with ultrapure MilliQ water to give AuNPs of concentration 4 nM, 4 nM, 0.4 nM and 0.4 nM respectively.

Zonyl Coating. A solution of Zonyl FSA surfactant (10 μL, 10%) was added to each of the resuspensions of AuNPs (2ml). The coated suspensions were centrifuged further under the same parameters as previously mentioned. The supernatant was removed, the pellet was extracted and resuspended in ultrapure MilliQ water to give AuNPs of concentrations for Au13NP, Au25NP, Au50NP and Au100NP at 2 nM, 2 nM, 0.2 nM and 0.2 nM respectively.

SPEG Coating. A solution of O-(2-carboxyethyl)-O'-(2-mercaptoethyl)heptaethylene glycol (SPEG) (100 μL, 0.1 mM) was added to the resuspensions of AuNPs (2ml). The coated suspensions were centrifuged further under the same parameters as previously mentioned. The supernatant was removed, the pellet was extracted and resuspended in ultrapure MilliQ water to give AuNPs of concentrations for Au13NP,

Au25NP, Au50NP and Au100NP at 2 nM, 2 nM, 0.2 nM and 0.2 nM respectively.

LPEG Coating. A solution of Poly(ethylene glycol) 2-mercaptoethyl ether acetic acid (LPEG) (100 μL, 0.1 mM) was added to the resuspensions of AuNPs. The coated suspensions were centrifuged further under the same parameters as previously mentioned. The supernatant was removed, the pellet was extracted and resuspended in ultrapure MilliQ water to give AuNPs of concentrations for Au13NP, Au25NP, Au50NP and Au100NP at 2 nM, 2 nM, 0.2 nM and 0.2 nM respectively.

IrS1 Coating on Zonyl coated AuNPs. IrS1 (1 μM) was added dropwise into a solution of AuNP with Zonyl, 10μL, 15μL, 25μL and 35μL, per 1ml of Au13NP, Au25NP, Au50NP and Au100NP respectively. The samples were centrifuged further and resuspended with ultrapure MilliQ water. To give final concentrations for Au13NP, Au25NP, Au50NP and Au100NP at 1nM, 1nM, 0.5nM and 0.1nM respectively.

IrS1 Coating on SPEG and LPEG coated AuNPs. IrS1 (0.1 μM) was added dropwise into a solution of AuNP with Zonyl, 80μL, 150μL, 150μL and 150μL, per 1ml of Au13NP, Au25NP, Au50NP and Au100NP respectively. The samples were centrifuged further and resuspended with ultrapure MilliQ water. To give final concentrations for Au13NP, Au25NP, Au50NP and Au100NP at 1nM, 1nM, 0.5nM and 0.1nM respectively.

2.7 Instrumentation

2.7.1 Synthesis Techniques

^{1}H NMR spectroscopy was carried out on a Bruker AVIII300 or AVIII400 spectrometer. Electrospray mass spectra were recorded on a Waters Micromass LCT time of flight mass spectrometer.

2.7.2 Photophysical Techniques

UV-VIS absorption spectroscopy was performed using a Varian Cary 5000 spectrometer at a 300nm min^{-1} acquisition rate between 250 to 800nm. Samples were prepared in 1cm path length quartz cuvettes at room temperature.

Luminescence measurements were performed on an Edinburgh Instrument FLS920 spectrometer, with a 450 W Xenon arc lamp illumination source. The detection system used incorporated an R928 visible Hamamatsu photomultiplier tube (PMT). The emission monochromator was fitted with a grating blazed at 500 nm. The data was recorded using the F900 spectrometer analysis software. Samples were prepared in quartz cuvettes with four transparent faces. Appropriate long-pass filters were used to eliminate second-order photon scattering. The excitation and emission spectra recorded were corrected or lamp instrument response and PMT response, respectively.

Luminescence lifetimes were measured with a 375 nm picosecond pulse length diode laser excitation source using the time-correlated single photon counting module of the Edinburgh Instruments FLS920 spectrometer with the Hamamatsu R928 photomultiplier tube (PMT). Lifetimes were tail-fitted using FAST PC software with an

error of ±10%, using a Marquardt-Levenberg algorithm. The reduced chi-square (χ^2) parameter was used to evaluate the quality of the fit results, obtaining values between 1.0 and 1.2. Samples were prepared in quartz cuvettes with four transparent faces. Appropriate long-pass filters were used to eliminate second-order photon scattering.

2.7.3 Nanoparticle Characterisation Techniques

Dynamic Light scattering sizing and Zeta potential measurements were performed on a Malvern Zetasizer nano ZSP calibrated with a zeta potential transfer standard. DLS size analysis measurements were recorded using a 1 cm disposable cuvette and zeta potential measurements were recorded using a folded capillary cell. The measurements were recorded using a standard operating procedure (SOP) with the following settings: Refractive index: 1.33, Absorption: 1.00, Dispersant: Water, Temperature: 25 ºC, Cell: DTS0012 disposable cuvette (Size measurements) and DTS1060 folded capillary cell (Zeta potential measurements).

Inductively coupled plasma mass spectroscopy (ICP-MS) were performed on an Agilent LC-ICP-MS (7900) with an integrated auto-sampler at the University of Warwick. Metal concentrations were determined using PlasmaCal calibration standards (QMX Laboratories), with R^2 >0.999 linear calibration curves in all cases. Samples were digested in ultrapure aqua-regia and then diluted.

2.8 Appendix

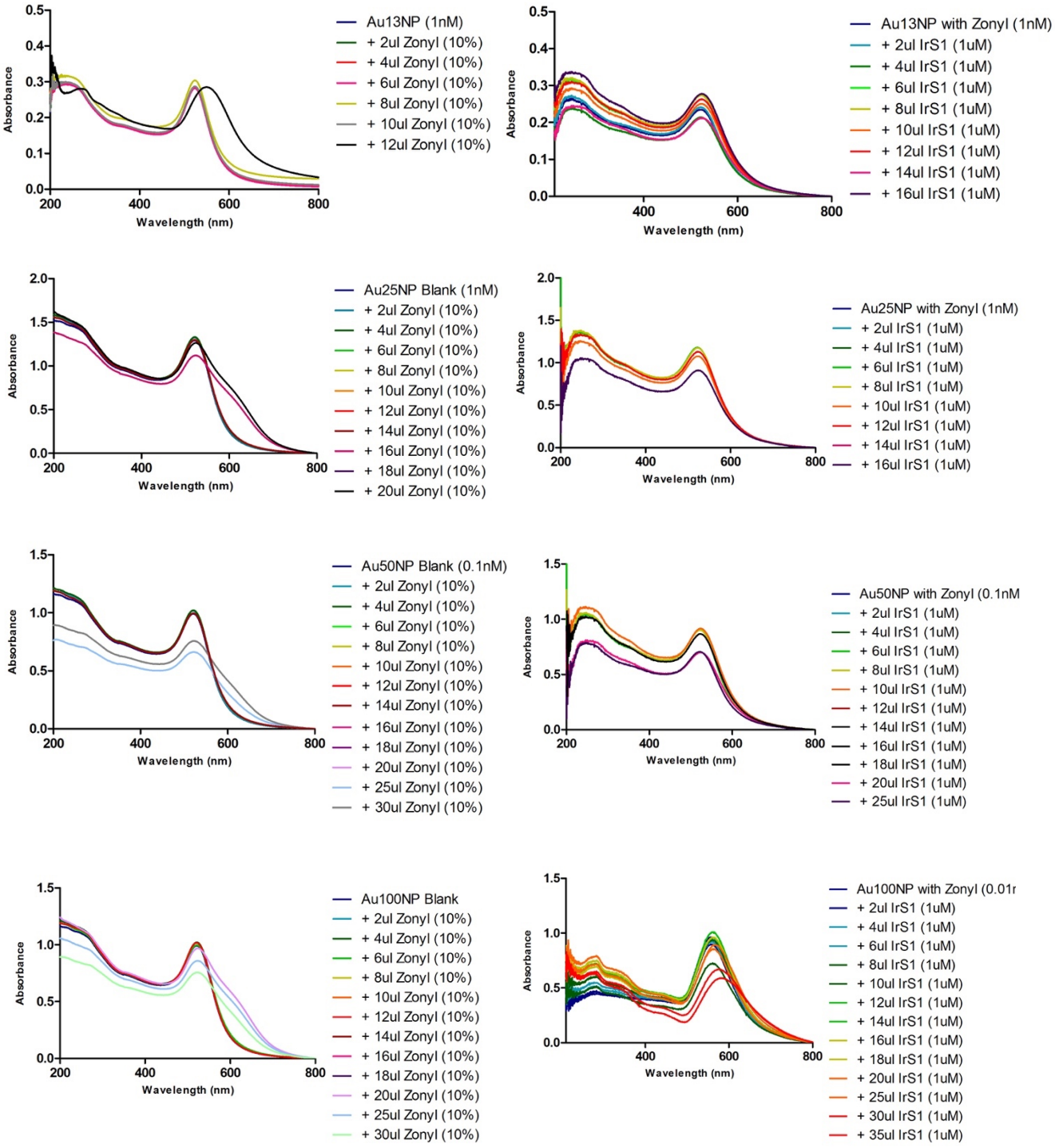

Appendix 2.1: UVVIS titrations for Au13NP(first row), Au25NP(second row), Au50NP(third row) and Au100NP(fourth row) with Zonyl(left column) and with IrS1(right column).

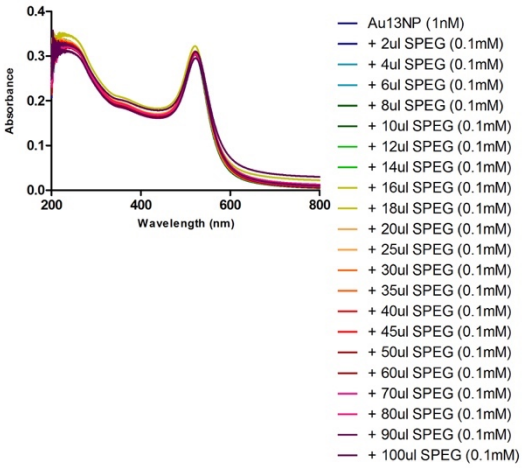
Absorbance
Wavelength (nm)
Au13NP (1nM)
+ 2ul SPEG (0.1mM)
+ 4ul SPEG (0.1mM)
+ 6ul SPEG (0.1mM)
+ 8ul SPEG (0.1mM)
+ 10ul SPEG (0.1mM)
+ 12ul SPEG (0.1mM)
+ 14ul SPEG (0.1mM)
+ 16ul SPEG (0.1mM)
+ 18ul SPEG (0.1mM)
+ 20ul SPEG (0.1mM)
+ 25ul SPEG (0.1mM)
+ 30ul SPEG (0.1mM)
+ 35ul SPEG (0.1mM)
+ 40ul SPEG (0.1mM)
+ 45ul SPEG (0.1mM)
+ 50ul SPEG (0.1mM)
+ 60ul SPEG (0.1mM)
+ 70ul SPEG (0.1mM)
+ 80ul SPEG (0.1mM)
+ 90ul SPEG (0.1mM)
+ 100ul SPEG (0.1mM)

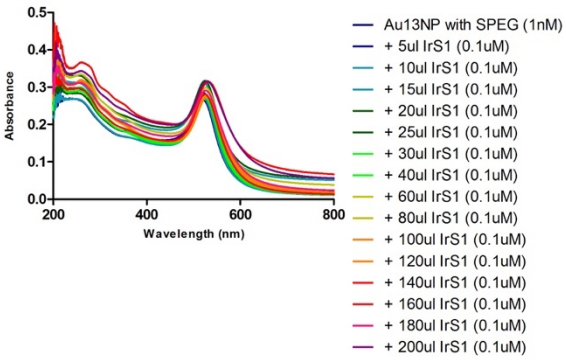
Absorbance
Wavelength (nm)
Au13NP with SPEG (1nM)
+ 5ul IrS1 (0.1uM)
+ 10ul IrS1 (0.1uM)
+ 15ul IrS1 (0.1uM)
+ 20ul IrS1 (0.1uM)
+ 25ul IrS1 (0.1uM)
+ 30ul IrS1 (0.1uM)
+ 40ul IrS1 (0.1uM)
+ 60ul IrS1 (0.1uM)
+ 80ul IrS1 (0.1uM)
+ 100ul IrS1 (0.1uM)
+ 120ul IrS1 (0.1uM)
+ 140ul IrS1 (0.1uM)
+ 160ul IrS1 (0.1uM)
+ 180ul IrS1 (0.1uM)
+ 200ul IrS1 (0.1uM)

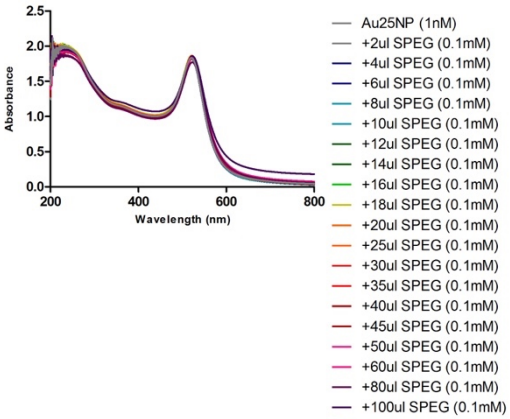
Absorbance
Wavelength (nm)
Au25NP (1nM)
+2ul SPEG (0.1mM)
+4ul SPEG (0.1mM)
+6ul SPEG (0.1mM)
+8ul SPEG (0.1mM)
+10ul SPEG (0.1mM)
+12ul SPEG (0.1mM)
+14ul SPEG (0.1mM)
+16ul SPEG (0.1mM)
+18ul SPEG (0.1mM)
+20ul SPEG (0.1mM)
+25ul SPEG (0.1mM)
+30ul SPEG (0.1mM)
+35ul SPEG (0.1mM)
+40ul SPEG (0.1mM)
+45ul SPEG (0.1mM)
+50ul SPEG (0.1mM)
+60ul SPEG (0.1mM)
+80ul SPEG (0.1mM)
+100ul SPEG (0.1mM)

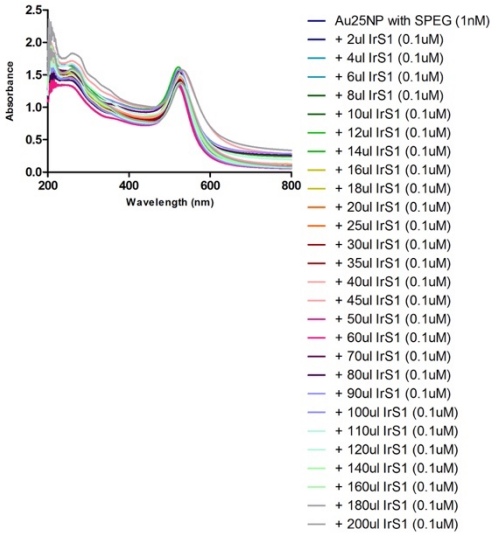
Absorbance
Wavelength (nm)
Au25NP with SPEG (1nM)
+ 2ul IrS1 (0.1uM)
+ 4ul IrS1 (0.1uM)
+ 6ul IrS1 (0.1uM)
+ 8ul IrS1 (0.1uM)
+ 10ul IrS1 (0.1uM)
+ 12ul IrS1 (0.1uM)
+ 14ul IrS1 (0.1uM)
+ 16ul IrS1 (0.1uM)
+ 18ul IrS1 (0.1uM)
+ 20ul IrS1 (0.1uM)
+ 25ul IrS1 (0.1uM)
+ 30ul IrS1 (0.1uM)
+ 35ul IrS1 (0.1uM)
+ 40ul IrS1 (0.1uM)
+ 45ul IrS1 (0.1uM)
+ 50ul IrS1 (0.1uM)
+ 60ul IrS1 (0.1uM)
+ 70ul IrS1 (0.1uM)
+ 80ul IrS1 (0.1uM)
+ 90ul IrS1 (0.1uM)
+ 100ul IrS1 (0.1uM)
+ 110ul IrS1 (0.1uM)
+ 120ul IrS1 (0.1uM)
+ 140ul IrS1 (0.1uM)
+ 160ul IrS1 (0.1uM)
+ 180ul IrS1 (0.1uM)
+ 200ul IrS1 (0.1uM)

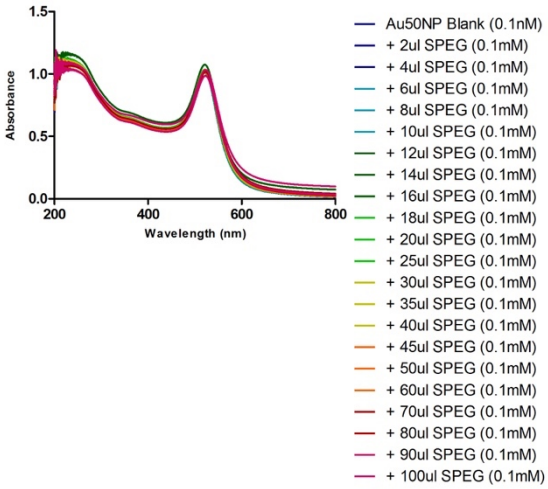
Absorbance
Wavelength (nm)
Au50NP Blank (0.1nM)
+ 2ul SPEG (0.1mM)
+ 4ul SPEG (0.1mM)
+ 6ul SPEG (0.1mM)
+ 8ul SPEG (0.1mM)
+ 10ul SPEG (0.1mM)
+ 12ul SPEG (0.1mM)
+ 14ul SPEG (0.1mM)
+ 16ul SPEG (0.1mM)
+ 18ul SPEG (0.1mM)
+ 20ul SPEG (0.1mM)
+ 25ul SPEG (0.1mM)
+ 30ul SPEG (0.1mM)
+ 35ul SPEG (0.1mM)
+ 40ul SPEG (0.1mM)
+ 45ul SPEG (0.1mM)
+ 50ul SPEG (0.1mM)
+ 60ul SPEG (0.1mM)
+ 70ul SPEG (0.1mM)
+ 80ul SPEG (0.1mM)
+ 90ul SPEG (0.1mM)
+ 100ul SPEG (0.1mM)

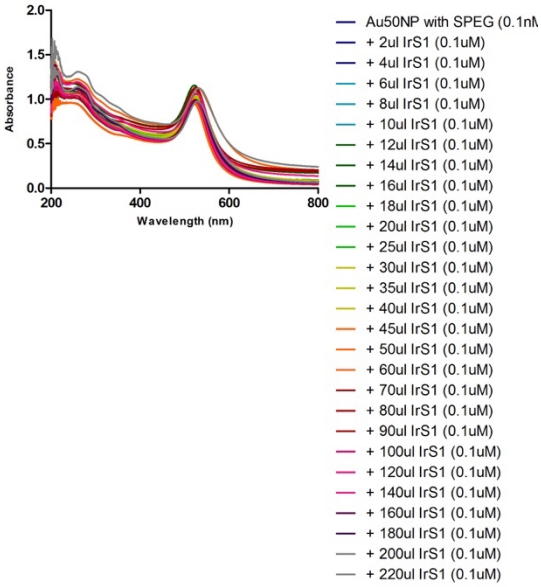
Absorbance
Wavelength (nm)
Au50NP with SPEG (0.1n
+ 2ul IrS1 (0.1uM)
+ 4ul IrS1 (0.1uM)
+ 6ul IrS1 (0.1uM)
+ 8ul IrS1 (0.1uM)
+ 10ul IrS1 (0.1uM)
+ 12ul IrS1 (0.1uM)
+ 14ul IrS1 (0.1uM)
+ 16ul IrS1 (0.1uM)
+ 18ul IrS1 (0.1uM)
+ 20ul IrS1 (0.1uM)
+ 25ul IrS1 (0.1uM)
+ 30ul IrS1 (0.1uM)
+ 35ul IrS1 (0.1uM)
+ 40ul IrS1 (0.1uM)
+ 45ul IrS1 (0.1uM)
+ 50ul IrS1 (0.1uM)
+ 60ul IrS1 (0.1uM)
+ 70ul IrS1 (0.1uM)
+ 80ul IrS1 (0.1uM)
+ 90ul IrS1 (0.1uM)
+ 100ul IrS1 (0.1uM)
+ 120ul IrS1 (0.1uM)
+ 140ul IrS1 (0.1uM)
+ 160ul IrS1 (0.1uM)
+ 180ul IrS1 (0.1uM)
+ 200ul IrS1 (0.1uM)
+ 220ul IrS1 (0.1uM)

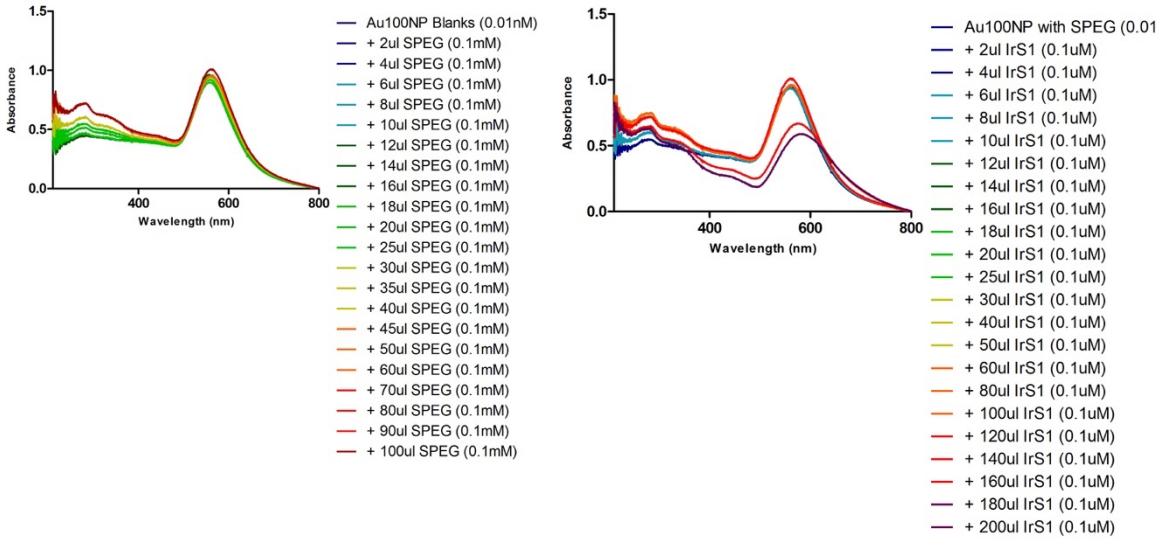

Appendix 2.2: UVVIS titrations for Au13NP(first row), Au25NP(second row), Au50NP(third row) and Au100NP(fourth row) with SPEGl(left column) and with IrS1(right column).

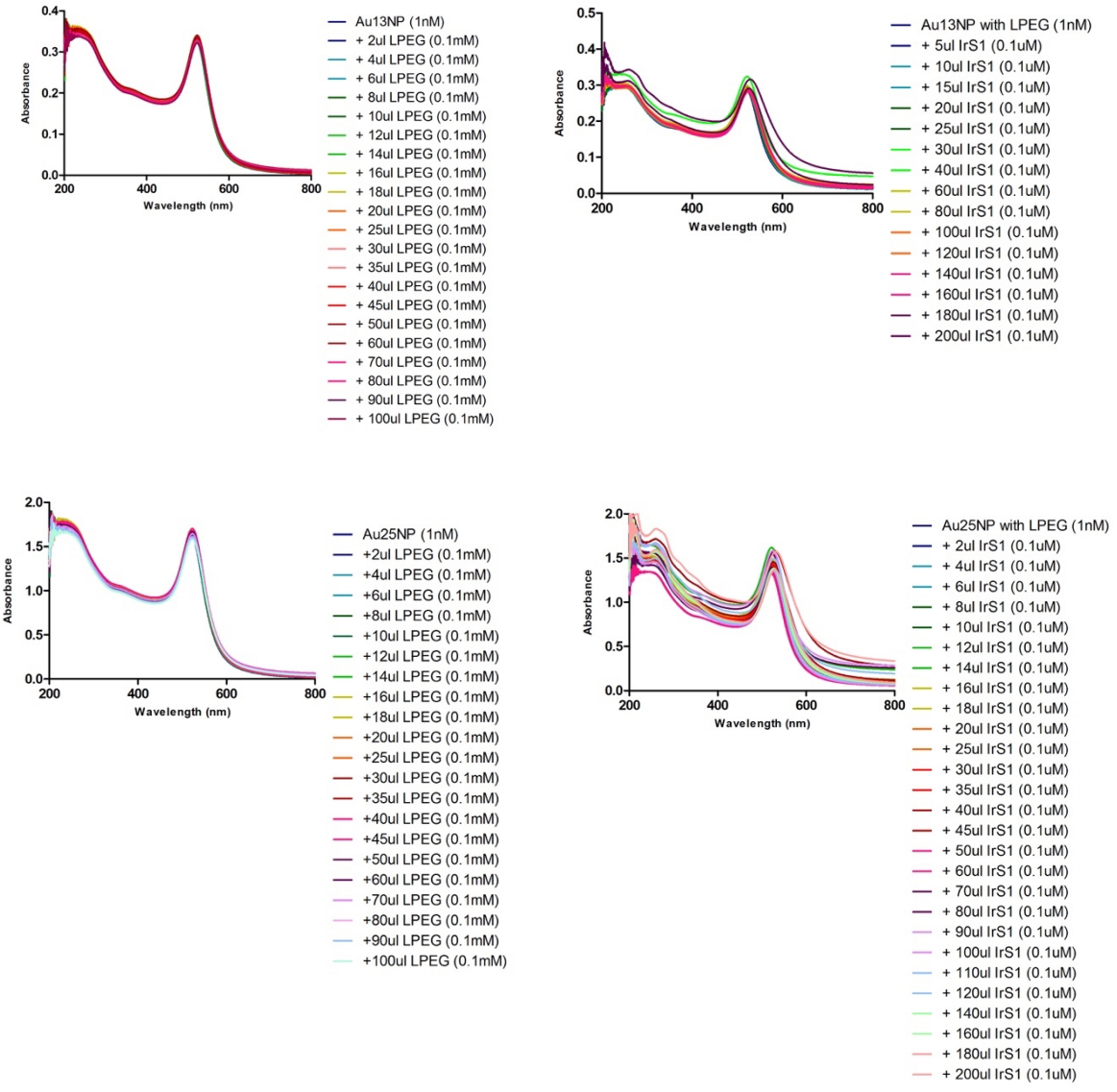

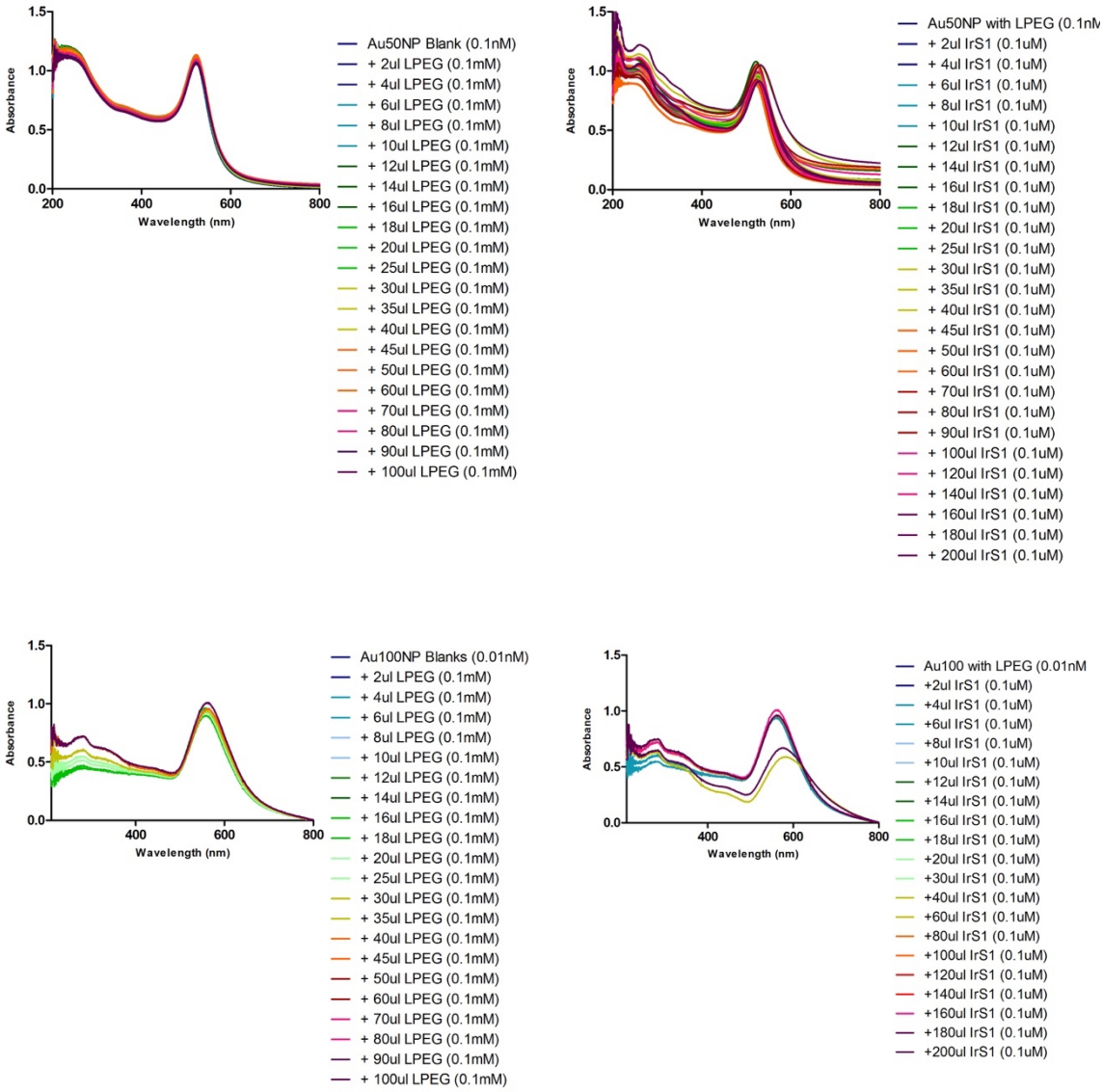

Appendix 2.3: UVVIS titrations for Au13NP(first row), Au25NP(second row), Au50NP(third row) and Au100NP(fourth row) with LPEGl(left column) and with IrS1(right column).

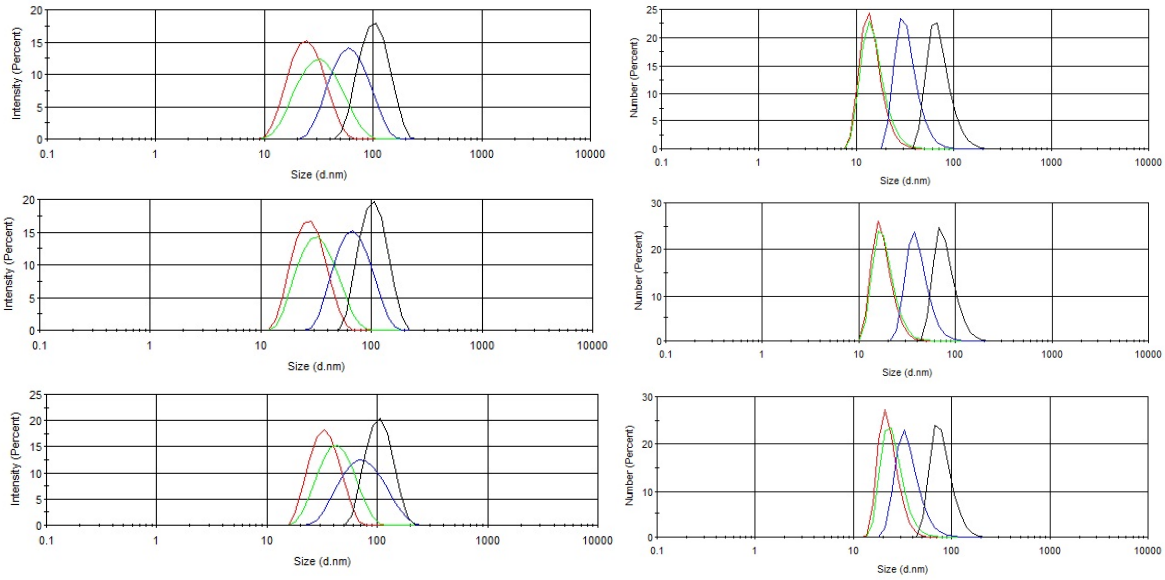

Appendix 2.4: DLS Size Graphs. (Right column) Size by intensity. (Left column) Size by number. (Red) Au13NP, (Green) Au25NP, (Blue) Au50NP, (Black) Au100NP. (Top row) Coated with Zonyl, (Middle row) coated with SPEG and (Bottom row) coated with LPEG.

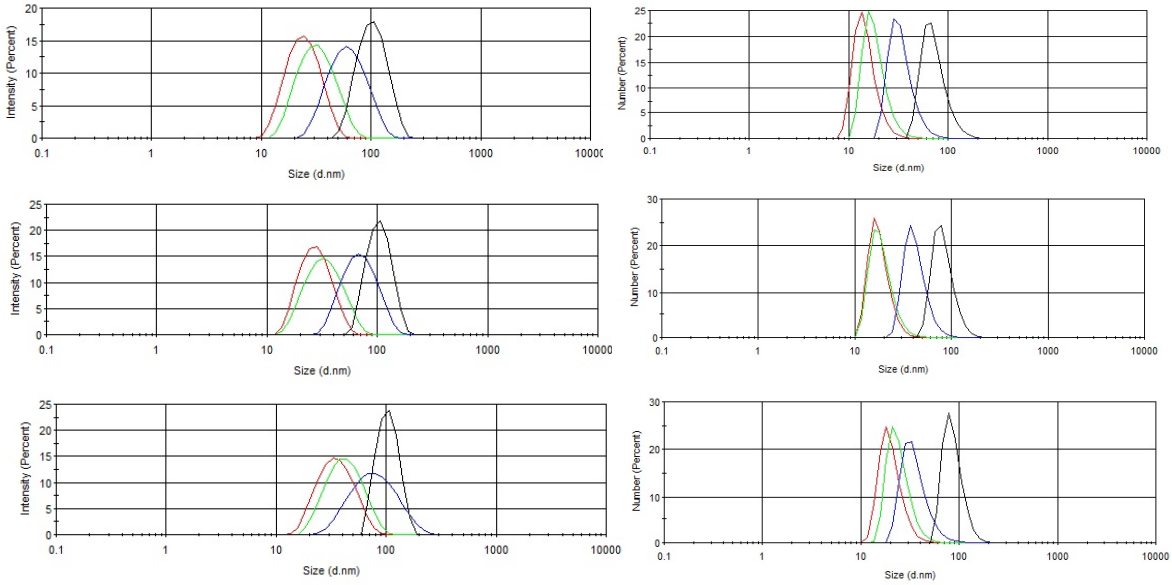

Appendix 2.5: DLS Size Graphs. (Right column) Size by intensity. (Left column) Size by number. (Red) Au13NP, (Green) Au25NP, (Blue) Au50NP, (Black) Au100NP. (Top row) Coated with Zonyl, (Middle row) coated with SPEG and (Bottom row) coated with LPEG. All AuNPs also coated with IrS1.

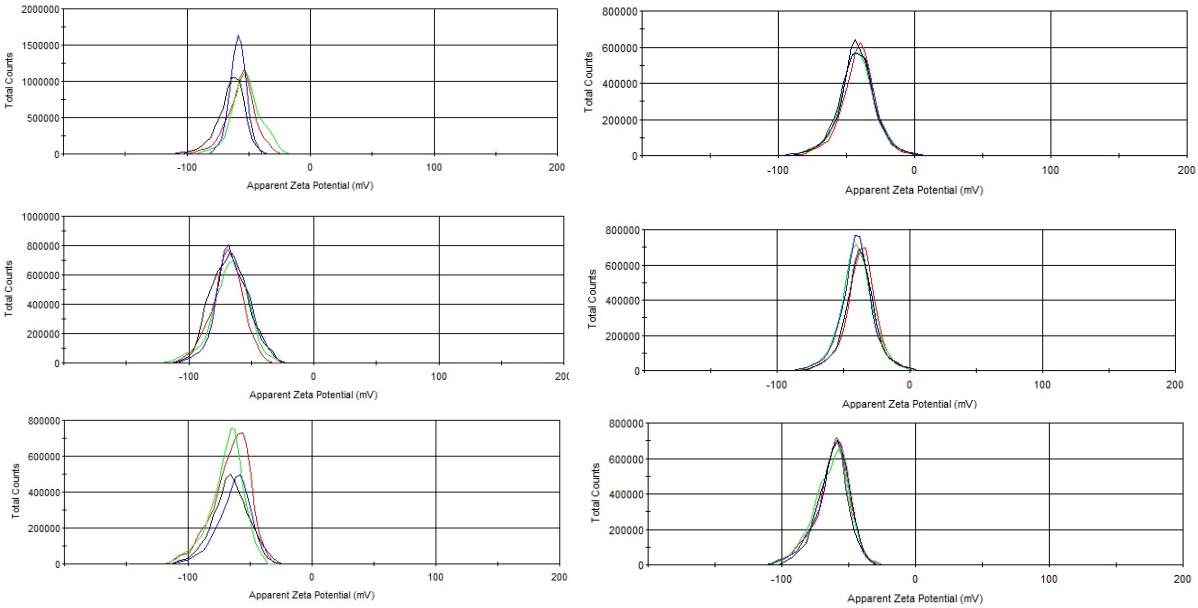

Appendix 2.6: Zeta Potential Graphs. (Right column) AuNP + Stabilising Agent. (Left column) AuNP + Stabilising Agent + IrS1. (Red) Au13NP, (Green) Au25NP, (Blue) Au50NP, (Black) Au100NP. (Top row) Coated with Zonyl, (Middle row) coated with SPEG and (Bottom row) coated with LPEG.

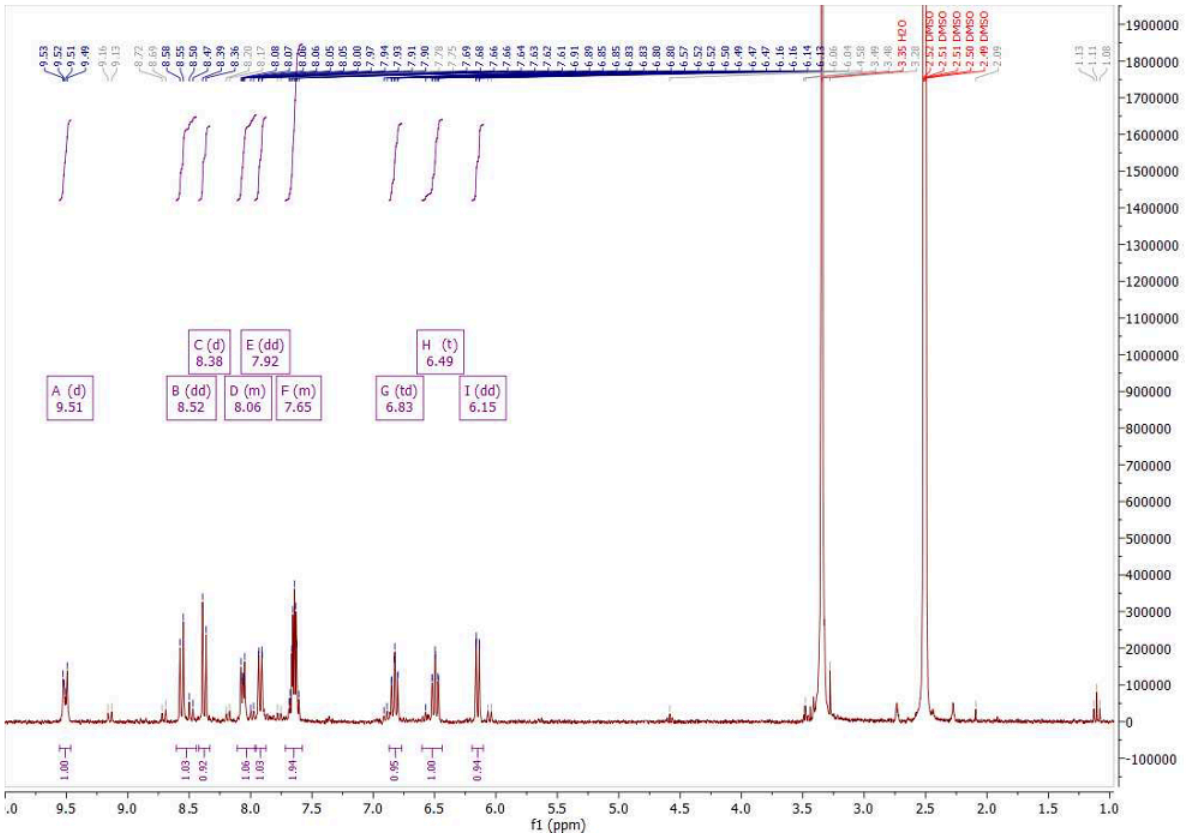

Appendix 2.7: ^{1}H NMR δ_{H} (300MHz, DMSO) of Tetrakis(2-phenylquinoline-C2,N')(μ-dichloro)diiridium.

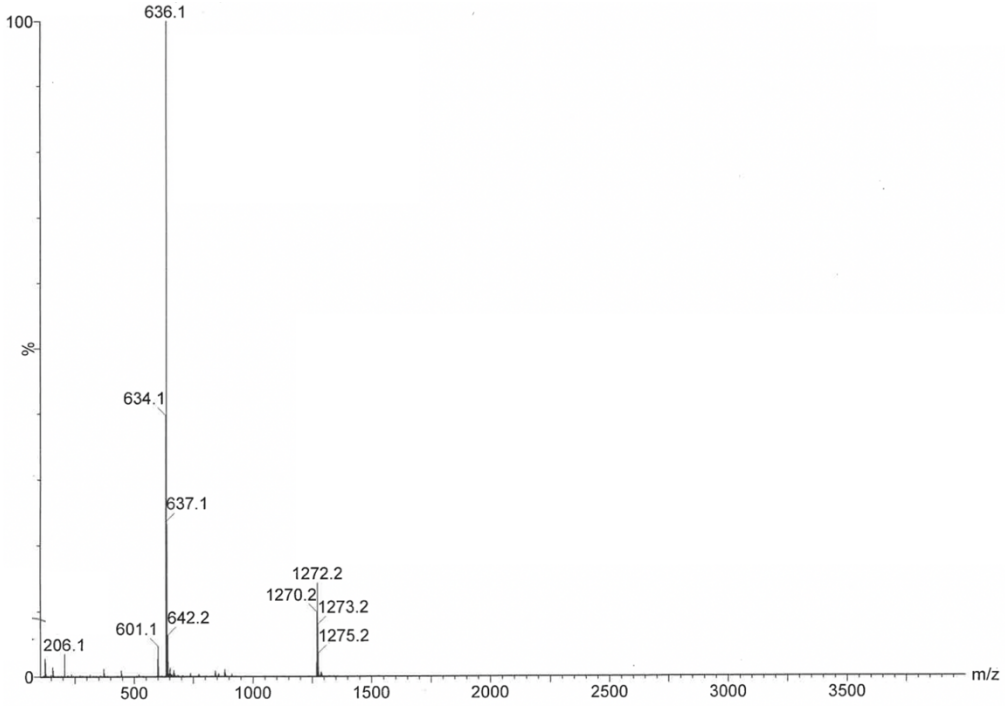

Appendix 2.8: Mass Spectrometry of Tetrakis(2-phenylquinoline-C2,N')(μ-dichloro)diiridium.

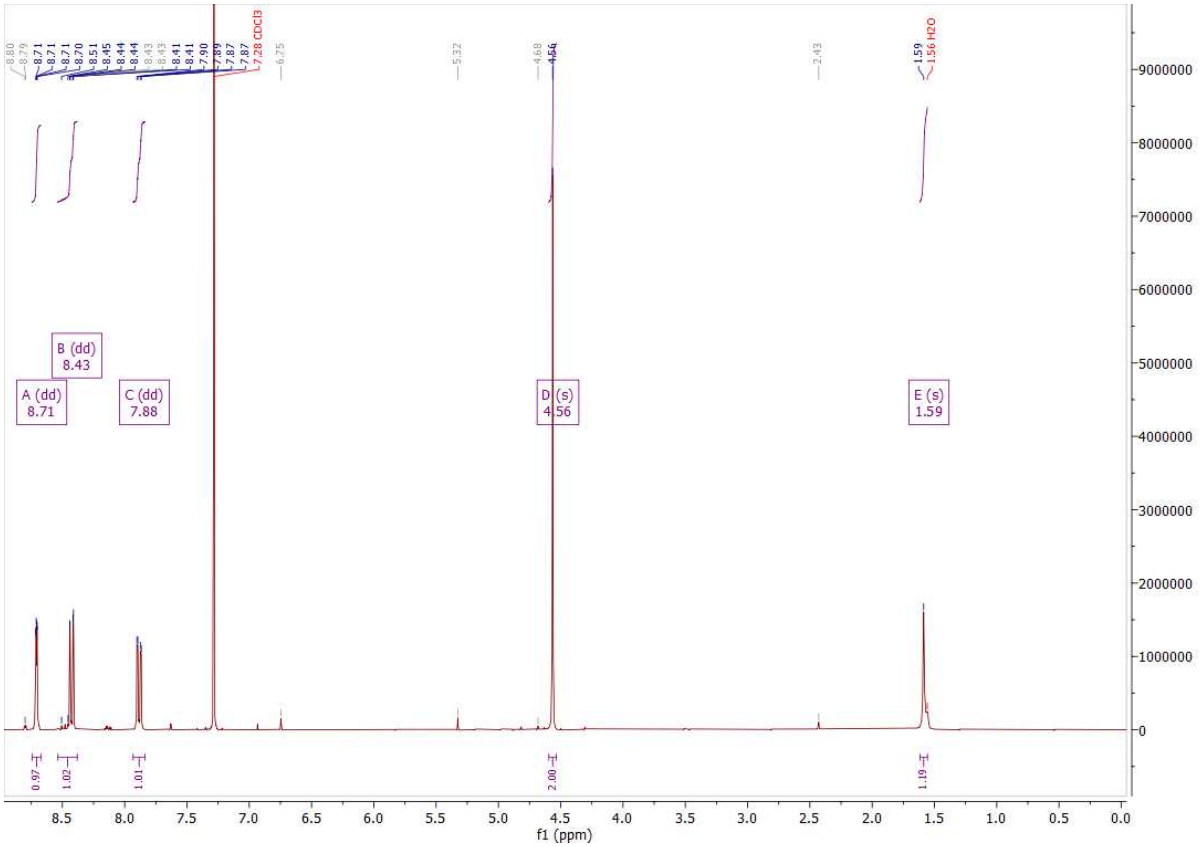

Appendix 2.9: ^{1}H NMR δ_{H} (300MHz, $CDCl_3$) of 5,5'-Bis(bromomethyl)-2,2'-bipyridine.

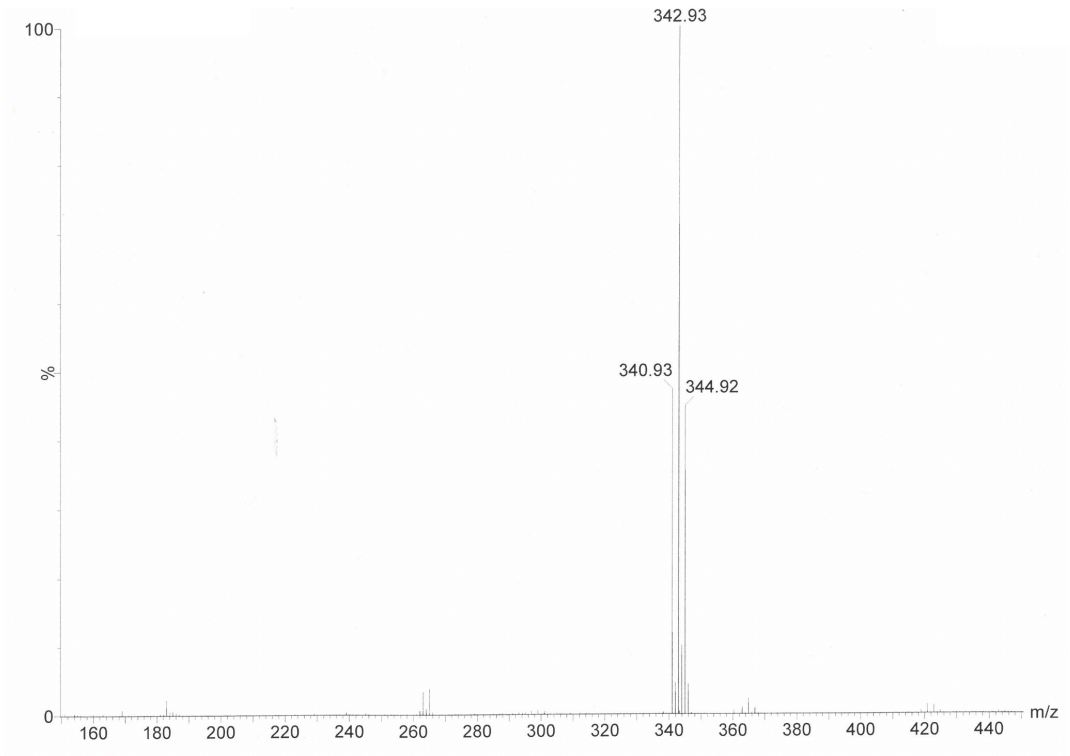

Appendix 2.10: Mass Spectrometry of 5,5'-Bis(bromomethyl)-2,2'-bipyridine.

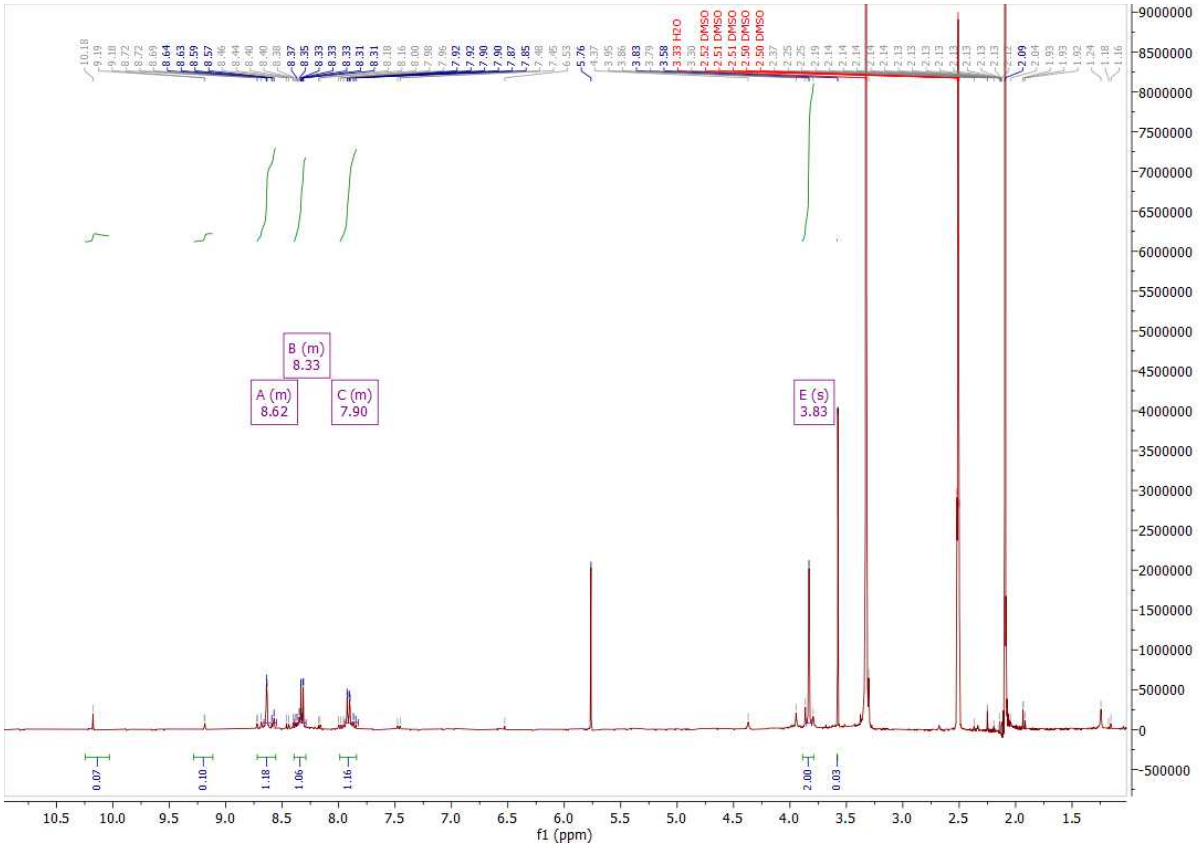

Appendix 2.11: ^{1}H NMR δ_{H} (400MHz, DMSO) of 5,5′-Bis(mercaptomethyl)-2,2′-bipyridine.

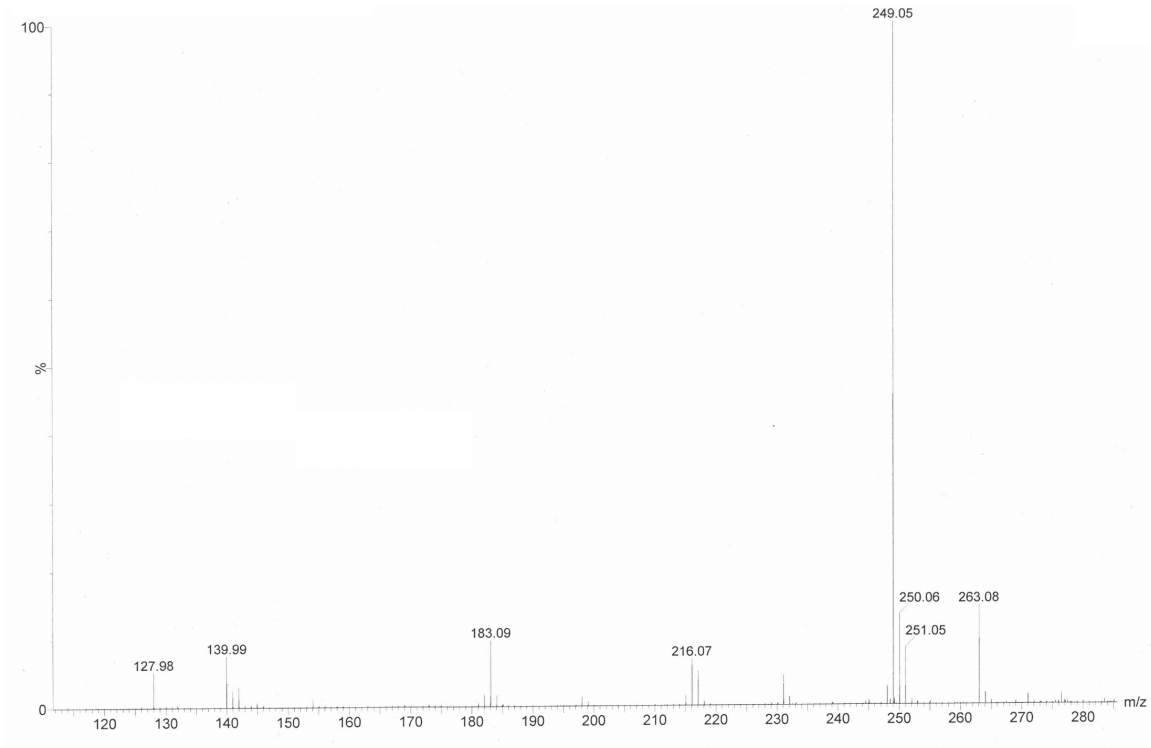

Appendix 2.12: Mass Spectrometry of 5,5′-Bis(mercaptomethyl)-2,2′-bipyridine.

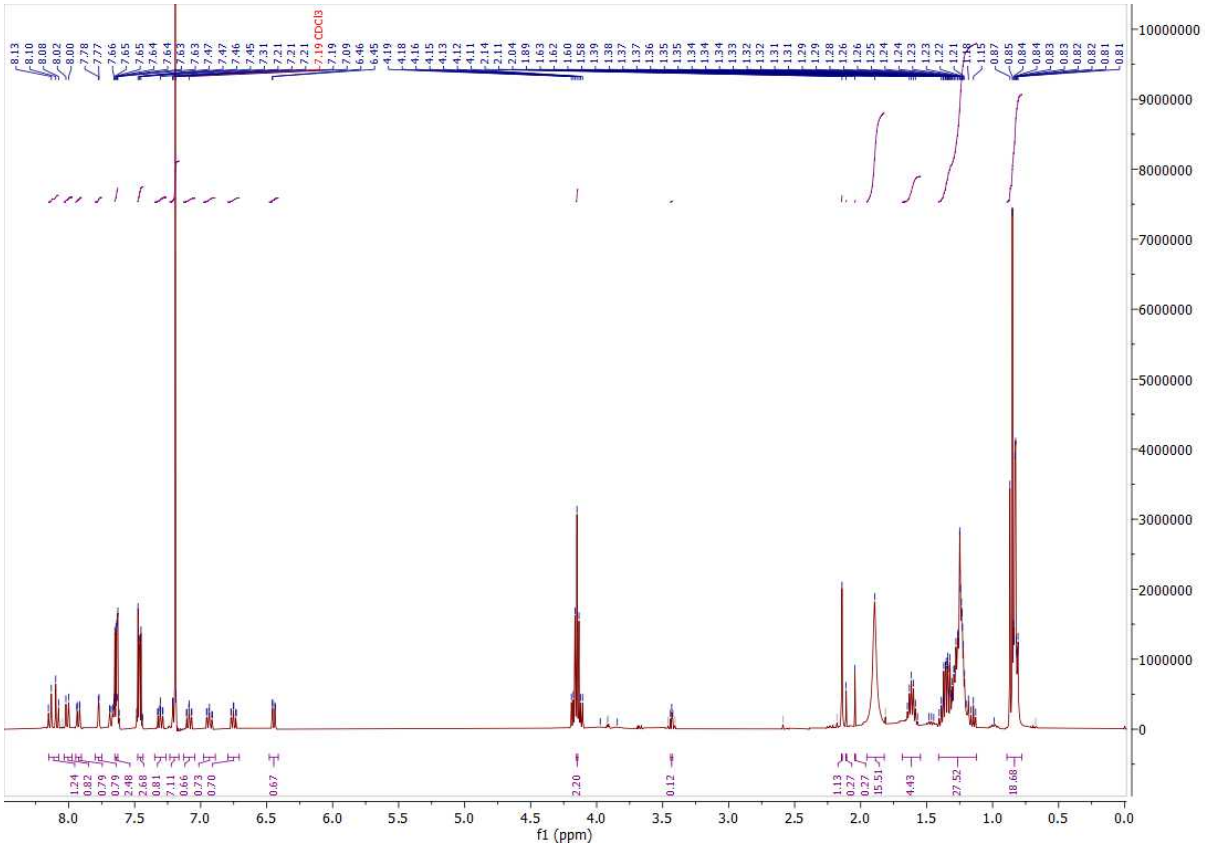

Appendix 2.13: ^{1}H NMR δ_{H} (400MHz, $CDCl_3$) of $[Ir(2\text{-}PQ)_2BPYSH]PF_6$.

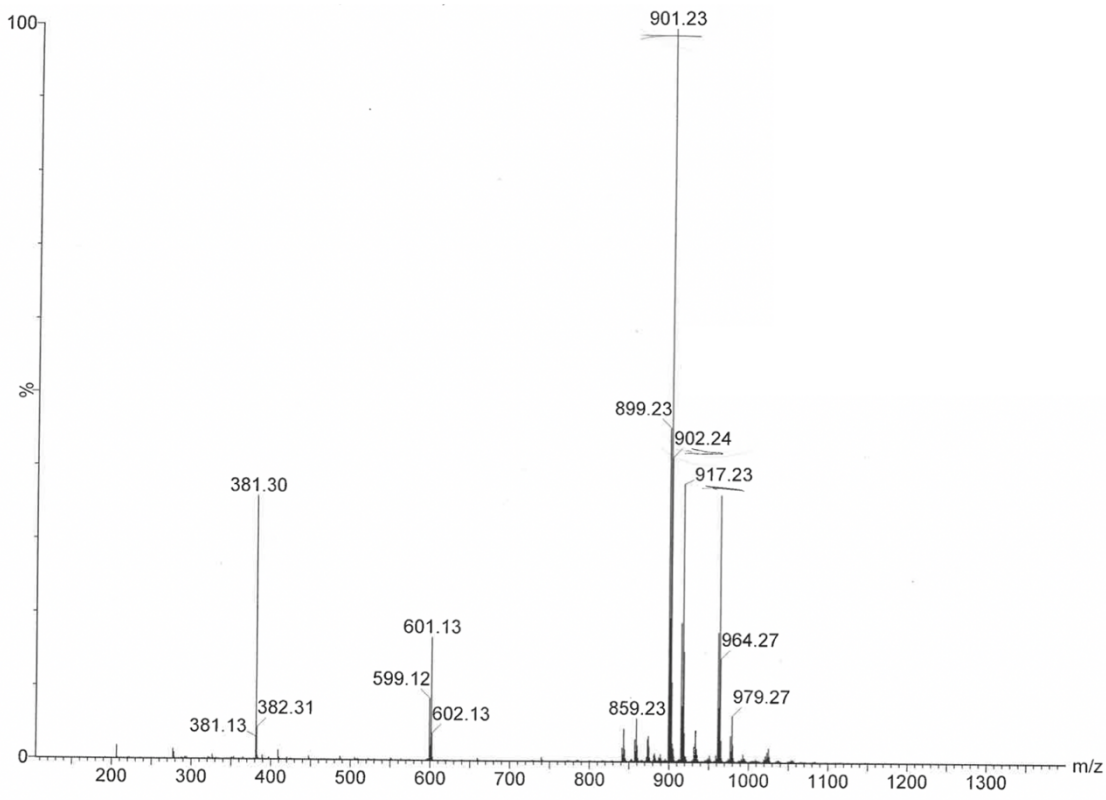

Appendix 2.14: Mass Spectrometry of $[Ir(2\text{-}PQ)_2BPYSH]PF_6$.

2.9 References

1. Chen, Y.; Qiao, L.; Ji, L.; Chao, H., Phosphorescent iridium (III) complexes as multicolor probes for specific mitochondrial imaging and tracking. *Biomaterials* **2014,** *35* (1), 2-13.
2. King, S. M.; Claire, S.; Teixeira, R. I.; Dosumu, A. N.; Carrod, A. J.; Dehghani, H.; Hannon, M. J.; Ward, A. D.; Bicknell, R.; Botchway, S. W., Iridium Nanoparticles for Multichannel Luminescence Lifetime Imaging, Mapping Localization in Live Cancer Cells. *Journal of the American Chemical Society* **2018,** *140* (32), 10242-10249.
3. Lo, K. K.-W.; Zhang, K. Y., Iridium (III) complexes as therapeutic and bioimaging reagents for cellular applications. *Royal Society of Chemistry advances* **2012,** *2* (32), 12069-12083.
4. Kalyanasundaram, K., *Photochemistry of polypyridine and porphyrin complexes*. Academic Press: 1991.
5. Lowry, M. S.; Bernhard, S., Synthetically tailored excited states: phosphorescent, cyclometalated iridium (III) complexes and their applications. *Chemistry–A European Journal* **2006,** *12* (31), 7970-7977.
6. Lo, K. K.-W.; Zhang, K. Y.; Leung, S.-K.; Tang, M.-C., Exploitation of the Dual-emissive Properties of Cyclometalated Iridium(III)–Polypyridine Complexes in the Development of Luminescent Biological Probes. *Angewandte Chemie International Edition* **2008,** *47* (12), 2213-2216.
7. Zhao, Q.; Yu, M.; Shi, L.; Liu, S.; Li, C.; Shi, M.; Zhou, Z.; Huang, C.; Li, F., Cationic Iridium(III) Complexes with Tunable Emission Color as Phosphorescent Dyes for Live Cell Imaging. *Organometallics* **2010,** *29* (5), 1085-1091.
8. Jiang, W.; Gao, Y.; Sun, Y.; Ding, F.; Xu, Y.; Bian, Z.; Li, F.; Bian, J.; Huang, C., Zwitterionic Iridium Complexes: Synthesis, Luminescent Properties, and Their Application in Cell Imaging. *Inorganic Chemistry* **2010,** *49* (7), 3252-3260.
9. Lo, K. K.-W.; Lee, P.-K.; Lau, J. S.-Y., Synthesis, Characterization, and Properties of Luminescent Organoiridium(III) Polypyridine Complexes Appended with an Alkyl Chain and Their Interactions with Lipid Bilayers, Surfactants, and Living Cells. *Organometallics* **2008,** *27* (13), 2998-3006.
10. Sardar, R.; Funston, A. M.; Mulvaney, P.; Murray, R. W., Gold nanoparticles: past, present, and future. *Langmuir* **2009,** *25* (24), 13840-13851.
11. Sperling, R. A.; Gil, P. R.; Zhang, F.; Zanella, M.; Parak, W. J., Biological applications of gold nanoparticles. *Chemical Society Reviews* **2008,** *37* (9), 1896-1908.
12. Ghosh, S. K.; Pal, T., Interparticle coupling effect on the surface plasmon resonance of gold nanoparticles: from theory to applications. *Chemical reviews* **2007,** *107* (11), 4797-4862.
13. Eustis, S.; El-Sayed, M. A., Why gold nanoparticles are more precious than pretty gold: noble metal surface plasmon resonance and its enhancement of the radiative and nonradiative properties of nanocrystals of different shapes. *Chemical society reviews* **2006,** *35* (3), 209-217.
14. Kelly, K. L.; Coronado, E.; Zhao, L. L.; Schatz, G. C., The optical properties of metal nanoparticles: the influence of size, shape, and dielectric environment. ACS Publications: 2003.

15. Woehrle, G. H.; Brown, L. O.; Hutchison, J. E., Thiol-functionalized, 1.5-nm gold nanoparticles through ligand exchange reactions: Scope and mechanism of ligand exchange. *Journal of the American Chemical Society* **2005,** *127* (7), 2172-2183.
16. Padmanabhan, P.; Kumar, A.; Kumar, S.; Chaudhary, R. K.; Gulyás, B., Nanoparticles in practice for molecular-imaging applications: An overview. *Acta Biomaterialia* **2016,** *41*, 1-16.
17. Giljohann, D. A.; Seferos, D. S.; Daniel, W. L.; Massich, M. D.; Patel, P. C.; Mirkin, C. A., Gold nanoparticles for biology and medicine. *Angewandte Chemie International Edition* **2010,** *49* (19), 3280-3294.
18. Dreaden, E. C.; Alkilany, A. M.; Huang, X.; Murphy, C. J.; El-Sayed, M. A., The golden age: gold nanoparticles for biomedicine. *Chemical Society Reviews* **2012,** *41* (7), 2740-2779.
19. Dong, Y.; Abaci, S.; Shannon, C.; Bozack, M. J., Self-assembly and electrochemical desorption of thioctic acid monolayers on gold surfaces. *Langmuir* **2003,** *19* (21), 8922-8926.
20. Slinker, J. D.; Gorodetsky, A. A.; Lowry, M. S.; Wang, J.; Parker, S.; Rohl, R.; Bernhard, S.; Malliaras, G. G., Efficient yellow electroluminescence from a single layer of a cyclometalated iridium complex. *Journal of the american chemical society* **2004,** *126* (9), 2763-2767.
21. Osborne, S. A. M.; Pikramenou, Z., Highly luminescent gold nanoparticles: effect of ruthenium distance for nanoprobes with enhanced lifetimes. *Faraday Discussions* **2015,** *185* (0), 219-231.
22. Adams, S. J.; Lewis, D. J.; Preece, J. A.; Pikramenou, Z., Luminescent Gold Surfaces for Sensing and Imaging: Patterning of Transition Metal Probes. *Journal of the american chemical society Applied Materials & Interfaces* **2014,** *6* (14), 11598-11608.
23. Bertoncello, P.; Kefalas, E. T.; Pikramenou, Z.; Unwin, P. R.; Forster, R. J., Adsorption Dynamics and Electrochemical and Photophysical Properties of Thiolated Ruthenium 2, 2 '-Bipyridine Monolayers. *The Journal of Physical Chemistry B* **2006,** *110* (20), 10063-10069.
24. Li, C.; Liu, Y.; Wu, Y.; Sun, Y.; Li, F., The cellular uptake and localization of non-emissive iridium (III) complexes as cellular reaction-based luminescence probes. *Biomaterials* **2013,** *34* (4), 1223-1234.
25. Ma, D. L.; Wong, W. L.; Chung, W. H.; Chan, F. Y.; So, P. K.; Lai, T. S.; Zhou, Z. Y.; Leung, Y. C.; Wong, K. Y., A highly selective luminescent switch-on probe for histidine/histidine-rich proteins and its application in protein staining. *Angewandte Chemie International Edition* **2008,** *47* (20), 3735-3739.
26. Ziegler, C.; Eychmuller, A., Seeded growth synthesis of uniform gold nanoparticles with diameters of 15− 300 nm. *The Journal of Physical Chemistry C* **2011,** *115* (11), 4502-4506.
27. Grabar, K. C.; Freeman, R. G.; Hommer, M. B.; Natan, M. J., Preparation and characterization of Au colloid monolayers. *Analytical chemistry* **1995,** *67* (4), 735-743.
28. Schulz, F.; Homolka, T.; Bastús, N. G.; Puntes, V.; Weller, H.; Vossmeyer, T., Little adjustments significantly improve the Turkevich synthesis of gold nanoparticles. *Langmuir* **2014,** *30* (35), 10779-10784.
29. Turkevich, J.; Stevenson, P. C.; Hillier, J., A study of the nucleation and growth processes in the synthesis of colloidal gold. *Discussions of the Faraday Society* **1951,** *11*, 55-75.
30. Zhao, P.; Li, N.; Astruc, D., State of the art in gold nanoparticle synthesis. *Coordination Chemistry Reviews* **2013,** *257* (3-4), 638-665.

31. Ji, X.; Song, X.; Li, J.; Bai, Y.; Yang, W.; Peng, X., Size control of gold nanocrystals in citrate reduction: the third role of citrate. *Journal of the American Chemical Society* **2007,** *129* (45), 13939-13948.
32. Ojea-Jiménez, I.; Bastús, N. G.; Puntes, V., Influence of the sequence of the reagents addition in the citrate-mediated synthesis of gold nanoparticles. *The Journal of Physical Chemistry C* **2011,** *115* (32), 15752-15757.
33. Xia, H.; Bai, S.; Hartmann, J. r.; Wang, D., Synthesis of monodisperse quasi-spherical gold nanoparticles in water via silver (I)-assisted citrate reduction. *Langmuir* **2010,** *26* (5), 3585-3589.
34. Ojea-Jiménez, I.; Campanera, J. M., Molecular modeling of the reduction mechanism in the citrate-mediated synthesis of gold nanoparticles. *The Journal of Physical Chemistry C* **2012,** *116* (44), 23682-23691.
35. Biggs, S.; Chow, M.; Zukoski, C. F.; Grieser, F., The role of colloidal stability in the formation of gold sols. Elsevier: 1993.
36. Chow, M.; Zukoski, C., Gold sol formation mechanisms: role of colloidal stability. *Journal of colloid and interface science* **1994,** *165* (1), 97-109.
37. Kumar, S.; Gandhi, K.; Kumar, R., Modeling of formation of gold nanoparticles by citrate method. *Industrial & Engineering Chemistry Research* **2007,** *46* (10), 3128-3136.
38. Zabetakis, K.; Ghann, W. E.; Kumar, S.; Daniel, M.-C., Effect of high gold salt concentrations on the size and polydispersity of gold nanoparticles prepared by an extended Turkevich–Frens method. *Gold Bulletin* **2012,** *45* (4), 203-211.
39. Carney, R. P.; Kim, J. Y.; Qian, H.; Jin, R.; Mehenni, H.; Stellacci, F.; Bakr, O. M., Determination of nanoparticle size distribution together with density or molecular weight by 2D analytical ultracentrifugation. *Nature Communications* **2011,** *2* (1), 335.
40. Haiss, W.; Thanh, N. T.; Aveyard, J.; Fernig, D. G., Determination of size and concentration of gold nanoparticles from UV− Vis spectra. *Analytical chemistry* **2007,** *79* (11), 4215-4221.
41. Pensa, E.; Cortes, E.; Corthey, G.; Carro, P.; Vericat, C.; Fonticelli, M.; Benítez, G.; Rubert, A., a.; Salvarezza, RC. *Accounts of Chemical Research* **2012,** *45* (8), 1183-1192.
42. Wu, Y.; Zhan, S.; Wang, F.; He, L.; Zhi, W.; Zhou, P., Cationic polymers and aptamers mediated aggregation of gold nanoparticles for the colorimetric detection of arsenic (III) in aqueous solution. *Chemical communications* **2012,** *48* (37), 4459-4461.
43. Zakaria, H. M.; Shah, A.; Konieczny, M.; Hoffmann, J. A.; Nijdam, A. J.; Reeves, M., Small molecule-and amino acid-induced aggregation of gold nanoparticles. *Langmuir* **2013,** *29* (25), 7661-7673.
44. Lou, T.; Chen, L.; Zhang, C.; Kang, Q.; You, H.; Shen, D.; Chen, L., A simple and sensitive colorimetric method for detection of mercury ions based on anti-aggregation of gold nanoparticles. *Analytical Methods* **2012,** *4* (2), 488-491.
45. Chhour, P.; Kim, J.; Benardo, B.; Tovar, A.; Mian, S.; Litt, H. I.; Ferrari, V. A.; Cormode, D. P., Effect of gold nanoparticle size and coating on labeling monocytes for CT tracking. *Bioconjugate chemistry* **2017,** *28* (1), 260-269.
46. Fröhlich, E., The role of surface charge in cellular uptake and cytotoxicity of medical nanoparticles. *International Journal of Nanomedicine* **2012,** *7*, 5577-5591.

Chapter 3:

Luminescent Iridium Coated Gold nanoparticles: Biological Assays Testing for Biocompatibility

3.1 Chapter Summary

This work investigates the luminescent-AuNP nanoprobe library post incubation with peripheral whole blood derived regulatory T-cells (Tregs). Whole blood was layered over Lympholyte® solution and layers separated via centrifugation isolating the lymphocytes (Figure 3.1(a)).

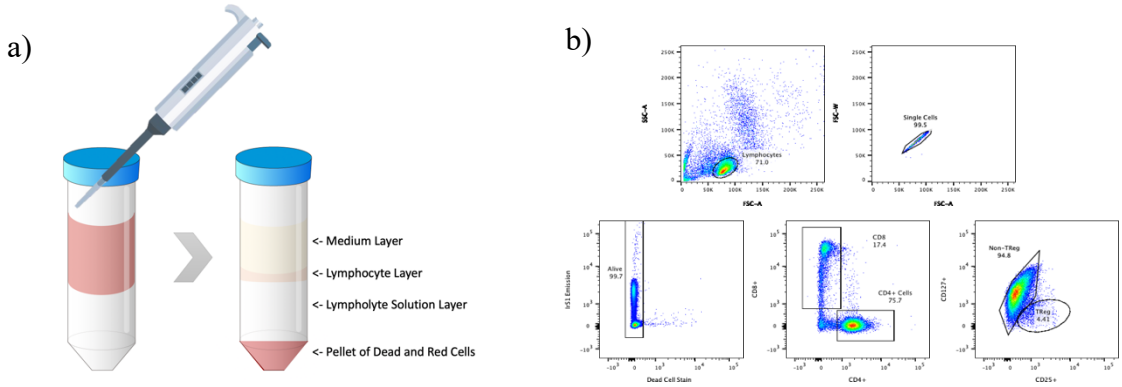

Fig. 3.1 (a) Schematic to show the layering of whole blood over Lympholyte® solution and layers separated via centrifugation isolating the lymphocytes. (b) Gating strategy for CD3+ cells to Tregs via antibody dyes for FACS on CD4, CD8, CD25 and CD127 receptors

The lymphocytes were extracted and CD3+ cells were isolated via a magnetic column using the Pan T Cell Isolation kit (MACS Miltenyi Biotec)[1-5]. Following CD3+ isolation, cells were incubated with the nanoprobe library before CD4, CD8, CD25 and CD127 fluorescent antibody stains were added to allow for Treg gating by flow cytometry (Flow assisted cell sorting, FACS) (Figure 3.1(b)). Cytotoxicity, percentage uptake and ICP-MS analysis were used to narrow the full nanoprobe library, with an AuNP core size of 25nm providing both the greatest uptake and fluorescence detection

whilst exhibiting little cytotoxicity, it was decided the Au25NP nanoprobes would be carried for further analysis.

Photophysical characteristics of the Tregs post incubation were analysed and showed the excitation, emission and lifetime features of IrS1 were retained in the biological environment with only slight shifts in emission. The phenotypical and functional behaviour of the Tregs were next investigated to ensure the presence of the nanoprobes would not disrupt any immune-regulatory activity post transplantation. The Au25NP.Zonyl.IrS1 nanoprobes were selected for further study as the PEG coated alternatives presented both upregulation and downregulation of various pro-inflammatory cytokines and chemokines where the Zonyl coated nanoprobes showed little change in the presence of suitable stimulants. Tregs were content to proliferate and function as expected post labelling with Au25NP.Zonyl.IrS1, with good retention within labelled cells in unlabelled cell environments.

3.1.1 Introduction

Regulatory T-cells can be used for CAR-T cell therapies, with research being translated to clinics for testing in patients suffering from autoimmune diseases (Figure 3.1.1)[6]. Tregs are, primarily, critical regulators of immune tolerance[7]. *Sakaguchi et al* were amongst the first to discover Treg activity via adoptive transfer studies[8]. Many studies that followed have shown the majority of chronic active hepatitis is related to immune-mediated liver injury[9]. Research into the pathogenesis of the disease has highlighted Treg infrequencies in the peripheral blood of patients with either acute liver injury, chronic liver disease or liver cancer[10, 11]. Tregs are exploitable due to their ability to exert their functions by either inhibiting the function or maturation of antigen presenting cells, by destroying target cells by induced apoptosis, by causing metabolic disruption of the adenosine pathway, by secreting immunosuppressive cytokines transforming growth factor beta and IL-2 or by competitive consumption of survival cytokines in particular IL-2[12].

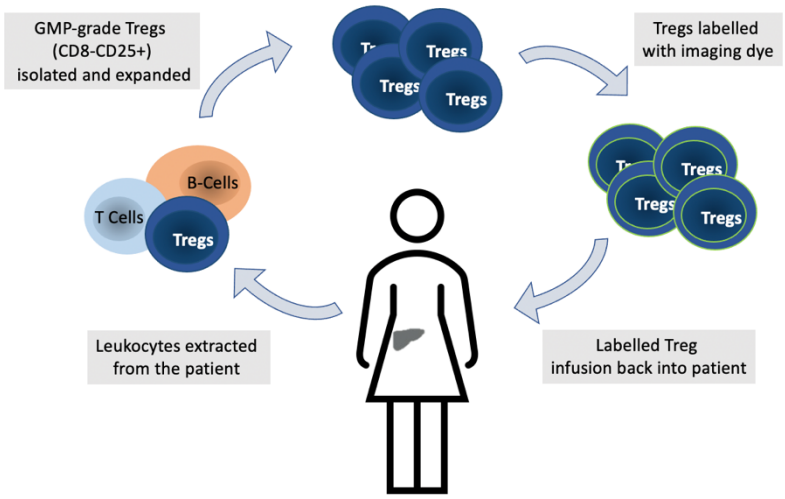

Fig. 3.1.1 Schematic of process involved with using regulatory T cells in immune therapy

Autoimmune disorders are chronic diseases caused by the breakdown of tolerance against self-antigens. This may be triggered by either a decrease in the number of Tregs or a lack of functioning Tregs as well as by the resistance of effector T-cells to suppression. Patients who receive high doses of immunosuppressants are left susceptible to life-threatening infections. Since Sakaguchi *et al* were able to protect thymectomized mice from autoimmunity using Treg therapy[8], many studies have gone on to demonstrate Tregs' ability to maintain an immune homeostasis with Tregs being identified by the expression of CD25+ and forkhead box P3 (FOXP3) markers. The methylation status of the Treg-specific demethylated region (TSDR), a conserved non-coding element within the FOXP3 gene locus, can be used to for the identification of human Tregs[13, 14]. Trzonkowski *et al* provided details of the first clinical trials using Tregs in 2009 to treat human diseases, providing the rationale and prospect for future use of the application[15].

Research conducted by a variety of groups has demonstrated the thymus as the central organ involved in the generation of Tregs[16]. Caramalho *et al* confirmed the differentiation of thymus derived Tregs depends on the strength and duration of T cell receptor signalling[16]. Naive FOXP3- CD4+ cells can also differentiate into Tregs in the periphery, commonly referred to as induced Tregs or peripheral Tregs, likely as a reaction to non-self-antigens found in foods, microbiota and allergens[17]. Tregs themselves are considered heterogeneous, mainly due to their capacity to adapt their features specific to the type of immune response they control[18]. Research has explored the further differentiation of Tregs into smaller subpopulations with respect to their expression of well-known functional markers, however it is difficult to accurately distinguish and quantify these subpopulations due to the overlap amongst many of the defining parameters.

Isolation of viable lymphocytes can be achieved, pre-clinic, from peripheral whole blood by the removal of both red and dead cells using Lympholyte® Cell Separation solution via the approved protocol[19-21].

For isolation under GMP conditions in the clinic CliniMACS (CliniMACS™ Instruments, Miltenyi Biotec) is used alongside Leukapheresis to produce autologous polyclonal GMP-grade Tregs[18, 22]. CliniMACS works by the depletion of the CD8+ fraction followed by enrichment of the CD25+ cell fraction. Another method used to isolate cells for clinical use is flow cytometry based purification where cells are isolated according to the expression of selected markers, however these have not been used in the UK to date in any clinical trials[23]. One major challenge for research in the use of Tregs for therapy is their inherently low frequencies. The percentage of Tregs found in whole blood is around 5-10% of all circulating CD4+ cells and so this means infusions of large cell populations becomes difficult to achieve. This requires expansion of Tregs *ex vivo*, whereby expansion may be defined as induced cell proliferation. Protocols exist where rapamycin, an immunosuppressant, is used to inhibit exclusively the proliferation of effector T-cells and favours FOXP3 upregulation[24]. Other protocols may expand Tregs in the presence of TGF-β which comparatively can produce a batch of Tregs with more demethylated TSDR than the initial batch of isolated cells (Figure 3.1.2)[25].

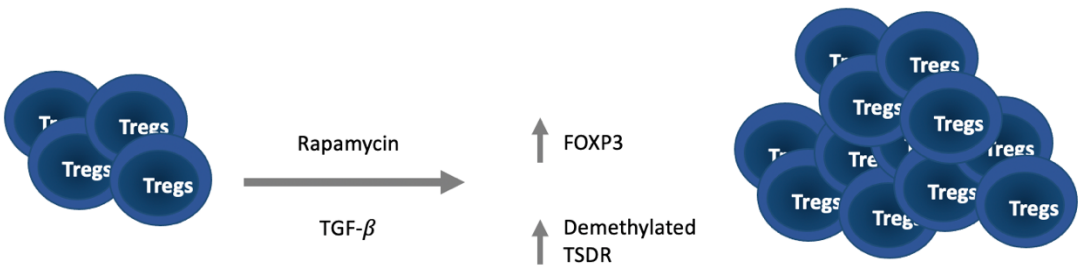

Fig. 3.1.2 Schematic of Treg expansion using rapamycin or TGF-β to facilitate the upregulation of FOXP3 and demethylated TSDR respectively

Cytokines are secreted proteins that regulate a range of biological activities including immunoregulation after cells experience some form of activation. For Tregs their phenotypical behaviour affects their functionality and ability to immune-regulate, especially post transplantation into patients as a form of therapy (Figure 3.1.3).

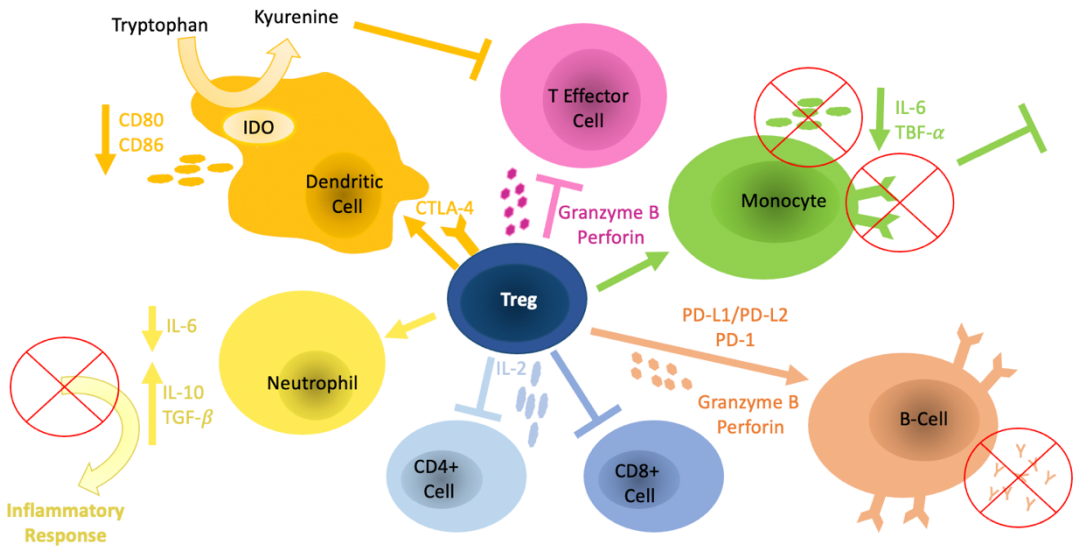

Fig 3.1.3 Treg mechanisms of action. CTLA-4 on the surface of Tregs bind to CD80/CD86 on dendritic cells leading to IDO-mediated tryptophan deprivation. Binding stimulates the induction of the enzyme Indoleamine 2, 3-dioxygenase (IDO) in CD123+ CCR6+ dendritic cells, which catalyses the conversion of Tryptophan to N′-Formylkynurenine. This Tryptophan depletion leads to CD4+ cell death. Release of Granzyme B and perforin by Treg leads to apoptosis of T effector cells. Deprivation of IL-2 from CD4+ T cells by CD25 on the Treg surface leads to cell death. Tregs have a direct effect on B-cells via PD-L1/PD-1 interaction. Tregs can also prevent monocyte differentiation into pro-inflammatory M1 macrophages. They can induce a suppressive phenotype in neutrophils by downregulation of IL6

Despite carrying out critical roles in the regulation of the adaptive immune responses, Dendritic cells are known to be involved in the pathogenesis of many autoimmune diseases. Tregs can either reduce the limiting enzyme for glutathione synthesis or can consume extracellular cysteine which disrupts the microenvironment in the immunological synapse provided by Dendritic cells. Tregs can also influence Dendritic cells in a leukocyte function-associated antigen-1 dependant manner, via compensatory mechanisms or by their ability to increase expression of Indoleamine

2,3-dioxygenase (IDO) to catalyse the degradation of tryptophan leading to the starvation of effector cells[26-29].

Monocyte regulation has been highlighted as a key function to reduce chronic inflammation in patients. Tregs can act directly on monocytes to inhibit their cytokine secretion, differentiation and antigen presenting functions. Tiemessen *et al* showed monocytes had a reduced ability to respond to pro-inflammatory stimuli post exposure to Tregs[30]. More recently, Romano *et al* showed that monocytes cultured with expanded Tregs showed a reduction in monocytes' pro inflammatory behaviour than with freshly isolated Tregs, which could be promising for clinical applications[31].

Tregs also have the ability to supress autoreactive B-cells to prevent the production of harmful autoantibodies in an antigen specific manner by the expression of PD-1 and 2 ligands on the Tregs themselves which interact with the PD-1 expressed on the B-cell[32]. When suppression proves insufficient, Tregs can kill B-cells by releasing granzyme B and perforin[33]. Tregs supress CD4+ T-cells and CD8+ cell activation and proliferation by contact dependant and independent mechanisms. A result of this mechanistic regulation is the reduced induction of high affinity effector and memory CD8+ T cells[26]. Granulocytes, particularly neutrophils have been attributed to aiding the cause of autoimmune diseases when they experience any dysfunction. Tregs have the ability to causes an adaptation in neutrophils so that they present a more immunosuppressive phenotype by producing more IL-10 and TGF-β with less IL-6[34].

Oo *et al* have treated autoimmune hepatitis patients with Tregs and found they are both immunosuppressive and possess functional markers making them metabolically competent[22]. The group used an ^{111}Indium tropolonate label to track the localisation of the cells in patients by SPECT-CT. Serial gamma camera imaging was

carried out at time intervals of 4, 24 and 72 hours after which the group observed the presence of the labelled GMP-Tregs in the liver, spleen and bone marrow.

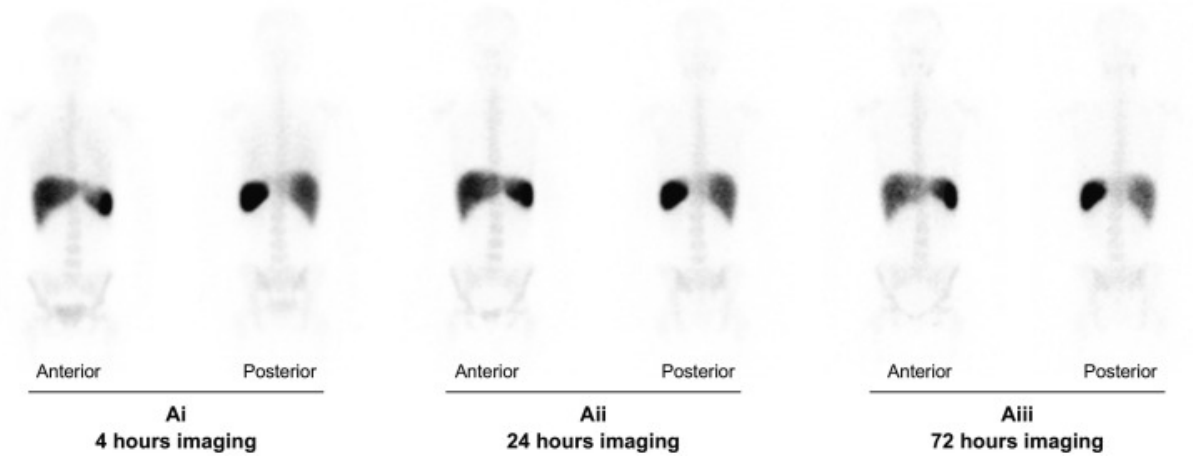

Fig. 3.1.3 Serial Gamma camera imaging performed at 4 h (Ai), 24 h (Aii) and 72 h (Aiii) post GMP-Treg infusion demonstrates the presence of indium tropolonate labelled GMP-Tregs in the liver, spleen and bone marrow. GMP-Tregs were present and remained in the liver for up to 72 h (Aiii). (Anterior = Gamma camera imaging scan from the anterior view; posterior = Gamma camera imaging scan from posterior view). GMP, Good Manufacturing Practice; Treg, regulatory T cell[22]
(Figure taken from reference 22)

No significant infusion related reactions, citrate toxicity or hypotensive behaviour was observed. However, a major limitation here would be the imaging resolution achieved with using ^{111}Indium tropolonate as a dye. SPECT-CT does not allow for any intra-organ localisation, because the signal from the dye is too large spread, nor does it allow for real time continuous tracking due to the associated toxicity related with the use of gamma rays.

3.2 Functional Assays with Luminescent Iridium Coated Gold Nanoparticles:

3.2.1 Cytotoxicity of Full Probe Library in PBMCs, CD3+ Cells and Tregs

The first course of investigation of the full nanoprobe library involved assessing their cytotoxicity at varying concentrations. Peripheral Blood Mononuclear Cells (PBMCs) were isolated from clinical patient blood and were incubated overnight with 0.5ml of 0.01nM, 0.05nM, 1nM and 2nM of AuNP.Coating.IrS1 per 1 million cells. Cells were plated in 12-well plates at a volume of 3ml per well with 10% FBS Gibco™ RPMI Media containing L-Glutamine and Phenyl Strep. Following incubation, cells were washed and stained with CD3+, CD4+, CD8+, CD127+ and CD25+ fluorescent antibody dyes along with a dead cell stain (Zombie NIR™) for FACS analysis (Appendix 3.9.11). This allowed for gating of the cell population into CD3+ and Tregs. Cell populations were then plotted against the fluorescence of the dead cell stain (Appendix 3.9.1).

For all three coatings, Au13NP and Au25NPs displayed similar toxicities, with little effect in PBMCs. However, a greater decrease in cell viability was observed at 2nM within the Treg population and slightly in the CD3+ population (Figure 3.2.1.1 and 3.2.1.2). For the larger AuNPs, Au50NP and Au100NP, a much greater decrease in cell viability can be seen at concentrations above 0.5nM and 0.01nM respectively (Figure 3.2.1.3 and 3.2.1.4). This difference in cell viability between the sizes of AuNPs is unsurprising given the total of volume of inorganic material entering the cell. As such, for all ensuing series of experiments it was decided 1nM, 1nM, 0.5nM and 0.01nM concentration for each set of Au13NP, Au25NP, Au50NP and Au100NPs respectively would be used. The cytotoxicity experiments showed the cells, especially Tregs, remained alive post incubation with the nanoprobes which overcomes the first hurdle in designing a nanoprobe for cell tracking in immunotherapy.

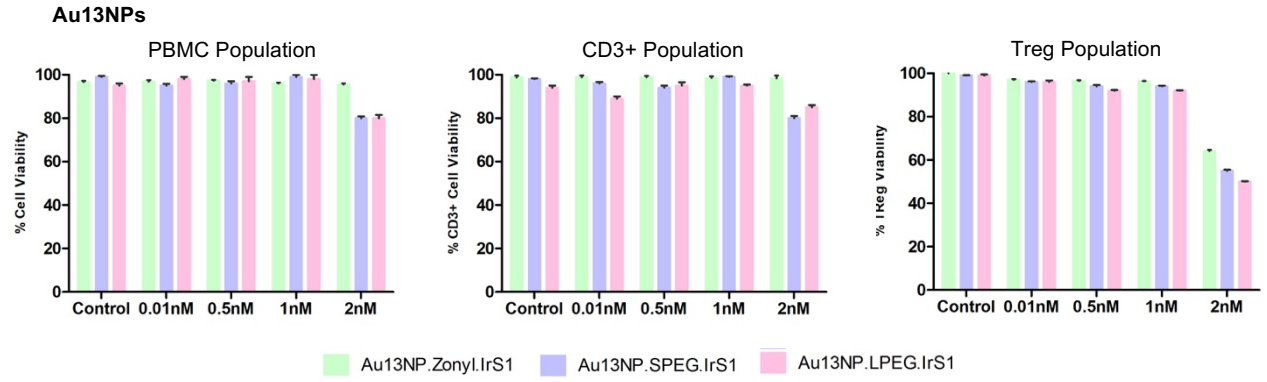

Fig 3.2.1.1 Cytotoxicity Assay Graphs of PBMCs (left), CD3+ (middle) and Tregs (right) incubated with 0nM, 0.01nM, 0.05nM, 1nM and 2nM of Au13NP.Coating.IrS1 per 1 million cells.

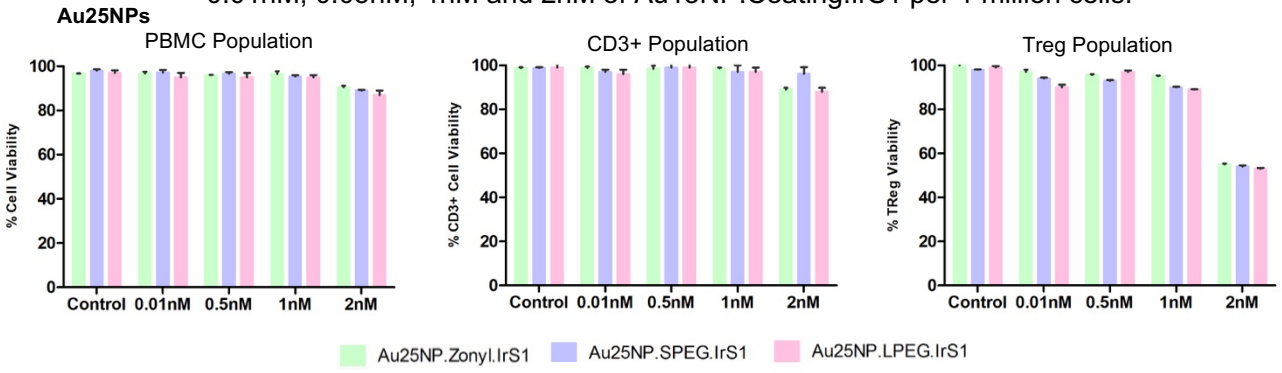

Fig 3.2.1.2 Cytotoxicity Assay Graphs of PBMCs (left), CD3+ (middle) and Tregs (right) incubated with 0nM, 0.01nM, 0.05nM, 1nM and 2nM of Au25NP.Coating.IrS1 per 1 million cells.

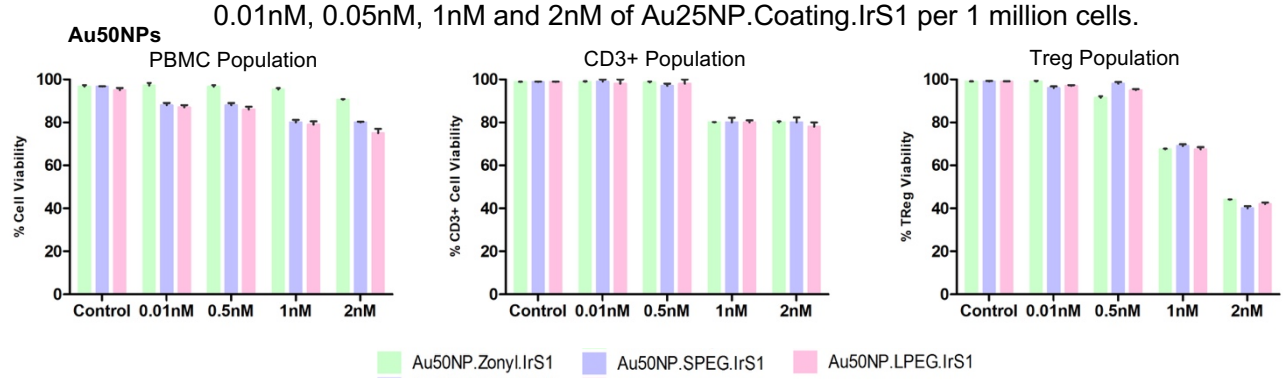

Fig 3.2.1.3 Cytotoxicity Assay Graphs of PBMCs (left), CD3+ (middle) and Tregs (right) incubated with 0nM, 0.01nM, 0.05nM, 1nM and 2nM of Au50NP.Coating.IrS1 per 1 million cells.

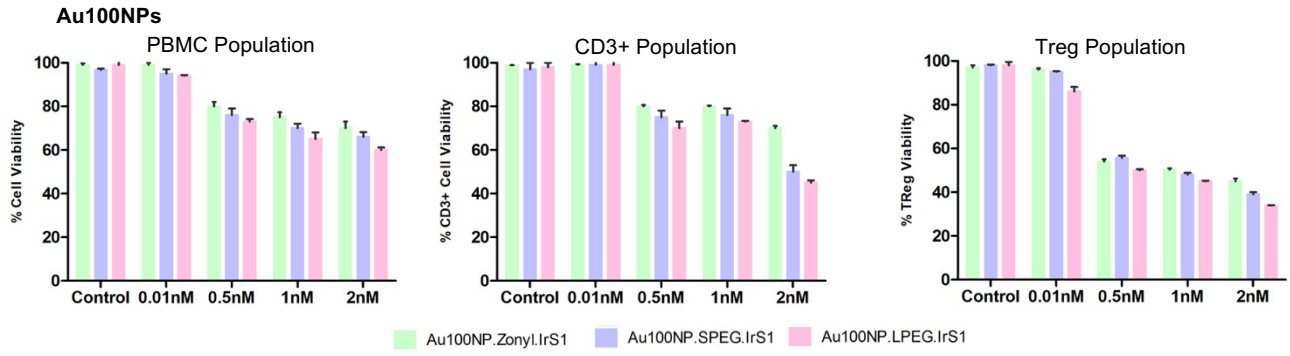

Fig 3.2.1.4 Cytotoxicity Assay Graphs of PBMCs (left), CD3+ (middle) and Tregs (right) incubated with 0nM, 0.01nM, 0.05nM, 1nM and 2nM of Au100NP.Coating.IrS1 per 1 million cells.

Alongside the cytotoxicity assay, it was also of interest to see if overnight incubation of Tregs with nanoprobes affected the number of Tregs isolated (Figure 3.2.1.5).

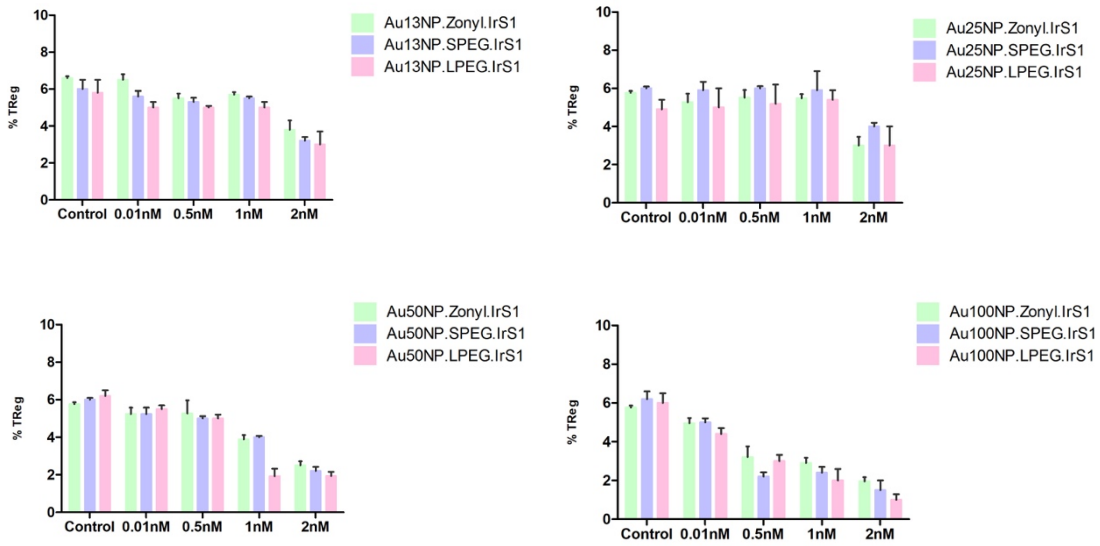

Fig 3.2.1.5 Percentage of Tregs incubated with 0nM, 0.01nM, 0.05nM, 1nM and 2nM of Au13NP.Coating.IrS1(top left), Au25NP.Coating.IrS1 (top right), Au50NP.Coating.IrS1 (bottom left) and Au100MP.Coating.IrS1 (bottom right) per 1 million cells.

Similar to the cytotoxicity results, a decrease in the percentage of Tregs was observed for Au13NPs and Au25NPs at 2nM whereas for the larger Au50NP and Au100NP, decreases in Treg populations was observed at concentrations above 0.5nM and 0.01nM respectively. These results further supported the decision to move forward with the allocated concentrations of 1nM, 1nM, 0.5nM and 0.01nM for each set of Au13NP, Au25NP, Au50NP and Au100NPs respectively. However, it should also be noted that Treg populations will differ greatly between patient samples, ranging anywhere between 5-10% of CD4+ cells. For the purpose of this study, 5 different patient bloods were used to compare the general trend of both cytotoxicity and %Treg for each nanoprobe being investigated to ensure observations can be attributed to effects of the nanoprobe and not the variations between blood samples. Additionally, a control group of cells were also used in each assay which were absent of any nanoprobes for an accurate reference.

3.2.2 Uptake of the Full Probe Library in CD3+ Cells and Tregs

The differing dose-able concentrations revealed through the cytotoxicity assay meant that the next step was to evaluate the ability to detect the probes at these different concentrations. Inherently, one would expect, the greater concentration of probe dosed, the greater the detectability. However, although lower concentrations of Au50NPs and Au100NPs are being used, the surface area of the larger AuNPs means more IrS1 complex will be attached at the surface, as seen by the ICP-MS data in tables 2.4.2.4, 2.4.2.5 and 2.4.2.6.

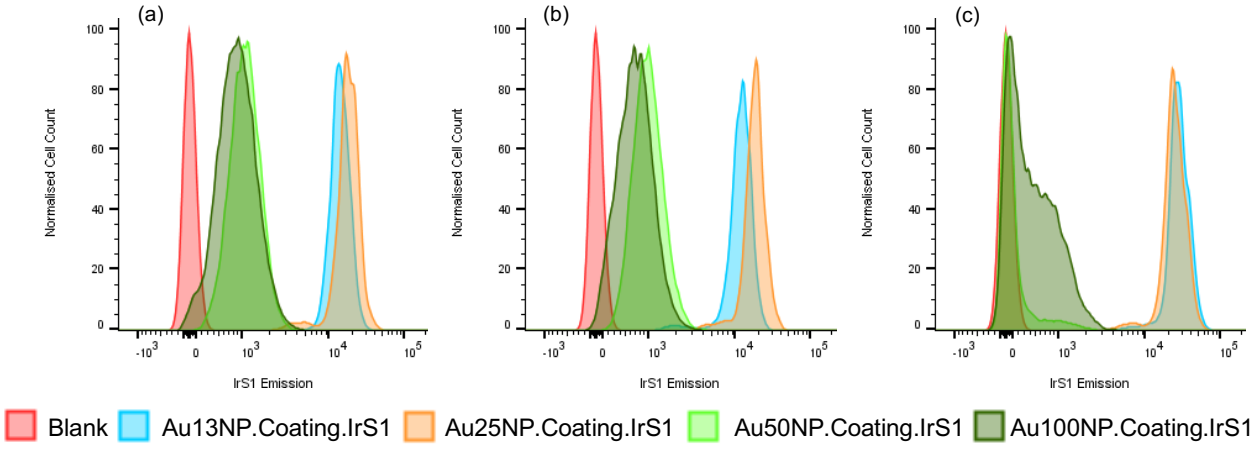

Fig 3.2.2.1 FACS histograms to show the IrS1 emission (λ_{em} 580nm) detected in CD3+ cells post overnight incubation with full probe library. (a) Zonyl coated nanoprobes, (b) SPEG coated nanoprobes and (c) LPEG coated nanoprobes at 1nM, 1nM, 0.5nM and 0.01nM for Au13NPs, Au25NPs, Au50NPs and Au100NPs respectively per 1 million cells.

FACS analysis showed that Au13NP.Coating.IrS1 and Au25NP.Coating.IrS1 gave a stronger emission per cell than their Au50NP.Coating.IrS1 and Au100NP.Coating.IrS1 alternatives (Figure 3.2.2.1, Appendix 3.9.2). For the Zonyl and SPEG coated nanoprobes, all four sizes of AuNPs were clearly detectable in cells, however, the larger Au50NP and Au100NP LPEG coated nanoprobes showed a more skewed distribution, suggesting there were a limited number of cells which had taken up the nanoprobes. It is implied the larger nanoprobes with the longer chain PEG were not favourable for uptake into the cells based on the overall size of the complex. It has

been reported in literature also that PEG compounds have the potential to interact with proteins on the surface of cells which may have acted as a deterrent, stopping the nanoprobes being taken into the cells[35-37].

Although not investigated in this series of experiments, it can be expected that the nanoprobes are taken into cells via receptor mediated endocytosis, or pinocytosis, following the formation of a protein corona around the nanoprobes[37]. Tregs are amongst the smaller cell types, typically ranging in size between 5-7μm and so there will be a limit to the amount of exogenous material the cells will be able to take in.

Here a decision to narrow the nanoprobe library under investigation was made. The cytotoxicity and uptake assays both supported the decision to eliminate the use of the larger nanoprobes, Au50NP.Coating.IrS1 and Au100NP.Coating.IrS1. They both exhibited weak uptake into cells and as such their fluorescence detectability was severely diminished.

With respect to the aforementioned cytotoxicity and uptake assays, ICP-MS data presented in tables 2.4.2.4, 2.4.2.5 and 2.4.2.6 indicate Au25NPs are able to carry more IrS1 than the Au13NPs, irrespective of coatings. The decision to continue with just Au25NP.Zonyl.IrS1, Au25NP.SPEG.IrS1 and Au25NP.LPEG.IrS1 was deemed the most appropriate as it is prudent to consider the multimodal aspect of the nanoprobe here too. Au25NPs have a greater volume of gold compared to Au13NPs and as such will be more readily detectable via Micro-CT. Additionally, although FACS didn't show much difference in the fluorescence detected between the Au13NPs and Au25NPs, multiphoton microscopy, to be used at a later date, may benefit from the greater volume of IrS1 per cell. As such only the Au25NP nanoprobes were carried forward for further investigation.

3.3 Functional Assays of Tregs with Luminescent Iridium Coated Gold Nanoparticles: Au25NPs

3.3.1 Time Course Assay

Overnight incubations of coated AuNPs into different cell types have been previously studied by the Pikramenou group and provided for an appropriate starting point for initial assays[38]. However, for Tregs in a clinical setting, shorter incubation times would be of greater benefit in order to minimise the time extracted cells are outside the patient's body. With Au25NP.Zony.IrS1, Au25NP.SPEG.IrS1 and Au25NP.LPEG.IrS1, the uptake into CD3+ cells was measured at incubation time intervals of 2, 4, 8, 16, 18 and 24 hours (Figure 3.3.1.1, Appendix 3.9.3).

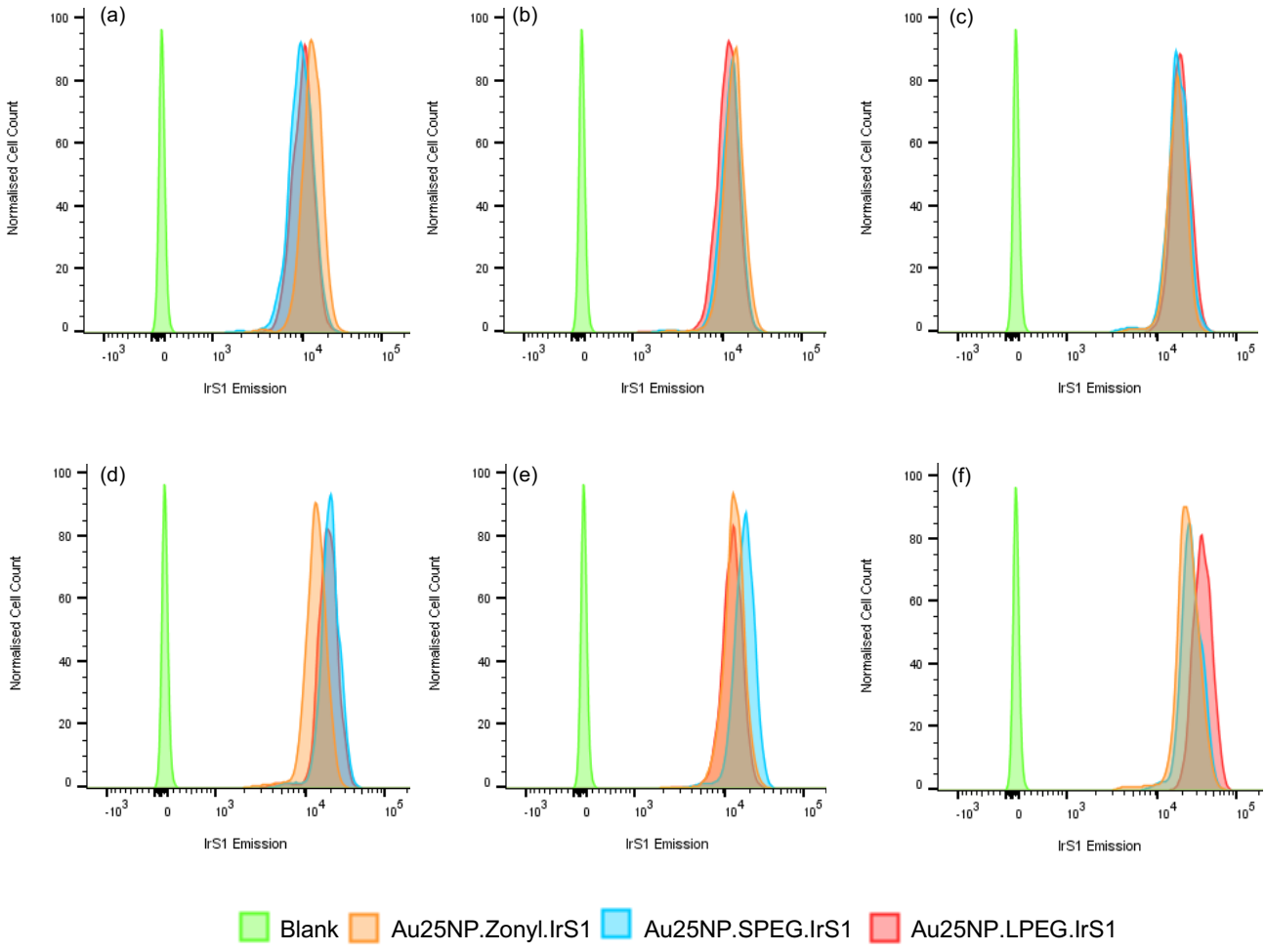

Fig 3.3.1.1 FACS histograms to show the IrS1 emission (λ_{em} 580nm) detected in CD3+ cells post incubation with Au25NP.Coating.IrS1. (a) 2 hours, (b) 4 hours, (c) 8 hours, (d) 16 hours, (e) 18 hours and (f) 24 hours at 1nM per 1 million cells.

Although the maximum emission for IrS1 was observed after 24 hours, a large uptake of probe was observed after even just two hours post incubation for all three types of nanoprobe. Notably, the Zonyl coated nanoprobes were taken up the most at the shorter incubation times and the PEG coated particles were taken up more given a longer incubation time. This trend can be attributed to the overall size of the nanoprobes, with the PEG coated particles having a larger conformation than the Zonyl coated counterparts. It is suggested that the PEG coated nanoprobes are taken up at a slower rate as their coating may interact with their uptake pathway as previously described.

3.3.2 Quantitative Analysis of Uptake into Cells

ICP-MS of CD3+ cells was conducted to quantify the number of nanoprobes per cell by detection of the number of gold atoms per 10 million cells (Table 3.3.2.1). ICP-MS indicated there was a larger uptake of Au25NP.Zonyl.IrS1 compared with both Au25NP.SPEG.IrS1 and Au25NP.LPEG.IrS1 following an 18hr incubation, further supporting the continuation of the Zonyl coated nanoprobe for future studies.

Table 3.3.2.1 ICP-MS calculated values for number of gold nanoparticles detected in CD3+ cells post incubation with Au25NP.Coating.IrS1 at 1nM per 1 million cells.

	Number of AuNPs per Cell calculated from ICP-MS	**Calculated number of IrS1 per AuNP from ICP-MS**	**Theoretical number of IrS1 per cell**
Au25NP.Zonyl.IrS1	3,500	2,800	9.8×10^6
Au25NP.SPEG.IrS1	1,600	2,700	4.3×10^6
Au25NP.LPEG.IrS1	700	2,700	1.9×10^6

3.3.3 Photophysical Characterisation of Cells with Luminescent Iridium Coated Gold Nanoparticles

For accurate fluorescent imaging of the labelled cells, CD3+ cells were analysed post incubation with all three nanoprobes for their fluorescent properties (Figure 3.3.3.1 and Table 3.3.3.1). Slight shifts in the emission λ_{max} can be seen in the detection of IrS1 inside the cells compared to on the nanoparticles in solution however,

more significantly, the long component lifetime of IrS1 in cells has increased from 410ns, 400ns and 420ns to 590ns, 560ns and 600ns respectively for Au25NP.Zonyl.IrS1, Au25NP.SPEG.IrS1 and Au25NP.LPEG.Ir1. The ~40% increase can be attributed to nanoprobe interaction with cellular proteins and chemicals.

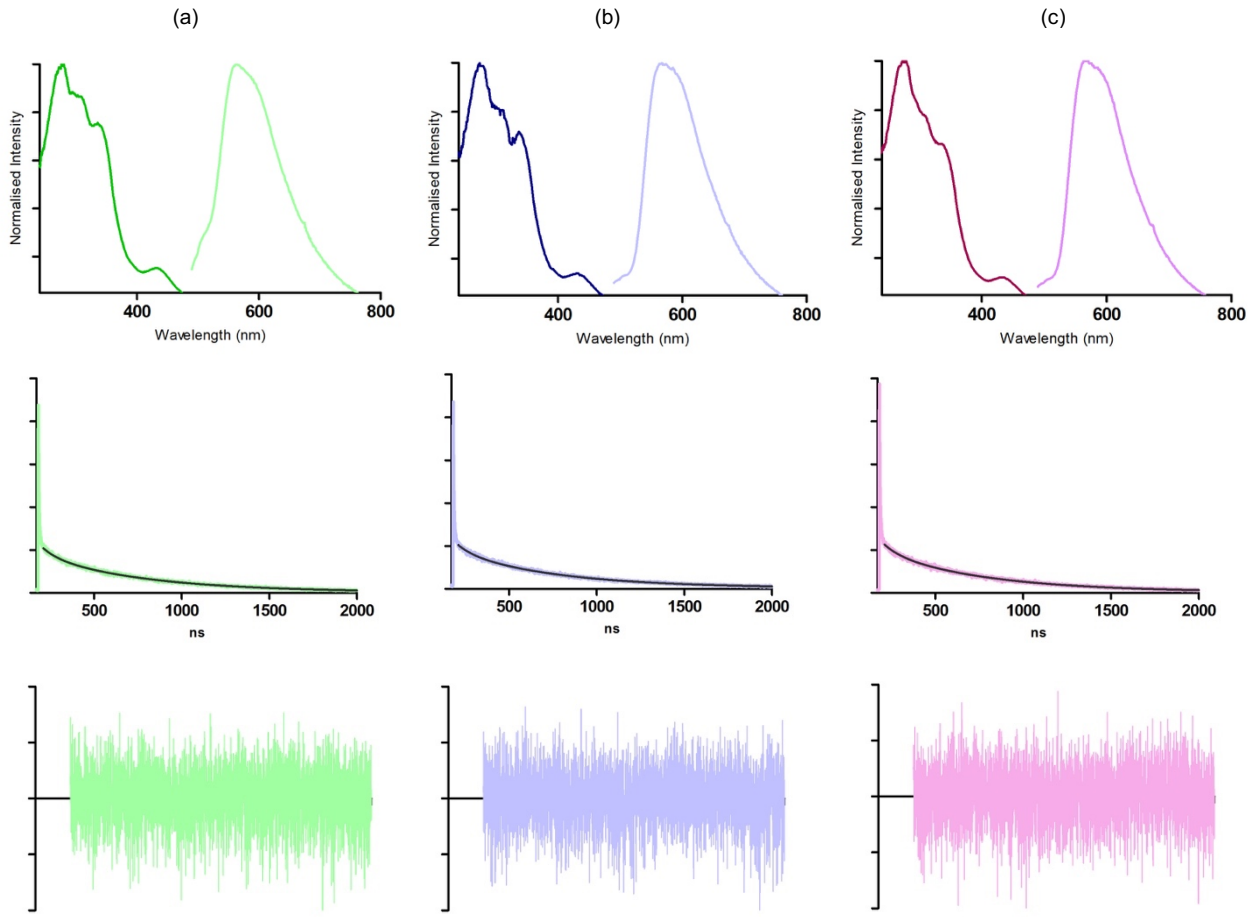

Fig 3.3.3.1 Top row: Excitation and emission profile for IrS1 emission (λ_{ex} 405,nm λ_{em} 580nm) detected in CD3+ cells post incubation with Au25NP.Coating.IrS1. Dark green, dark blue and dark pink = Excitation profile. Light green, light blue and light pink = Emission profile Middle Row: Lifetime plot for IrS1 detected in CD3+ cells post incubation. Bottom row: Residuals for lifetime plots for IrS1 detected in CD3+ cells post incubation. Column: (a) Au25NP.Zonyl.IrS1, (b) Au25NP.SPEG.IrS1, (c) Au25NP.LPEG.IrS1 at 1nM per 1 million cells.

Table 3.3.3.1 Emission and lifetime data for IrS1 emission (λ_{ex} 405,nm λ_{em} 580nm) detected in CD3+ cells post incubation with Au25NP.Coating.IrS1at 1nM per 1 million cells.

	Emission λ_{max} /nm	χ^2	τ /ns
Au25NP.Zonyl.IrS1	568	0.997	590 (97%)
			90 (3%)
Au25NP.SPEG.IrS1	587	0.980	560 (98%)
			70 (2%)
Au25NP.LPEG.IrS1	584	0.990	600 (97%)
			90 (3%)

3.4 Phenotypical Assays of Tregs with Luminescent Iridium Coated Gold Nanoparticles: Au25NPs

3.4.1 Chemokine Assay

CAR-T cells, especially Tregs, must be able to perform specific tasks to fulfil their therapeutic purpose. Chemokine expression is vital in cell migration via the induction of directed chemotaxis in nearby responsive cells. CXCR3 is highly expressed in T-cells and plays an important role in T-cell trafficking and function. Tregs that express CXCR3 acquire trafficking properties to allow them to localise and control excessive T helper cell responses at sites of inflammation. Another chemokine of interest is CCR6 which only binds to chemokine receptor CCLR20 (macrophage inflammatory protein). Pro inflammatory cells migrate via the chemokine gradient of CCLR20 to inflammatory sites and can express more CCLR20 to bring in more Tregs. This can lead to chronic inflammation and so low expression of CCR6 is desired.

For this study, it was crucial to maintain the 'normal' expression of chemokines on the Tregs, i.e., to keep phenotypical behaviour the same before and post labelling with nanoprobes. Post incubation of Au25NP.Zonyl.IrS1 in CD3+ cells, the variation in the expression of CCR6 was not significant in the whole CD3+ and CD4+ populations, with only a slight decrease in Tregs (Figure 3.4.1.1 and Table 3.4.1.1, Appendix 3.9.4 and 3.9.5). A similar trend was observed with Au25NP.SPEG.IrS1. There is implication that a more significant decrease in the number of cells expressing CCR6 post incubation with Au25NP.LPEG.IrS1 could be due to the nanoprobes larger conformation blocking the CCR6 receptor sites, having not been completely taken up by the cells. Conversely, the CD3+ population saw an upregulation of CXCR3 post incubation with Au25NP.LPEG.IrS1, but not in the CD4+ nor Treg population implying there may have been an up-regulatory interaction within the CD8+ cell population. Ultimately, across all samples there was little significant effect on CXCR3 expression

in the Treg population, the cell type of interest. Of the batches tested for this assay, the uptake of probe within each sub-population of cells was also analysed and showed over 90% Tregs were labelled with Au25NP.Zonyl.IrS1 and Au25NP.SPEG.IrS1 and over 80% were labelled with Au25NP.LPEG.IrS1.

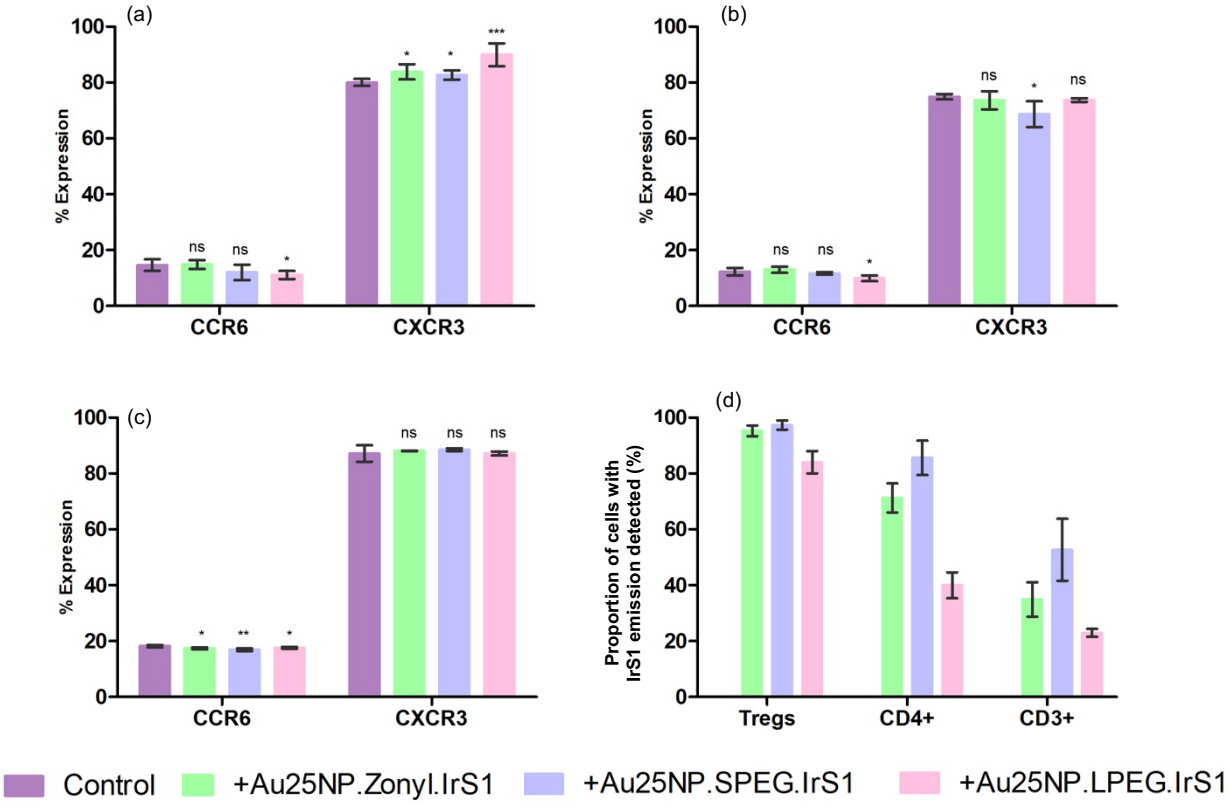

Fig 3.4.1.1 FACS analysis for the percentage of cells expressing chemokines CXCR3 and CCR6 of (a) CD3+ cells (b) CD4+ cells and (c) Tregs at 1nM per 1 million cells. (d) Percentage of cells showing nanoprobe uptake based on detection of IrS1 emission (λ_{ex} 405,nm λ_{em} 580nm). Paired T test, $P < 0.05$ was considered statistically significant. ns = not significant * = little significance ** = significant *** = very significant

Table 3.4.1.1 FACS analysis for the percentage of cells expressing chemokines CXCR3 and CCR6 of CD3+ cells CD4+ cells and Tregs at 1nM per 1 million cells.

	CD3+		CD4+		Tregs	
Chemokine Expressed:	**% CCR6**	**% CXCR3**	**% CCR6**	**% CXCR3**	**% CCR6**	**% CXCR3**
Control	15±2	80±1	12±1	75±1	18±0.5	87±3
Au25NP.Zonyl.IrS1	15±2	84±3	13±1	74±3	17±0.4	88±0.1
Au25NP.SPEG.IrS1	12±3	83±2	12±0.5	69±5	17±0.5	89±0.5
Au25NP.LPEG.IrS1	11±1	90±4	10±1	74±1	18±0.3	87±0.7

3.4.2 Cytokine Assay

Cytokines are small, secreted proteins released by cells to have a specific effect on the interactions and communications between cells. Post stimulation with PMA and Ionomycin followed by blocking with Brefeldin A, to allow for enhanced detection of intracellular cytokines, CD3+ cells were analysed for their production of IL-17, TNFα and IFNγ (Figure 3.4.1.2 and Table 3.4.1.2, Appendix 3.9.6 and 3.9.7). IL-17 is a pro inflammatory cytokine which induces pro inflammatory responses and is involved in the pathogenesis of various diseases whilst playing critical roles in antimicrobial defence and controlling autoimmunity and inflammation. TNFα is involved in systemic inflammation and is produced by activated macrophages and CD4+ lymphocytes. Its primary role is in immune cell regulation, promoting the inflammatory response. IFNγ is an immune interferon which induces T helper cells' immune response.

CD3+, CD4+ and Tregs showed no significant change in their expression of either IL-17, TNFα nor IFNγ after incubation with Au25NP.Zonyl.IrS1. However, Au25NP.SPEG.IrS1 and Au25NP.LPEG.IrS1 incubated cells showed a decreased expression of TNFα and IFNγ across all three sub populations of cells and a largely significant upregulation of IL-17 in CD4+ and Treg populations. It can be postulated that the PEG coatings are participating in an internal interaction which may be causing changes in cytokine production. As described in the literature, PEG compounds are bio-active and may engage with cellular proteins to either inhibit or alter cell behaviour. There is also the possibility that the nanoparticles are interacting with the stimulants leading to adverse effects on the cells, seen by a significant decrease in the percentage of cells displaying probe uptake in comparison with other assays described previously (Figure 3.4.1.2(d)).

although, for the purpose of clinical application, where there is no requirement for external stimulation, Au25NP.Zonyl.IrS1 presents itself as the most appropriate candidate to take forward for further testing. The change in cytokine production seen by Au25NP.SPEG.IrS1 and Au25NP.LPEG.IrS1 incubated cells could lead to unwanted responses in the body. Au25NP.Zonyl.IrS1 incubated cells showed an indifference in their phenotype compared with blank cells.

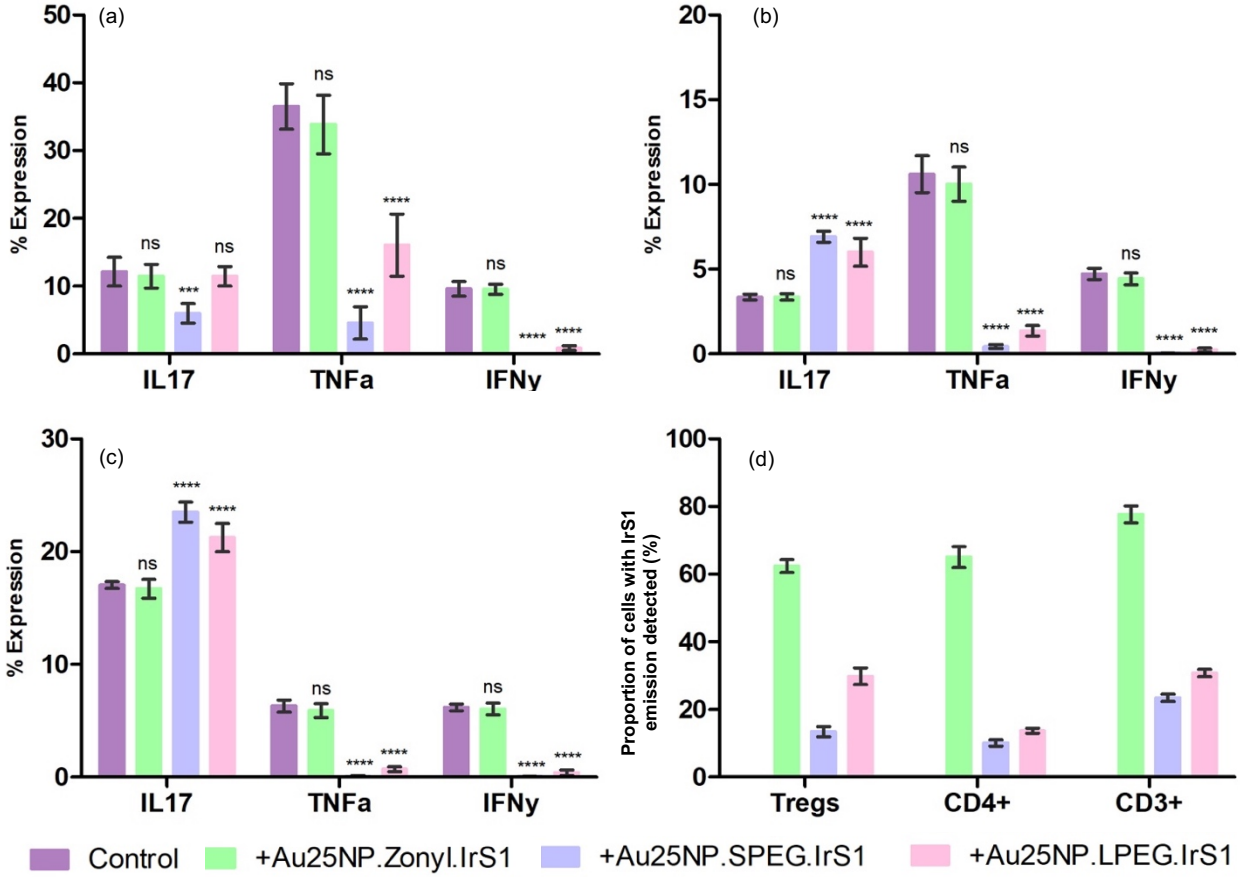

Fig 3.4.1.2 FACS analysis for the percentage of cells expressing cytokines IL17, TNFα and IFNγ of (a) CD3+ cells (b) CD4+ cells and (c) Tregs at 1nM per 1 million cells. (d) Percentage of cells showing nanoprobe uptake based on detection of IrS1 emission (λ_{ex} 405,nm λ_{em} 580nm). Paired T test, $P < 0.05$

Table 3.4.1.2 FACS analysis for the percentage of cells expressing cytokines IL17, TNFα and IFNγ of CD3+ cells, CD4+ cells and Tregs at 1nM per 1 million cells.

	CD3+			CD4+			Tregs		
Cytokine Expressed:	**% IL17**	**% TNFα**	**% IFNγ**	**% IL17**	**% TNFα**	**% IFNγ**	**% IL17**	**% TNFα**	**% IFNγ**
Control	12±2	37±3	10±1	3±0.2	11±1	5±1	17±0.3	6±0.5	6±0.3
Au25NP.Zonyl.IrS1	12±2	34±4	10±1	3±2	10±1	4±0.3	17±0.8	6±0.6	6±0.5
Au25NP.SPEG.IrS1	6±1	5±2	0.03±0.04	7±0.3	0.4±0.1	0.05±0.01	23±0.9	0.1±0.04	0.07±0.01
Au25NP.LPEG.IrS1	12±1	16±5	1±0.4	6±0.8	1±0.3	0.2±0.1	21±1	0.7±0.2	0.4±0.2

3.5 Pre- *In Vivo* Testing with Au25NP.Zonyl.IrS1

3.5.1 Proliferation Assay

CD4+ cells post incubation with Au25NP.Zonyl.IrS1 were stimulated with T-cell activation beads and stained with VioTrace and allowed to proliferate for up to 6 generations (Figure 3.5.1.1). As each generation passed, the mean intensity of VioTrace remained constant between the blank cells and the incubated cells, with the incubated cells showing no difference in their ability to proliferate as normal under the equivalent conditions. In addition to the VioTrace being distributed between daughter cells, the assay also showed the distribution of IrS1 emission amongst daughter cells (Appendix 3.9.8). This observation is especially interesting as it both confirms internalisation of the nanoprobes, but also affords the ability to track the daughter cells of the therapeutically delivered cells with a consistent emission intensity.

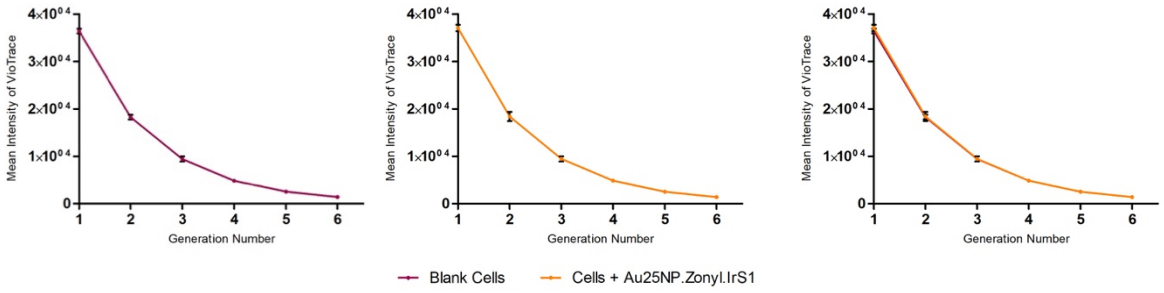

Fig 3.5.1.1 FACS analysis for the stimulated proliferation of CD4+ cells compared to CD4+cells post nanoprobe uptake based on detection of IrS1 emission (λ_{ex} 405,nm λ_{em} 580nm) and the mean intensity of VioTrace to detect daughter cells post incubation with Au25NP.Zonyl.IrS1 at 1nM per 1 million cells.

3.5.2 CyTOF Assay in PBMCs

CyTOF (Mass Cytometry by Time of Flight) analysis was used in conjunction with FACS to show the distribution of Au25NP.Zonyl.IrS1 in CD3+ and Tregs when incubated as PBMCs (Figure 3.5.2.1 and Table 3.5.2.1, Appendix 3.9.9). Both techniques showed CD4+, CD8+ and Tregs to have a split population of cells whereby only a percentage of the cells had taken up the Au25NP.Zonyl.IrS1.

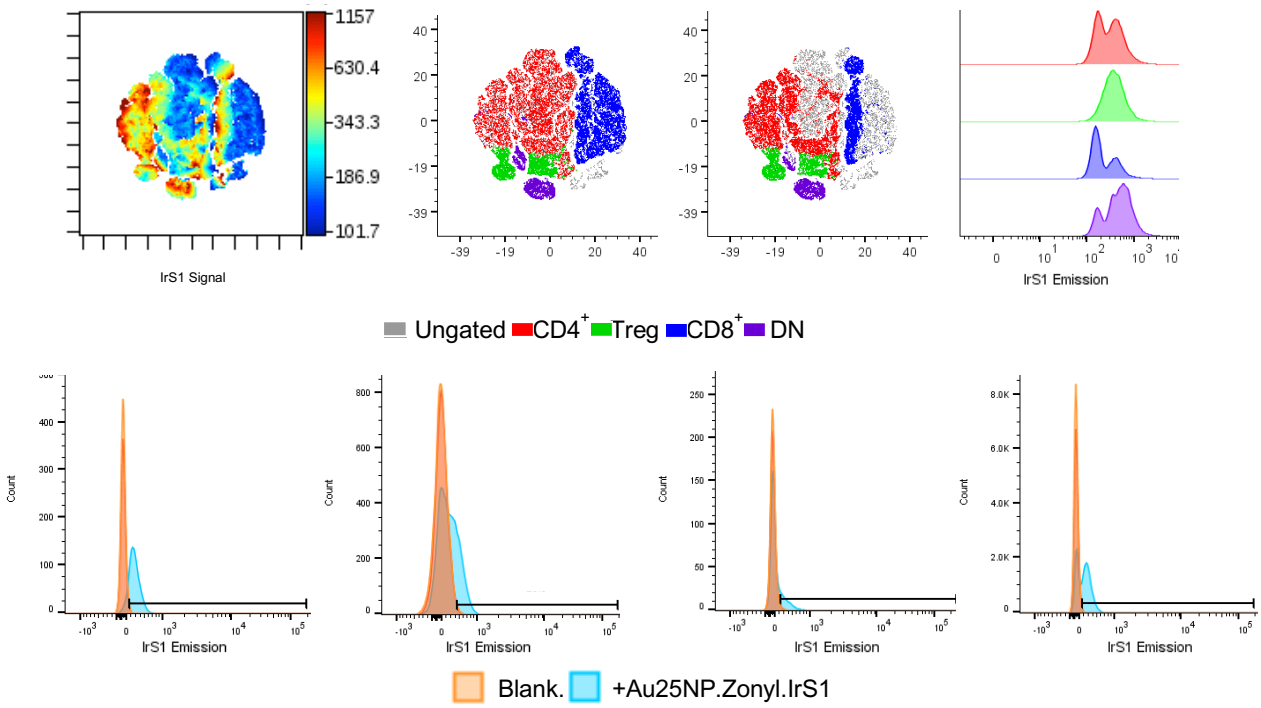

Fig 3.5.2.1 Top: CyTOF analysis to determine the percentage of cells showing nanoprobe uptake based on detection of gold atoms, Bottom: FACS analysis to determine the percentage of cells showing nanoprobe uptake based on IrS1 emission (λ_{ex} 405,nm λ_{em} 580nm) of PBMCs incubated with Au25NP.Zonyl.IrS1 at 1nM per 1 million cells.

Notably there are a variety of sub populations of cells present and so it can be expected that no one sub population would be favoured for uptake. However, both CyTOF and FACS showed Tregs to have the greatest percentage uptake of Au25NP.Zonyl.IrS1 even in this highly diverse collection of cells, which is noteworthy given Tregs constitute the smallest subpopulation of cells recorded (Table 3.5.2.1). Although there may be a slight indication of selectivity, it is not conclusive given other cell types also showed over 50% uptake of the nanoprobe. As CD8+ and CD4+ cells make up a greater proportion of the cells in a CD3+ population it is suggested there may be a greater scope for variation in uptake as seen by the CYTOF data showing a 40% and 50% uptake whereas FACS data shows a 20% and 20% uptake respectively. Further investigation of this experiment with CYTOF would provide clarification on the root cause of this variation and may provide information on whether this is a donor specific variance.

Table 3.5.2.1 CyTOF and FACS analysis to determine the percentage of cells showing nanoprobe uptake based on detection of gold atoms and IrS1 emission (λ_{ex} 405,nm λ_{em} 580nm) of PBMCs incubated with Au25NP.Zonyl.IrS1 at 1nM per 1 million cells.

Cell Sub-Type	% Cells with IrS1 with CYTOF	% Cells with IrS1 with FACS
Treg	80	90
CD8+	40	20
DN	60	60
CD4+	50	20

3.5.3 Post-Incubation Blank Cell Exposure Assay

When tracking CAR-T cells *in vivo*, one has to assume only the transplanted cells are being tracked for the entirety of the imaging process. It is, therefore, key to check the retention of Au25NP.Zonyl.IrS1 in cells when exposed to blank cells of different sub populations. Labelled CD3+ cells were exposed to blank CD3- cells and incubated for a further 4 hours, after which FACS was used to detect any IrS1 emission in the CD3- cells (Figure 3.5.3.1, Appendix 3.9.10).

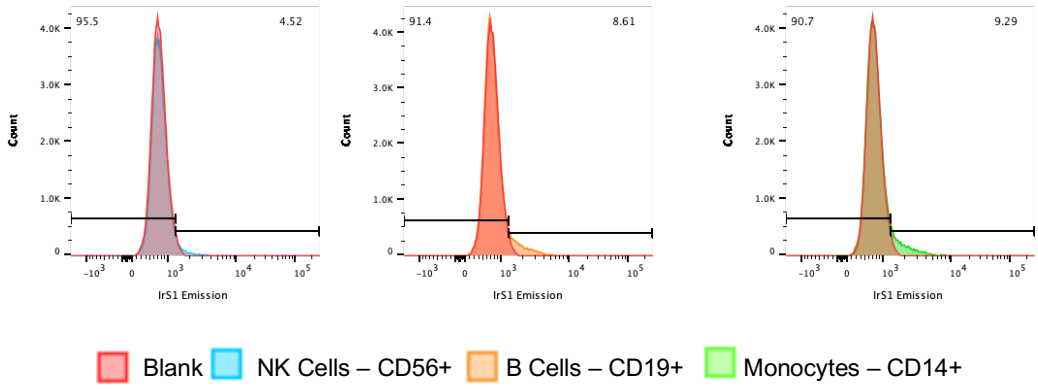

Fig 3.5.3.1 FACS analysis to determine the percentage of cells showing nanoprobe uptake based on IrS1 emission (λ_{ex} 405,nm λ_{em} 580nm) of CD3- cells post co-incubation with Au25NP.Zonyl.IrS1 labelled CD3+ cells at 1nM per 1 million cells.

5%, 9% and 9% of NK cells, B cells and Monocytes, respectively, showed slight emission where IrS1 emission would be expected, on average. It can be argued a small percentage of the emission detected may be attributed to the bleed through of antibody dyes used to label the cells. Nonetheless, the small percentage of IrS1 emission detected would be below the threshold for imaging *in vivo* and so could be considered negligible.

3.6 Conclusion

This chapter investigated the biocompatibility of the nanoprobe library, which funnelled down to the use of just Au25NP.Zonyl.IrS1. Cytotoxicity and uptake data supported the use of smaller gold nanoparticle cores, suggesting the larger particles were not taken up as well given the large amount of exogenous inorganic material entering the cells. ICP-MS data showed Au25NPs were able to carry larger amounts of IrS1 compared to Au13NPs and so an AuNP core size of 25nm was deemed the most effective.

Phenotypical behaviour of the cells, namely their ability to express cytokines and chemokines 'normally' whilst in the presence of the nanoprobes was analysed under stimulatory conditions and found the PEG coated nanoprobes may be interacting with the cells undesirably. PEG chains are known to network with cellular proteins and chemicals, which in other settings may be advantageous, however, for this work this was not the outcome required. As such, Au25NP.Zonyl.IrS1 proved to be the particles with the best uptake whilst allowing the cells to retain their regulatory functionality.

Au25NP.Zonyl.IrS1 labelled CD3+ cells were stimulated for proliferation and co-incubated with blank CD3- cells and displayed their ability to be selectively tracked even when the nanoprobe concentration gradient of the cells vs their surroundings is unfavourable. This finding is especially promising as it addresses a major challenge faced by exiting tracking probes and alludes to the fact that during imaging, the probe is retained in the cells and so true cell tracking can be achieved. They also displayed retention in their daughter cells. Therefore Au25NP.Zonyl.IrS1 was selected to be carried forward in experiments using labelled cells with liver tissue for imaging applications.

3.7 Materials and Methods

Venous blood was obtained from patients with hemochromatosis who were admitted to the Liver Unit at the Queen Elizabeth Hospital, Birmingham, UK (Local Research Ethics Committee reference no. 18/WA/0214). For each set of results, 5 different donor blood bags were used, and experiments carried out in triplicate.

All solutions, antibody kits, antibody dyes and chemicals were sourced from Thermo Fisher, Miltenyi Biotec, BD, BioLegend, Merck (Sigma) and Cedarlane Labs.

PBMC isolation

An aliquot volume of Lympholyte® was added into a 50ml tube equal to the volume of blood layered (i.e., Lympholyte® and blood at 1:1 volumes). The tube was held at 45° and the blood was layered on top of the Lympholyte® using a Stripette. Tubes were centrifuged (800 x g, 20min, acc = 5, dec = 3) so the plasma may be removed and the PBMC layer was extracted to a new 50ml tube. The PBMCs were then washed with PBS twice at (2000rpm, 10min, acc 9, brake 9) and (1100rpm, 5min, acc 9, brake 9). The cell pellet was then aspirated and resuspended in PBS/2%FCS/MACS buffer/Media as appropriate. The volume may change as appropriate and the expected total cell number is approximately 1million per ml of blood.

CD3+ isolation

CD3+ cells were isolated from PMBCs using the Miltenyi Biotec Pan T Cell Isolation Kit, human (130-096-535) following the manual magnetic labelling protocol and subsequent manual cell separation. PBMCs were suspended in buffer (PBS, pH 7.2, 0.5% bovine serum albumin and 2mM EDTA) at (40μl per 10^7 cells) before addition of the Pan T Cell Biotin-Antibody cocktail at (10μl per 10^7 cells) and incubation

for 5 minuets at 2-8^{o}C. Another aliquot of buffer was added to the cells at (30μl per 10^7 cells) along with Pan T Cell MicroBead Cocktail at (20μl per 10^7 cells) and incubated further for 10 minutes at 2-8^{o}C. An LS Column was placed into a magnetic field and the cells were passed through. The collected flow-through contained the unlabelled enriched T cells. The cell pellet was then aspirated and resuspended in PBS/2%FCS/MACS buffer/Media as appropriate. Cell numbers were estimated using Trypan Blue dead cell stain and a hemocytometer under a light microscope.

AuNP incubation

CD3+ cells were resuspended in RPMI Media (1640 Gibco) containing L-Glutamine (0.5%), PhenylStrep (0.5%) and Fetal Bovine Serum (FBS) (10%). Cells were plated in a 12 well plate at a concentration of 1 million cells per well. Nanoprobes were resuspended in 10% FBS Media before addition to each well. Total volume of each well was made to 3ml.

Antibody staining

Post incubation with nanoprobes, cells were washed and resuspended in PBS containing Zombie NIR™ (0.1%) and incubated in foil for 15 minutes. Cells were washed, resuspended in 2% FBS and incubated for 30 minuets on ice with the antibody dye panel selected for each experiment at concentration of 1% per antibody dye. Cells were then washed and resuspended in 200ul of 0.5% BSA Solution.

Cell fixing

Cells were fixed using 3% paraformaldehyde solution for 10 minutes before being resuspended in 1ml PBS.

Cytokine Stimulation

Post incubation with the nanoprobes, cells were stimulated with PMA (1/200 dilution) and Ionomycin (1/2000 dilution) for 1 hour, followed by Brefeldin A blocking (1/2000 dilution) for a 4-hour incubation. Cells were then washed and stained with surface markers and dead cell stains before fixing by the same protocol mentioned. Intracellular markers were stained using saponin permeabilization methods. Antibody dyes were diluted in 0.1% saponin at 1% concentration and incubated in cells for 30 minutes. Cells were then washed with 0.1% saponin and resuspended in PBS.

Proliferation assay

CD3+ cells were stimulated with T Cell activation beads and stained with VioTrace and allowed to proliferate for up to 6 generations. Cells were then washed and stained with surface markers and dead cell stains before fixing by the same protocol mentioned.

Cytof assay

Antibody Tags: CD4 (145Nd), CD8 (146Nd), CD25 (149Sm), CD45(89Y), CD3(154Sm) and CD127(176Yb) at ~0.1% PBS on ice were added to labelled cells post incubation with FC block (15 minutes) (blocks receptors found on CD3- cells to prevent additional binding which causes false positive results) and washed with cell staining medium. Rhodamine tag (1/2000 dilution) was added in addition to 2% paraformaldehyde to fix cells. Cells were frozen in 10% DMSO in preparation for running on CyTOF.

Co-incubation assay

Following the Pan T Cell Isolation for CD3+ cells, the column was flushed in order to collect the CD3- cells which were then used in the co-incubation with labelled CD3+ cells. Per well, 500,000 labelled CD3+ cells were added to 500,000 CD3- cells.

3.8 Instrumentation

3.8.1 Single Cell Analysis Techniques

FACS analysis was carried out on a BD LSR Fortessa X-20 Cell analyser using the antibody panel described in Appendix 3.9.11. The analyser has 5 lasers to detect up to 16 parameters simultaneously. The acquisition software is DIVA. The software for analysis was FlowJo version 10.6.2 and GraphPad Prism.

CyTOF® studies were conducted using a Helios™ Mass Cytometer - CyTOF®. The high performance mass cytometer enables the analysis of more than 40 markers and uniquely allows their quantitative determination with negligible spectral overlap, a result of exquisite resolution between mass detection channels. The software for analysis was Arc and FlowJo version 10.6.2.

3.9 Appendix

Gating for Cytotoxicity Assay

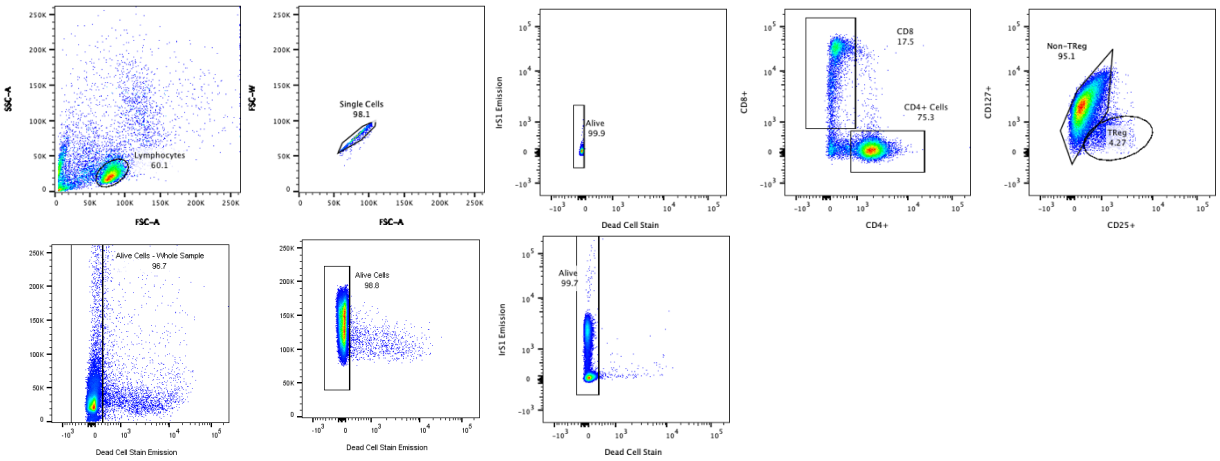

Fig 3.9.1 Gating strategy for cytotoxicity assay.

Gating for Uptake assay

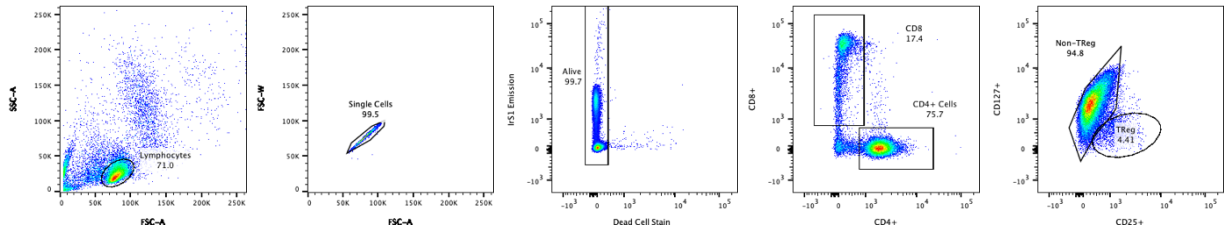

Fig 3.9.2 Gating strategy for uptake assay.

Gating for Time Course Assay

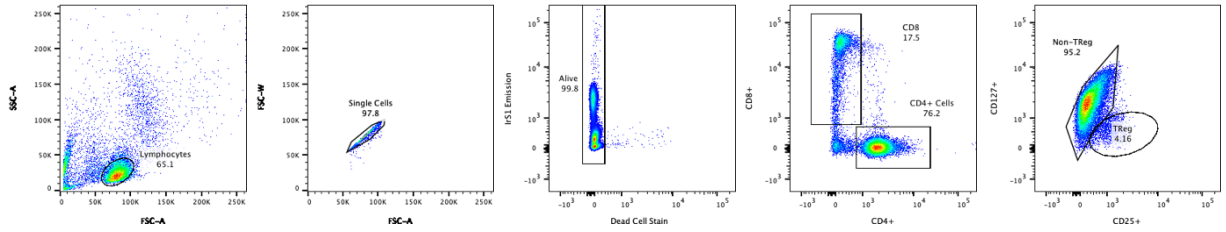

Fig 3.9.3 Gating strategy for Time course assay.

Gating for Chemokine Assay

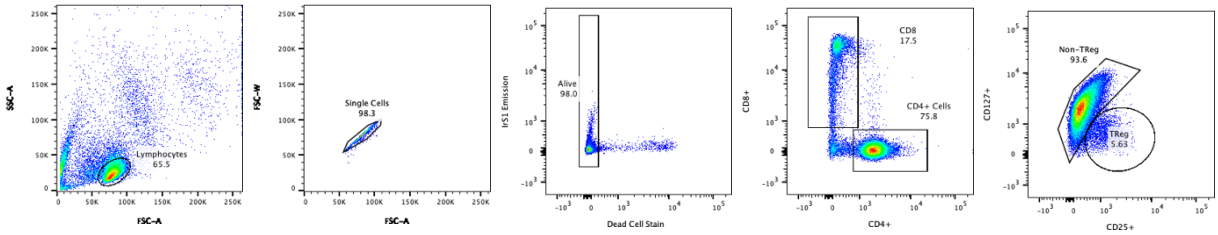

Fig 3.9.4 Gating strategy for chemokine assay.

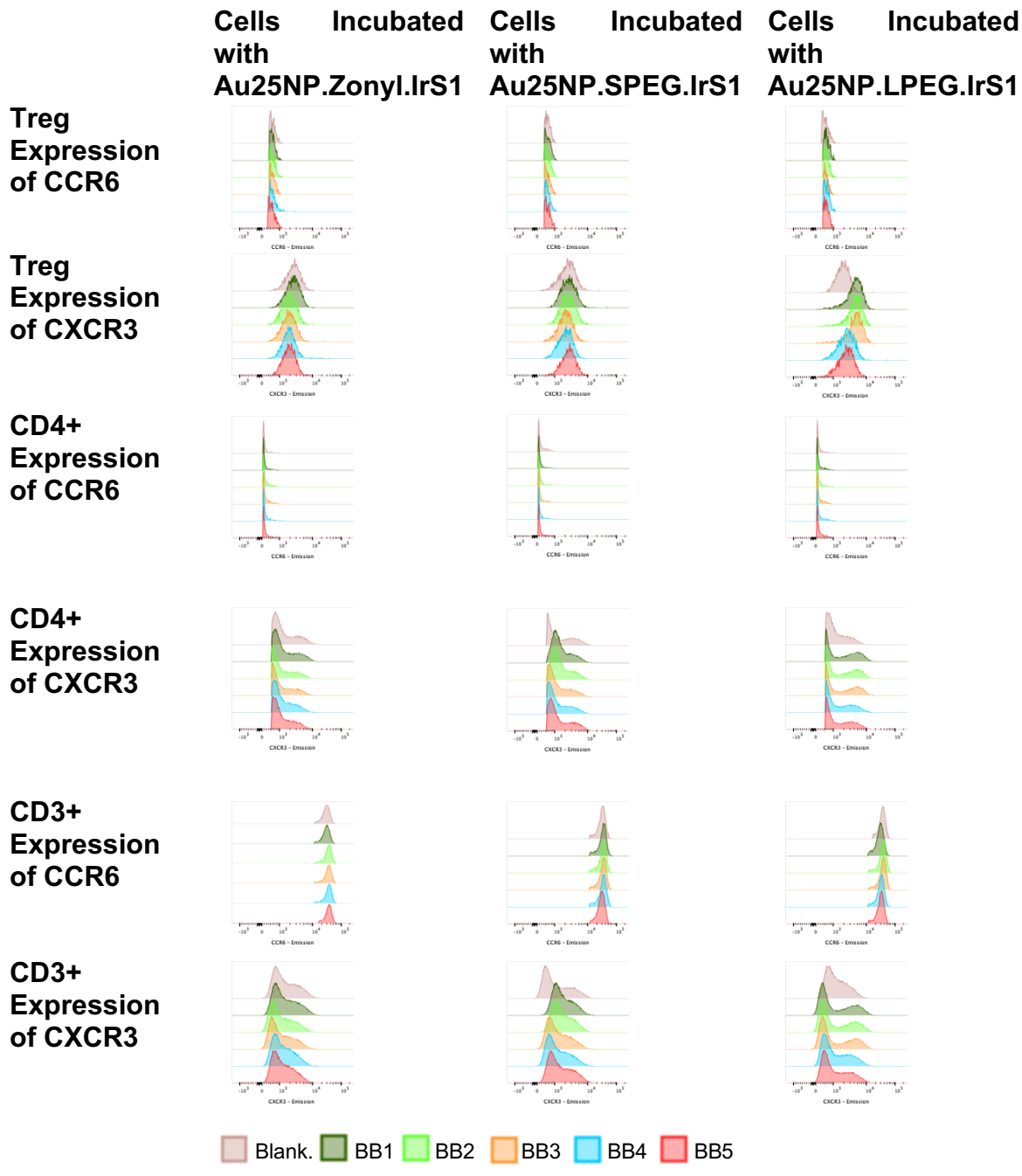

Fig 3.9.5 FACS histograms for chemokine assay.

Gating for Cytokine Assay

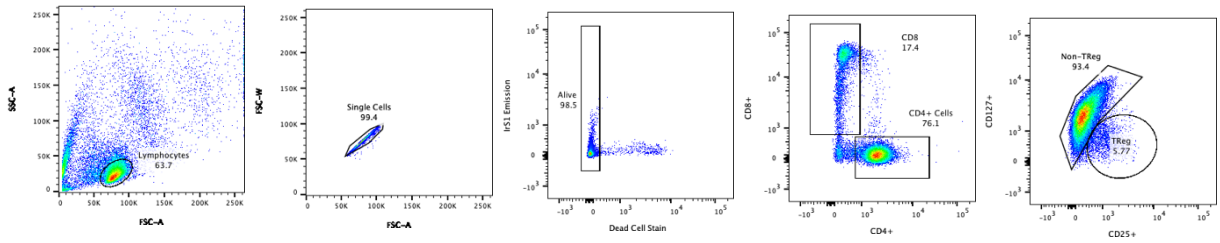

Fig 3.9.6 Gating strategy for cytokine assay.

	IL17 Expression	TNFα Expression	IFNγ Expression
Tregs incubated with Au25NP.Zonyl.IrS1	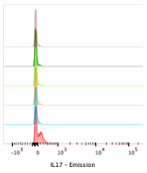	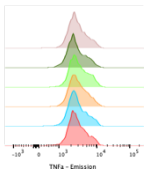	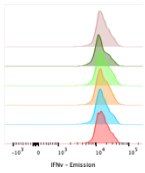
Tregs incubated with Au25NP.SPEG.IrS1	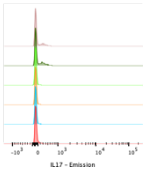	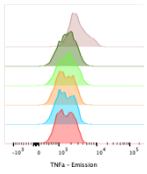	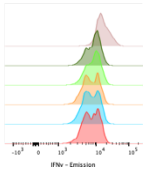
Tregs incubated with Au25NP.LPEG.IrS1	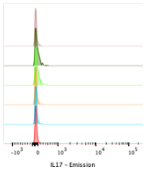	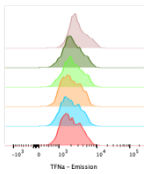	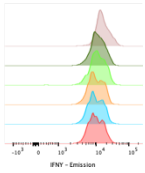
CD4+ cells incubated with Au25NP.Zonyl.IrS1	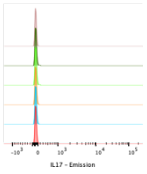	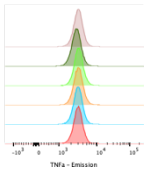	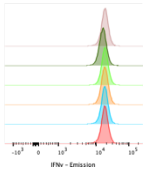
CD4+ cells incubated with Au25NP.SPEG.IrS1	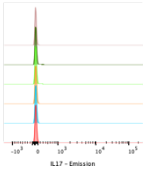	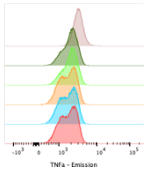	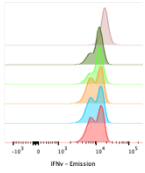
CD4+ cells incubated with Au25NP.LPEG.IrS1	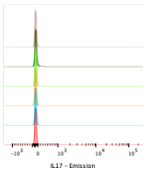	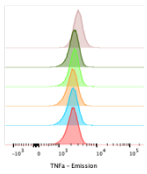	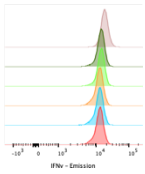

CD3+ cells incubated with Au25NP.Zonyl.IrS1

CD3+ cells incubated with Au25NP.SPEG.IrS1

CD3+ cells incubated with Au25NP.LPEG.IrS1

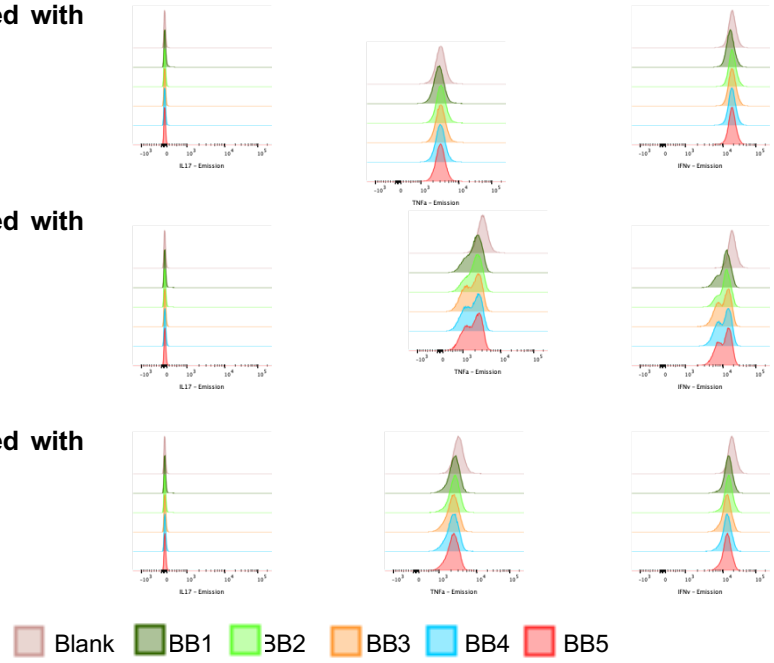

Fig 3.9.7 FACS histograms for cytokine assay.

Gating for Proliferation Assay

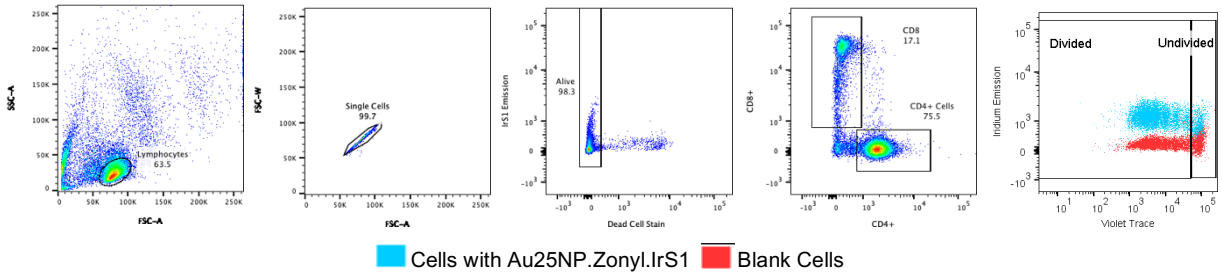

Fig 3.9.8 Gating strategy for proliferation assay.

Gating for CYTOF Assay

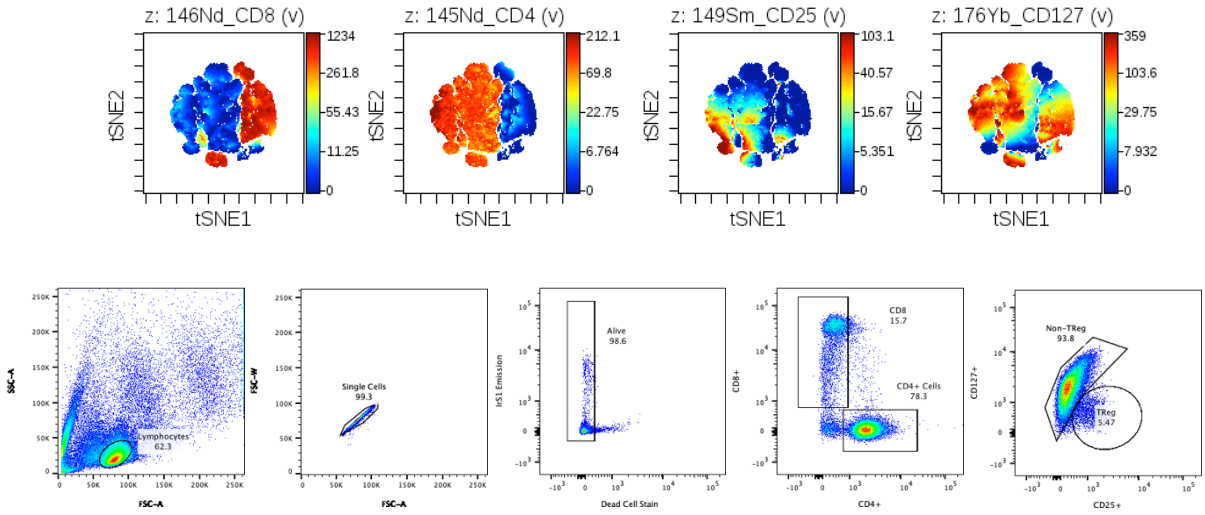

Fig 3.9.9 Gating strategy for Cytof assay.

Gating for Post-Incubation Blank Cell Exposure Assay

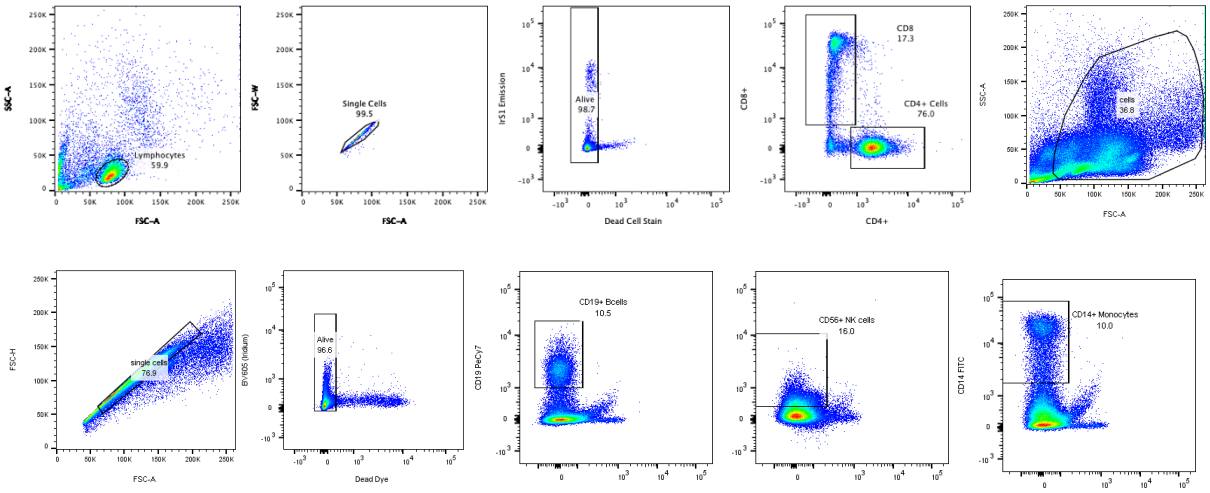

Fig 3.9.10 Gating strategy for post-incubation blank cell exposure assay.

Antibody Dyes

	Fluorophore	React	Isotype	$\lambda_{max\ (Ex)}$ - $\lambda_{max\ (Em)}$ / nm
CD4	BV650	Hu	Mouse IgG, κ	407 – 650
CD8	Per-CP	Hu	Mouse IgG, κ	482 – 678
CD25	BV421	Hu	Mouse IgG, κ	407 – 421
CD127	Pe-Cy7	Hu	Mouse IgG, κ	496 – 785
CCR6	Alexa Fluor 700	Hu	Mouse IgG, κ	696 – 719
CXCR3	BV421	Hu	Mouse IgG, κ	407 – 421
Il17	Pe-Cy7	Hu	Mouse IgG, κ	496 – 785
TNFα	Alexa Fluor 700	Hu	Mouse IgG, κ	696 – 719
IFNγ	BV421	Hu	Mouse IgG, κ	407 – 421
CD56	BV421	Hu	Mouse IgG, κ	407 – 421
CD19	PE-Cy7	Hu	Mouse IgG, κ	496 – 785
CD14	FITC	Hu	Mouse IgG, κ	488 – 525

Fig 3.9.11 Antibody dye staining panel.

3.10 References

1. Wagner, M.; Poeck, H.; Jahrsdoerfer, B.; Rothenfusser, S.; Prell, D.; Bohle, B.; Tuma, E.; Giese, T.; Ellwart, J. W.; Endres, S., IL-12p70-dependent Th1 induction by human B cells requires combined activation with CD40 ligand and CpG DNA. *The Journal of Immunology* **2004,** *172* (2), 954-963.
2. Finney, H. M.; Akbar, A. N.; Lawson, A. D., Activation of resting human primary T cells with chimeric receptors: costimulation from CD28, inducible costimulator, CD134, and CD137 in series with signals from the TCRζ chain. *The Journal of Immunology* **2004,** *172* (1), 104-113.
3. Faure, S.; Salazar-Fontana, L. I.; Semichon, M.; Tybulewicz, V. L.; Bismuth, G.; Trautmann, A.; Germain, R. N.; Delon, J., ERM proteins regulate cytoskeleton relaxation promoting T cell–APC conjugation. *Nature immunology* **2004,** *5* (3), 272-279.
4. Bukczynski, J.; Wen, T.; Ellefsen, K.; Gauldie, J.; Watts, T. H., Costimulatory ligand 4-1BBL (CD137L) as an efficient adjuvant for human antiviral cytotoxic T cell responses. *Proceedings of the National Academy of Sciences* **2004,** *101* (5), 1291-1296.
5. Hafsi, N.; Voland, P.; Schwendy, S.; Rad, R.; Reindl, W.; Gerhard, M.; Prinz, C., Human dendritic cells respond to Helicobacter pylori, promoting NK cell and Th1-effector responses in vitro. *The Journal of Immunology* **2004,** *173* (2), 1249-1257.
6. Mohseni, Y. R.; Tung, S. L.; Dudreuilh, C.; Lechler, R. I.; Fruhwirth, G. O.; Lombardi, G., The Future of Regulatory T Cell Therapy: Promises and Challenges of Implementing CAR Technology. *Frontiers in Immunology* **2020,** *11* (1608).
7. Jeffery, H. C.; Braitch, M. K.; Brown, S.; Oo, Y. H., Clinical potential of regulatory T cell therapy in liver diseases: an overview and current perspectives. *Frontiers in immunology* **2016,** *7*, 334.
8. Sakaguchi, S.; Sakaguchi, N.; Asano, M.; Itoh, M.; Toda, M., Immunologic self-tolerance maintained by activated T cells expressing IL-2 receptor alpha-chains (CD25). Breakdown of a single mechanism of self-tolerance causes various autoimmune diseases. *The Journal of Immunology* **1995,** *155* (3), 1151-1164.
9. Adams, D. H.; Ju, C.; Ramaiah, S. K.; Uetrecht, J.; Jaeschke, H., Mechanisms of immune-mediated liver injury. *Toxicological Sciences* **2010,** *115* (2), 307-321.
10. Oo, Y. H.; Banz, V.; Kavanagh, D.; Liaskou, E.; Withers, D. R.; Humphreys, E.; Reynolds, G. M.; Lee-Turner, L.; Kalia, N.; Hubscher, S. G., CXCR3-dependent recruitment and CCR6-mediated positioning of Th-17 cells in the inflamed liver. *Journal of hepatology* **2012,** *57* (5), 1044-1051.
11. Peiseler, M.; Sebode, M.; Franke, B.; Wortmann, F.; Schwinge, D.; Quaas, A.; Baron, U.; Olek, S.; Wiegard, C.; Lohse, A. W., FOXP3+ regulatory T cells in autoimmune hepatitis are fully functional and not reduced in frequency. *Journal of hepatology* **2012,** *57* (1), 125-132.
12. Vignali, D. A.; Collison, L. W.; Workman, C. J., How regulatory T cells work. *Nature reviews immunology* **2008,** *8* (7), 523-532.
13. Polansky, J. K.; Kretschmer, K.; Freyer, J.; Floess, S.; Garbe, A.; Baron, U.; Olek, S.; Hamann, A.; von Boehmer, H.; Huehn, J., DNA methylation controls Foxp3 gene expression. *European journal of immunology* **2008,** *38* (6), 1654-1663.
14. Toker, A.; Engelbert, D.; Garg, G.; Polansky, J. K.; Floess, S.; Miyao, T.; Baron, U.; Düber, S.; Geffers, R.; Giehr, P., Active demethylation of the Foxp3 locus leads to the

generation of stable regulatory T cells within the thymus. *The Journal of Immunology* **2013,** *190* (7), 3180-3188.
15. Trzonkowski, P.; Bieniaszewska, M.; Juścińska, J.; Dobyszuk, A.; Krzystyniak, A.; Marek, N.; Myśliwska, J.; Hellmann, A., First-in-man clinical results of the treatment of patients with graft versus host disease with human ex vivo expanded CD4+ CD25+ CD127− T regulatory cells. *Clinical immunology* **2009,** *133* (1), 22-26.
16. Caramalho, Í.; Nunes-Cabaço, H.; Foxall, R. B.; Sousa, A. E., Regulatory T-cell development in the human thymus. *Frontiers in immunology* **2015,** *6*, 395.
17. Kretschmer, K.; Apostolou, I.; Hawiger, D.; Khazaie, K.; Nussenzweig, M. C.; von Boehmer, H., Inducing and expanding regulatory T cell populations by foreign antigen. *Nature immunology* **2005,** *6* (12), 1219-1227.
18. Romano, M.; Fanelli, G.; Albany, C. J.; Giganti, G.; Lombardi, G., Past, present, and future of regulatory T cell therapy in transplantation and autoimmunity. *Frontiers in immunology* **2019,** *10*, 43.
19. Spinelli, E.; Caporale, R.; Buchi, F.; Masala, E.; Gozzini, A.; Sanna, A.; Sassolini, F.; Valencia, A.; Bosi, A.; Santini, V., Distinct signal transduction abnormalities and erythropoietin response in bone marrow hematopoietic cell subpopulations of myelodysplastic syndrome patients. *Clinical Cancer Research* **2012,** *18* (11), 3079-3089.
20. Colasanti, T.; Alessandri, C.; Capozzi, A.; Sorice, M.; Delunardo, F.; Longo, A.; Pierdominici, M.; Conti, F.; Truglia, S.; Siracusano, A., Autoantibodies specific to a peptide of β2-glycoprotein I cross-react with TLR4, inducing a proinflammatory phenotype in endothelial cells and monocytes. *Blood, The Journal of the American Society of Hematology* **2012,** *120* (16), 3360-3370.
21. Pievani, A.; Belussi, C.; Klein, C.; Rambaldi, A.; Golay, J.; Introna, M., Enhanced killing of human B-cell lymphoma targets by combined use of cytokine-induced killer cell (CIK) cultures and anti-CD20 antibodies. *Blood, The Journal of the American Society of Hematology* **2011,** *117* (2), 510-518.
22. Oo, Y. H.; Ackrill, S.; Cole, R.; Jenkins, L.; Anderson, P.; Jeffery, H. C.; Jones, N.; Jeffery, L. E.; Lutz, P.; Wawman, R. E.; Athwal, A. K.; Thompson, J.; Gray, J.; Guo, K.; Barton, D.; Hirschfield, G. M.; Wong, T.; Guest, P.; Adams, D. H., Liver homing of clinical grade Tregs after therapeutic infusion in patients with autoimmune hepatitis. *Journal of hepatology Reports* **2019,** *1* (4), 286-296.
23. Bluestone, J. A.; Buckner, J. H.; Fitch, M.; Gitelman, S. E.; Gupta, S.; Hellerstein, M. K.; Herold, K. C.; Lares, A.; Lee, M. R.; Li, K., Type 1 diabetes immunotherapy using polyclonal regulatory T cells. *Science translational medicine* **2015,** *7* (315), 315ra189-315ra189.
24. Thomson, A. W.; Turnquist, H. R.; Raimondi, G., Immunoregulatory functions of mTOR inhibition. *Nature Reviews Immunology* **2009,** *9* (5), 324-337.
25. Mathew, J. M.; Jessica, H.; LeFever, A.; Konieczna, I.; Stratton, C.; He, J.; Huang, X.; Gallon, L.; Skaro, A.; Ansari, M. J., A phase I clinical trial with ex vivo expanded recipient regulatory T cells in living donor kidney transplants. *Scientific Reports* **2018,** *8* (1), 1-12.
26. Schmidt, A.; Oberle, N.; Krammer, P. H., Molecular mechanisms of treg-mediated T cell suppression. *Frontiers in immunology* **2012,** *3*, 51.
27. Tang, Q.; Boden, E. K.; Henriksen, K. J.; Bour-Jordan, H.; Bi, M.; Bluestone, J. A., Distinct roles of CTLA-4 and TGF-β in CD4+ CD25+ regulatory T cell function. *European journal of immunology* **2004,** *34* (11), 2996-3005.

28. Huang, C.-T.; Workman, C. J.; Flies, D.; Pan, X.; Marson, A. L.; Zhou, G.; Hipkiss, E. L.; Ravi, S.; Kowalski, J.; Levitsky, H. I., Role of LAG-3 in regulatory T cells. *Immunity* **2004,** *21* (4), 503-513.
29. Yan, Z.; Garg, S. K.; Banerjee, R., Regulatory T cells interfere with glutathione metabolism in dendritic cells and T cells. *Journal of Biological Chemistry* **2010,** *285* (53), 41525-41532.
30. Tiemessen, M. M.; Jagger, A. L.; Evans, H. G.; van Herwijnen, M. J.; John, S.; Taams, L. S., CD4+ CD25+ Foxp3+ regulatory T cells induce alternative activation of human monocytes/macrophages. *Proceedings of the national academy of sciences* **2007,** *104* (49), 19446-19451.
31. Romano, M.; Fanelli, G.; Tan, N.; Nova-Lamperti, E.; McGregor, R.; Lechler, R. I.; Lombardi, G.; Scottà, C., Expanded regulatory T cells induce alternatively activated monocytes with a reduced capacity to expand T helper-17 cells. *Frontiers in immunology* **2018,** *9*, 1625.
32. Gotot, J.; Gottschalk, C.; Leopold, S.; Knolle, P. A.; Yagita, H.; Kurts, C.; Ludwig-Portugall, I., Regulatory T cells use programmed death 1 ligands to directly suppress autoreactive B cells in vivo. *Proceedings of the National Academy of Sciences* **2012,** *109* (26), 10468-10473.
33. Iikuni, N.; Lourenço, E. V.; Hahn, B. H.; La Cava, A., Cutting edge: regulatory T cells directly suppress B cells in systemic lupus erythematosus. *The Journal of Immunology* **2009,** *183* (3), 1518-1522.
34. Lewkowicz, N.; Klink, M.; Mycko, M. P.; Lewkowicz, P., Neutrophil–CD4+ CD25+ T regulatory cell interactions: a possible new mechanism of infectious tolerance. *Immunobiology* **2013,** *218* (4), 455-464.
35. Chinen, A. B.; Guan, C. M.; Ko, C. H.; Mirkin, C. A., The impact of protein corona formation on the macrophage cellular uptake and biodistribution of spherical nucleic acids. *Small* **2017,** *13* (16), 1603847.
36. Melby, E. S.; Lohse, S. E.; Park, J. E.; Vartanian, A. M.; Putans, R. A.; Abbott, H. B.; Hamers, R. J.; Murphy, C. J.; Pedersen, J. A., Cascading effects of nanoparticle coatings: Surface functionalization dictates the assemblage of complexed proteins and subsequent interaction with model cell membranes. *Journal of the American chemical society nano* **2017,** *11* (6), 5489-5499.
37. Mirshafiee, V.; Kim, R.; Park, S.; Mahmoudi, M.; Kraft, M. L., Impact of protein pre-coating on the protein corona composition and nanoparticle cellular uptake. *Biomaterials* **2016,** *75*, 295-304.
38. King, S. M.; Claire, S.; Teixeira, R. I.; Dosumu, A. N.; Carrod, A. J.; Dehghani, H.; Hannon, M. J.; Ward, A. D.; Bicknell, R.; Botchway, S. W., Iridium Nanoparticles for Multichannel Luminescence Lifetime Imaging, Mapping Localization in Live Cancer Cells. *Journal of the American Chemical Society* **2018,** *140* (32), 10242-10249.

Chapter 4:

Luminescent Iridium coated Gold nanoparticles: Imaging in Immune Cells and in Liver Tissue

4.1 Chapter Summary

The experiments detailed in this chapter were designed to investigate the detectability and imaging properties of the nanoprobes developed to test their ability to be used as tracking agents when administered to CD3+ cells. Transition electron microscopy was implemented to check the viability of the AuNPs prior to cell labelling and was then also utilised to examine labelled cells. This investigation provided information on the uptake of the nanoprobes by the cells and was instrumental in the decision to narrow the probe library further by supporting the use of only Au25NP.Zonyl.IrS1 for liver tissue studies.

This chapter will also detail human liver tissue imaging using multiphoton microscopy and micro-CT of sections post administration with labelled and unlabelled CD3+ cells. The images obtained suggest the multimodal nature of the probe developed has been successful as both techniques displayed regions of high light intensity attributed to either the IrS1 fluorophore or X-ray attenuation of the AuNPs.

The specific combination of imaging techniques employed in this work, transition electron microscopy, confocal microscopy, multiphoton microscopy and micro-CT, have provided information from a sub-cellular level, with the localisation of the nanoprobes, to the tracking of cells in thick sections of liver tissue.

4.1.1 Introduction

Studies have shown the liver can be imaged with most standard microscopes[1]. Confocal microscopy historically has major applications in the field of biomedical sciences and may be applied to both fixed and living tissues that have been successfully labelled with a fluorescent probe. With conventional light microscopes, fluorescence in samples from all focal planes interfere with the resolution of structures in the region of interest being imaged, reducing their focus[2]. Confocal microscopy allows for a slight increase in both the lateral and axial resolution of the imaging region. Illumination of a confocal microscope is achieved by scanning one or more focused beams of light from a laser across the sample (Figure 4.1.1) [1, 3].

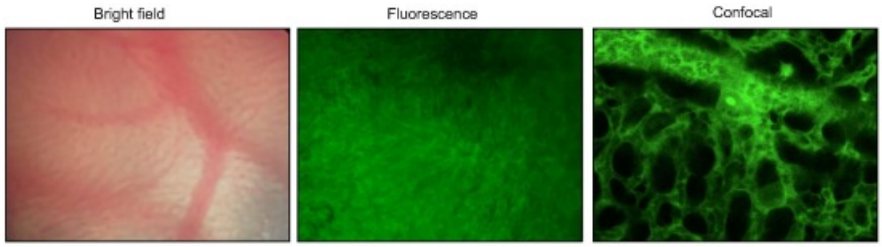

Fig. 4.1.1 Liver intravital microscopy of mouse liver performed using different imaging modalities, injected with 5mg of FITC-conjugated albumin[1]
(Figure taken from reference 1)

During widefield fluorescence imaging, the sample tissue is primarily illuminated by a block of excitation light as it is simultaneously focused on the targeted sample plane resulting in multiple focal planes being excited above and below the plane of interest. Following excitation of multiple planes, these then all emit light, negatively impacting the resultant image[4]. The pinhole adaptation applied in confocal microscopy rejects light emitted from any plane other than that in the same focal plane as the detector. Bright field microscopy may be sufficient in evaluating general leukocyte trafficking and behaviour, however, to understand mechanisms of specific cell types, which require the use of fluorescent antibodies, a deeper mechanistic approach may be required. Laser scanning confocal microscopy is ideal for moderate

tissue penetration while maintaining thin optical sections and provides an opportunity to optimize the pinhole size for a variety of objective lenses. Nonetheless, image acquisition by laser scanning results in longer acquisition times that impedes examination of processes that occur in real time. This prolonged exposure to the lasers results in a high sample toxicity and photobleaching effect.

Multiphoton imaging is an advanced and more powerful form of confocal imaging in which focally limited imaging is achieved in the absence of a pinhole[4]. Multiphoton microscopy employs pulse lasers to produce a stream of infrared photons which are lower in energy than their non-infrared counterparts. As such, a near simultaneous absorption of two photons per fluorophore is required to excite the fluorophore, using wavelengths much longer (infrared) than those used in confocal microscopy[5].

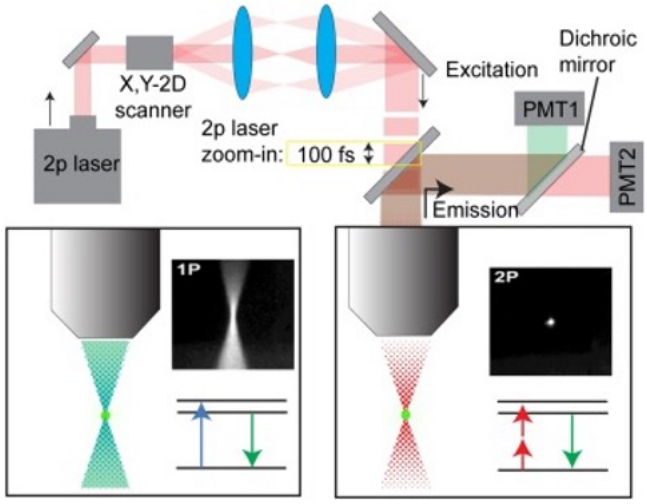

Fig. 4.1.2 Schematic layout of a multiphoton microscope and comparison with a confocal distribution of fluorescence in the x-z plane during one photon excitation[6]
(Figure taken from reference 6)

The beam is focused through the microscope optics causing the photons to be closer in space, increasing the chance that two photons may be absorbed by a single fluorophore (Figure 4.1.2)[6]. This design means that there is a small volume downstream of the objective, in the focal plane, where the probability of two photons

exciting the same fluorophore is sufficiently high enough that excitation can occur, ultimately resulting in the excitation of fluorophores which are in the focal plane only.[7].

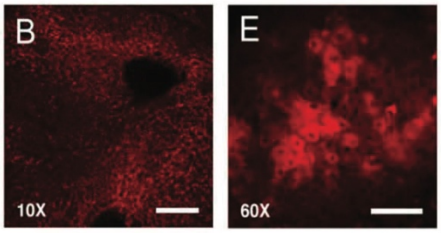

Fig. 4.1.3 Multiphoton microscopy of human fibrotic liver, $\lambda_{(excitation)}$ 810nm[7]
(Figure taken from reference 7)

Similar to confocal, multiphoton microscopy operates in a point-scanning mode, which works across the sample in a pixel-by-pixel approach. These attributes make multiphoton microscopy ideal for deep tissue penetration so thicker samples, like livers (Figure 4.1.3), may be imaged and because excitation only occurs at the focal plane, sample integrity is maintained, minimizing photobleaching over the whole sample[7, 8]. However, it can be difficult to image multiple colours using a multiphoton microscope due to the lack of dye and laser combinations available so confocal microscopy can be a good first-in-line method to narrow the imaging window prior to multiphoton imaging. Multiphoton imaging has been successfully applied to visualise tumorigenesis, angiogenesis and their related deep tissue processes that were previously difficult to analyse due to inefficient fluoresce techniques available[9, 10].

Interestingly, the strong surface plasmon resonance of AuNPs has shown to enhance the multiphoton imaging effect in samples containing AuNPs[11]. Dur *et al* labelled cancer cells with gold nanorods with an aspect ratio of 3.4$\pm$0.6 by modifiying the anti-EGFR antibody on the cell surface (Figure 4.1.4)[12]. The group were able to visualise the cells clearly at an excitation wavelength of 760nm.

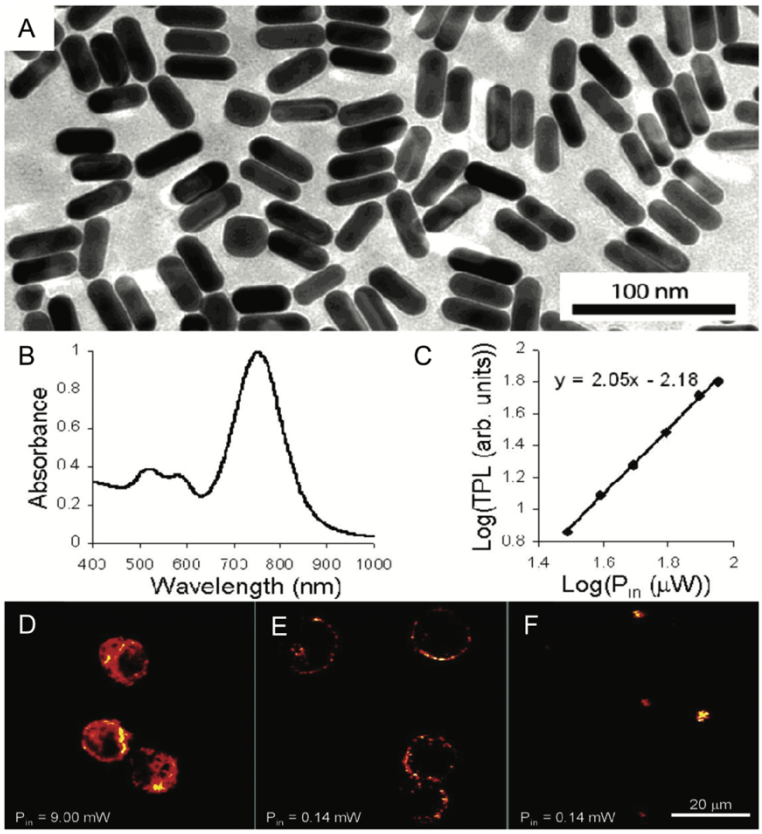

Fig. 4.1.4 A) TEM image of Au NRs. (B) Absorption spectrum of an Au NR aqueous dispersion. (C) Linear fitting of the excitation power-dependent emission intensity (λ_{ex} = 760 nm) function of the Au NR. (D) A multiphoton image of unlabelled cancer cells. Excitation power = 9mW. (E) A multiphoton image of Au NR-labelled cancer cells. Excitation power = 140 μW. (F) An MPM image of non-specifically labelled cells. Excitation power = 140 μW[12]
(Figure taken from reference 12)

However, the translation of using gold nanoparticles for multiphoton imaging to clinical application has not yet occurred due to several factors including the lack of animal studies conducted which will allow for a full analysis on the safety and durability of the technique. Furthermore, it is predicted that there may be a thermal effect experienced on tissue samples as a result of multiphoton excitation which would be damaging to surrounding tissue[13]. Research into the most biocompatible preparations of the AuNPs with different coatings and compositions is needed before clinical application.

An established imaging technique which utilises gold nanoparticles in cell tracking is computed tomography (CT)[14]. AuNPs have a high X-ray absorption coefficient, approximately 2.5 times greater than that of existing iodine agents,

affording an 88% contrast enhancement of samples containing AuNPs at low energies (Figure 4.1.5)[15]

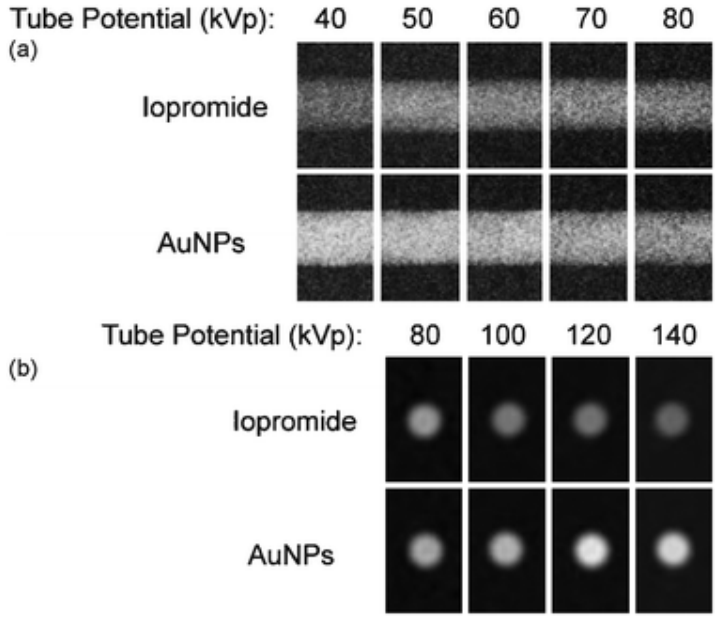

Fig. 4.1.5 Images of contrast phantoms containing AuNPs and iopromide with exposures recorded at different tube potentials at low and high energies[15]
(Figure taken from reference 15)

Given that gold is more dense than iodine, AuNPs result in a much higher attenuation of the X-ray beam, this in addition to the excitation of the surface electrons by the X-ray leads to a superior contrast in images when compared to iodine based contrast agents[16, 17].

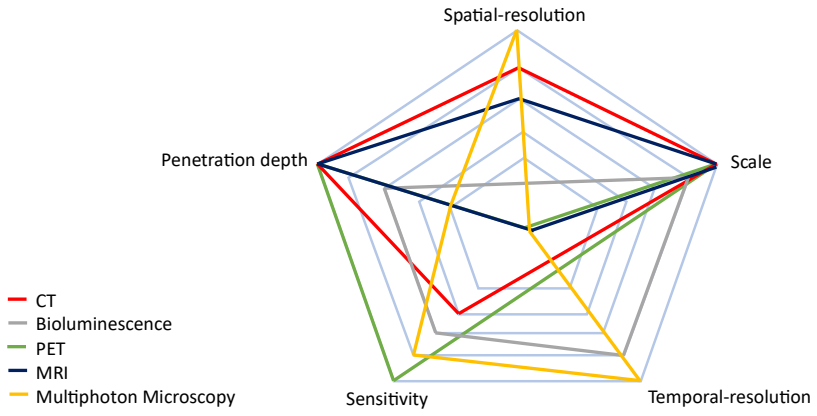

Fig. 4.1.6 A comparison of different imaging modalities. Outermost is the best and center is the worst[6]

Long term intravital tracking of single cells will allow scientists to gain an unique insight into the longitudinal changes in the morphology, migration and function of cells in clinical therapies[6]. The main challenge currently is the availability of technology available. Multimodal imaging is the most attractive way forward owing to the fact it pulls together the advantages of more than one imaging technique. Multiphoton microscopy enhances the sensitivity, temporal resolution and spatial resolution achieved by confocal microscopy and CT provides the penetration depth and scalability required to move cell tracking into a more clinical setting (Figure 4.1.6)[18, 19].

4.2 Imaging of Nanoprobes within CD3+ Cells

FACS analysis confirmed CD3+ cells, especially Tregs, were effectively labelled with the nanoprobes developed. However, FACS does not provide qualitative information on the type of labelling experienced by the cells. Transition electron microscopy (TEM) is used to investigate whether the nanoprobes had either entered the cells or were attached to surface receptors on the outside of the cell. Studies have looked at the uptake of fluorescent gold nanoparticles into a variety of cells and discuss the most likely pathway of uptake is either receptor mediated endocytosis or pinocytosis[20]. Although either of the processes mentioned could be applicable, the research here is novel due the combination of variables under investigation, including cell type, nanoparticle size, coating and iridium probe, and as such TEM was used to confirm the internalisation of the nanoprobes. Firstly, images of the gold nanoparticles independently were characterised (Figures a,b and c in 4.2.1, 4.2.2 and 4.2.3).

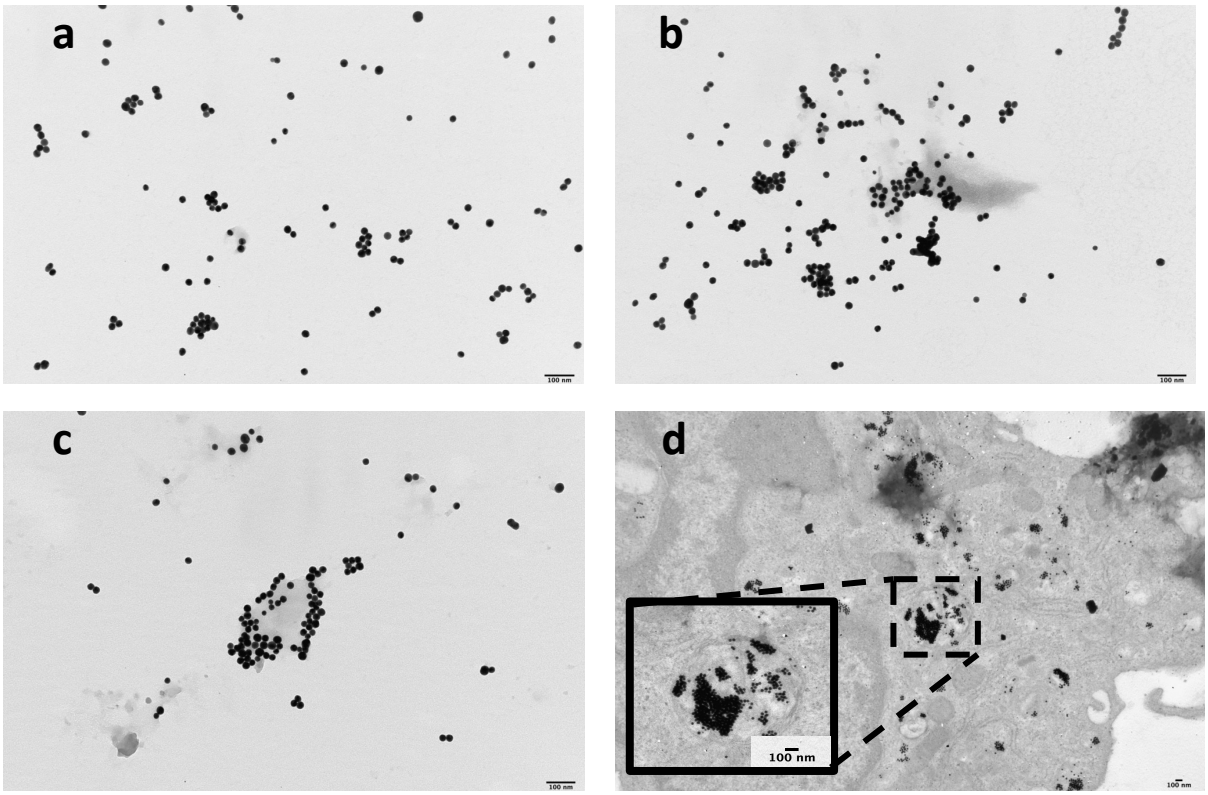

Fig 4.2.1 TEM of a) Citrate coated Au25NPs, b) Zonyl coated Au25NPs, c) Au25NPs.Zonyl.IrS1 and d) CD3+ cells post incubation with Au25NP.Zonyl.IrS1. Image analysis performed by ImageJ, giving average size of Au25NPs as ~26nm$\pm$3nm. Scale Bar = 100nm

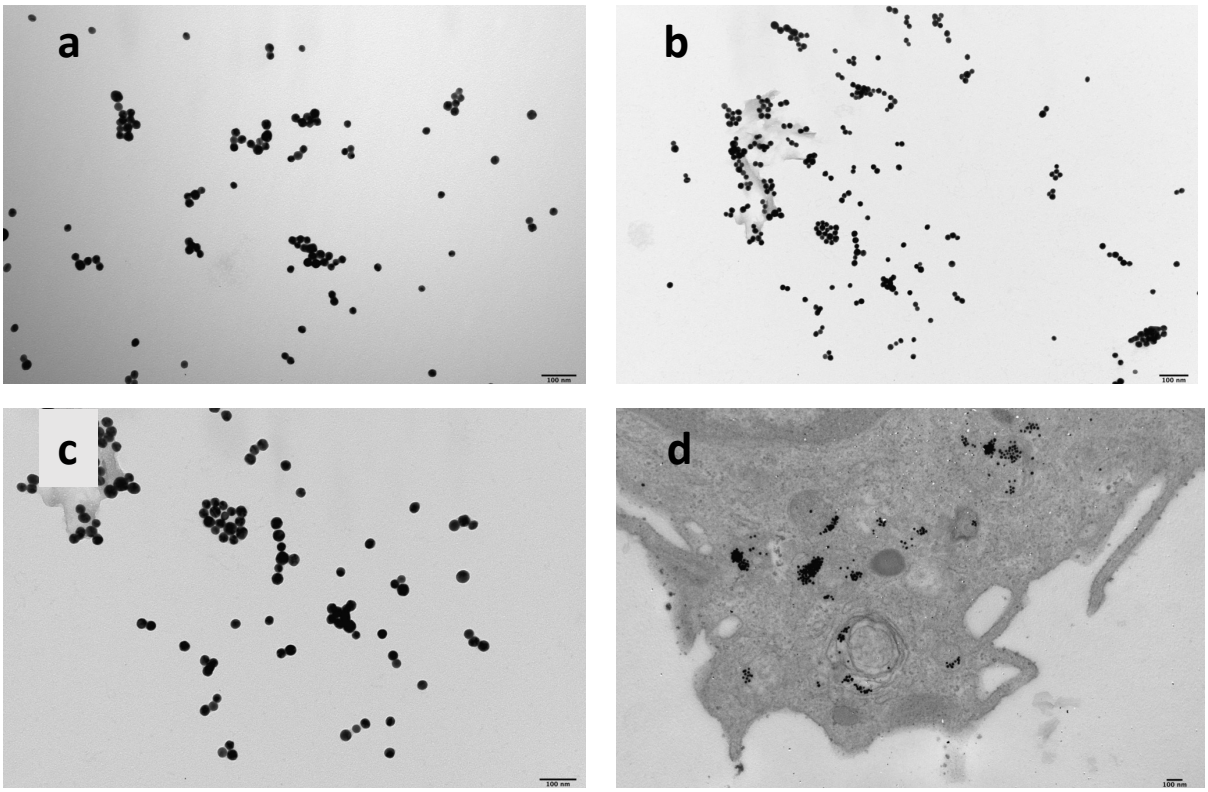

Fig 4.2.2 TEM of a) Citrate coated Au25NPs, b) SPEG coated Au25NPs, c) Au25NPs.SPEG.IrS1 and d) CD3+ cells post incubation with Au25NP.SPEG.IrS1. Image analysis performed by ImageJ, giving average size of Au25NPs as ~26nm±3nm. Scale Bar = 100nm

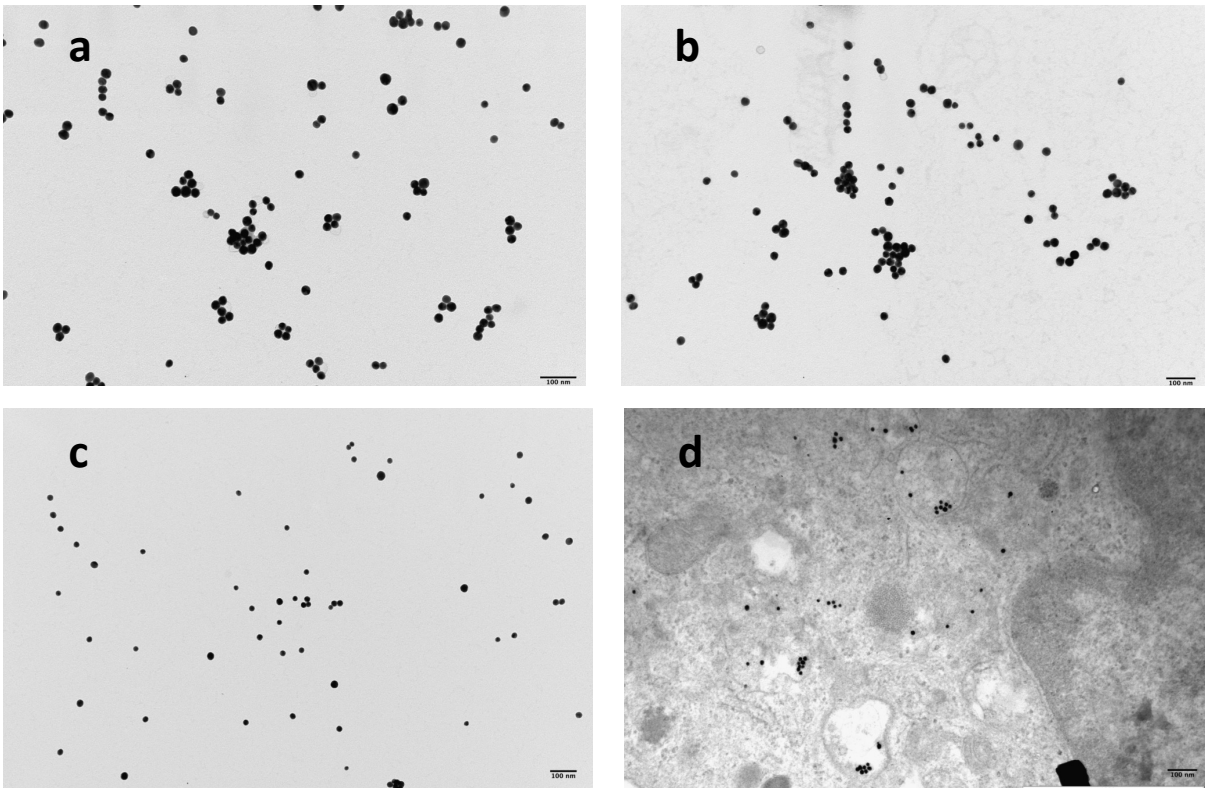

Fig 4.2.3 TEM of a) Citrate coated Au25NPs, b) LPEG coated Au25NPs, c) Au25NPs.LPEG.IrS1 and d) CD3+ cells post incubation with Au25NP.LPEG.IrS1. Image analysis performed by ImageJ, giving average size of Au25NPs as ~26nm±3nm. Scale Bar = 100nm

Post-acquisition image analysis showed the gold nanoparticle average size to be 25nm±3nm. Clearly identifiable, monodisperse Au25NPs were seen after each stage of coating, confirming the addition of Zonyl, SPEG, LPEG and IrS1 had not caused excessive aggregation of the AuNPs.

CD3+ cells were then incubated with all three nanoprobes and fixed for analysis with TEM (Figures d in 4.2.1, 4.2.2 and 4.2.3) and Confocal Microscopy (Figure 4.2.4). TEM image analysis showed nanoparticles clustering inside the cells for each of the nanoprobes under investigation. Although no organelle specific stains were used, it is visible that the majority of nanoparticles are encapsulated within circular structures, shifting the likelihood that receptor mediated endocytosis could be the uptake pathway utilised here. Closer analysis also shows some smaller groups of nanoparticles, as well as individual nanoparticles, suggesting some may have been taken up through pinocytosis. A control group of CD3+ cells which hadn't been exposed to any nanoprobes was also imaged and showed no spherical dark structures (Appendix 4.8.1a). In agreements in ICP-MS data and fluorescence studies in chapter three, the cells incubated with Au25NP.LPEG.IrS1 showed the least amount of nanoparticles per image and also showed the presence of nanoparticles on the outside of the cells supporting the idea that the LPEG coated particles were less readily taken up in comparison to the two other nanoprobes investigated (Appendix 4.8.1b).

Confocal microscopy showed the detection of both the IrS1 in the λ_{ex} 405nm, λ_{em} 550-620nm channel and the Au25NPs in the reflectance channel, λ_{ex} 633nm, λ_{em} 633nm. Darkfield light scattering reflectance of gold nanoparticles in confocal microscopy is achieved due to the SPR at the surface of the gold nanoparticles[21]. This nature of detection is largely size dependant as the larger nanoparticles will afford a

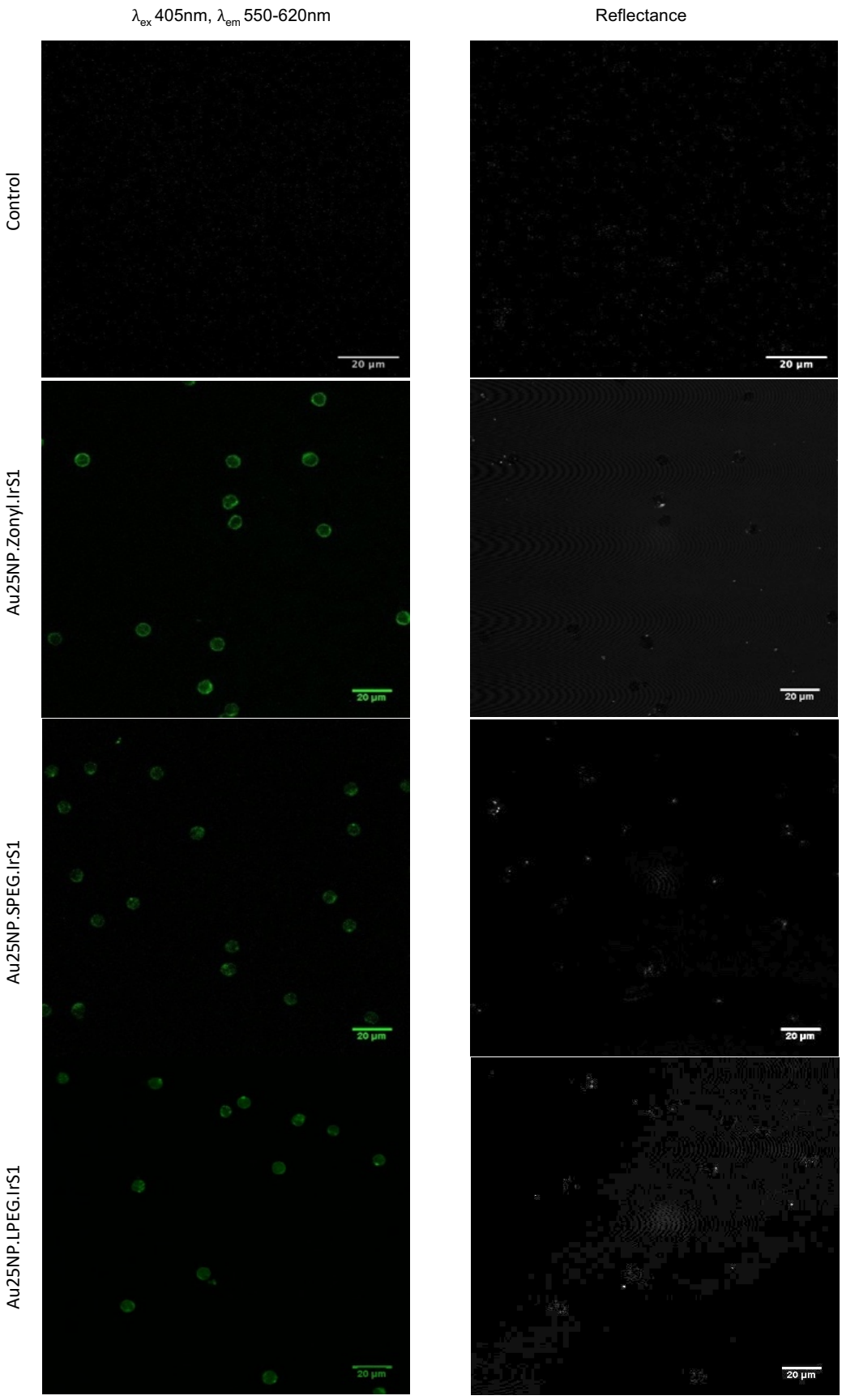

Fig 4.2.4 (Left Column) Confocal Microscopy images of CD3+ cells post incubation with Au25NP nanoprobes, λ_{ex} 405nm, λ_{em} 550-620nm and (Right Column) Reflectance of Au25NPs in the nanoprobes of cells incubated with each nanoprobe, λ_{ex} 633nm, λ_{em} 633nm. Image analysis performed by ImageJ. Scale bar = 20μm

greater signal, however slight reflectance can be observed for Au25NPs which co-localise with the fluorescence of IrS1.

Henceforth, liver tissue studies with multiphoton microscopy and micro-CT were performed with Au25NP.Zonyl.IrS1 only, based on data collected from ICP-MS, FACS and TEM.

4.3 Imaging of Au25NP.Zonyl.IrS1 in Labelled CD3+ Cells Administered to Liver Sections using Multiphoton Microscopy

As previously mentioned, multiphoton microscopy has the advantage of imaging larger and thicker tissue samples compared with confocal microscopy. To investigate the detectability of the nanoprobe, CD3+ cells incubated with Au25NP.Zonyl.IrS1 were fixed to slides and imaged under the multiphoton microscope. Emission was collected within the 575-645nm band, whilst excitation was varied between 800 to 900nm at 10nm intervals. Ultimately the 800nm excitation wavelength was selected, although not much variation was seen between the wavelengths. Figure 4.3.1 shows the images produced at λ_{ex} 800nm, λ_{em} 575-645nm, with FV30 FGR filter for both control cells and cells incubated with Au25NP.Zonyl.IrS1.

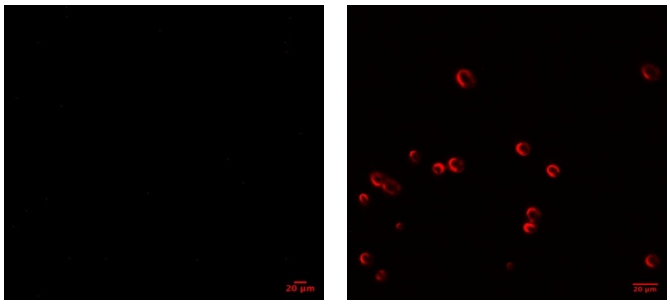

Fig 4.3.1 Left: Blank CD3+ cells. Right: CD3+ cells incubated with Au25NP.Zony.IrS1. λ_{ex} 800nm, λ_{em} 575-645nm. Image analysis performed by ImageJ. Scale bar = 20μm

As the detectability assay proved successful with the visualisation of the CD3+ cells compared to the control blank cells, it was deemed viable to continue with the investigation with human liver sections and labelled cells. Human liver wedge samples were isolated and cut into 5 subsections and placed into individual wells in a 6-well plate with RMPI cell media for incubation with Au25NP.Zonyl.IrS1 labelled cells. One subsection was incubated with control cells which contained no Au25NP.Zonyl.IrS1. Cells were administered, using a pipette, directly into visible blood vessels in the tissue

wedges (Figure 4.3.2). Cells were allowed to disperse into the liver sections for up to 2, 4, 8 and 24 hours before the tissue was fixed for imaging.

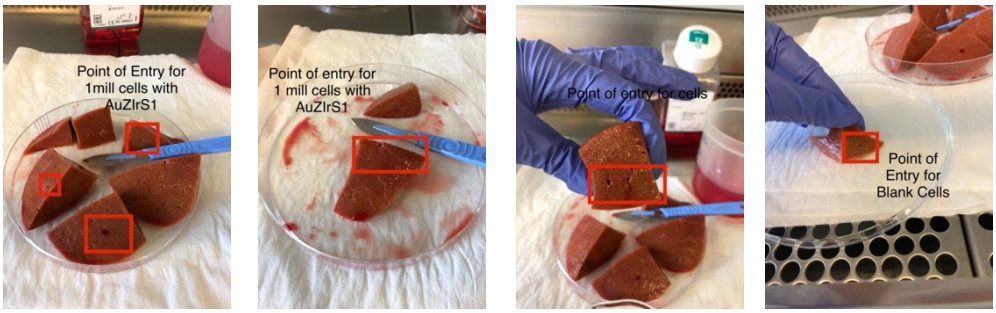

Fig 4.3.2 Left: Pictures of liver wedge divided and blood vessel openings chosen for points of entry of cells

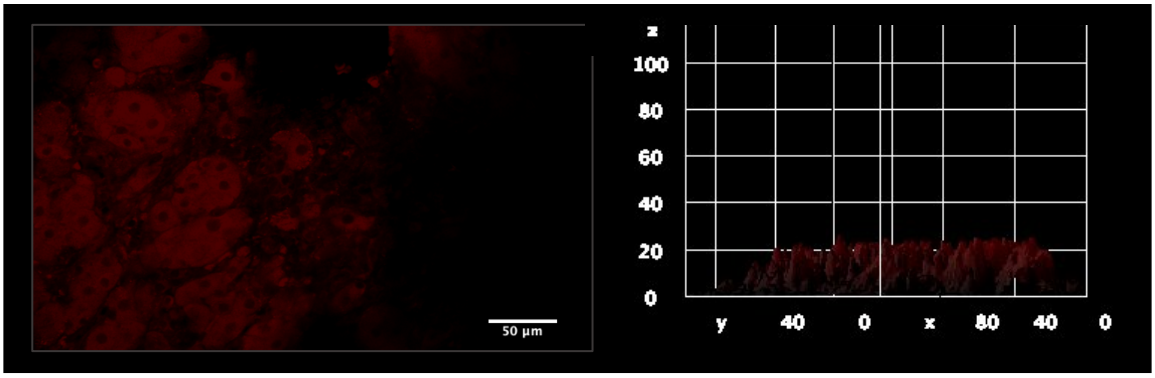

Fig 4.3.3 Left: Multiphoton image of liver tissue with administered blank CD3+ cells at λ_{ex} 800nm, λ_{em} 575-645nm. Right: 3D surface plot of the image where the z axis represents pixel intensity. Image analysis performed by ImageJ

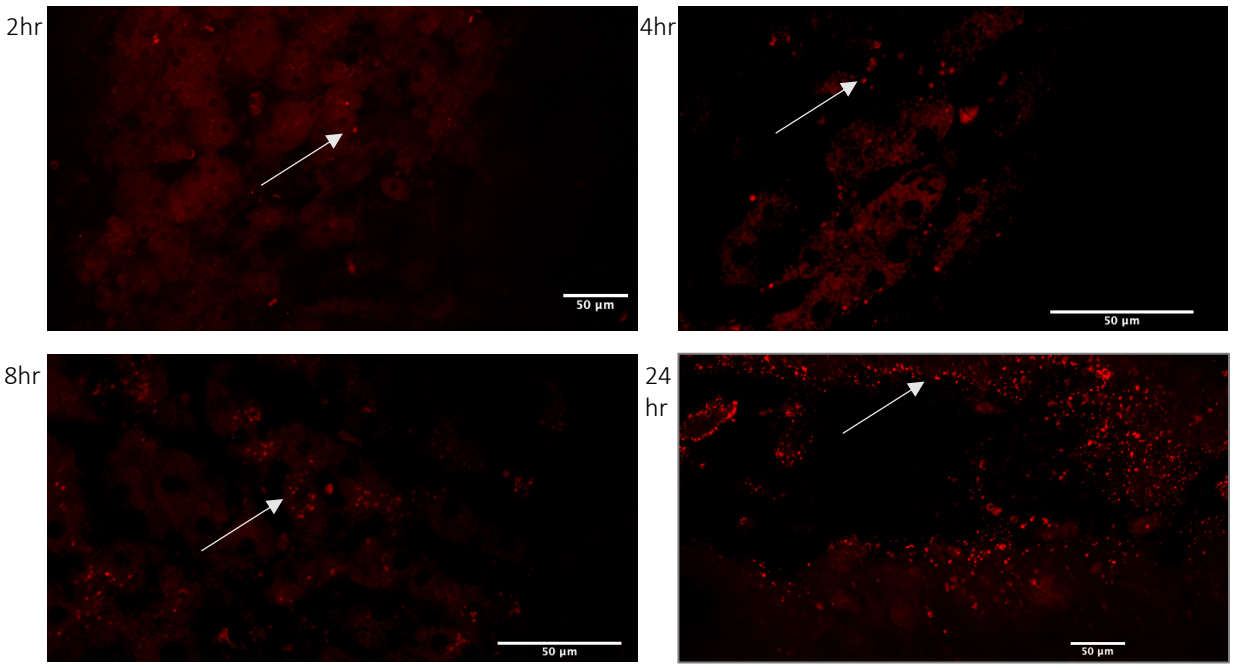

Fig 4.3.4 Multiphoton images of liver tissue with administered Au25NP.Zonyl.IrS1 labelled CD3+ cells at λ_{ex} 800nm, λ_{em} 575-645nm. Image analysis performed by ImageJ

Figure 4.3.3 shows the autofluorescence detected by multiphoton microscopy of the liver tissue injected with blank CD3+ cells at λ_{ex} 800nm, λ_{em} 575-645nm. The image shows clear structures of liver hepatocytes. The 3D surface plot of the image for the control sample showed no pixel intensity over ~20% in the observed channel.

Imaging of the liver tissue sections following the administration of Au25NP.Zonyl.IrS1 labelled CD3+ cells (Figure 4.3.4) displayed distinctly brighter spots of fluorescence attributed to IrS1. The 3D surface plot analysis of the images indicates IrS1 responsible for the brighter spots, showing pixel intensities well above 20% (Figure 4.3.5). Image analysis also found the brighter spots had a diameter of approximately 7-11μm, the expected size of CD3+ cells.

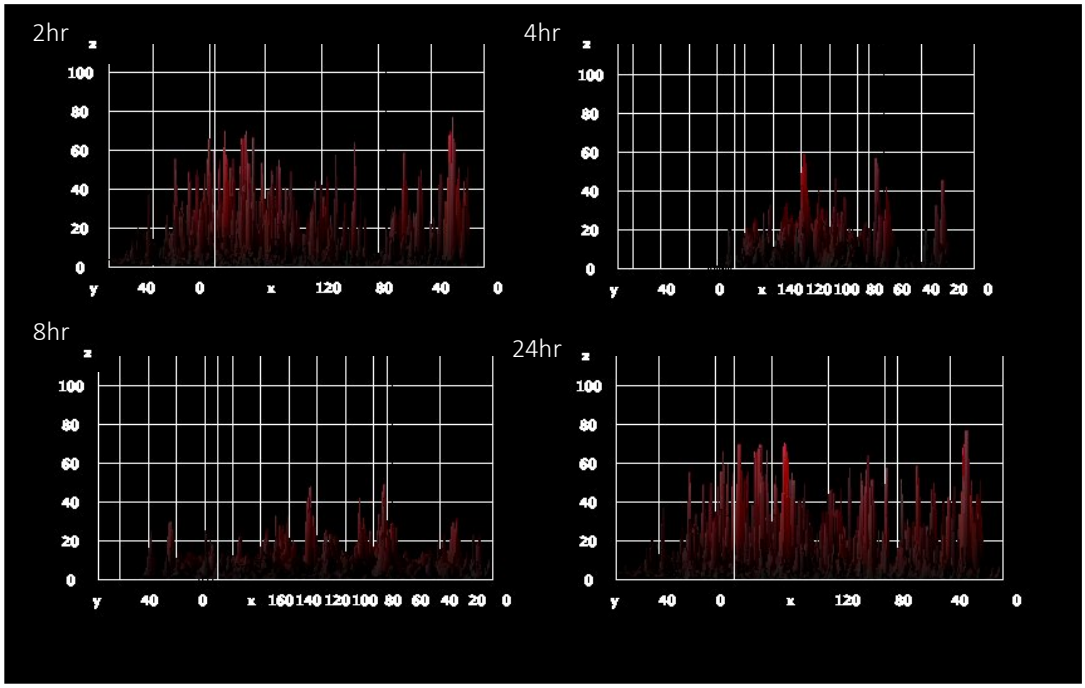

Fig 4.3.5 3D surface plot analysis of the multiphoton images of liver tissue with administered Au25NP.Zonyl.IrS1 labelled CD3+ cells at λ_{ex} 800nm, λ_{em} 575-645nm.
Image analysis performed by ImageJ

Interestingly, a greater pixel intensity of close to 80% is observed after just 2 hours post administration of labelled CD3+ cells, which is also seen in images after 24-hours. A drop in pixel intensity is observed at the 4- and 8-hour intervals suggesting

cells are circulating even in the absence of a steady blood flow. Ideally, one would wish to create a system in which the cells are administered at the same rate as the flow of blood in a human body. However, for the purpose of this study, liver tissue was incubated in RMPI cell media in order to facilitate some cell flow based on the principles of concentration gradient. During the incubation periods, cells would move to regions of low cell concentrations and so there would be a minor flow throughout the liver tissue. Although this is not an ideal method of simulating blood flow, the multiphoton images and 3D surface plot analysis implies some movement of cells has occurred during the incubation period. The greater pixel intensity and greater number of brighter spots seen after 24 hours of incubation could suggest the majority of labelled cells had settled into the liver tissue by this time.

During therapy, it is believed that cells would arrive to the liver within the first 4 hours post administration of the cells[22]. The results obtained from multiphoton imaging implies Au25NP.Zonyl.IrS1 would be effective for at least 24 hours post administration and potentially longer, however, it was not feasible to test longer timepoints because of consideration of the health of the liver tissue outside the human body. The fluctuation of pixel intensity over the 24-hour period could indicate that chemokine expression has not been diminished as chemotaxis of the cells has remained functioning, although further analysis of the inflammation sites in the tissue would be needed to confirm this observation. The liver tissue obtained for these experiments was from a patient with alcoholic liver disease, so sites of inflammation would be expected throughout the tissue. Although no other tissue stains were used for these assays, it would be of interest to use other surface stains to co-localise the final positions of the labelled CD3+ cells with areas on the liver tissue.

4.4 Imaging of Au25NP.Zonyl.IrS1 in Labelled CD3+ Cells Administered to Liver Sections using Micro-CT

The fixed liver sections used for multiphoton microscopy were next analysed with Micro-CT. A practical advantage of using a nanoprobe such as Au25NP.Zonyl.IrS1 is that in addition to the gold nanoparticle acting as a scaffold, they are themselves detectable in Micro-CT. Figure 4.4.1 shows reconstructed images obtained from the liver sections post 2, 4 and 8 hours administration with CD3+ cells labelled with Au25NP.Zonyl.IrS1 as well as the control sample.

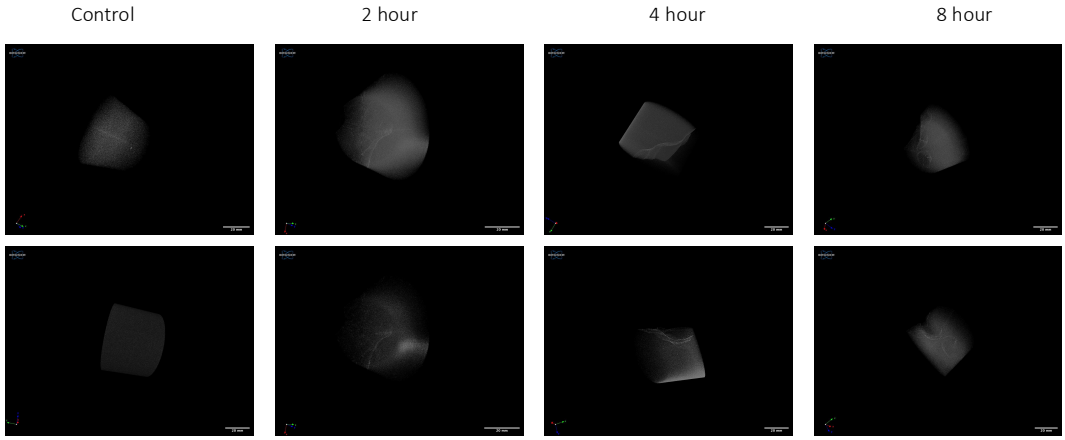

Fig 4.4.1 Micro-CT reconstructed image liver tissue with administered Au25NP.Zonyl.IrS1 labelled CD3+ cells. X-ray 100kV, average intensity of x-ray 40-60%. 50mm FOV. Image analysis performed by ImageJ. Scale bar = 20mm

Structures with enhanced intensity were observed at each time point. The whiter regions are indicative of the greater attenuation of X-rays facilitated by the presence of gold nanoparticles. Following the same trend seen with multiphoton microscopy, the liver wedges after 4- and 8-hours incubation showed a lower intensity, however this fluctuation is seen less using the Micro-CT due to the much larger imaging field. The images obtained after 24 hours showed the greatest intensity (Figure 4.4.2). The length of the visible vessel in the view was measured at approximately 6mm, which would correspond to blood vessels observed in the liver pre-cell administration, however some variation is expected when fixing the tissue.

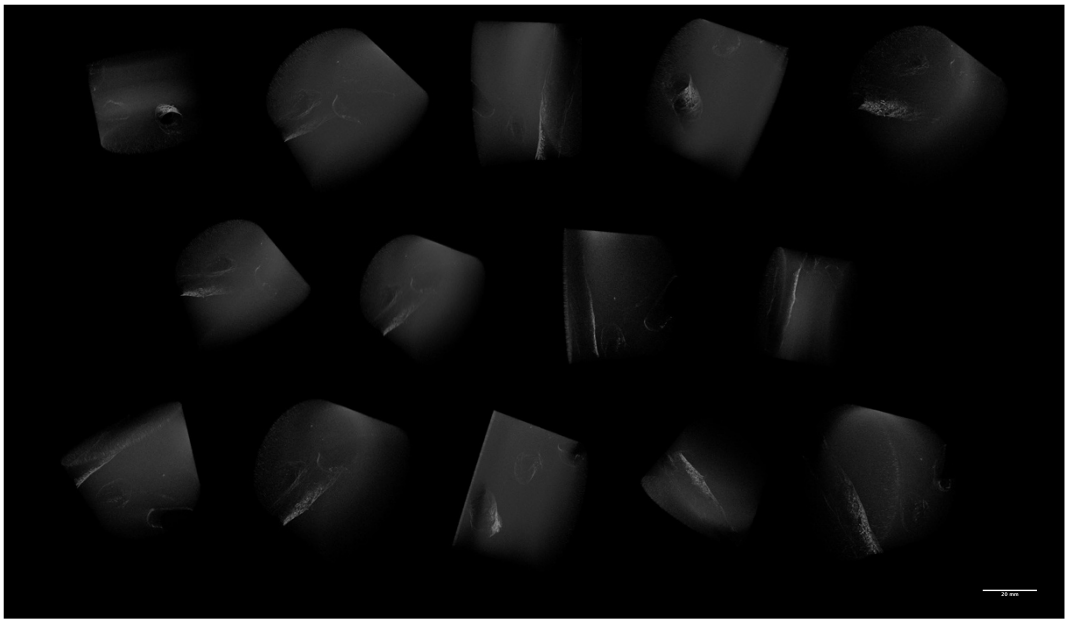

Fig 4.4.2 Micro-CT reconstructed image liver tissue with administered Au25NP.Zonyl.IrS1 labelled CD3+ cells post 24 hour incubation. X-ray 100kV, average intensity of x-ray 40-60%. 50mm FOV. Image analysis performed by ImageJ.
Scale bar = 20mm. Each image is a different orientation of the same sample

3D surface plots were used to analysis the pixel intensity of the blank sample and the sample after 24-hour incubation (Figure 4.4.3).

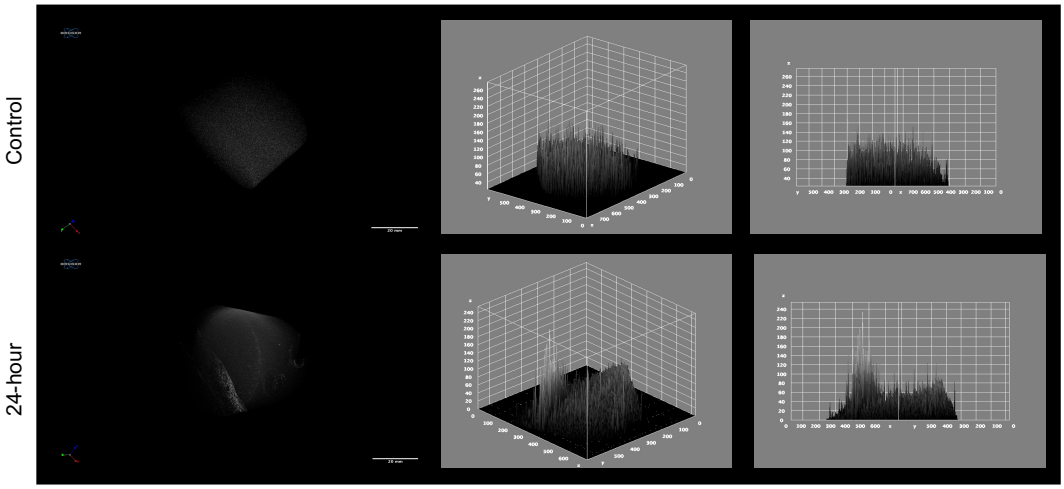

Fig 4.4.3 Micro-CT reconstructed image liver tissue with administered Au25NP.Zonyl.IrS1 labelled CD3+ cells post 24 hour incubation. X-ray 100kV, average intensity of x-ray 40-60%. 50mm FOV. Image analysis performed by ImageJ. Corresponding 3D surface plots of pixel intensity of each image. Scale bar = 20mm

Biological samples, including human liver tissue, are prone to scattering X-rays and as such the blank sample shows an average pixel intensity of 100%. However, the 24-hour sample displays a much greater pixel intensity, peaking at over 200%. This increased signal is attributed to the attenuation caused by the gold nanoparticles.

4.5 Conclusion

This chapter investigated the imaging properties and detectability of CD3+ cells labelled with nanoprobes having a gold core diameter of 25nm. TEM of the gold nanoparticles themselves confirmed not only the size but also the monodispersity of the AuNPs through each stage of coating which agreed with DLS and UV-VIS data characterised in chapter two. TEM was then employed to provide information on the internalisation of the nanoprobes into the cells. This experiment was of particular interest as its outcomes suggested an endocytic uptake pathway with the presence of vesicular structures around the nanoparticles and also agreed with ICP-MS data provided in chapter three in that the LPEG coated nanoprobes were less effectively taken up by the cells. This along with the conclusions made in chapter three strengthened the decision to only use Au25NP.Zonyl.IrS1 labelled cells for experiments with the human liver tissue.

Multiphoton microscopy showed distinct regions of high intensity light emission which can be translated to clusters of the labelled CD3+ cells in the liver tissue. Although it would be difficult to match up exactly the regions of tissue imaged in the multiphoton microscope to the images obtained using the micro-CT, regions of high light intensity can be observed with micro-CT imaging which correspond to the attenuation of X-rays by the gold nanoparticles.

The fluctuating light intensity of the samples between incubation times is suggestive of cell migration through the tissue and as such has demonstrated the ability to track the labelled cells using the Au25NP.Zonyl.IrS1 probe. The experiments of this chapter are pivotal in establishing the use of inorganic nanoprobes for cell tracking with multimodal applications in human liver tissue.

4.6 Materials and Methods

Human liver sections were obtained from patients who were admitted to the Liver Unit at the Queen Elizabeth Hospital, Birmingham, UK (Local Research Ethics Committee reference no.18/WA/0214). All donor livers included in this study were originally retrieved with the primary intention for transplantation as per the policy of the National Health Service Blood and Transplant (NHSBT). The organs were subsequently rejected for transplantation by all UK liver transplant centers and, following that, were offered nationally for research by NHSBT. This was done by the transplant surgeons at each center. Informed consent for research use of donor organs was obtained by specialist nurses in organ donation from the donor's next of kin during informed consent for organ donation. Authorisation for research was mediated by each centre's specialist nurse in organ donation.

Preparation of AuNPs for TEM

2nM concentration of Au25NPs, Au25NP.Coating and Au25NP.Coating.IrS1 were prepared via centrifugation of stock Au25NPs. These were resuspended in ultrapure water. Using a glass pipette, a drop of the sample was administered to a formvar-coated copper grid (Agar Scientific) and allowed to dry overnight.

Preparation of CD3+ Cells for TEM

CD3+ cells were isolated from human HFE blood as described previously using a CD3+ negative isolation kit, please see chapter three, and incubated with 1nM nanoprobe per 1 million cells overnight for 18hours. For this study, a sample of cells remained unlabelled as a control batch. Cells were then fixed with a 20% glutamine fixative and centrifuged to form a pellet in the sample tube and covered with 2ml of

fixative. The pellet was then sectioned for TEM imaging by the team at the imaging suite and mounted onto the copper grids without staining.

Preparation of CD3+ Cells for Confocal and Multiphoton Microscopy

CD3+ cells were isolated from human HFE blood as described previously using a CD3+ negative isolation kit, please see chapter three, and incubated with 1nM nanoprobe per 1 million cells overnight for 18hours. For this study, a sample of cells remained unlabelled as a control batch. Cells were fixed using 3% paraformaldehyde solution for 10 minutes before being resuspended in 200μl PBS. A Scientific Cytospin^{TM} (ThermoFisher) cytocentrifuge was used to adhere 100μl of cells to slides. The slides were washed in formal saline solution (10%) and dried overnight after which the slides were washed in pure water before drying and attaching the cover slip with a hydromount-mounting medium. The slides were fixed overnight.

Preparation of Labelled CD3+ Cells Administered to Liver Sections

CD3+ cells were isolated from human HFE blood as described previously using a CD3+ negative isolation kit, please see chapter three, and incubated with 1nM nanoprobe per 1 million cells overnight for 18hours. For this study, a sample of cells remained unlabelled as a control batch. Cells were transferred to FACS tubes and resuspended in 2% FCS. The human liver wedges were sectioned using a scalpel into smaller sections and cells ($1x10^6$ per 100μl) were administered to the liver section at a blood vessel entry point. Liver sections were incubated in RMPI cell media (1640 Gibco) containing L-Glutamine (0.5%), PhenylStrep (0.5%) and Fetal Bovine Serum (FBS) (10%) with the administered cells for 2, 4, 8 and 24 hours before being fixed with formaldehyde for 48 hours. $1cm^3$ sections in PBS were taken forward for imaging.

4.7 Instrumentation

Transmission electron microscopy (TEM) imaging was performed at the University of Birmingham Centre for Electron Microscopy. The Jeol 1400 Ex Bio TEM is fitted with an Oxford Instruments INCA EDS system. Samples were dried to copper grids prior to imaging.

Confocal imaging was performed on a Nikon A1R inverted confocal microscope with laser scanning equipped with a Perfect Focus System (PFS), piezo-z, multi laser beds and an inverted motorized stage at the University of Birmingham BALM facility. Laser lines 405nm used for these studies.

Multiphoton microscopy was performed using an intravital microscope IVM3 Olympus FV-MPE (Upright Multiphoton) (WXG96) at the University of Birmingham, Institute of Cardiovascular Sciences. Microscope settings: laser 0.2%, 500V, Gain 1.5x, Offset 0%.

Micro-CT was performed using a Skycan 1172 instrument (Brucker, Belgium) over 360° angular range with rotation steps 0.2° at the University of Birmingham. An excitation voltage of 100kV and 20% beam hardening and the detector pixel size of 3.02μm was used for all projections. The average intensity if X-rays was 40-60%. Images were collected by a 11 megapixel 12-bit digital CCD-camera, 50mm field of view.

4.8 Appendix

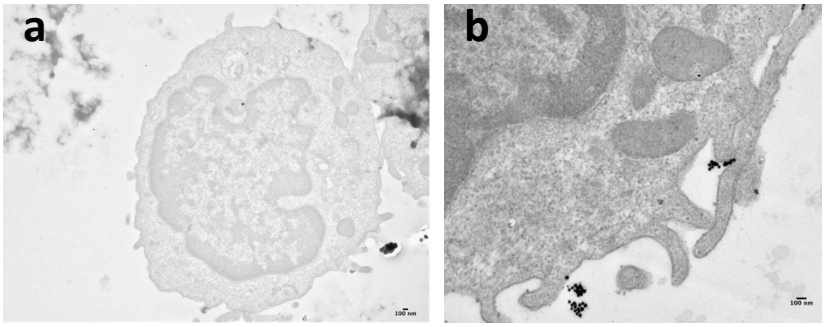

Appendix 4.8.1 TEM of CD3+ cell a) blank b) incubated with Au25NP.LPEG.IrS1

4.9 References

1. Marques, P. E.; Oliveira, A. G.; Chang, L.; Paula-Neto, H. A.; Menezes, G. B., Understanding liver immunology using intravital microscopy. *Journal of Hepatology* **2015,** *63* (3), 733-742.
2. Paddock, S. W., Confocal laser scanning microscopy. *Biotechniques* **1999,** *27* (5), 992-1004.
3. Paddock, S. W., Principles and practices of laser scanning confocal microscopy. *Molecular biotechnology* **2000,** *16* (2), 127-149.
4. Kavanagh, D. P. J.; Kalia, N., Live Intravital Imaging of Cellular Trafficking in the Cardiac Microvasculature—Beating the Odds. *Frontiers in Immunology* **2019,** *10* (2782).
5. Weigel, A.; Sebesta, A.; Kukura, P., Dark field microspectroscopy with single molecule fluorescence sensitivity. Journal of the *American Chemical Society photonics* **2014,** *1* (9), 848-856.
6. Liang, Y.; Walczak, P., Long term intravital single cell tracking under multiphoton microscopy. *Journal of Neuroscience Methods* **2021,** *349*, 109042.
7. Lin, H.; Fan, T.; Sui, J.; Wang, G.; Chen, J.; Zhuo, S.; Zhang, H., Recent advances in multiphoton microscopy combined with nanomaterials in the field of disease evolution and clinical applications to liver cancer. *Nanoscale* **2019,** *11* (42), 19619-19635.
8. Denk, W.; Strickler, J. H.; Webb, W. W., Two-photon laser scanning fluorescence microscopy. *Science* **1990,** *248* (4951), 73-76.
9. Ellenbroek, S. I.; Van Rheenen, J., Imaging hallmarks of cancer in living mice. *Nature Reviews Cancer* **2014,** *14* (6), 406-418.
10. Brown, E. B.; Campbell, R. B.; Tsuzuki, Y.; Xu, L.; Carmeliet, P.; Fukumura, D.; Jain, R. K., In vivo measurement of gene expression, angiogenesis and physiological function in tumors using multiphoton laser scanning microscopy. *Nature medicine* **2001,** *7* (7), 864-868.
11. Wang, H.; Huff, T. B.; Zweifel, D. A.; He, W.; Low, P. S.; Wei, A.; Cheng, J.-X., In vitro and in vivo two-photon luminescence imaging of single gold nanorods. *Proceedings of the National Academy of Sciences* **2005,** *102* (44), 15752-15756.
12. Durr, N. J.; Larson, T.; Smith, D. K.; Korgel, B. A.; Sokolov, K.; Ben-Yakar, A., Two-photon luminescence imaging of cancer cells using molecularly targeted gold nanorods. *Nano letters* **2007,** *7* (4), 941-945.
13. Tong, L.; Cobley, C. M.; Chen, J.; Xia, Y.; Cheng, J. X., Bright Three-Photon Luminescence from Gold/Silver Alloyed Nanostructures for Bioimaging with Negligible Photothermal Toxicity. *Angewandte Chemie International Edition* **2010,** *49* (20), 3485-3488.
14. Chandrasekaran, R.; Madheswaran, T.; Tharmalingam, N.; Bose, R. J. C.; Park, H.; Ha, D.-H., Labeling and tracking cells with gold nanoparticles. *Drug Discovery Today* **2021,** *26* (1), 94-105.
15. Jackson, P. A.; Rahman, W. N. W. A.; Wong, C. J.; Ackerly, T.; Geso, M., Potential dependent superiority of gold nanoparticles in comparison to iodinated contrast agents. *European Journal of Radiology* **2010,** *75* (1), 104-109.
16. Xi, D.; Dong, S.; Meng, X.; Lu, Q.; Meng, L.; Ye, J., Gold nanoparticles as computerized tomography (CT) contrast agents. *Royal Society of Chemistry Advances* **2012,** *2* (33), 12515-12524.
17. Cormode, D. P.; Naha, P. C.; Fayad, Z. A., Nanoparticle contrast agents for computed tomography: a focus on micelles. *Contrast media & molecular imaging* **2014,** *9* (1), 37-52.

18. Choo, Y. W.; Jeong, J.; Jung, K., Recent advances in intravital microscopy for investigation of dynamic cellular behavior in vivo. *British Medical Bulletin reports* **2020,** *53* (7), 357.
19. Niesner, R. A.; Hauser, A. E., Recent advances in dynamic intravital multi-photon microscopy. *Cytometry Part A* **2011,** *79* (10), 789-798.
20. Zauner, W.; Farrow, N.; Haines, A., In Vitro Uptake of Polystyrene Microspheres: Effect of Particle Size, Cell Line and Cell Density. *Journal of controlled release: official journal of the Controlled Release Society* **2001,** *71* (1), 39-51.
21. Jain, P. K.; Lee, K. S.; El-Sayed, I. H.; El-Sayed, M. A., Calculated Absorption and Scattering Properties of Gold Nanoparticles of Different Size, Shape, and Composition: Applications in Biological Imaging and Biomedicine. *The Journal of Physical Chemistry B* **2006,** *110* (14), 7238-7248.
22. Oo, Y. H.; Ackrill, S.; Cole, R.; Jenkins, L.; Anderson, P.; Jeffery, H. C.; Jones, N.; Jeffery, L. E.; Lutz, P.; Wawman, R. E.; Athwal, A. K.; Thompson, J.; Gray, J.; Guo, K.; Barton, D.; Hirschfield, G. M.; Wong, T.; Guest, P.; Adams, D. H., Liver homing of clinical grade Tregs after therapeutic infusion in patients with autoimmune hepatitis. *Journal of Hepatology Reports* **2019,** *1* (4), 286-296.

Chapter 5

General Conclusions and Future Works

Cell based therapies are revolutionising the field of autoimmune regulation in a time where biologics for treatments are providing a drug free alternative which could prove highly effective for disease regulation and drastically improve patient outcomes. The greatest challenges facing cell-based therapies are the vast arrays of known side effects experienced by patients. A contributory factor to the progression of these side effects is the off-target activity of the transplanted cells due to the systemic circulation of the therapy. Much research has been focused on controlling these side effects. The ability to track the cells administered, in real time, during their circulation could aid in preventing the unwanted side effects by allowing physicians to block or inhibit unwanted activity before it has occurred.

The work conducted and detailed in this thesis explores the development of a multimodal nanoprobe for labelling transplanted immune cells and to track their migration through tissue.

A novel probe library was created which encompassed 12 different nanoprobes based on gold nanoparticle cores with diameters of 13, 25, 50 and 100nm with differing stabilising agents, Zonyl, SPEG and LPEG, each with the same fluorophore, IrS1. For this work, the gold nanoparticle acted as a scaffold to carry multiple units of IrS1 fluorophores, enhancing its photophysical properties whilst remaining as biocompatible as possible. Although it is logical to assume the larger nanoparticles would be advantageous as it would mean more IrS1 could be added to the surface, in a biological context, the amount of exogenous material entering a cell must be considered as to not cause excessive damage to the cell.

To investigate this further, a series of experiments with isolated CD3+ cells from HFE blood were conducted in which the phenotypical and functional behaviour of the cells were assessed. As expected, the larger nanoprobes induced higher levels of cytotoxicity than their smaller counter parts. This along, with ICP-MS and TEM studies suggested the ideal AuNP size for this work would be those with a 25nm diameter. They exhibited low cytotoxicity whilst still holding a detectable amount of IrS1.

The biological impact of the stabilising agent coating was also investigated. Although there is much research in the literature on the use of PEG compounds to assist in the uptake of exogenous material into cells, something that is not so commonly addressed is the impact of PEG compounds on the phenotypical behaviour of cells. Cytokine and chemokine production and expression assays suggested the PEG coated nanoprobes were interfering with the expected cytokine and chemokine activity of the cells and so it was deemed appropriate to move forward with the Zonyl coated Au25NPs which had little to no significant impact on phenotypical behaviour.

Labelled CD3+ cells were then administered to sections of human liver via open blood vessels in the tissue. The images obtained of these liver sections by multiphoton microscopy and micro-CT encapsulate the multimodal tracking ability of the Au25NP.Zonyl.IrS1 nanoprobe developed.

The work conducted in this thesis has showcased a nanoprobe with real abilities to be tracked in cells that have been transplanted into tissue. The collection of imaging techniques used have been possible due to the multimodal design of the nanoprobe, making use of the optical properties of gold nanoparticles and the fluorescence properties of the IrS1.

The development of Au25NP.Zonyl.IrS1 has addressed some of the aforementioned challenges faced by cell tracking systems which are currently being used in clinic. Firstly, the multimodal facet of Au25NP.Zonyl.IrS1 means imaging can occur at a sub-cellular level, all the way to organ tissue level using a variety of imaging modalities. This means information on the interaction of the probes within a biological environment can be obtained to highlight the source of any adverse events occurring as a result of the labelling process. Secondly, the probe showed long term retention in cells, measured up-to 24 hours, when incubated with non-labelled cells. This data shows real promise as it suggests tracking of labelled cells only. Thirdly, the absence of any significant affect on phenotypical behaviour of the labelled cells means that transplanted cells should continue to behave and exert functionality as expected, a vital requirement for immune therapies to be successful. This thesis also highlights the feasibility of detecting the probe in labelled cells post administration to liver tissue.

Moving forward, the next stages of experiments would ideally involve a whole liver perfusion experiment in which labelled cells would be perfused around a whole liver at a steady flow replicating that of human blood flow. After 4 hours the liver would be biopsied at an array of locations to be imaged by both multiphoton microscopy and micro-CT to examine the localisation of the labelled cells. An advantage of the multiphoton microscopy is that the labelled cells are very distinguishable against the hepatic background, so in checking the localisation of the cells, one could also examine the tissue to confirm the nanoprobes have remained in the transplanted cells and haven't bled through to the hepatocytes. This experiment had been planned for the final stages of this thesis, unfortunately due to COVID-19

restrictions, access to whole organs for perfusion, as well as access to hospital facilities meant this was not feasible under the current climate.

With further optimisation, other cell types in the liver tissue could also be stained for to study interactions of the transplanted cells with surrounding cells.

Intravital, real-time tracking could be achieved with transplanted cells being administered to mouse models. However, this would require extensive optimisation as mouse lymphocytes would need to be used rather than human lymphocytes, as is in this work. Nonetheless, intravital imaging such as this has been conducted using the multiphoton microscope with the major advantage of being able to examine the systemic circulation of the labelled cells. Here an experiment to determine qualitatively the amount of labelled cells found in the liver would be desirable to indicate any off target activity.